Daniel Gasser, Dipl.-Ing., BSc

Investigations on the horizontal stress state of non-cohesive soils due to deep vibro compaction

MASTER'S THESIS

to achieve the university degree of

Diplom-Ingenieur

Master's degree programme: Civil Engineering Sciences, Geotechnics and Hydraulics

submitted to

Graz University of Technology

Supervisor

Univ.-Prof. Dipl.-Ing. Dr.techn., Roman Marte

Institute of Soil Mechanics, Foundation Engineering and Computational Geotechnics

Univ.-Prof. Dipl.-Ing. Dr.techn., Franz Tschuchnigg

Graz, November 2020

AFFIDAVIT

I declare that I have authored this thesis independently, that I have not used other than the declared sources/resources, and that I have explicitly indicated all material which has been quoted either literally or by content from the sources used. The text document uploaded to TUGRAZonline is identical to the present master‘s thesis.

Date

Signature

Acknowledgements

At this point I would like to thank those who supported me during the past few months.

As my thesis supervisor, professor Roman MARTE supported me in all stages of this work. He is the initiator of this project and he always gave me advice and the opportunity to discuss, despite his busy agenda.

I would like to acknowledge the assistance of professor Franz TSCHUCHNIGG who offered me valuable suggestions especially for the numerical studies.

I extend my sincere thanks to all members of the Institute of Soil Mechanics, Foundation Engineering and Computational Geotechnics, and all those who contributed directly or indirectly to the thesis. In particular, I wish to express my gratitude to Simon OBERHOLLENZER and Laurin HAUSER for generously sharing their expertise and for their helpful suggestions whenever I had problems during the studies.

Furthermore, I sincerely thank Andreas HASAWEND from the geotechnical laboratory of the Graz University of Technology. Without his help the experimental investigations would not have been possible.

From Keller Grundbau Ges.mbH I would like to thank Franz RATHMAIR and Astrid KAINEDER who supported me at the test area in Linz. A special thanks goes also to the working teams for the realization of the large scale deep vibro compaction experiment.

I want to thank Martin SCHLEGEL from Premstaller Geotechnik ZT-GmbH for the performance of the compaction control techniques on-site.

Without the support of all members of my family, I would never have finished this thesis and I would never have found the courage to overcome all the difficulties during this work. My thanks go to my parents Hildegard NIEDERBACHER and Erwin GASSER for their confidence and their love during all these years. My thanks go also to my sister Melanie GASSER and my brother Fabian GASSER for their unconditional support at any time.

Finally, I would like to thank all my friends in Graz who made the studies an unforgettable and nice time.

This work was supported by Keller Grundbau Ges.mbH.

Abstract

Vibratory compaction methods for deep-reaching improvement of non-cohesive soils have been used since the 1930s. Either depth vibrators or top vibrators can be applied. The compaction process leads to a change in soil stiffness, soil strength, horizontal stress, permeability, etc.

This thesis focuses on the horizontal stress increase in the subsoil due to deep vibro compaction. In cooperation with Keller Grundbau Ges.mbH a large scale compaction experiment was realized. At two test areas the inclinodeformeter was used the first time for this application. Additionally, conventional compaction control techniques (dynamic probing tests, cone penetration tests, seismic cone penetration tests) were performed.

Using existing empirical relationships, soil properties could be estimated before and after compaction. The correlations were critically questioned in the thesis.

The inclinodeformeter measurements provided findings on the horizontal stress increase. The mean inclinometer pipe diameter was not appropriate to evaluate the stress increase. The ovalization value was a suitable parameter.

The second part of the thesis includes numerical studies with the finite element method. The behaviour of the inclinometer pipe cross section at different model approaches and load scenarios was investigated. Furthermore, parts of both test areas were modelled, and the compaction process was simulated in a simplified way. The calibration of the numerical models on selected measurement results allowed an evaluation of the horizontal stress increase.

Kurzfassung

Untersuchungen zur Horizontalverspannung nicht bindiger Böden durch die Rütteldruckverdichtung

Vibrationsverdichtungsverfahren zur tiefreichenden Verbesserung nicht bindiger Böden werden seit den 1930er Jahren eingesetzt. Zum Einsatz kommen entweder Tiefenrüttler oder Aufsatzrüttler. Der Rüttelvorgang führt im Boden zu einer Veränderung der Steifigkeit, Festigkeit, Horizontalspannung, Durchlässigkeit, usw.

Schwerpunkt dieser Arbeit ist die Horizontalverspannung im Untergrund zufolge der Rütteldruckverdichtung. In Kooperation mit Keller Grundbau Ges.mbH wurde ein großmaßstäblicher Verdichtungsversuch realisiert. An zwei Versuchsfeldern kam das Inklinodeformeter erstmals für diesen Anwendungsfall zum Einsatz. Begleitend wurden konventionelle Verdichtungskontrollen (Rammsondierungen, Drucksondierungen, Seismische Drucksondierungen) durchgeführt.

Durch die Anwendung existierender empirischer Zusammenhänge konnten Bodeneigenschaften vor und nach der Verdichtung abgeschätzt werden. Die Korrelationen wurden in der Arbeit kritisch hinterfragt.

Die Inklinodeformetermessungen lieferten Erkenntnisse zur Horizontalverspannung. Der mittlere Inklinometerrohrdurchmesser war für die Bewertung der Verspannung ungeeignet. Hingegen eignete sich der Ovalisierungswert als Kenngröße.

Der zweite Teil der Arbeit umfasst numerische Studien unter Anwendung der Finite Elemente Methode. Zunächst wurde das Verhalten des Inklinometerrohrquerschnitts bei unterschiedlichen Modellansätzen und verschiedenen Lastszenarien untersucht. Darauf aufbauend wurden Ausschnitte der beiden Versuchsfelder nachmodelliert und der Verdichtungsprozess vereinfacht simuliert. Die Kalibrierung der numerischen Modelle an ausgewählten Messergebnissen ermöglichte eine Bewertung der Horizontalverspannung.

Table of Contents

List of Abbreviations

A	measurement direction A
-A	associated with test area A (grid spacing: 2.70 m x 2.70 m)
B	measurement direction B
-B	associated with test area B (grid spacing: 3.10 m x 3.10 m)
C	measurement direction C
CPTu	cone penetration test with pore water pressure measurement
D	measurement direction D
DPH	dynamic probing heavy
DVC	deep vibro compaction
GLAC	ground level after compaction
GLBC	ground level before compaction
GWL	groundwater level
IDM	inclinodeformeter
IPC	inclinometer pipe connection
LC	load case
MCD	maximum compaction depth
PVC	polyvinyl chloride
SCPT	seismic cone penetration test
000	measurement in direction
180	measurement in opposite direction

1 Introduction

1.1 Motivation

Realization of structures always makes use of the soil on which, in which or with which they are built. Whenever engineers find that the natural conditions of the soil are inadequate for the envisaged work they are faced with the following alternatives:

1. redesigning the structure for these conditions,
2. removing the unsuitable soil and replacing it with appropriate soil,
3. bypassing the unsuitable soil by choosing a deep foundation,
4. improving these conditions to the necessary extent, cf. [6, p. 1].

There exist various methods for ground improvement. Before an appropriate measure is selected it is necessary to determine the requirements, which follow from the ultimate and serviceability limit state of design. This includes:

- increase of density and shear strength with positive effect on stability problems,
- reduction of compressibility with positive effect on deformations,
- reduction/ increase of permeability to reduce water flow/ to accelerate consolidation,
- improvement of homogeneity to equalise deformation, cf. [6, p. 1].

Since the development of deep vibro compaction during the 1930s and of deep vibro replacement stone columns in the 1970s, they have become the most frequently used ground improvement methods worldwide due to their unrivalled versatility and wide range of application. Each of the methods has its own characteristics and manner of execution. Even machine types are different for the two systems of ground improvement, as are design principles, field testing and quality control, cf. [6, pp. 2 - 3].

For the deep vibro compaction method, design and quality control have remained almost entirely empirical until today. The development of predictive techniques based on soil dynamics to calculate the improved properties of the soil after compaction was probably inhibited by the simplicity of in situ penetration testing. There exist correlations to assess the improvement based on the measurement results.

The entire effect of the deep vibro compaction on the subsoil is not yet completely known. The stiffness changes due to the grain redistribution effect are undisputable. The amount is in general determined by using the mentioned empirical correlations. Also first numerical attempts exist. Concerning the changes in stress state and the potential overconsolidation in the subsoil, only first approaches can be found in the literature. The predicted state of overconsolidation is controversial and at the time subject of several publications.

Certainly, all three mentioned effects (stiffness changes, changes in stress state and overconsolidation) have an important influence on the settlement calculation and consequently also on the efficiency and the economy of the method.

Means for improving unsuitable soils must be practical, efficient, economical and environmentally acceptable. Especially the last criteria is one of the major strengths of the deep vibro methods. The deep vibro compaction as well as the deep vibro replacement stone columns technique generates considerably lower greenhouse gases, notably carbon dioxide, as the conventional foundation systems and requires only natural materials for the execution. Furthermore, the impact on the ground and the groundwater is environmentally harmless.

Further work and research on the subject enable further plant development and improvement of the existing design and quality control techniques. This is the basis for an increase in practicability, efficiency and economy of the method.

1.2 Goal

This thesis should provide new knowledge about the effects of the deep vibro compaction method on the subsoil. The focus is on the changes in stress state and the potential overconsolidation in the subsoil. By the first-time usage of the inclinodeformeter at a deep vibro compaction field new significant data is expected. In connection with the measurement results from traditional quality control techniques an extensive data base should be created. On this basis empirical correlations should be evaluated and numerical studies should be performed.

The utilization of the collected data at further research activities is not excluded.

1.3 Thesis structure

The first part of the thesis (chapter 2) includes the theoretical background. First, the deep compaction methods suitable for non-cohesive soils are introduced. The compactibility of these soils is discussed and the current state of knowledge about the effects on the subsoil is documented. Finally, the generally used compaction control techniques are described. In addition, the inclinodeformeter method is explained.

The second part (chapter 3) covers the large scale deep vibro compaction experiment performed in cooperation with Keller Grundbau Ges.mbH. The concept and the planned test area are described in detail. The procedure on-site is documented with figures and explanations. In the last section the measurement results are evaluated, and the test results are shown and interpreted.

The third part (chapter 4) includes numerical studies concerning the inclinometer pipe as well as the test area A and the test area B. By using selected measurement results findings about the horizontal earth pressure changes and the potential overconsolidation in the subsoil after the compaction are expected.

2 Theory

In this chapter the deep compaction methods appropriate for non-cohesive soils, the compactibility of non-cohesive soils, the mode of action of deep compaction methods and finally the available compaction control techniques are discussed.

2.1 Deep compaction methods for non-cohesive soils

2.1.1 Vibratory compaction methods

The most efficient way to densify deep deposits of granular material is to introduce the compaction energy at depth. The energy can either be applied by vertical or horizontal vibration, or a combination of both. Several deep vibratory compaction methods were developed during the past decades and are used for a variety of applications, cf. [8, p. 34].

2.1.1.1 Vibroflotation method

This method was invented in Germany during the 1930s and its development has continued mainly there and in North America, where it was introduced in the 1940s. Vibroflotation is today the most widely used deep compaction method and extensive experience has been accumulated over time.

The design principles of modern depth vibrators have little changed since the time they were invented and then further developed to suit the needs of practical use on sites. The vibrator is essentially a cylindrical steel tube with external diameters ranging between 300 mm and almost 500 mm, containing internally as its main feature an eccentric weight at the bottom, mounted on a vertical shaft which is linked to a motor in the body of the machine above. The length of the vibrator is typically between 3.0 m and 4.5 m and its weight ranges from 1500 kg to about 4500 kg.

When set in motion, the eccentric weight rotates around its vertical axis and causes horizontal vibrations that are needed for the vibro compaction method. The dynamic horizontal forces are thus applied directly to the surrounding soil through the tubular casing of the vibrator.

A flexible, vibration dampening device or coupling connects the vibrator with follower tubes of the same or slightly smaller diameter providing extension for deep penetration into the ground. These tubes contain water and power lines for the motor, occasionally also air pipes for jets located at the nose of the vibrator and at opposite sides generally just above the coupling.

Motor drive is either electric or hydraulic, powered by a generator or power pack which is generally mounted as a counterweight on the rear of the suspending crane. Common

power ratings of vibrator motors are between 50 kW and 180 kW with the largest machines developing up to 220 kW. The rotational speed of the eccentric weight, which can also be split into two or more parts for structural reasons, is with electrically driven machines determined by the frequency of the current and the polarity of the electric motor. A 50 Hz power source results in a 3000 rpm or 1500 rpm rotational motion with a single or double pole drive. When operating at 60 Hz, the rotational speed is 3600 rpm or 1800 rpm respectively, cf. [6, p. 31].

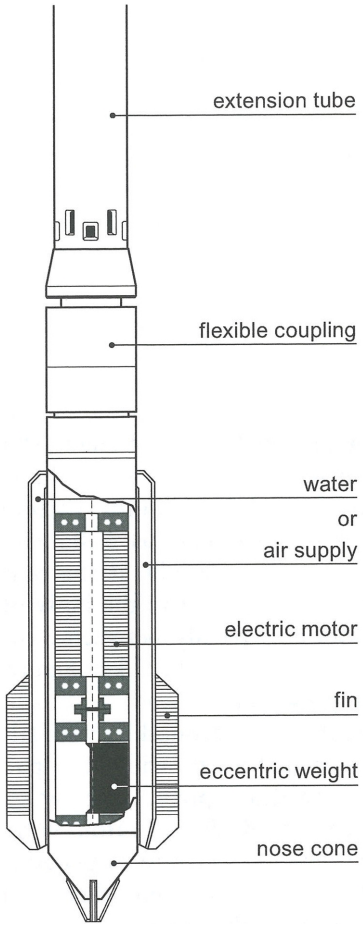

Figure 2.1: Cross section through the depth vibrator according to [6, p. 32]

The width of the horizontal oscillation, or double amplitude, is linearly distributed over the length of the vibrator. It is zero at the vibrator coupling and reaches its maximum, typically between 10 mm and almost 50 mm, at the point or nose cone of the freely suspended vibrator when operating without any lateral confinement. This is also the point of maximum acceleration at the vibrator surface, which can reach over 50 g.

The centrifugal force is resulting from the rotational speed of the eccentric weight with the mass M and an eccentricity of e, and acts as lateral impact force on the surrounding soil causing its compaction. The centrifugal force ranges between 150 kN for smaller vibrators and over 700 kN for the heaviest depth vibrators. When the machine is in normal working conditions it is restrained by the ground and oscillation amplitudes and surface accelerations are much less despite the constant centrifugal force, cf. [6, pp. 32 - 33].

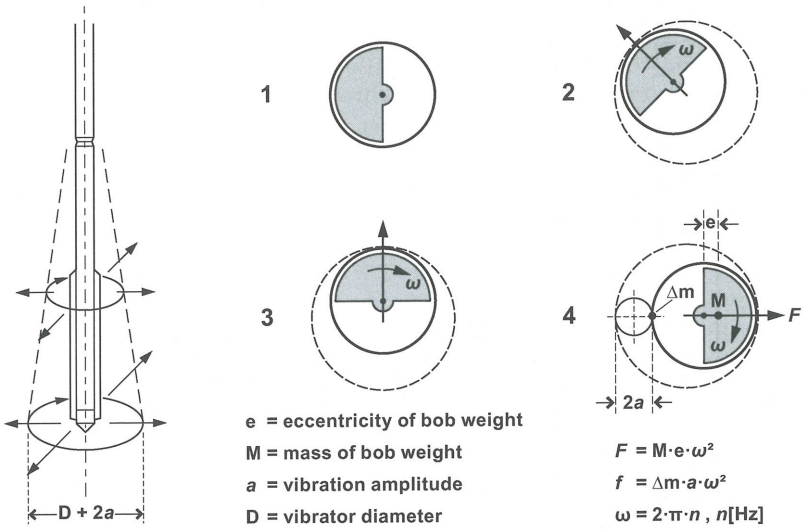

Figure 2.2: Principle of vibro compaction and vibrator accelerations in the horizontal plane according to [6, p. 33]

The procedure is explained and illustrated in the following figures.

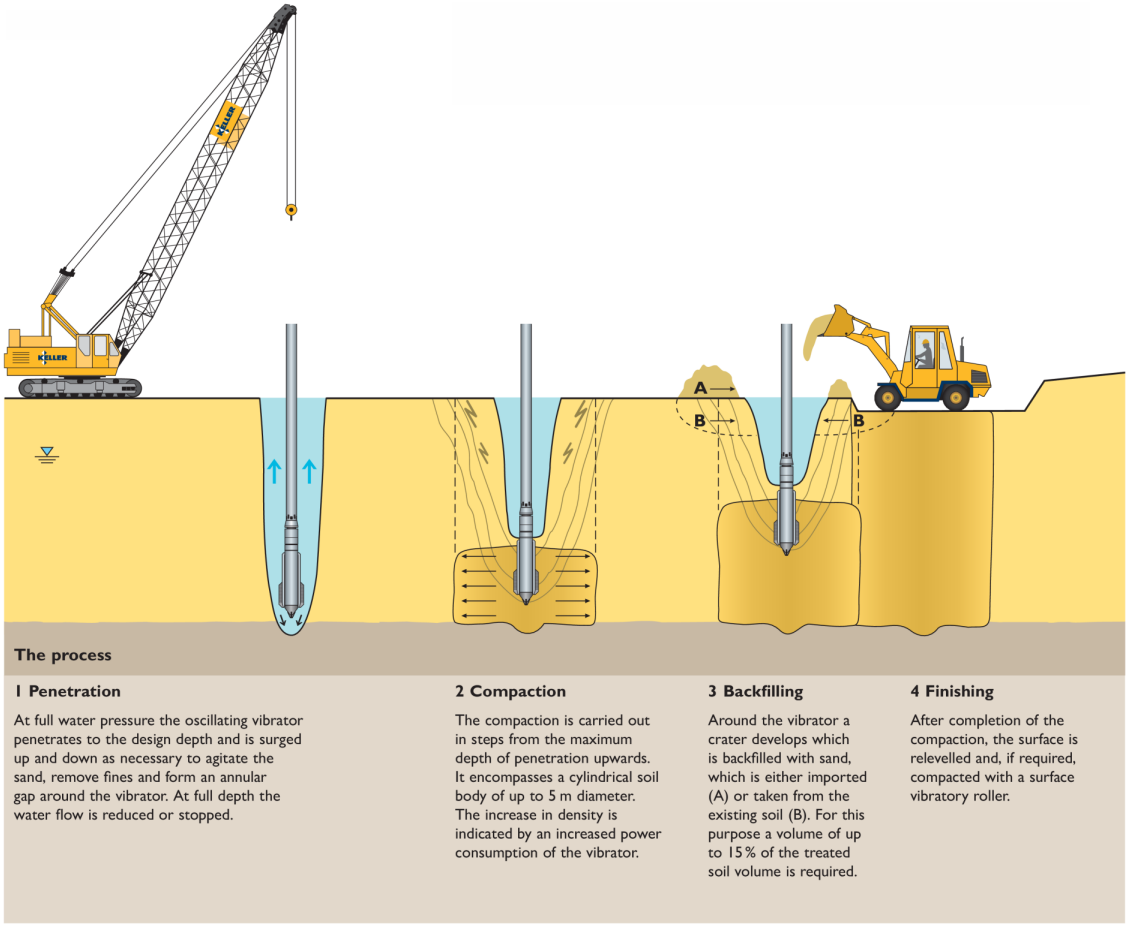

Figure 2.3: Procedure vibroflotation method - sketch according to [5]

Figure 2.4: Procedure vibroflotation method - photographs

2.1.1.2 Vibro-Wing method

The Vibro-Rod method exists in several different variations. A compaction probe is inserted in the ground with the aid of a heavy, vertically oscillating vibrator, attached to the upper end of the compaction rod. The insertion and extraction process is repeated several times, thereby gradually improving the soil. Different types of compaction probes have been developed, ranging from conventional tubes or sheet pile profiles to more sophisticated tools. The Vibro-Rod method was initially developed in Japan, where a slender rod was provided with short ribs. The rod was vibrated, using conventional vibratory pile driving equipment, cf. [8, p. 34].

The Vibro-Wing method was developed in Sweden and is a further improvement of the Vibro-Rod method. An up to 15 m long steel rod is provided with about 0.8 to 1.0 m long radial wings, at a vertical spacing of approximately 0.5 m. The vibratory hammer is usually operated from a piling rig. The frequency of the vibrator can be varied to fit the conditions at a particular site. The duration of vibration and rate of withdrawal of the probe is chosen depending on the permeability of the soil, the depth of the soil deposit and the spacing between the compaction points. The duration of compaction, the grid spacing and the number of probe insertions are chosen empirically or are determined by field tests. The maximum depth of compaction depends on the capacity of the vibrator and size of the piling rig and is on the order of 10 to 15 m, cf. [8, p. 34].

The resonance compaction method is similar to the Vibro-Rod method but uses the

vibration amplification effect, which occurs when the vibrator, the compaction probe and the soil are vibrating at resonance. In this state, ground vibrations are strongly amplified and the efficiency of vibratory soil densification increases. A heavy vibrator with variable frequency is attached to the upper end of a flexible compaction probe. The probe is inserted into the ground at a high frequency (around 30 Hz) in order to reduce the soil resistance along the shaft and the toe. When the probe reaches the required depth, the frequency is adjusted to the resonance frequency of the vibrator-soil system.

The probe is oscillated in the vertical direction and the vibration energy is transmitted to the surrounding soil along the entire probe surface. At resonance, the soil layer vibrates in phase with the compaction probe. At this state, vibration energy is transferred very efficiently from the vibrator to the compaction probe and to the surrounding soil, as the relative movement between the compaction probe and the soil is small. This is an important advantage, compared to conventional vibratory compaction methods. At resonance, which occurs typically between 10 to 20 Hz, the required compaction energy decreases. In this phase of soil compaction, the oil pressure of the vibrator decreases, which reduces the fuel consumption and the wear on the vibratory equipment.

The compaction probe is an essential component of the system and is designed to achieve optimal transfer of energy from the vibrator to the soil. The probe profile has a double Y-shape, which increases the compaction influence area. Reducing the stiffness of the probe further increases the transfer of energy to the surrounding soil. This is achieved by openings in the probe. The openings also have the advantage of making the probe lighter and thereby providing larger displacement amplitude during vibration, compared to a massive probe of the same size.

The dynamic response of the soil deposit during compaction can also be used to monitor the compaction effect. With increasing densification of the soil layers, the resonance compaction frequency rises. With the aid of vibration sensors placed on the ground surface, the change in wave propagation velocity can be determined, which reflects the change of soil stiffness and soil strength, cf. [8, pp. 35 - 36].

Figure 2.5: Resonance compaction method according to [3]

2.1.2 Compaction by vertical, pulsed impacts

2.1.2.1 Dynamic compaction

The dynamic compaction method is based on an ancient principle. Louis Ménard rediscovered the technique in the 1960s.

By the impact of a properly shaped steel pounder, weighing between 10 to 40 t and released in free fall from a height of 5 to 40 m, high-energy shock waves are created and transferred to the subsoil. In order to obtain sufficiently high impact energy lattice-boom cranes are generally used. At the same grid point about 5 to 10 impacts are performed, cf. [1].

The method consists of two pounding stages. In the first stage deep layers are compacted and in the second stage intermediate layers. After completion of the two stages the surface compaction is carried out within the entire improved area.

First, a test field is usually created to determine the grid spacing and the necessary impact energy (weight and shape of the pounder and drop height).

Figure 2.6: Dynamic compaction method according to [12]

2.1.2.2 Impulse compaction

For the impulse compaction a hydraulic hammer mounted on an excavator is used. The hammer with a weight ranging from 5 to 12 t is dropped freely from a height of maximum 1.2 m on a large circular steel foot (diameter of 1.5 m). Impacts repeated at a rate ranging from 40 to 60 blows per minute plunge the steel foot in the soil and create a crater which is backfilled with appropriate material.

The control system installed in the operator's cabin allows the control of the compaction process and the record of parameters such as impact energy or foot penetration. Also the height from which the hammer is dropped can be changed.

The subsoil can be compacted with this method up to about 4.5 to 7 m below the ground surface, cf. [1].

First, a test field is usually created where the compaction is performed for various spacing and rates of blows. By testing the local compaction of the improved soil, the optimal grid spacing and the number of blows per grid point can be determined.

Figure 2.7: Impulse compaction method according to [12]

2.2 Compactibility of non-cohesive soils

Grain size distribution curves can be used as an indicator for the appropriate choice of the ground treatment method. When sands and gravel with less then 10% fines are encountered, vibro compaction is suitable. In all other cases, the soil can be improved by the vibro replacement method.

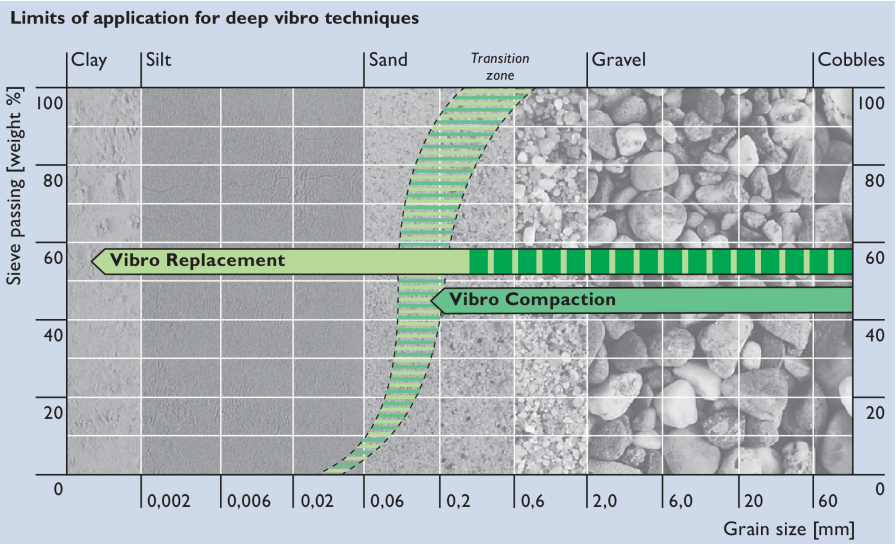

Figure 2.8: Limits of application for deep vibro techniques according to [5]

According to [14, p. 9] the following geotechnical properties of non-cohesive soils are substantial for the performance of deep vibratory compaction methods:

- grain size distribution
- fine fraction
- density index
- cementation, suction and cohesion
- hazard of grain crushing
- permeability

The following table can be used for a quick assessment of the suitability of granular soils for the vibroflotation method.

Table 2.1: Suitability of granular soils for the vibroflotation method according to [6, p. 76]

soil type	comment on suitability for the vibroflotation method
gravel, well graded	well suited for vibro compaction, potential penetration difficulties with less powerful machines
gravel, poorly graded	if $D_{60}/D_{10} \leq 2$ compaction only marginal (trial compaction recommended)
gravel, silty or clayey	compaction not possible if clay content $> 2\%$ and silt content $> 10\%$
sand, well graded	ideally suited
sand, poorly graded	if $D_{60}/D_{10} \leq 2$ compaction only marginal (trial compaction recommended)
sand, silty	compaction inhibited if silt content $> 8\%$
sand, clayey	compaction inhibited if clay content $> 2\%$

In addition to the grain size distribution of the soil, cone penetration test results may also be used to establish the compaction suitability of soils. The following figure shows an empirical relationship between the cone resistance and the friction ratio. The three zones describe the compactibility of the soil.

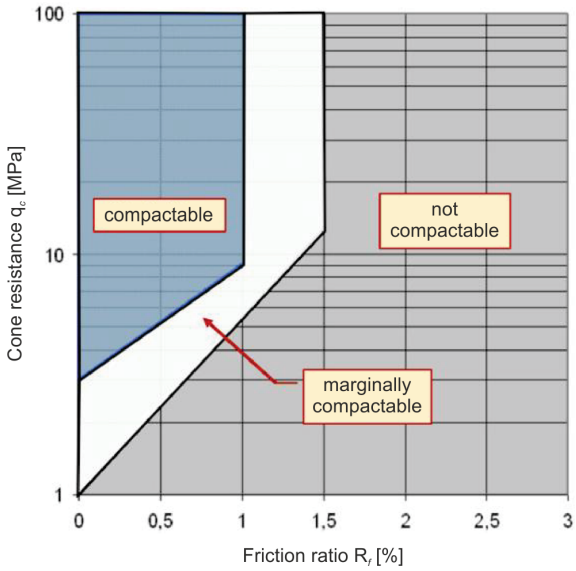

Figure 2.9: Compactibility of soils based on cone penetration tests according to [7]

Permeability plays an important role in speed and effectiveness of vibro compaction. With decreasing permeability below 10^{-5} m/s, compaction is increasingly inhibited, while very high permeability in excess of 10^{-2} m/s may slow penetration of the vibrator as a result of the loss of water, cf. [6, p. 78].

2.3 Mode of action of deep compaction methods

The mode of action of deep compaction methods is subject of research activities until today. In the following essential findings concerning the vibroflotation method, recorded in [6], are mentioned.

With increasing radial distance from the vibrator, the ground vibrations are attenuated by the forces acting between the soil particles. Compaction is therefore only possible when their frictional contact is broken by overcoming the residual frictional strength of the soil. Only then the soil particles will rearrange themselves to find a state of lower potential energy, i.e. from loose to dense. For this purpose, a minimum dynamic force is required with a dependent acceleration sufficiently high to break the soil strength. Where, despite continuing transmission of attenuated weak vibrations, the resisting forces within the soil prevent further compaction there is a limit to how far from the vibrator effective vibrations reach.

It has been found that the stability of the structure of granular soils is destroyed by dynamic stresses when a critical acceleration of over 0.5 g is reached. With increasing accelerations, the shear strength of the sand decreases until it reaches a minimum between 1.5 g and 2.0 g. At this point the soil is fluidised, and a further increase of acceleration causes dilation.

In a stage of fluidisation, the shear strength of the soil is reduced but not eliminated completely. Therefore vibrations, although of course dampened, can be transmitted through this zone where particle contacts are continuously broken and remade. As the acceleration transmitted from the vibrator decreases with increasing distance from its source several annular density zones surrounding the vibrator can be defined.

In water bearing soils, fluidisation occurs principally when the rate of the pore water pressure increase, that is induced by the vibrations, exceeds the rate of dissipation, until this pressure overcomes the normal pressure acting between the particles. It may also occur in dry soils by the action of water jetting or when the upward directed vertical component of acceleration exceeds gravity. As modern machines easily produce accelerations in excess of 10 g fluidisation is induced in the vicinity of the vibrator normally as a combination of the two effects. Soil instability directly caused by the action of acceleration in dry soils is referred to as fluidisation, whereas in saturated soils the vibrator induced oscillations cause liquefaction depending on pore fluid pressure.

Interpretations suggest that the fluidised zone, which is characterised by minimum shear strength, is a measure of the soil's transmissibility of vibrations and thus is responsible for the radius of influence of the vibratory treatment. In the transitional or plastic zone, the dynamic forces are not sufficient to fluidise the soil but still strong enough to shear the soil particles from each other at such a rate that they can find a closer packing. From the point of maximal achievable density attenuation of vibration occurs until it reaches certain threshold shear strength in the ground where any further compaction is inhibited. Water saturation reduces the effective stresses and therefore increases the radius of the compaction zone. It is for this reason that in dry soils the use of flushing water and even flooding of the whole site extends the radius of compaction.

Practical experience gained from construction sites, where depth vibrators with different compaction frequencies were working side by side, has shown, that sand can generally be most effectively compacted by vibrating frequencies that are close to what we might call their

natural frequency. For this reason, specialist contractors have developed vibrators capable of compacting granular soils using frequencies as low as 25 to 30 Hz. Occasionally the accompanying reduction of centrifugal force with frequency was found to be advantageous in optimising the compaction effect.

Theoretical studies of these observations that treat vibro compaction as a plastic-dynamic problem, confirm some fundamental findings that have been acquired in practice under operational conditions: i.e. at constant impact force the effective range of the vibrations increases with decreasing vibrator frequency, whereas the degree of compaction increases with an increasing impact force.

It is a well-established fact that granular soils can be better compacted by repeated shearing rather than by compression, and that the degree of compaction achieved depends in the first place on the shear strain amplitude. If the induced strain is too low the minimum density cannot be reached even with very large numbers of load cycles; conversely with large strain amplitudes optimal densification may not be obtained owing to the effects of dilatancy of the sand, cf. [6, pp. 36 - 39].

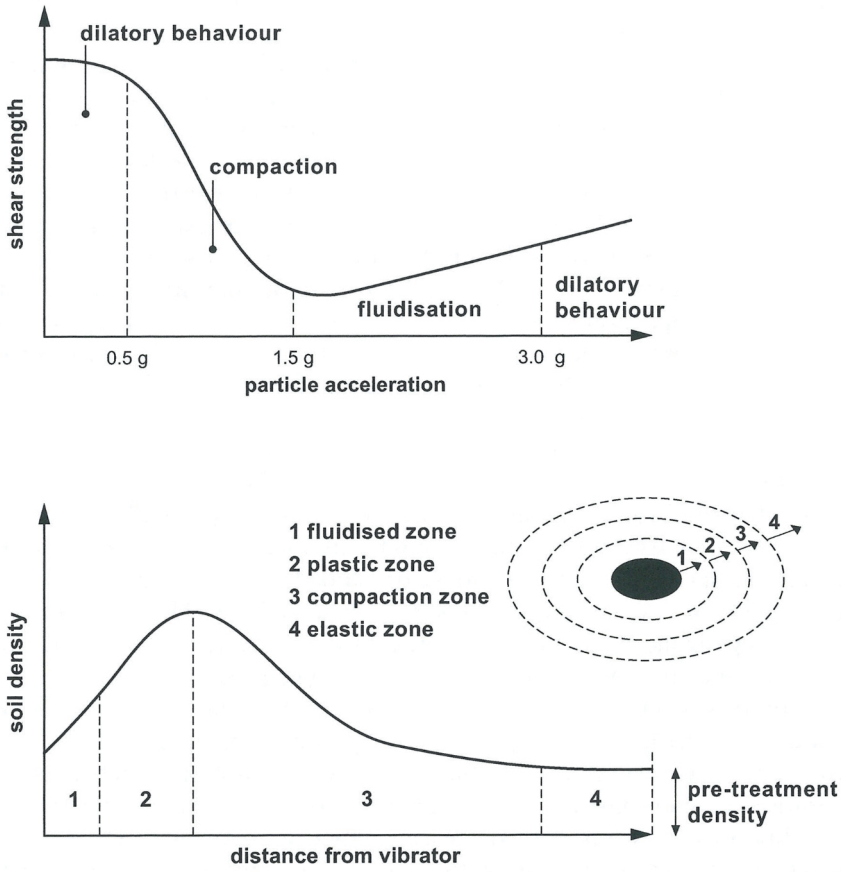

Figure 2.10: Idealised response of granular soils to vibration according to [6, p. 37]

There is a fundamental difference between the Vibro-Rod and the vibroflotation method. In case of the Vibro-Rod and the resonance compaction method, compaction is caused by vertically polarised shear waves, which propagate as a cylindrical wave front from along the entire shaft of the compaction probe. In addition, also horizontal compression waves are emitted. In the case of resonance compaction, a significant amount of energy can be generated at the lower end of the compaction probe. In the case of vibroflotation, the soil is densified as a result of horizontal impact of the compaction probe at the lower end. The compaction action is primarily in the lateral direction and gives rise to compression waves. The compaction zone is limited to the length of the compaction probe and the soil is improved in steps during extraction of the probe, cf. [8, p. 36].

2.4 Compaction control techniques

2.4.1 Work-integrated compaction control

In contrast to the indirect ground exploration methods the work-integrated compaction control techniques allow a continuous monitoring of the compaction success without necessary interruption. Thus, deviations can be recognized immediately and the compaction works can be performed in a shorter period of time.

2.4.1.1 Tiefenschreiberprotokoll

To control the process, to monitor the quality and to record the production, the relevant parameters for each compaction column can be measured, graphically displayed and saved. Usually the time, the depth, the penetration/ pullout speed, the pulldown force and the current are observed. If required also the energy consumption can be recorded. For the operator the values are illustrated on a display unit in the cabin. The printout version is generally known as „Tiefenschreiberprotokoll“.

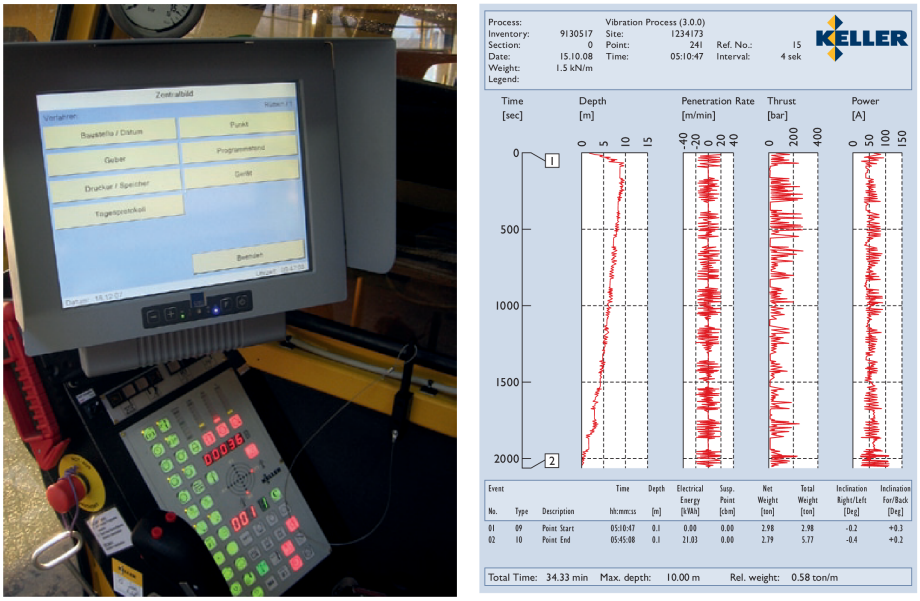

(a) display unit (b) Tiefenschreiberprotokoll

Figure 2.11: Quality control according to [5]

2.4.1.2 VibroScan system

The VibroScan system is an invention of Keller Grundbau Ges.mbH and allows to visualize various process parameters in three dimensions. Furthermore, an online access to the measured parameters is provided. Thus, a continuous control of the quality and the performance on-site is possible, cf. [13, p. 42].

The system represents the process parameters along the entire compaction area. The interpretation and the evaluation of the data is so much easier and less time-consuming.

2.4.2 Indirect ground exploration methods

In this subsection the dynamic probing, the cone penetration test, the flat dilatometer test, seismic investigations and the inclinodeformeter test are discussed.

2.4.2.1 Dynamic probing

With this test method the resistance of soils and soft rocks in situ to the dynamic penetration of a cone is determined. A sliding hammer of a given mass and falling height, depending on the selected procedure, is used to drive the steel cone vertically into the ground. The penetration resistance is defined as the number of blows required to drive the penetrometer over a defined distance, usually 10 cm. The record is continuous over the depth, but no samples can be collected, cf. [15, p. 51].

Four different procedures must be distinguished:

- dynamic probing light (DPL)
- dynamic probing medium (DPM)
- dynamic probing heavy (DPH)
- dynamic probing superheavy (DPSH)

The results obtained from the dynamic probing test can be correlated to the standard penetration test.

2.4.2.2 Cone penetration test

The cone penetration test was first introduced in the Netherlands in the 1930s as a mechanical test and in the 1960s the cone was updated to incorporate electric strain-gauged load cells. Today various international standards and manuals are available.

During the test a cylindrical probe is pushed vertically into the ground at 2 cm/s and the cone resistance stress, the sleeve friction stress and sometimes also the dynamic pore pressure are recorded continuously. The pore pressure is typically measured behind the cone, cf. [16, p. 1763].

The cone penetration test results are commonly used as input parameters for the soil behaviour type charts.

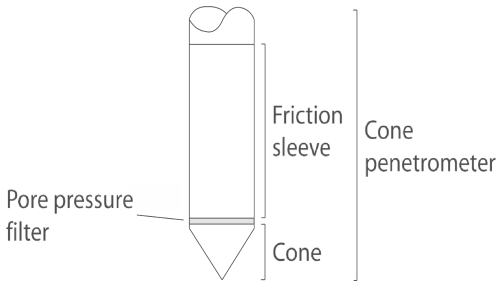

Figure 2.12: Terminology for cone penetrometers according to [18, p. 6]

2.4.2.3 Flat dilatometer test

The flat plate dilatometer test was developed in Italy by professor Silvano Marchetti. It was introduced in 1980. Today various international standards and manuals are available, cf. [16, p. 1762].

The test consists in advancing a blade shaped probe vertically into the ground using common field machines (usually a static penetrometer or a drill rig) and stopping at each test depth, usually every 20 cm, for collecting the readings. The circular steel membrane, mounted on one side of the blade, is used for measuring two pressure readings which correspond to two fixed levels of the membrane deformation.

1. A-reading: the pressure at which the membrane lifts off
   (the acoustic signal turns from on to off)
2. B-reading: the pressure necessary to expand the membrane 1.1 mm from its centre
   (the acoustic signal turns from off back to on)

The A-reading should be obtained between 10 to 20 s after the penetration has stopped, the B-reading should be obtained between 10 to 20 s after the A-reading. If requested, the C-reading corresponds to the pressure on the membrane when, deflating the gas after the B-reading, the membrane returns to the original closed position (A-reading), reactivating the acoustic signal.

If a non-penetrable layer of soil is present, it can be potentially drilled using a casing with an internal diameter of at least 100 mm. The push rods and the blade are then lowered to the bottom of the borehole and the test can be continued below, cf. [20].

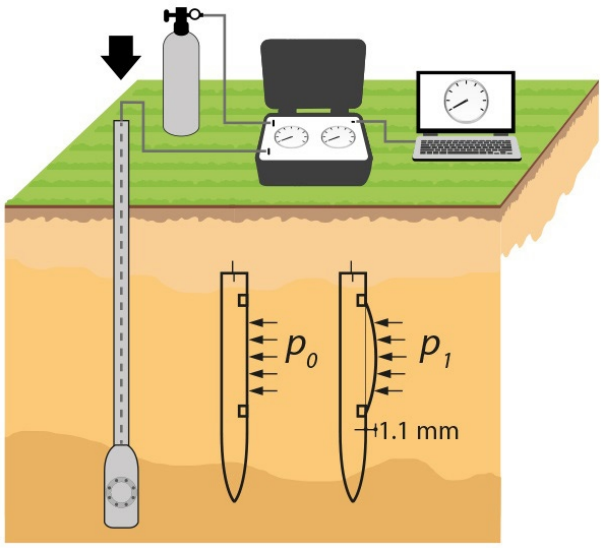

Figure 2.13: Flat dilatometer test according to [20]

2.4.2.4 Seismic investigations

Seismic investigations are in general time-consuming and expensive. Thus, these tests are in rare cases used to evaluate the compaction success. Nevertheless, seismic investigations allow the exploration of large areas in the subsoil.

Regarding the quality control after compaction the focus is on the shear wave velocity parameter. Usually measurements are performed along profiles over the depth.

In addition to the seismic cone penetration test and the seismic dilatometer test also non-invasive surface wave methods like the spectral analysis of surface waves and the multichannel analysis of surface waves are used.

In the following the measurement principle is explained for the seismic dilatometer test. For the seismic cone penetration test it is the same.

For the seismic dilatometer test the standard flat dilatometer is combined with a seismic module for the measurement of the shear wave velocity and optionally also of the compression wave velocity. The beam of the shear wave source must be positioned so that the (horizontal) direction of the hammer hitting it, is perpendicular to a line between the centre of the beam and the rods. The beam of the compression wave can be placed in any direction. In both cases the beam should be as close as possible to the rods (generally between 0.30 m to 1.20 m). At each test depth penetration is stopped, typically at depth intervals of 0.50 m (or 1.00 m). When the hammer strikes the beam, the generated shear wave is recorded by the two receivers. The data is sent to the laptop computer where both seismograms are plotted. The software evaluates the delay in the arrival of the shear wave and provides the interpretation of the shear wave velocity in real time.

The shear wave velocity is obtained as the ratio between the difference in distance between the source and the two receivers and the wave arrival delay between the first and the second receiver. At each test depth at least three distinct measurements should be taken. The repeatability of the shear wave velocity is a good indicator for the quality of the result, which is usually considered acceptable if the correlation coefficient is within 3%, cf. [20].

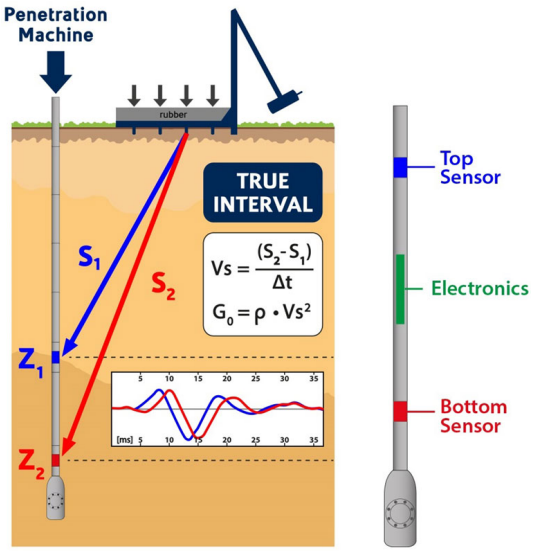

Figure 2.14: Seismic dilatometer test according to [20]

2.4.2.5 Inclinodeformeter test

The inclinodeformeter is a novel device for determining changes in lateral earth pressure. The device makes use of the existing and widely used technology of inclinometer measurements. It was developed at the ETH Zürich in 2013 and is protected by a patent. Until now the device was used for measurements in creeping landslides and in the vicinity of excavations.

The inclinodeformeter technology comprises a device to measure dimensions of an inclinometer pipe installed in a vertical borehole in soil and a method to interpret the measurements in terms of lateral earth pressure changes. Finally, a continuous profile of lateral earth pressure changes is obtained, cf. [19, p. 187].

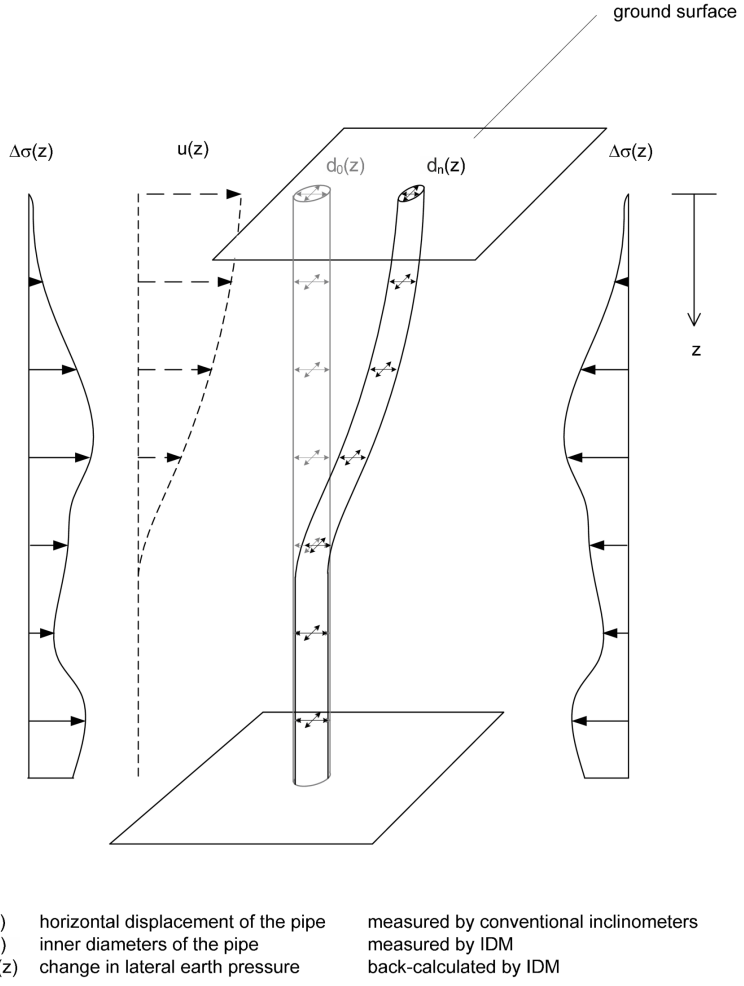

Figure 2.15: Conceptual diagram inclinodeformeter test according to [19, p. 189]

The device measures the inner diameter of the cross section of an inclinometer pipe at a predetermined longitudinal position. Thus, it consists of a probe detecting the diameter and of a positioning system detecting the longitudinal position, cf. [19, p. 187].

The inclinodeformeter probe is lowered down the pipe on three wheels guided along the channels of the pipe. The upper and the lower wheels roll in the same channel and are fixed to the probe. The middle wheel is connected via a lever with two springs, so that it is pressed against the opposite channel. A change in the diameter leads to a change of

the position of the middle wheel in respect to the probe. There are two tilt sensors to measure the inner diameter of the pipe: One sensor is located on the top of the probe and detects the inclination of the probe; Another tilt sensor is located on the lever of the middle single wheel and detects the inclination of the lever. The inner diameter is a function of the relative inclination. The base of the lever is given by the distance from the centre of rotation of the lever to the centre of rotation of the middle single wheel. The centre of rotation of the lever is located at a known distance from the line connecting the centres of rotations of the upper and the lower wheel, cf. [19, p. 190].

The inner diameter is calculated from the known geometry and the two measured inclinations.

$$\mathrm{d} = \mathrm{d}_W + \mathrm{X} + \mathrm{Y} \cdot \sin(\alpha_L - \alpha_P) \tag{2.1}$$

d	inner diameter of the inclinometer pipe
d_W	diameter of the wheels of the probe
X	distance describing the location of the centre of rotation of the lever
Y	base length of the lever
α_L	inclination of the lever
α_P	inclination of the probe

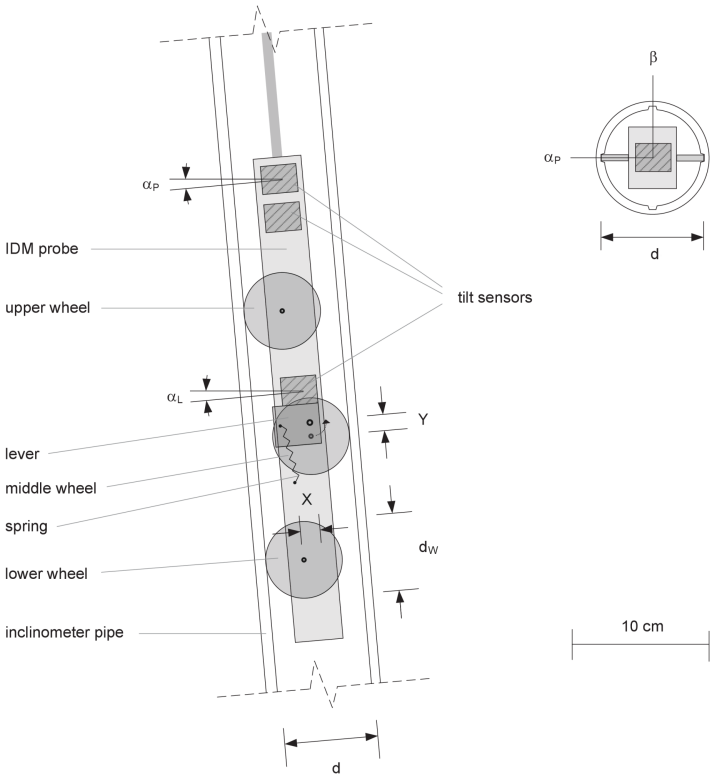

Figure 2.16: Inclinodeformeter probe according to [19, p. 191]

In addition to the two sensors in the plane of the measured diameter, there is another tilt sensor measuring the inclination of the probe in a perpendicular direction out of the plane. This sensor is used for correction of the measurements due to the out-of-plane inclination of the probe, cf. [19, p. 191].

Above the top wheel there is a pressure cell to measure the water pressure in the inclinometer pipe. The temperature of the probe is also measured continuously in order to give an opportunity to correct for the influence of the temperature.

The same probe can be used for different kind of inclinometer pipes with different inner diameters. Therefore the bearings of the lever can be fixed in two different positions, cf. [19, p. 192].

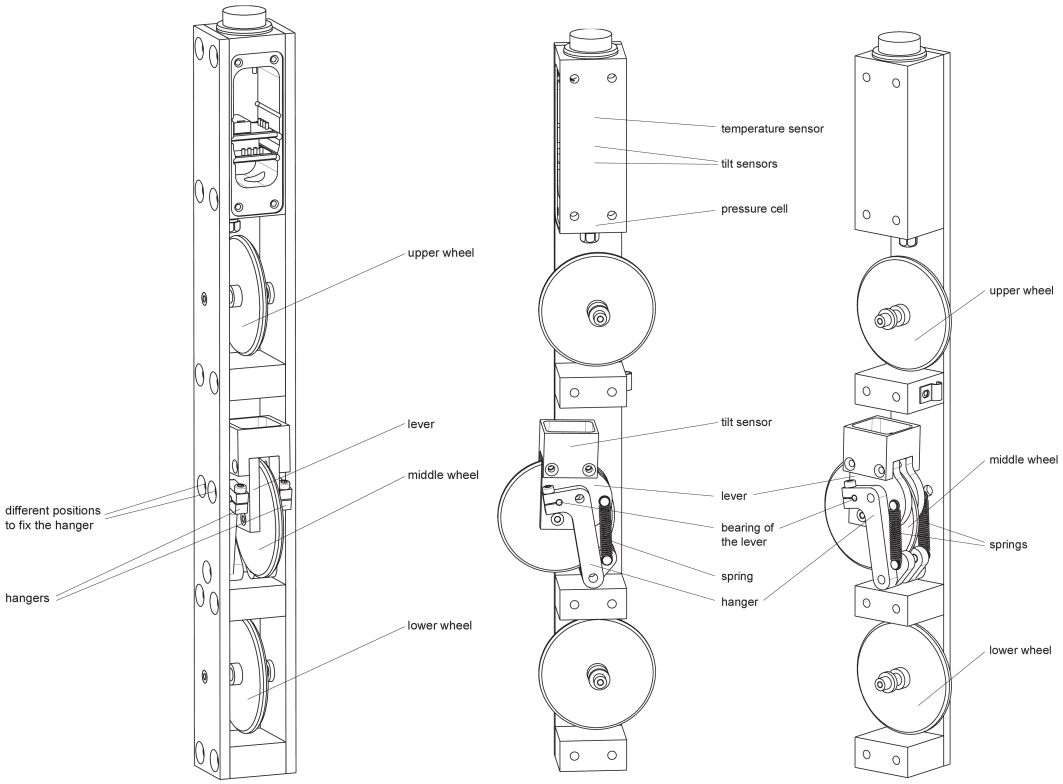

Figure 2.17: Inclinodeformeter probe - mechanical design according to [19, pp. 193 - 194]

At the top of the borehole, the cable on which the probe is hanging goes around a wheel. An incremental rotation sensor measures the wheel rotation, which determines the longitudinal position of the probe in the pipe. As the probe is lowered down, all the sensor measurements are saved for the corresponding longitudinal position.

A connecting piece of pipe is fixed on top of the inclinometer pipe in order to elongate the pipe above the ground surface. The winch is fixed on top of the connecting piece. In order to be able to compare measurements it is essential to take reliable and precise measurements of the position of the probe. Therefore, corresponding markers on the cable and on the winch exactly define the starting position of the probe. The position of the probe is recorded relative to the starting position.

The change in position is measured by the rotation of the winding wheel. In order to reach high precision, slippage of the cable must be avoided by squeezing it between the winding

wheel and another wheel. The centre of rotation of the winding wheel is not fixed vertically. Therefore, the load of the cable on the winding wheel is used to squeeze the cable. The contact pressure where the cable is squeezed increases with the length of the winded cable. This setup automatically increases friction as necessary, cf. [19, p. 195].

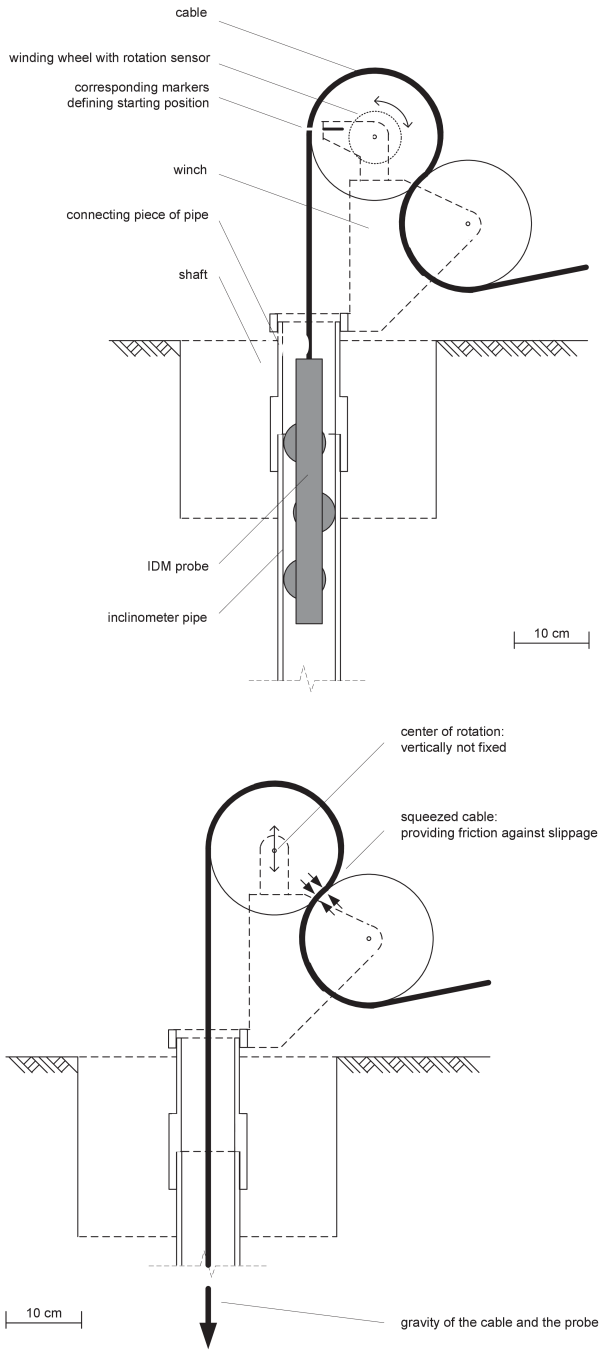

Figure 2.18: Positioning system according to [19, pp. 196 - 197]

The procedure comprises 11 steps:

1. A borehole is drilled
2. wherein an inclinometer pipe is installed.
3. Inner diameter readings are taken
4. and corrected
5. in order to derive the ovalization of the cross section of the pipe.
6. Several measurements are required over time
7. to obtain the change in ovalization
8. which is corrected for effects of longitudinal bending
9. and averaged with depth.
10. The stiffness of the pipe and the soil is assessed
11. in order to back calculate the change in lateral earth pressure, cf. [19, p. 187].

A detailed description of the single steps is available in [19, pp. 200 - 212].

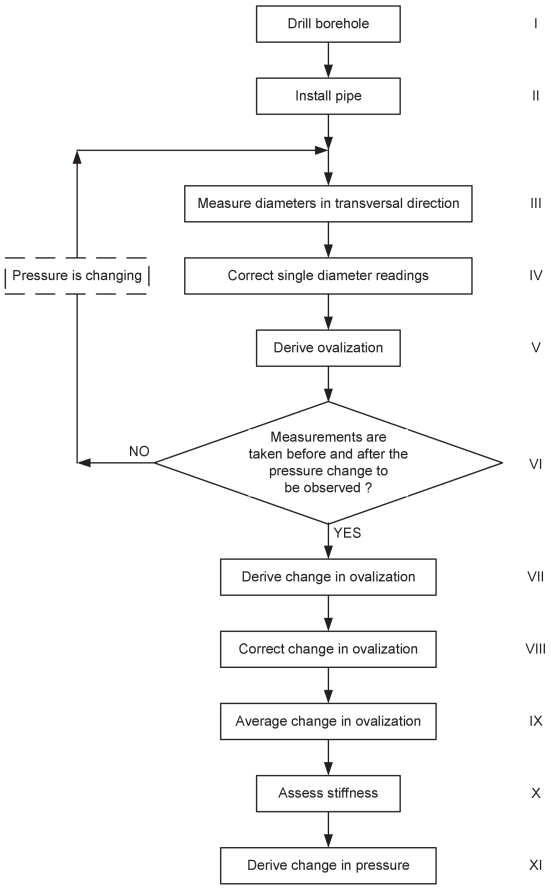

Figure 2.19: Method flow diagram according to [19, p. 200]

The pressure changes with depth are back calculated by solving the corresponding boundary value problem given in a horizontal cross section at each predetermined longitudinal position. The change in pressure at each position is obtained from the change in the static boundary condition, which has to be applied in order to reproduce the measured pipe deformations, cf. [19, p. 211].

3 Experimental investigations

This chapter includes the general concept for the experimental investigations, the description of the test area (location, geology, layout and procedure), the documentation of the performed investigations and finally the yielded test results.

3.1 Concept

In cooperation with Keller Grundbau Ges.mbH a large scale deep vibro compaction experiment was planned. At the test area all practical relevant and on-site possible compaction control techniques should be performed. For the first time the inclinodeformeter should be used for horizontal earth pressure measurements at compacted subsoil. To check the suitability of the device already in July 2019 a simplified preliminary test had been performed at the geotechnical laboratory of the Graz University of Technology. The results are summarized in the technical report „Ermittlung der Änderung des mittleren Rohrdurchmesser unter hydrostatischer Belastung auf das IDM-Rohr“ (see appendix 1). By using the measurement device, a better understanding of the horizontal earth pressure change as well of the possible overconsolidation in the subsoil was expected. The investigation program had to be performed in connection with a concrete construction project.

Two test fields, called hereafter test area A and test area B, were planned. The compaction grid was quadratic for both fields but differed in spacing. The grid spacing depends on the already determined spacing for the construction project and the unproblematic performance of the compaction control techniques. Investigations were always performed in the centre between two compaction columns and between four compaction columns. To have enough potential measurement points for each test field available at least 20 compaction columns were necessary for each field. The compaction should reach in a depth of at least 8.00 m. The compaction device used on-site depends on the conditions of the construction project. The vibroflotation ground improvement technique using the back-step construction method was applied.

The investigations should be performed at four different times. One measurement epoch was planned before the deep vibro compaction (epoch 0). Immediately after the compaction measure an additional measurement epoch should be performed (epoch 1). To get information about the recompaction over time two epochs were planned following epoch 1 (epoch 2 about two weeks after epoch 1 and epoch 3 about eight weeks after epoch 1).

The work schedule of the construction project specified in section 3.2.1 allowed for compaction works in spring 2020. Hence, the temporal frame for the experimental investigations was defined.

3.2 Test area

This section includes the description of the location of the test area, information about the geology on-site and finally the geometric arrangement and the chronology of the investigations on both test fields.

3.2.1 Location

The test area, called „GIWOG Pichling Versuchsfeld“, is located on a construction area confined by the Traundorfer Straße and the Seiderstraße in 4030 Linz (Oberösterreich, Austria).

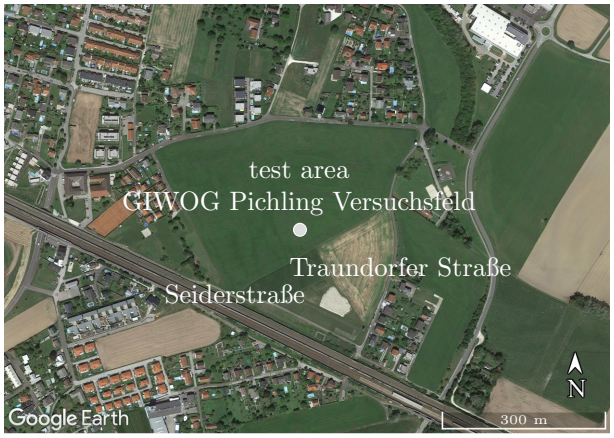

Figure 3.1: Location of the test area

The following figure shows the test area A with both inclinometer pipes (IDM1-A and IDM2-A) immediately after the installation of the pipes.

Figure 3.2: Test area A immediately after the installation of the inclinometer pipes

3.2.2 Geology

To determine the ground conditions and texture a trench had been excavated, soil samples (sample 1, sample 2 and sample 3) had been collected and sieve analyses were performed in the geotechnical laboratory. The following figures show the excavated trench on-site.

Figure 3.3: Excavated trench on-site

Soil identification (0.00 m ≡ 248.94 müA):

0.00 to 0.25 m	sand-silt-mixture, slightly gritty, dark brown
0.25 to 0.60 m	gravel (predominantly fine to medium gravel), slightly sandy, rounded coarse components, grey-brown
0.60 to 0.90 m	sand, slightly gritty, very slightly silty, grey
0.90 to 1.20 m	gravel (predominantly medium to coarse gravel), sandy to slightly sandy, rounded coarse components, grey, **sample 1**
1.20 to 1.40 m	gravel (predominantly medium gravel), slightly sandy to very slightly sandy, russet to brown, **sample 2**
1.40 to 1.80 m	gravel, sandy, very slightly silty, grey
1.80 to 2.00 m	gravel (predominantly medium gravel), very slightly sandy, grey
2.00 to 3.40 m	gravel, sandy to slightly sandy, rounded coarse components, grey, **sample 3**
3.40 m	total depth (groundwater table not reached)

Fig. 3.4, Fig. 3.5 and Fig. 3.6 show the grain size distribution of the soil sample 1, soil sample 2 and soil sample 3.

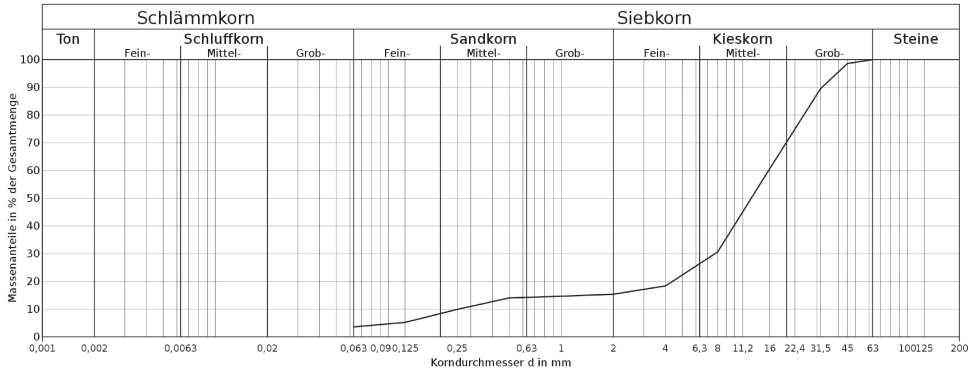

Lab.Nr.	Signatur	Anteile kleiner Ø [mm]	Ton	Schluff	Sand	Kies	Steine	Anteile größer Ø [mm]	Bodenart	D10	D30	D60	Cu	Cc
21411	——	0,063: 3,6	-	-	11,8	84,6	-	-	sa' Gr	0,2529mm	7,7235mm	15,7582mm	62,31	14,97

Figure 3.4: Grain size distribution of the soil sample 1

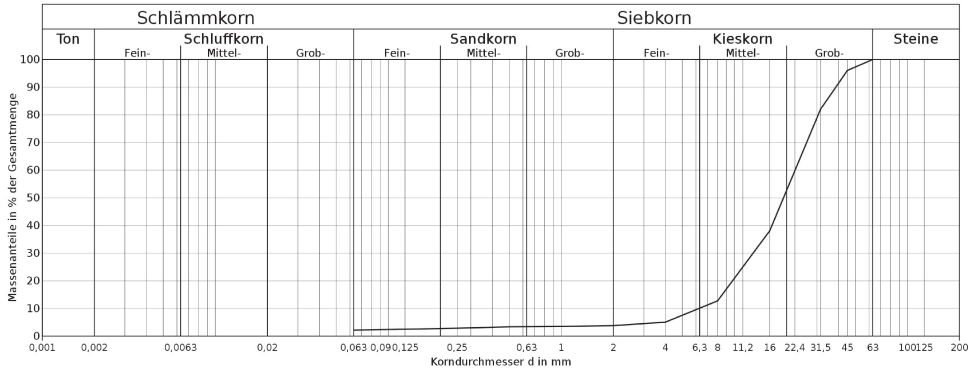

Lab.Nr.	Signatur	Anteile kleiner Ø [mm]	Ton	Schluff	Sand	Kies	Steine	Anteile größer Ø [mm]	Bodenart	D10	D30	D60	Cu	Cc
21412	——	0,063: 2,2	-	-	1,6	96,2	-	-	Gr	6,2324mm	12,8239mm	22,4258mm	3,60	1,18

Figure 3.5: Grain size distribution of the soil sample 2

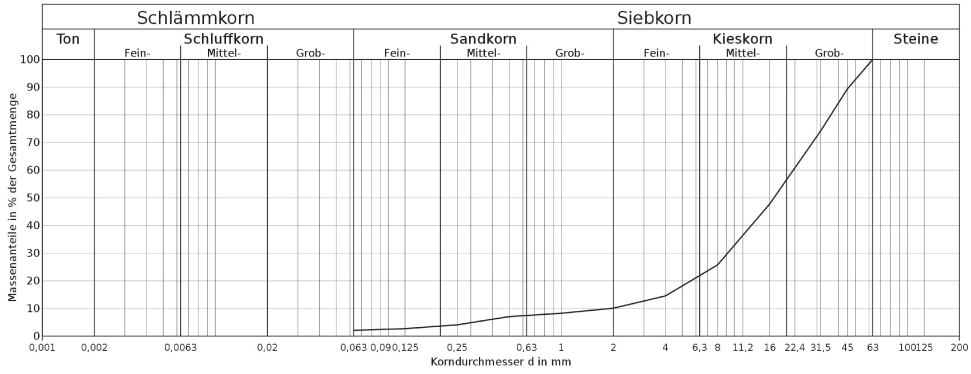

Lab.Nr.	Signatur	Anteile kleiner Ø [mm]	Ton	Schluff	Sand	Kies	Steine	Anteile größer Ø [mm]	Bodenart	D10	D30	D60	Cu	Cc
21413	——	0,063: 2,1	-	-	8,0	89,9	-	-	sa' Gr	1,9116mm	9,1365mm	21,8916mm	11,45	1,99

Figure 3.6: Grain size distribution of the soil sample 3

Before the compaction measures four heavy dynamic probing tests, two cone penetration tests with pore water pressure measurement and two seismic cone penetration tests were performed on the test area. The results are shown in the following figures.

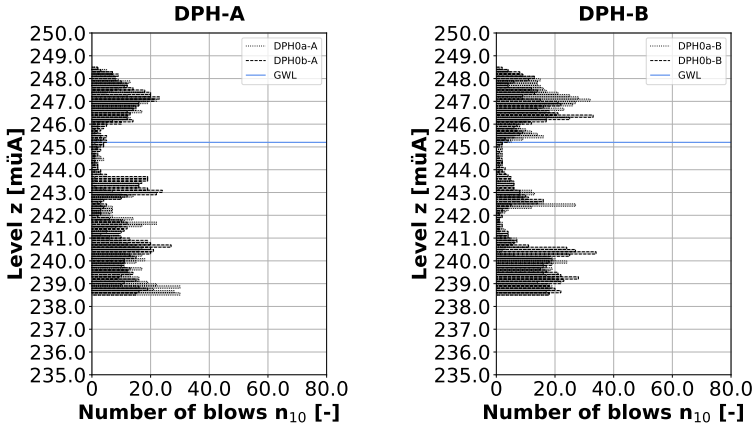

Figure 3.7: Heavy dynamic probing tests

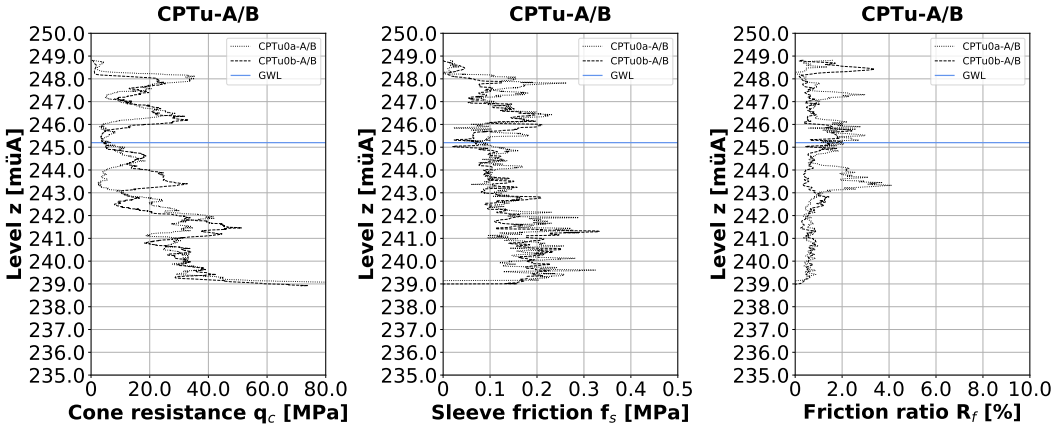

Figure 3.8: Cone penetration tests with pore water pressure measurement (1)

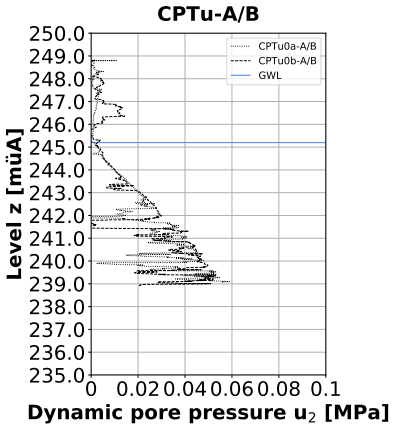

Figure 3.9: Cone penetration tests with pore water pressure measurement (2)

According to the measurement results shown in Fig. 3.9 the groundwater level is at 245.20 müA.

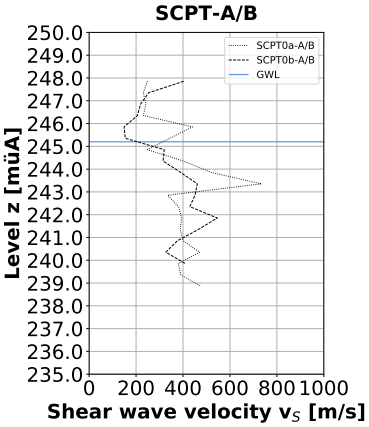

Figure 3.10: Seismic cone penetration tests

[22, p. 186] includes reference values for the classification of coarse grained material.

Table 3.1: Reference values for the classification of coarse grained material according to [22, p. 186]

	very loose	loose	medium dense	dense	very dense
density index I_D [%]	< 15	15 - 35	35 - 65	65 - 85	85 - 100
dynamic probing heavy n_{10} [-]	< 5	5 - 10	10 - 15	15 - 20	> 20
cone penetration test q_c [MPa]	< 5	5 - 8	8 - 15	15 - 20	> 20
seismic cone penetration test v_S [m/s]		< 150	220	350	450

The following figure shows the compactibility of the ground on-site. The evaluation is based on the results of the cone penetration tests. The soil should be well compactable.

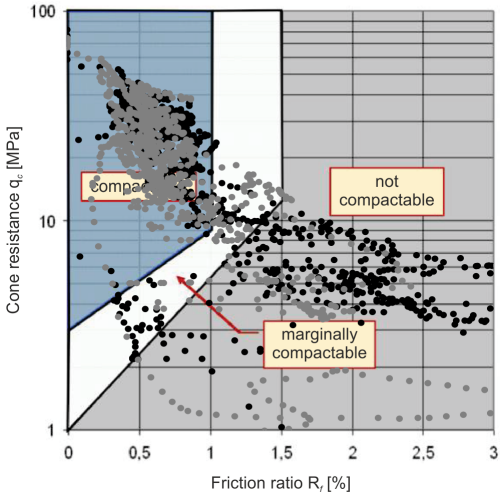

Figure 3.11: Compactibility of the ground on-site according to [7] - CPTu0a-A/B (black) and CPTu0b-A/B (grey)

3.2.3 Layout

The chosen geometric parameters of both test areas are summarized in Tab. 3.2.

Table 3.2: Geometric parameters of both test areas

test area	grid spacing	distance to centre between four compaction columns	distance to centre between two compaction columns
A	2.70 m x 2.70 m	1.91 m	1.35 m
B	3.10 m x 3.10 m	2.19 m	1.55 m

Fig. 3.12 and Fig. 3.13 show the exact position of the investigations at the different dates. Furthermore, the realized chronological order of the compaction columns on-site is marked by a red dashed line (see also the consecutive numbering of the columns).

At each test area the following investigations were carried out:

12 inclinodeformeter measurements
8 heavy dynamic probing tests
11 cone penetration tests with pore water pressure measurement
11 seismic cone penetration tests

The number of inclinodeformeter measurements includes the measurements immediately after the installation of the pipes and the twice performed reference measurements. Finally, the cone penetration tests and seismic cone penetration tests at epoch 0 were not performed for both test areas separately but only once.

After compaction, the installed inclinometer pipes should reflect the expected horizontal earth pressure changes by diameter changes. With the inclinodeformeter probe the pipe deformations can be measured. The conventional compaction control techniques should provide information on the compaction success. By using existing empirical correlations soil properties before and after compaction can be derived.

3.2.4 Procedure

The inclinometer pipes were installed one day before the reference measurements (epoch 0). Immediately after the installation (on the same day) additional measurements on all four pipes were performed with the inclinodeformeter device (measurements called hereafter installation). The compaction work was carried out on 24.02.2020 and 25.02.2020.

The dates for the investigations were set as follows:

epoch 0	21.02.2020	before deep vibro compaction
epoch 1	27.02.2020	after deep vibro compaction
epoch 2	10.03.2020	after deep vibro compaction
epoch 3	21.04.2020	after deep vibro compaction

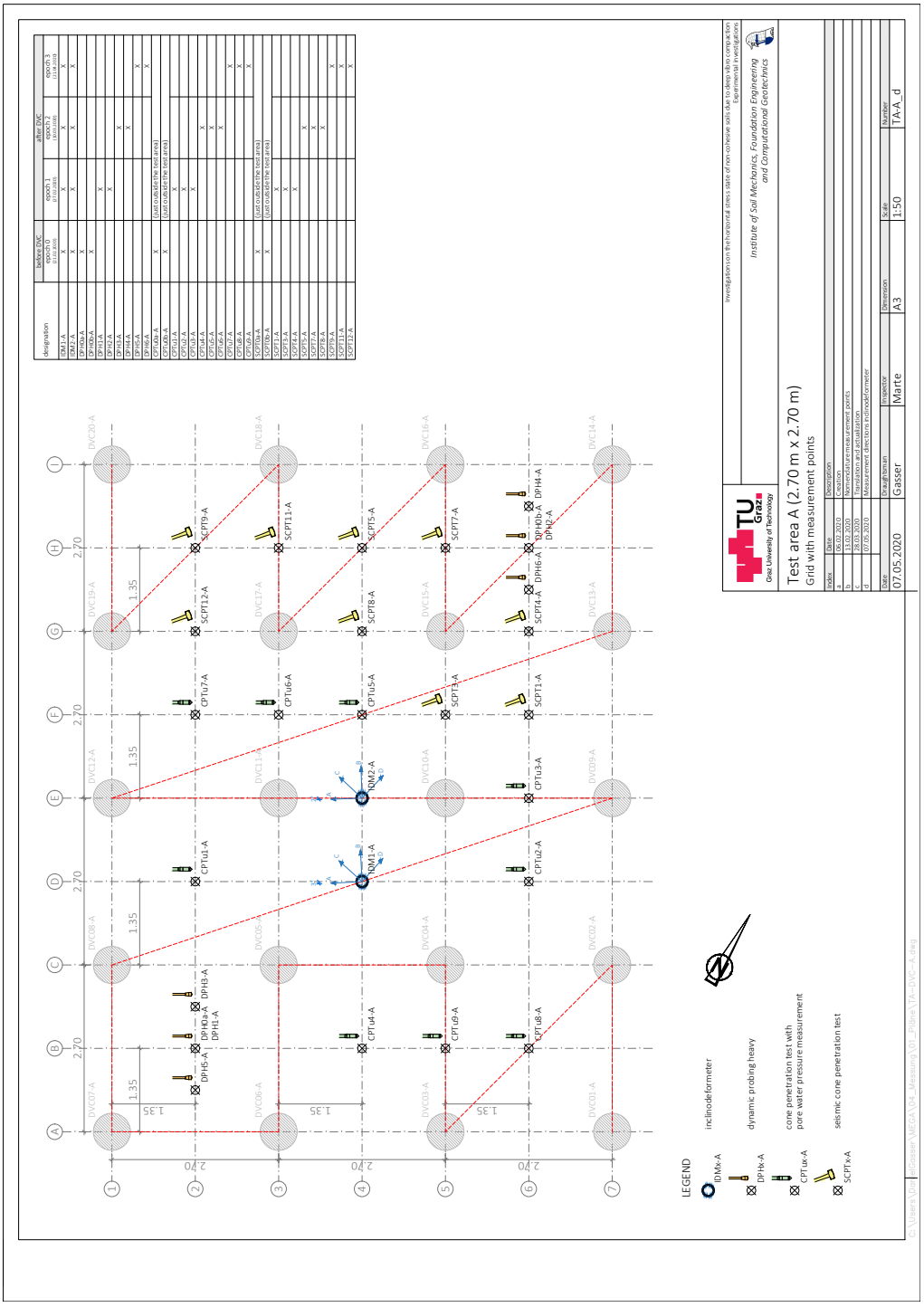

Figure 3.12: Layout of the test area A

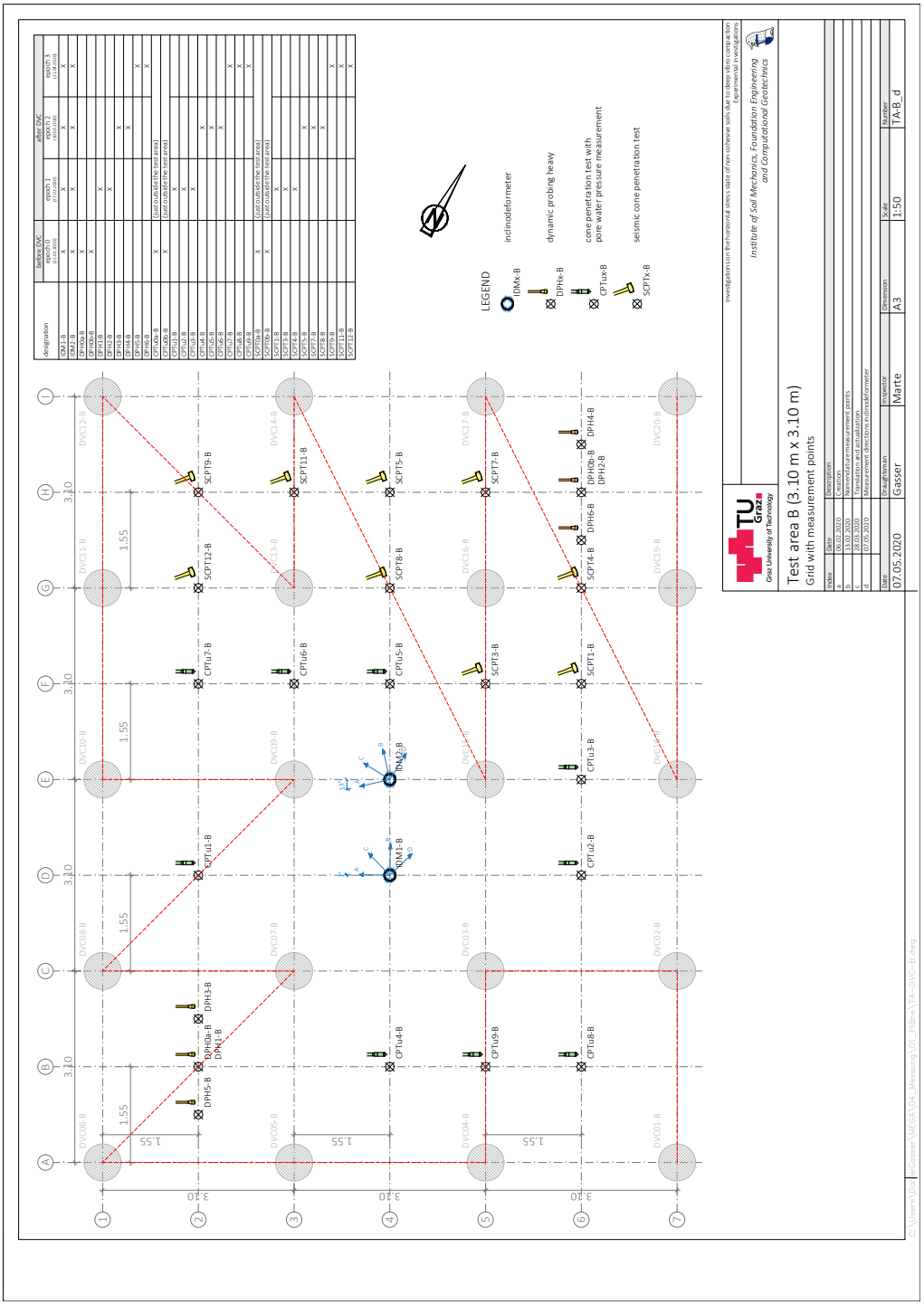

Figure 3.13: Layout of the test area B

3.3 Documentation

In this section the compaction works on-site as well as the performed compaction control techniques (inclinodeformeter, dynamic probing heavy, cone penetration test and seismic cone penetration test) are documented.

3.3.1 Deep vibro compaction

The compaction works on both test fields were performed by trouper of Keller Grundbau Ges.mbH on 24.02.2020 and 25.02.2020. The exact chronological order of the compaction columns, as already mentioned, is shown in Fig. 3.12 and Fig. 3.13. The depth vibrator model S340 with a length of 3.10 m and a diameter of 0.43 m was used (vibroflotation ground improvement technique).

As usual, the compaction process was carried out bottom up after lowering the vibrator body to the maximum compaction depth (about 8.00 m). The penetration of the vibrator was aided by water flushing with jets of variable pressure. At full depth the water flow was stopped. Continuously the vibrator was withdrawn about 0.50 m and then lowered again by about the half of the withdrawing depth (back-step construction method) until reaching the top ground surface. The penetration process, in this case, was supported by hydraulic pull down pressure. To backfill the crater around the vibrator existing soil was used.

(a) penetration of the vibrator (b) backfill of the crater

Figure 3.14: Deep vibro compaction on-site

During the compaction works the process parameters were recorded and monitored continuously (see Fig. 3.15). Especially the power consumption of the vibrator engine expressed in terms of electrical current is of importance. An increase in density is usually indicated by an increased power consumption of the vibrator.

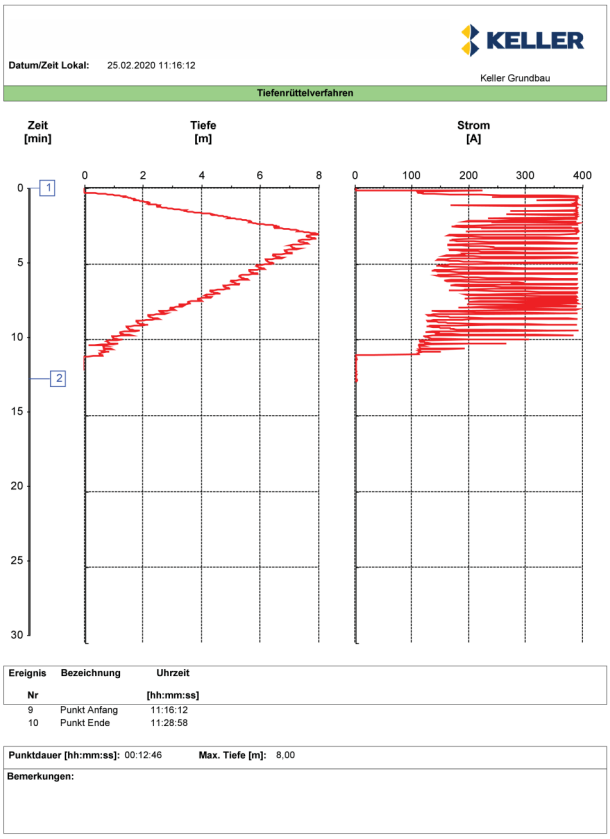

Figure 3.15: Recorded process parameters on-site

3.3.2 Inclinodeformeter

In this subsection first the inclinometer pipe installation, then the measurement procedure with the inclinodeformeter device and finally some laboratory tests concerning the back-fill material will be discussed.

3.3.2.1 Pipe installation

The inclinometer pipe installation on both test fields was performed by trouper of Keller Grundbau Ges.mbH on 20.02.2020. Inclinometer pipes with eight channels and an outer diameter of 84.00 mm, manufactured by Swiss Environment SA (for further technical data see appendix 3), were used on-site. Due to the limited length of one pipe (3.00 m), four pieces had to be connected to reach at each measurement point the desired depth of at least 10.50 m.

Figure 3.16: Inclinometer pipes with eight channels

First the end cover was attached on a pipe. The connection was realized in the same manner as at the pipe joints. Initially silicon glue was applied on one piece, then both pieces were sticked together. With a boring machine the holes for riveting were drilled. The connection was riveted manually. Finally, a waterproof tape was fixed. In horizontal position at most two pipes were connected to avoid potential failure during insertion of the inclinometer pipe in the cased borehole.

(a) silicon glue

(b) sticking together

(c) drilling holes

(d) riveting

(e) waterproof tape

(f) connected pipes

Figure 3.17: Connection of the inclinometer pipes

With a drill rig a cased borehole was created on the marked position. The borehole reached below the groundwater level. Afterwards, the pipes were inserted in the cased borehole and connected in vertical position. To avoid potential buoying upwards the pipe was entire filled with water immediately after insertion. The channels of the inclinometer pipe were aligned as good as possible to the grid of the test area. Finally, the pipe was continuously backfilled with gravel (see section 3.3.2.3) for at most 1.00 m and the casing was withdrawn in the same amount. Thereby the friction acting on the pipe was low enough to avoid any vertical movement of the inclinometer pipe.

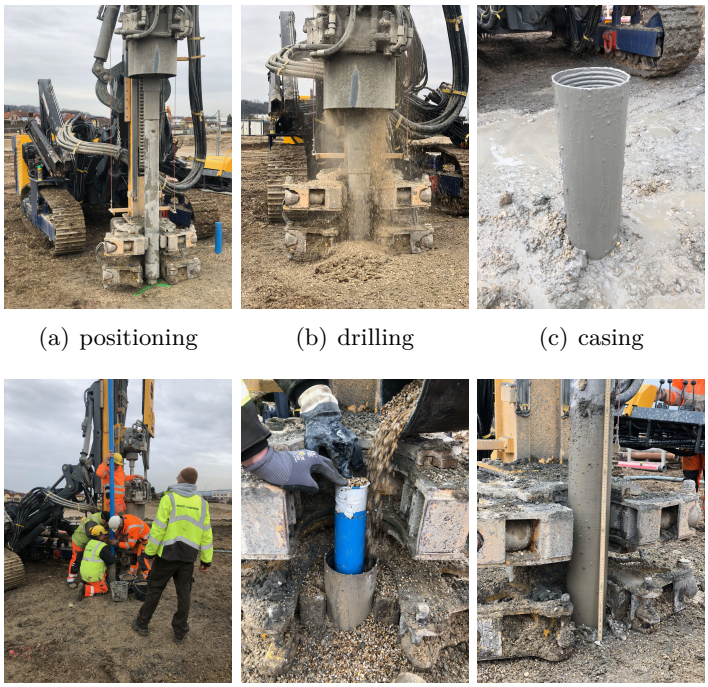

(a) positioning (b) drilling (c) casing

(d) pipe connection (e) backfilling (f) casing withdraw

Figure 3.18: Inclinometer pipe installation

At the end the pipe was flushed with water bottom up to ensure a clean inside for the measurement (see section 3.3.2.2). The top cover was only temporary fixed. Next to the installed pipes a hoarding was constructed.

(a) flushing with water (b) hoarding

Figure 3.19: Installed inclinometer pipes

3.3.2.2 Measurement

The measurement procedure was conducted according to the detailed explanations in [21, pp. 39 - 44]. At each epoch measurements were performed in all four directions A, B, C and D (the exact orientation of the directions for each inclinometer pipe is shown in Fig. 3.12 and Fig. 3.13 - caused by the installation process the orientation is not always perfectly the same). It was measured in direction 000 as well as in opposite direction 180 (rotation of the inclinodeformeter device by 180°). By averaging both measurements diameter reading errors due to the geometry of a curved pipe (see [19, pp. 203 - 204]) can be simplified corrected.

(a) inclinodeformeter device (b) setup (c) connecting piece

Figure 3.20: Measurement procedure with the inclinodeformeter device

To know the settlements of the pipes and of the ground the altitude at the top cover and the distance between top cover and ground were measured for each pipe at each epoch. Tab. 3.3 shows the recorded data. The vibro compaction lead to a lowering of the ground level of about 0.35 m.

Table 3.3: Altitude at the top cover and distance between top cover and ground

	IDM1-A	IDM2-A	IDM1-B	IDM2-B
epoch 0	248.910 müA	248.892 müA	249.036 müA	249.033 müA
	0.370 m	0.338 m	0.610 m	0.614 m
epoch 1	248.920 müA	248.910 müA	249.050 müA	249.060 müA
	0.622 m	0.672 m	0.880 m	0.963 m
epoch 2	248.890 müA	248.910 müA	249.020 müA	249.040 müA
	0.622 m	0.671 m	0.880 m	0.962 m
epoch 3	248.900 müA	248.890 müA	249.040 müA	249.040 müA
	0.618 m	0.669 m	0.884 m	0.961 m

3.3.2.3 Laboratory test

At the geotechnical laboratory of the Graz University of Technology some tests were performed using the back-fill material.

Figure 3.21: Back-fill material

The determined grain size distribution is shown in Fig. 3.22.

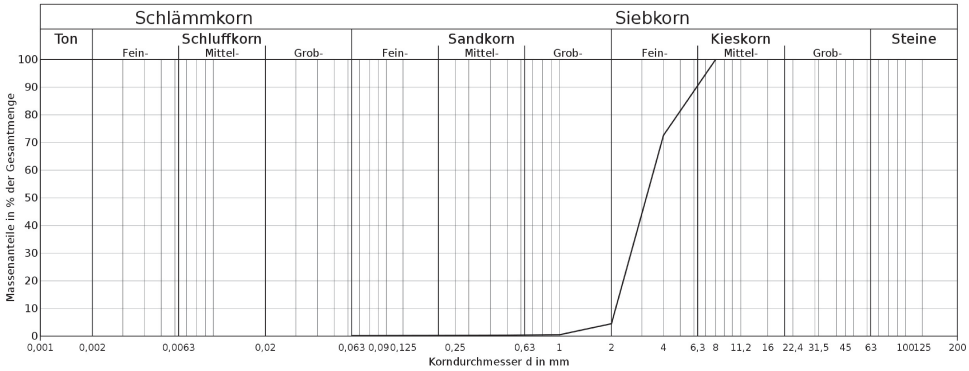

Lab.Nr.	Signatur	Anteile kleiner Ø [mm]	Ton	Schluff	Sand	Kies	Steine	Anteile größer Ø [mm]	Bodenart	D10	D30	D60	Cu	Cc
21414	——	0,063: 0,2	-	-	4,3	95,5	-	-	sa'' Gr	2,1151mm	2,5924mm	3,5177mm	1,66	0,90

Figure 3.22: Grain size distribution of the back-fill material

A direct shear test provided for the mentioned material a friction angle of about 47°.

To know the angle of wall friction (inclinometer pipe - back-fill material) a simple tilt test was performed. The normal stress, in this case, was relatively low with about 1.20 kN/m^2 (assumption: contact along the entire surface). Thereby any scratching of the gravel at the surface of the inclinometer pipe could be prevented.

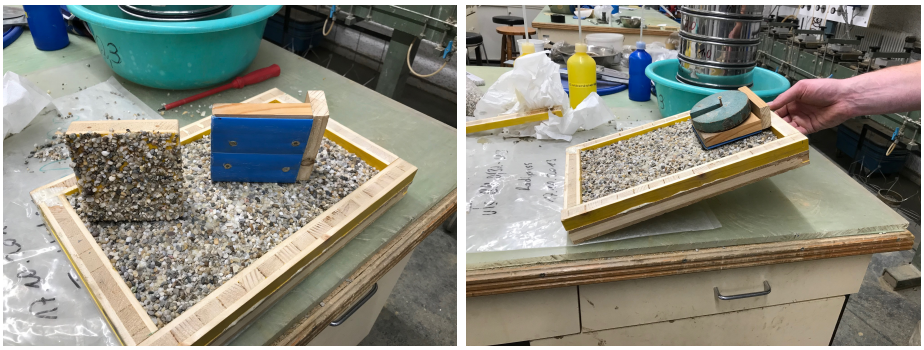

(a) setup (b) test

Figure 3.23: Simple tilt test

To check the reliability of the test also gravel on gravel was investigated. A friction angle of about 49° ±3° was the test result. For PVC on gravel the friction angle was about 21° ±3°.

3.3.3 Dynamic probing heavy

The heavy dynamic probing tests were performed by Keller Grundbau Ges.mbH. This subsection gives only some idea about the procedure on-site. For detailed information about the test see section 2.4.2.1.

Figure 3.24: Dynamic probing heavy - device

Figure 3.25: Dynamic probing heavy - test

3.3.4 Cone penetration test with pore water pressure measurement

The cone penetration tests with pore water pressure measurement were performed by Premstaller Geotechnik ZT-GmbH. Due to the ground conditions after the deep vibro compaction it was not always possible to reach the desired depth of penetration. This subsection gives only some idea about the procedure on-site. For detailed information about the test see section 2.4.2.2.

Figure 3.26: Cone penetration test with pore water pressure measurement - device

3.3.5 Seismic cone penetration test

The seismic cone penetration tests were performed by Premstaller Geotechnik ZT-GmbH. Due to the ground conditions after the deep vibro compaction it was not always possible to reach the desired depth of penetration. This subsection gives only some idea about the procedure on-site. For detailed information about the test see section 2.4.2.4.

Figure 3.27: Seismic cone penetration test - test

3.4 Test results

This section includes the test results on the test area A and on the test area B.

3.4.1 Test area A

In this subsection the results of the performed compaction control techniques (inclinodeformeter, dynamic probing heavy, cone penetration test and seismic cone penetration test) on the test area A are documented.

3.4.1.1 Inclinodeformeter

The test evaluation provides information about the diameters, the mean diameter, the ovalization values and the curvatures of the inclinometer pipes including the changes between the epochs.

Diameter

The diameters were measured with the inclinodeformeter device. Due to the diameter reading error occurring if the device is inclined out of the plane (see [19, pp. 38 - 39]), the measured values were corrected using the already existing MATLAB code [21, pp. 93 - 99]. To get interpretable information, the corrected diameters (continuously measured over the depth) were averaged over a length of 0.33 m (see appendix 4 for extended MATLAB code). By discretization measurement noise can be effective eliminated. To reduce the effects of the joints at the pipe connections 0.25 m at the edges of the single pipe elements were neglected.

The measurement in direction and in opposite direction was, as already mentioned (see section 3.3.2.2), averaged to correct the results from potential reading errors due to the geometry of a curved pipe (Eq. (3.1)).

$$\mathrm{d}_{A(B,\ C\ or\ D)} = \frac{\mathrm{d}_{A000(B000,\ C000\ or\ D000)} + \mathrm{d}_{A180(B180,\ C180\ or\ D180)}}{2} \tag{3.1}$$

$\mathrm{d}_{A(B,\ C\ or\ D)}$	inner diameter in measurement direction A, B, C or D
$\mathrm{d}_{A000(B000,\ C000\ or\ D000)}$	inner diameter in measurement direction A, B, C or D (measurement in direction)
$\mathrm{d}_{A180(B180,\ C180\ or\ D180)}$	inner diameter in measurement direction A, B, C or D (measurement in opposite direction)

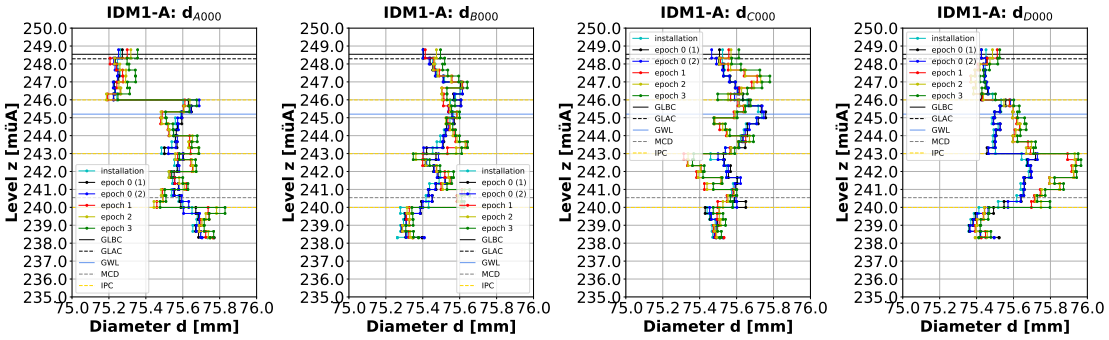

Figure 3.28: Diameters of the inclinometer pipe IDM1-A - 000

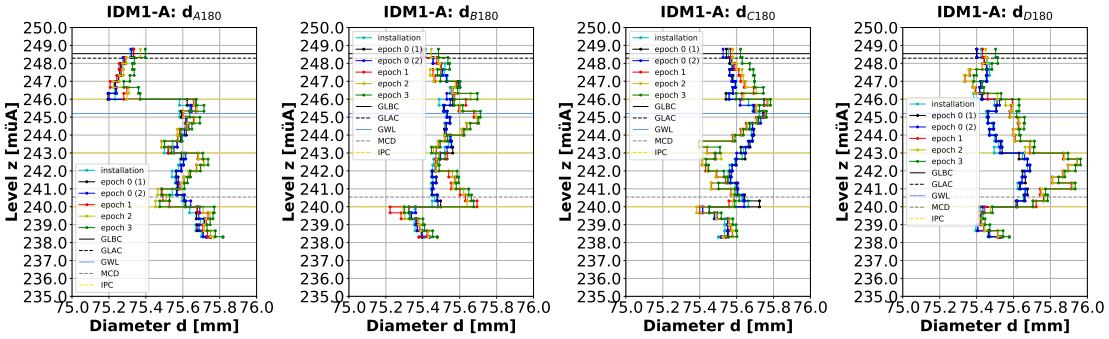

Figure 3.29: Diameters of the inclinometer pipe IDM1-A - 180

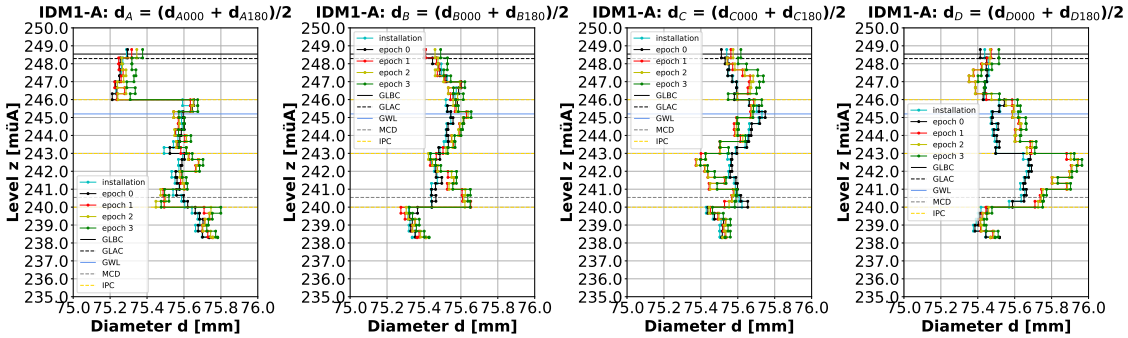

Figure 3.30: Diameters of the inclinometer pipe IDM1-A

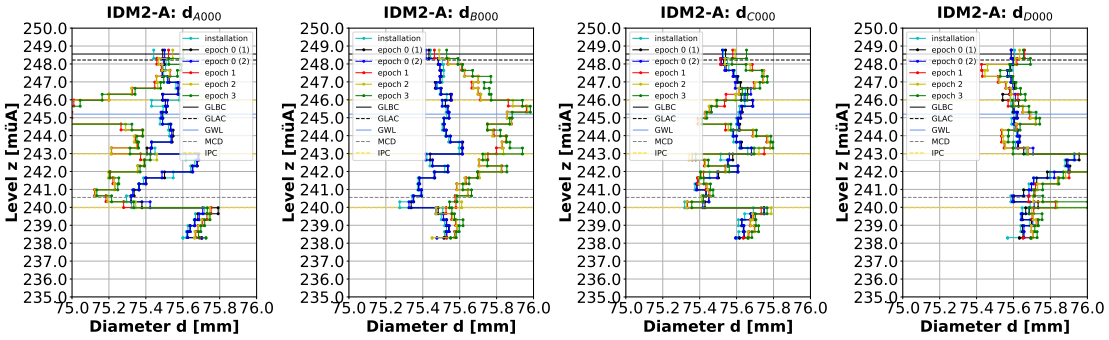

Figure 3.31: Diameters of the inclinometer pipe IDM2-A - 000

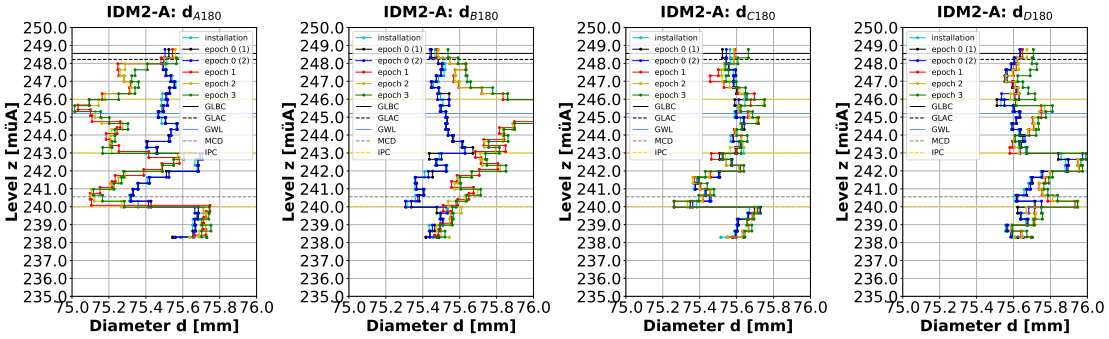

Figure 3.32: Diameters of the inclinometer pipe IDM2-A - 180

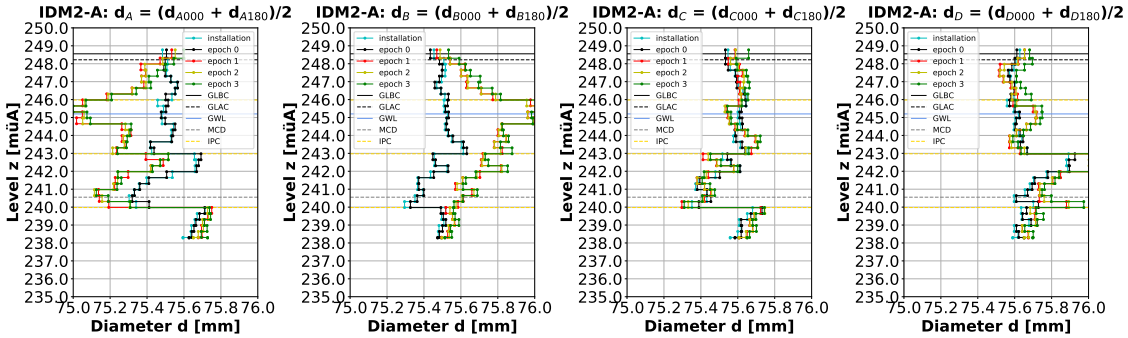

Figure 3.33: Diameters of the inclinometer pipe IDM2-A

Change in diameter

For better interpretability the changes in diameter were calculated in relation to epoch 0 and epoch 1.

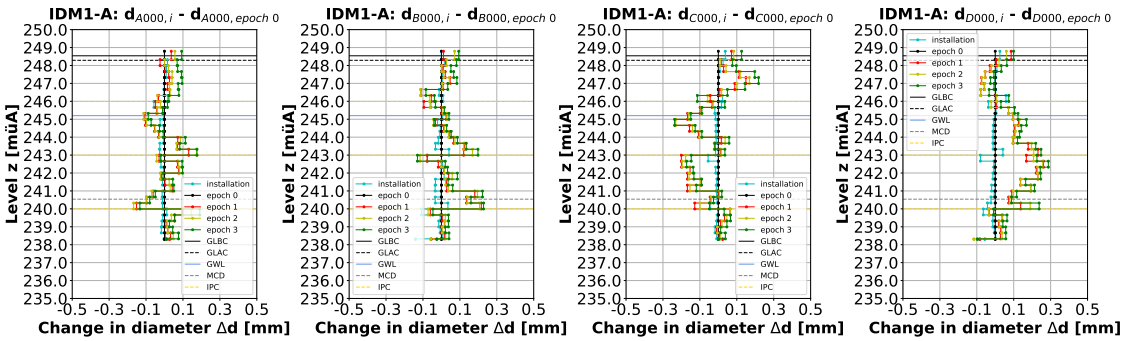

Figure 3.34: Changes in diameter of the inclinometer pipe IDM1-A - 000, epoch 0

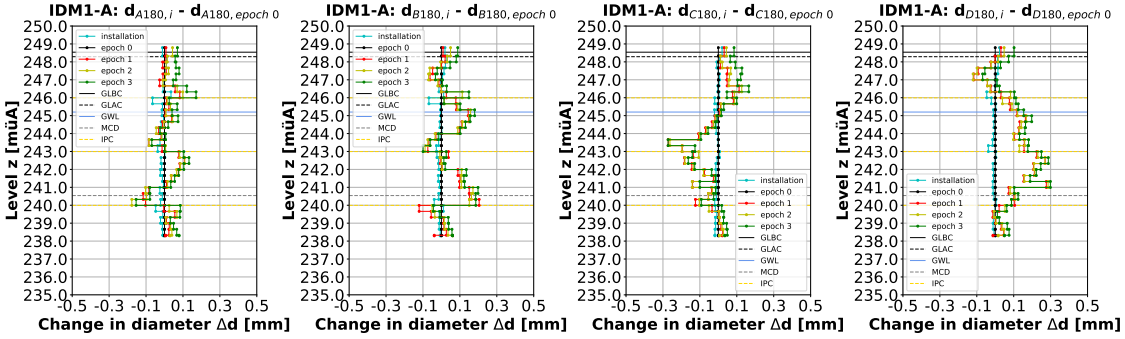

Figure 3.35: Changes in diameter of the inclinometer pipe IDM1-A - 180, epoch 0

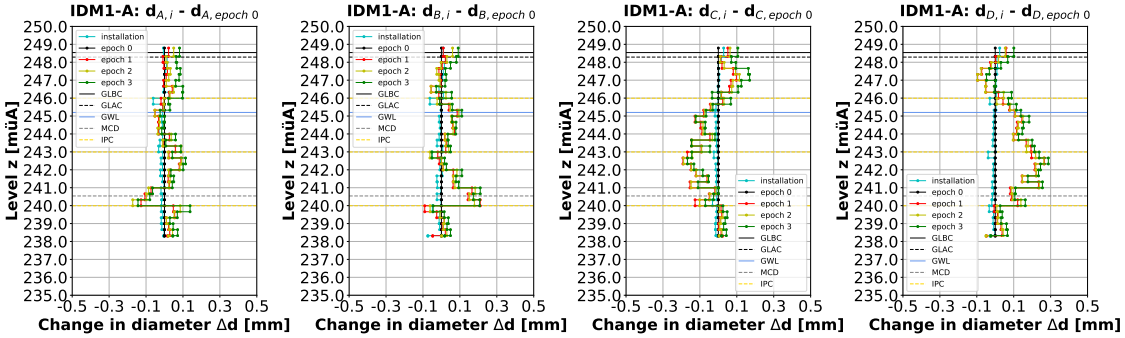

Figure 3.36: Changes in diameter of the inclinometer pipe IDM1-A - epoch 0

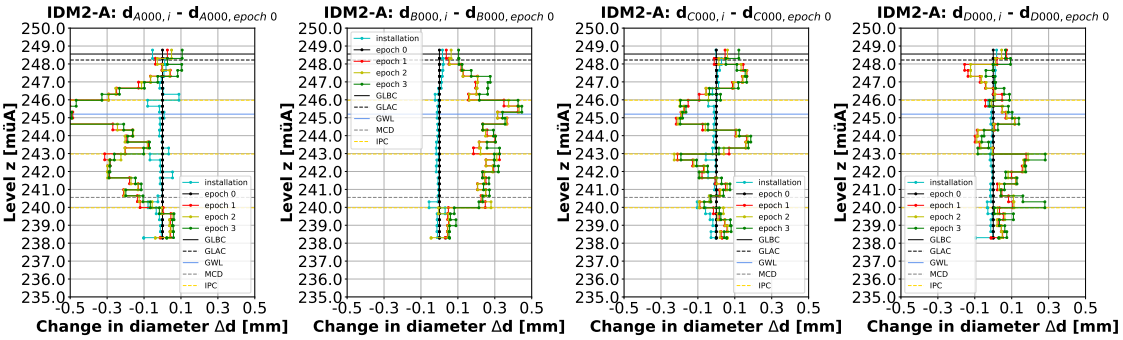

Figure 3.37: Changes in diameter of the inclinometer pipe IDM2-A - 000, epoch 0

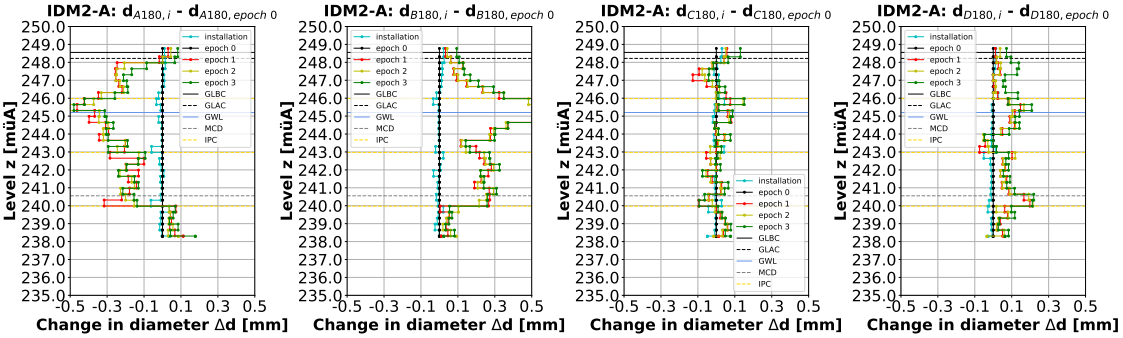

Figure 3.38: Changes in diameter of the inclinometer pipe IDM2-A - 180, epoch 0

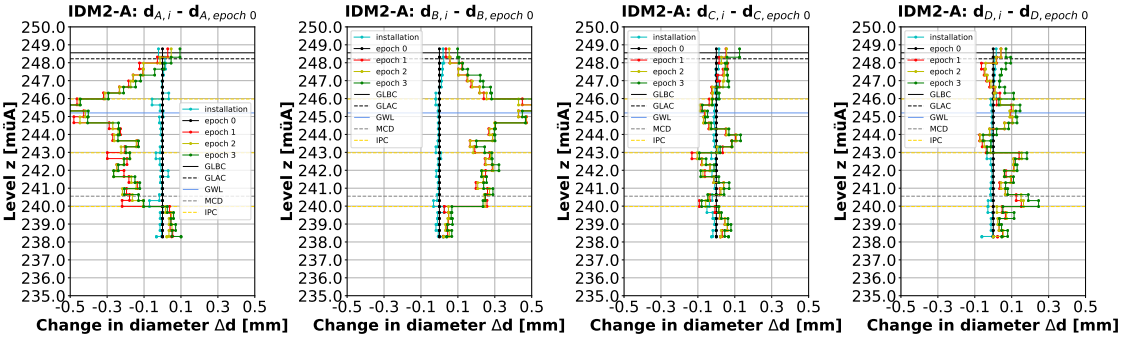

Figure 3.39: Changes in diameter of the inclinometer pipe IDM2-A - epoch 0

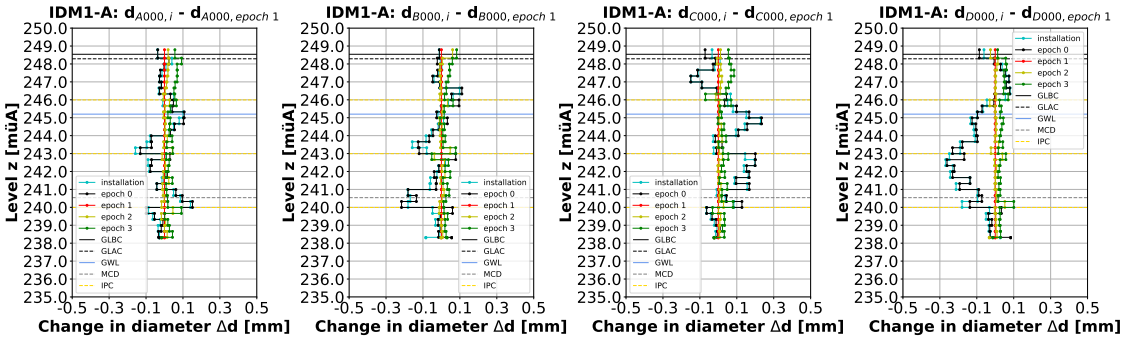

Figure 3.40: Changes in diameter of the inclinometer pipe IDM1-A - 000, epoch 1

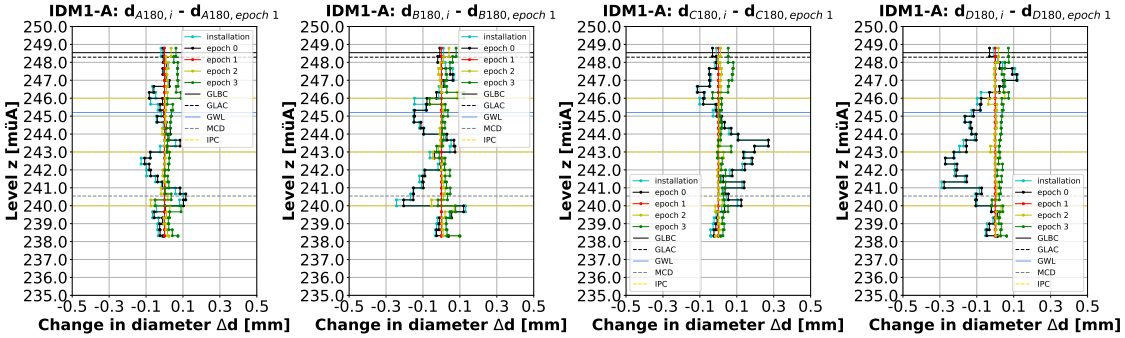

Figure 3.41: Changes in diameter of the inclinometer pipe IDM1-A - 180, epoch 1

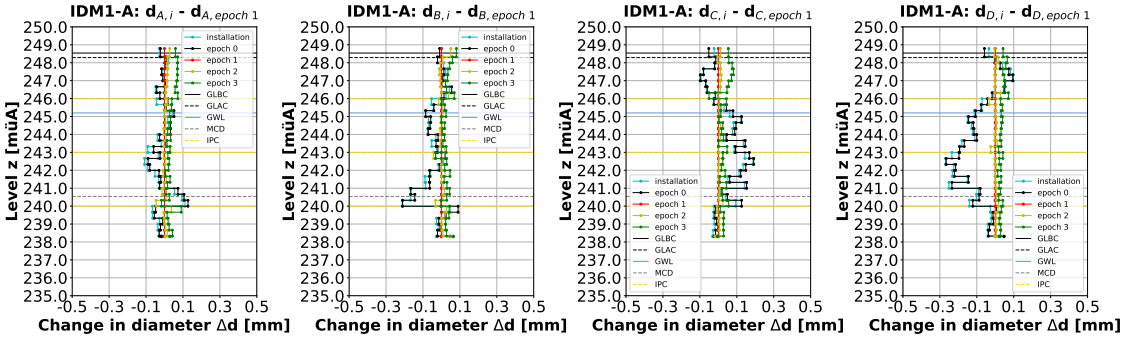

Figure 3.42: Changes in diameter of the inclinometer pipe IDM1-A - epoch 1

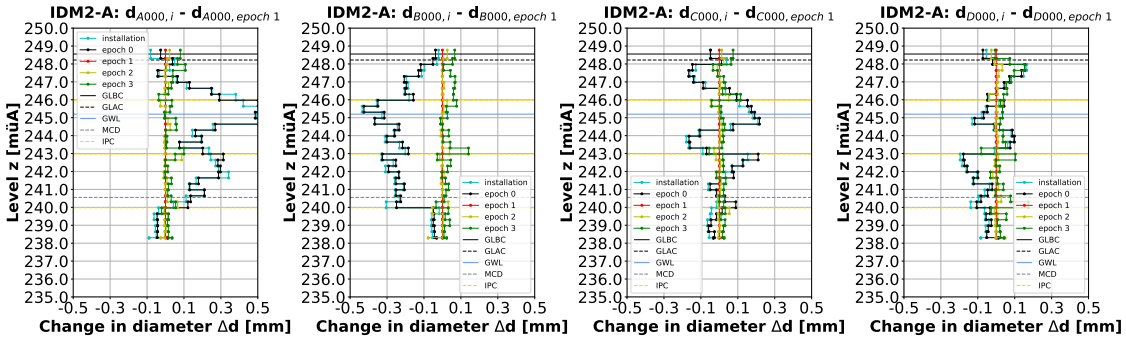

Figure 3.43: Changes in diameter of the inclinometer pipe IDM2-A - 000, epoch 1

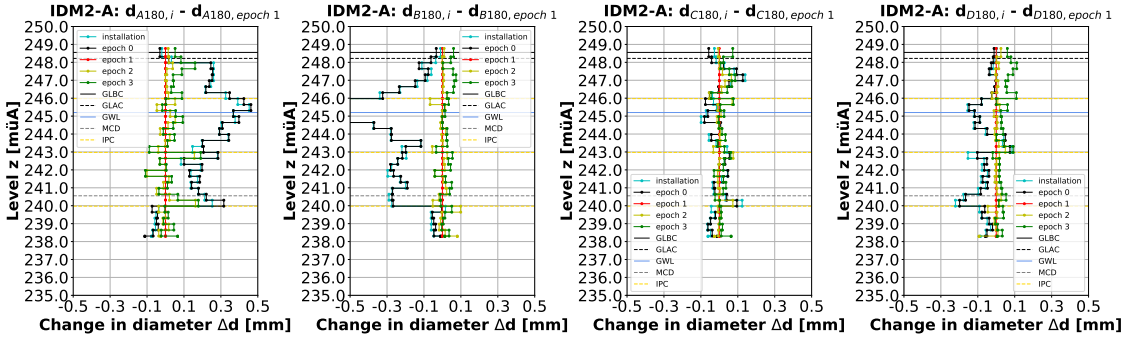

Figure 3.44: Changes in diameter of the inclinometer pipe IDM2-A - 180, epoch 1

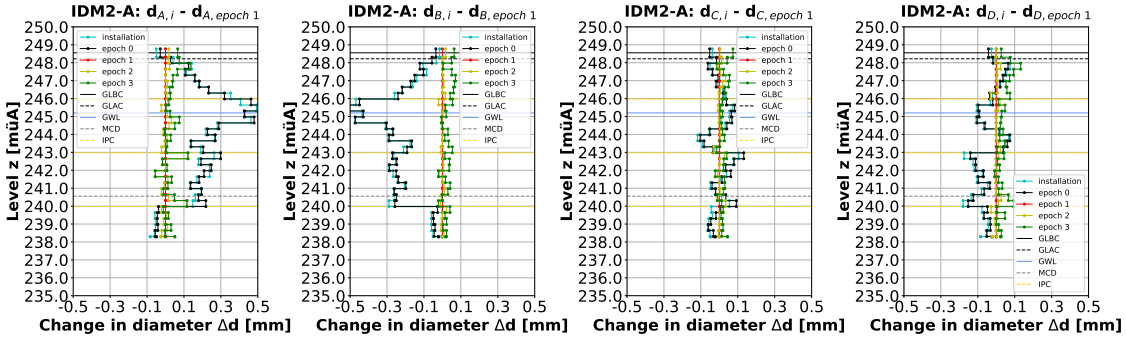

Figure 3.45: Changes in diameter of the inclinometer pipe IDM2-A - epoch 1

Mean diameter and change in mean diameter

For a statement concerning the horizontal earth pressure change the mean diameter (Eq. (3.2)) and the changes in relation to epoch 0 and epoch 1 were calculated.

$$d_m = \frac{d_A + d_B + d_C + d_D}{4} \tag{3.2}$$

d_m inner mean diameter
d_A inner diameter in measurement direction A
d_B inner diameter in measurement direction B
d_C inner diameter in measurement direction C
d_D inner diameter in measurement direction D

The mean diameter of an inclinometer pipe decreases if the horizontal stresses acting on the pipe increases, which is the issue of this thesis. However, the mean diameter of an inclinometer pipe increases if a longitudinal directed load is acting on the outer mantel of the pipe. Due to the friction acting on the mantel of the pipe (as result of the deep vibro compaction) the longitudinal directed load on the pipe increases with depth. The result is shown in the figure below (see epoch 1). The recompaction effect over time amplifies the mean diameter increase (see epoch 2 and epoch 3). Next to the surface another external influence can be observed. If the air temperature changes also the mean diameter of the pipe changes until a certain depth. Especially between epoch 2 (10.03.2020) and epoch 3 (21.04.2020) the effect can be observed. With the coefficient of thermal expansion for PVC of about 7 - 10 $\cdot$ 10^{-5} $^{o}C^{-1}$ the change in air temperature can be roughly back calculated.

The explanations above show that the mean diameter is not an appropriate value to evaluate the horizontal earth pressure changes. Thus, the ovalization value was used for further analyses.

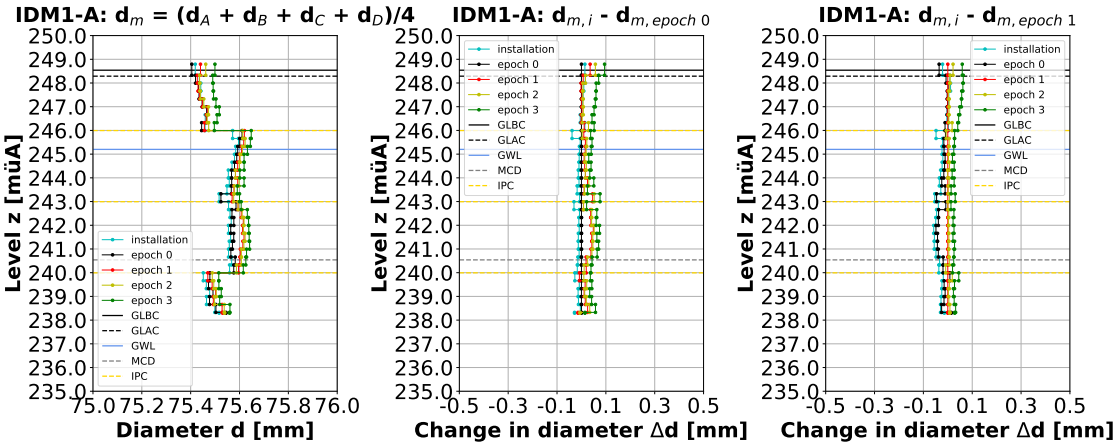

Figure 3.46: Mean diameter and changes in mean diameter of the inclinometer pipe IDM1-A - epoch 0, epoch 1

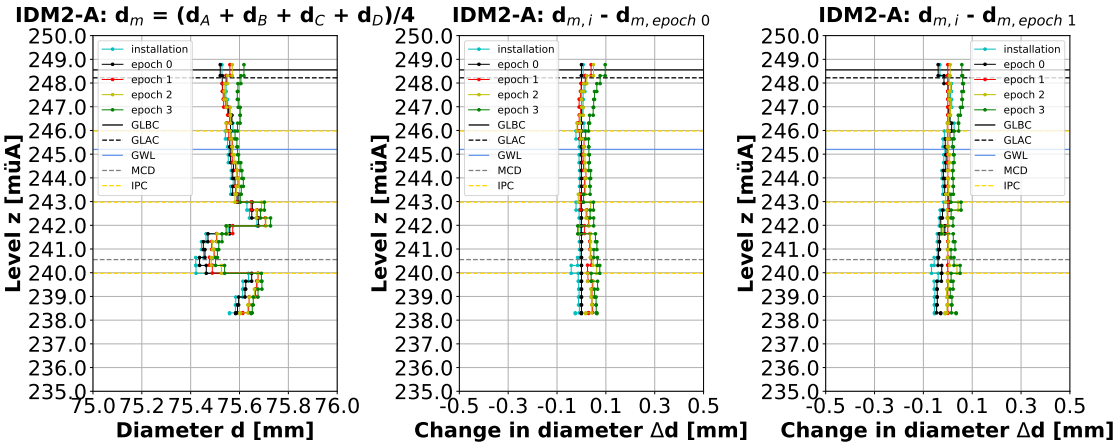

Figure 3.47: Mean diameter and changes in mean diameter of the inclinometer pipe IDM2-A - epoch 0, epoch 1

Ovalization value

In [19] the ovalization value (Eq. (3.3)) is discussed and subsequently used for back calculation of earth pressure changes in creeping landslides and in a vicinity of an excavation. The definition of the ovalization value allows for effective reduction of errors affecting both diameter measurements (e.g. influence of the long-term stability of the probe; influence of the actual field conditions: temperature, humidity, water pressures inside and outside the pipe), cf. [19, pp. 40 - 41].

$$\Omega_{AB(CD)} = \frac{\mathrm{d}_{B(D)} - \mathrm{d}_{A(C)}}{\mathrm{r}} \tag{3.3}$$

$\Omega_{AB(CD)}$	ovalization value in measurement direction AB or CD
$\mathrm{d}_{B(D)}$	inner diameter in measurement direction B or D
$\mathrm{d}_{A(C)}$	inner diameter in measurement direction A or C
r	nominal outer radius of the inclinometer pipe

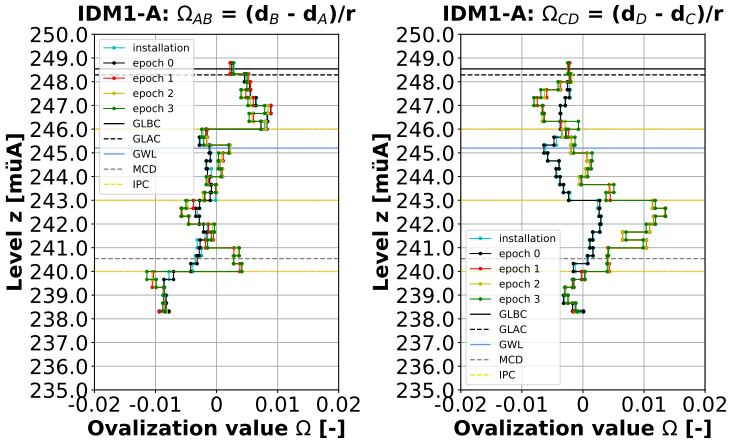

Figure 3.48: Ovalization values of the inclinometer pipe IDM1-A

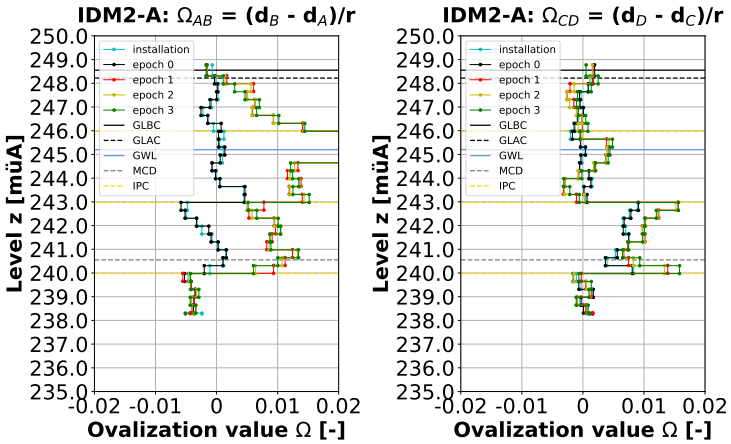

Figure 3.49: Ovalization values of the inclinometer pipe IDM2-A

Change in ovalization value

For better interpretability the changes in ovalization value were calculated in relation to epoch 0 and epoch 1.

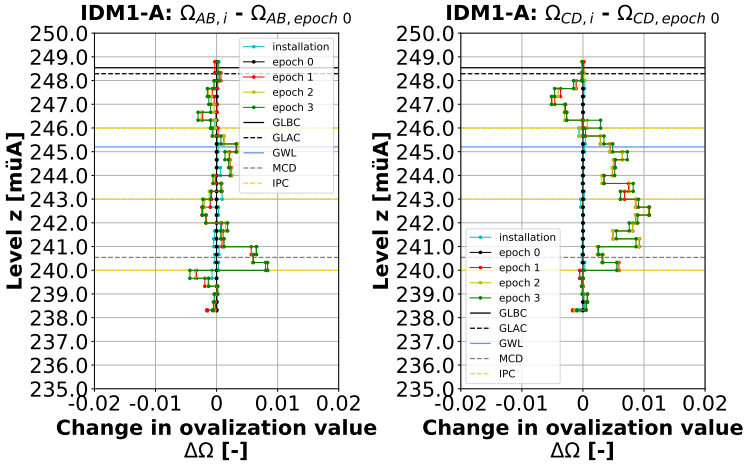

Figure 3.50: Changes in ovalization value of the inclinometer pipe IDM1-A - epoch 0

In Fig. 3.50 an ovalization in the direction CD (above: C - extension, D - compression; below: C - compression, D - extension) after the compaction works can be observed. The ovalization develops with depth and reaches at a specific level a more or less constant value. The ovalization value is below the maximum compaction depth MCD of course almost zero. The ovalization value in the direction AB is generally smaller, changes several times the sign and doesn't represent an obvious ovalization.
Due to the increasing stiffness caused by the ongoing compaction works the inclinometer pipe between four columns should be finally compressed in the direction of the first realized compaction column. For the inclinometer pipe IDM1-A is this the case. Compaction column DVC04-A, produced first, is located exactly in direction C.

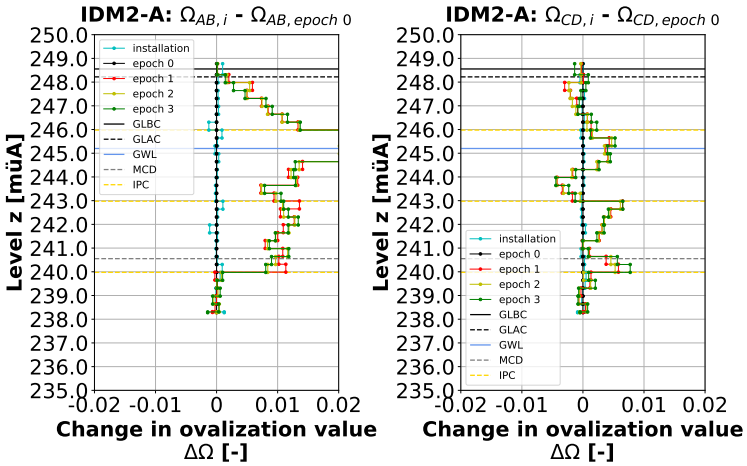

Figure 3.51: Changes in ovalization value of the inclinometer pipe IDM2-A - epoch 0

In Fig. 3.51 an ovalization in the direction AB (A - compression, B - extension) after the

compaction works can be observed. The ovalization develops with depth and reaches at a specific level a more or less constant value. The ovalization value is below the maximum compaction depth of course almost zero. The ovalization value in the direction CD is generally smaller, changes several times the sign and doesn't represent an obvious ovalization.

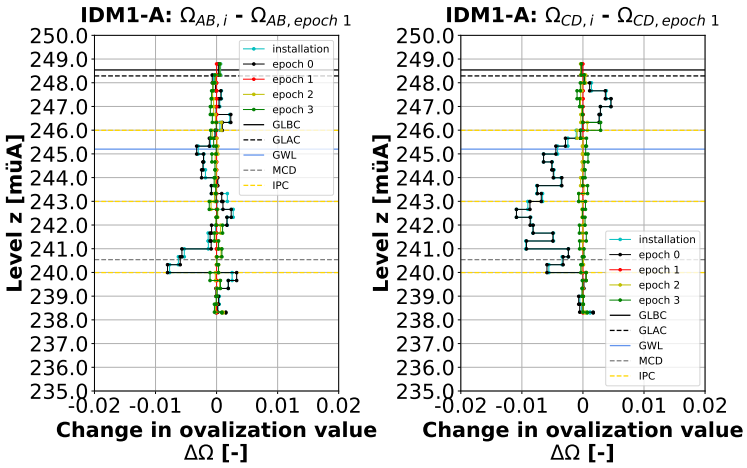

Figure 3.52: Changes in ovalization value of the inclinometer pipe IDM1-A - epoch 1

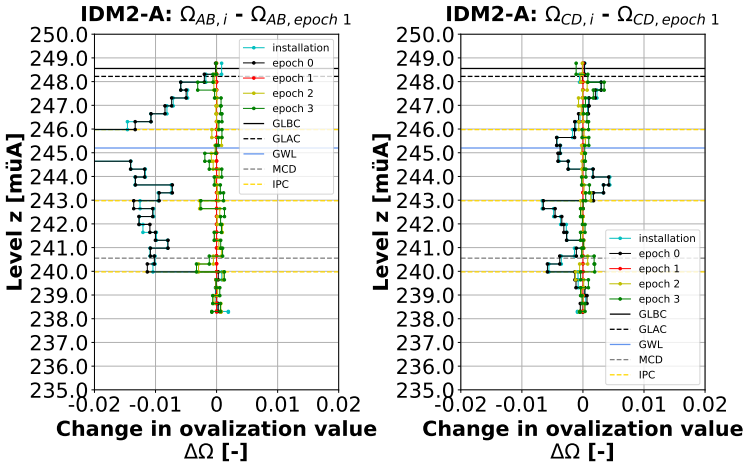

Figure 3.53: Changes in ovalization value of the inclinometer pipe IDM2-A - epoch 1

Curvature

A change in ovalization of an inclinometer pipe doesn't only occur because of changes in horizontal earth pressure. If the pipe is bent longitudinally the cross section flattens to an oval shape. The inclinometer pipe can be subjected to bending due to displacements of the surrounding soil, which may not be related to earth pressure changes. Thus, the measurements should be corrected for the amount of change in ovalization value due to longitudinal bending.

The change in ovalization due to bending can be described as function of the curvature of the pipe (see [19, pp. 101 - 104] for an inclinometer pipe with four channels). The curvature can be calculated by numerical differentiation of the inclination of the pipe, which is anyway always measured by the inclinodeformeter device in a profile over depth.

For many applications the effect of longitudinal bending can be neglected. The cross-sectional deformations due to bending are usually smaller than the precision of the inclinodeformeter device, cf. [19, p. 99].

First, the measured inclinations of the pipe were averaged over a length of 0.33 m (see appendix 4 for extended MATLAB code). By discretization measurement noise can be effective eliminated. To reduce the effects of the joints at the pipe connections 0.25 m at the edges of the single pipe elements were neglected. Finally, the curvatures were calculated by numerical differentiation of the averaged inclinations.

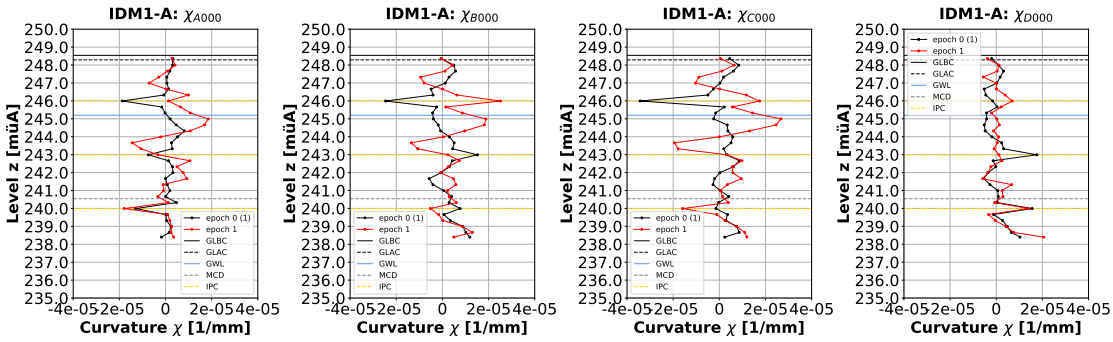

Figure 3.54: Curvatures of the inclinometer pipe IDM1-A - 000

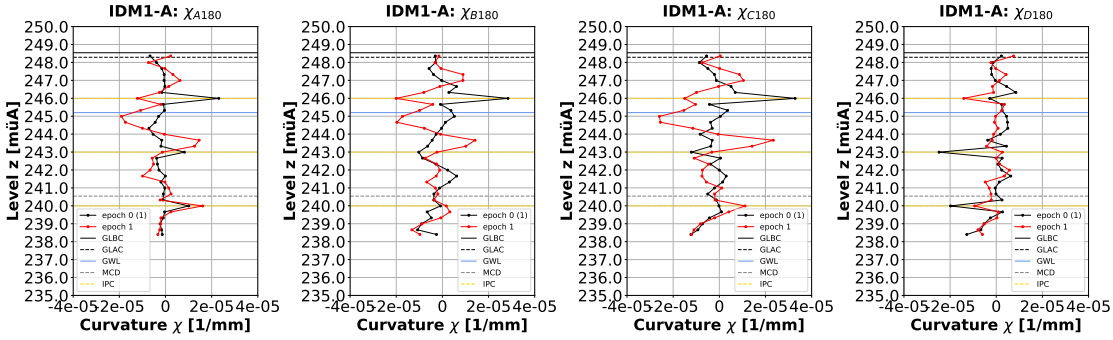

Figure 3.55: Curvatures of the inclinometer pipe IDM1-A - 180

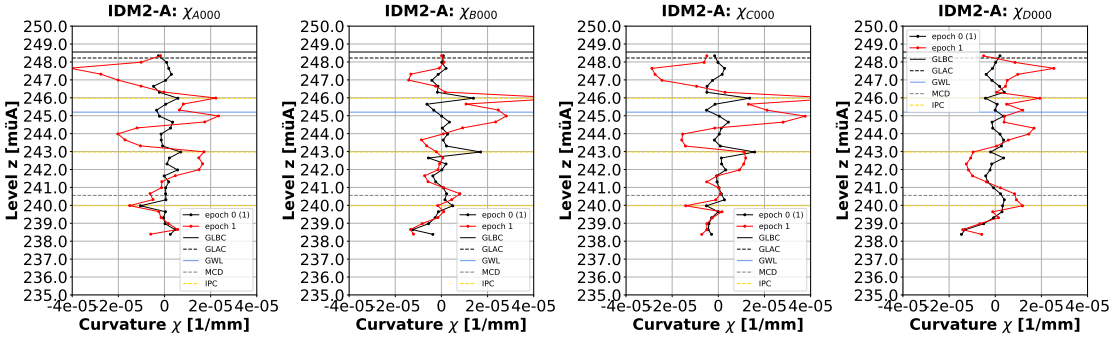

Figure 3.56: Curvatures of the inclinometer pipe IDM2-A - 000

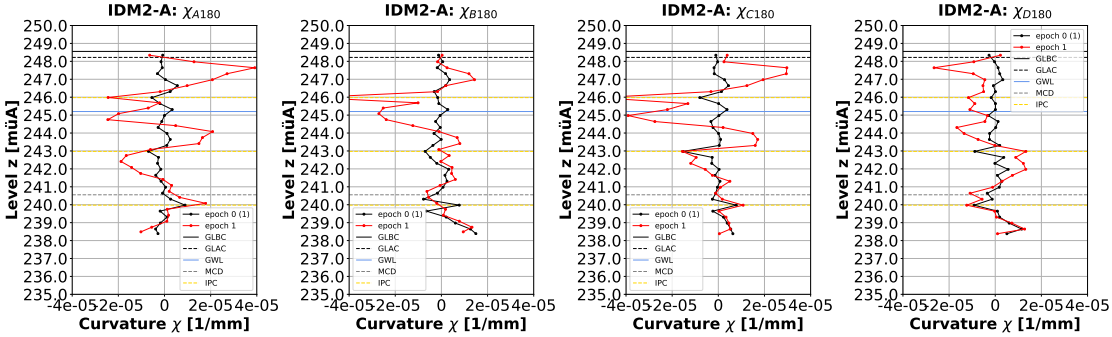

Figure 3.57: Curvatures of the inclinometer pipe IDM2-A - 180

Change in curvature

No correction is needed if the change in ovalization due to bending is smaller than the precision of the inclinodeformeter measurement. In consideration of conservative assumptions the condition for the curvature to be neglected is $\left|\chi_i^2 - \chi_{epoch\ 0}^2\right| \leq 1.7 \cdot 10^{-10}\ 1/\text{mm}^2$ (valid for an inclinometer pipe with a nominal outer radius of 42.00 mm and four channels), cf. [19, p. 104]. Even if for the investigation pipes with eight channels were used, the mentioned condition is for estimating purposes shown in the following figures. The criteria show that primarily near the surface some local corrections would be necessary.

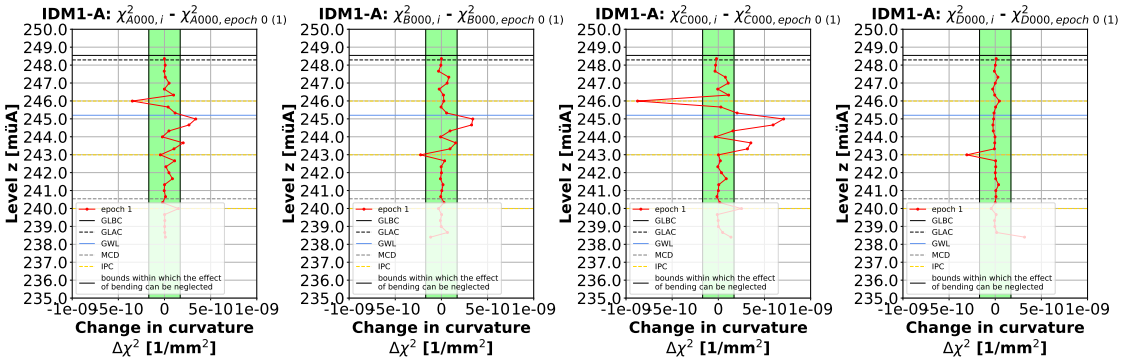

Figure 3.58: Changes in curvature of the inclinometer pipe IDM1-A - 000

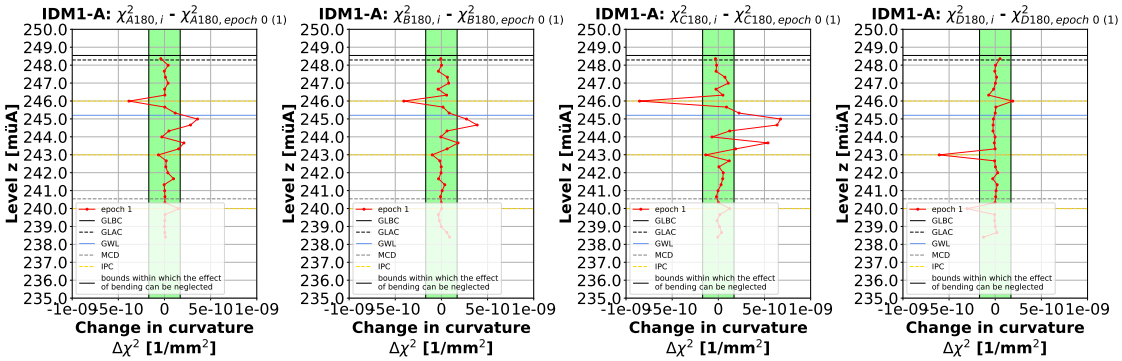

Figure 3.59: Changes in curvature of the inclinometer pipe IDM1-A - 180

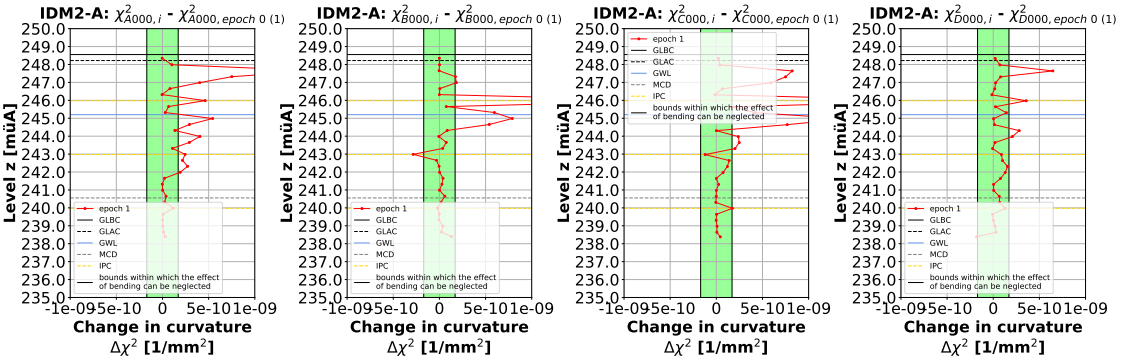

Figure 3.60: Changes in curvature of the inclinometer pipe IDM2-A - 000

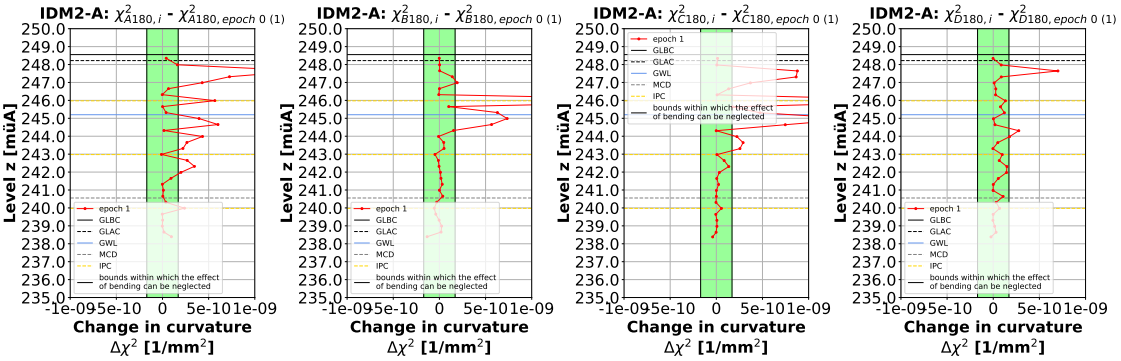

Figure 3.61: Changes in curvature of the inclinometer pipe IDM2-A - 180

3.4.1.2 Dynamic probing heavy

For better interpretability the original data were averaged over a length of 0.30 m. The test results show the loosening of the ground next to the surface and the compaction of the ground at deeper levels as a result of the compaction works. Furthermore, the homogenization effect can be observed.

The loosening of the ground next to the surface, caused by the low overburden, is mostly the reason for a subsequent compaction of the surface with a surface vibratory roller after completion the deep vibro compaction works.

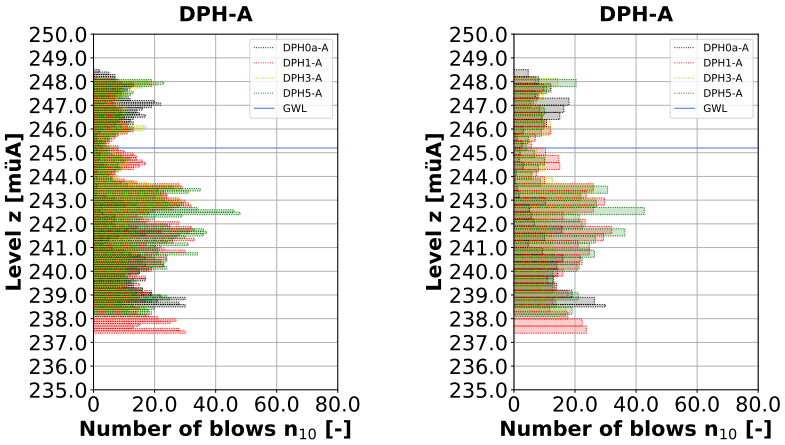

(a) original (b) averaged

Figure 3.62: Heavy dynamic probing tests - test area A, above left

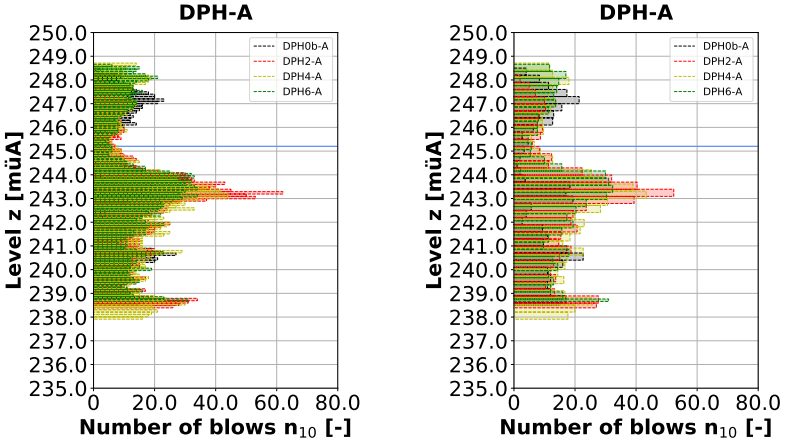

(a) original (b) averaged

Figure 3.63: Heavy dynamic probing tests - test area A, below right

3.4.1.3 Cone penetration test with pore water pressure measurement

In the following first the measurement results are documented and then some derived parameters are described.

Measurement results

For better interpretability the original data were averaged over a length of 0.30 m. The cone penetration test results show, that after treatment both, the cone resistance and the sleeve friction increased by approximately the same degree. The friction ratio remained therefore approximately unchanged. This behaviour is also mentioned in [11, p. 373].

The dynamic pore pressure measurements give, as already mentioned in section 3.2.2, information about the groundwater level. Due to the high permeability of the subsoil no relevant dynamic pore pressure changes were recorded after the compaction works.

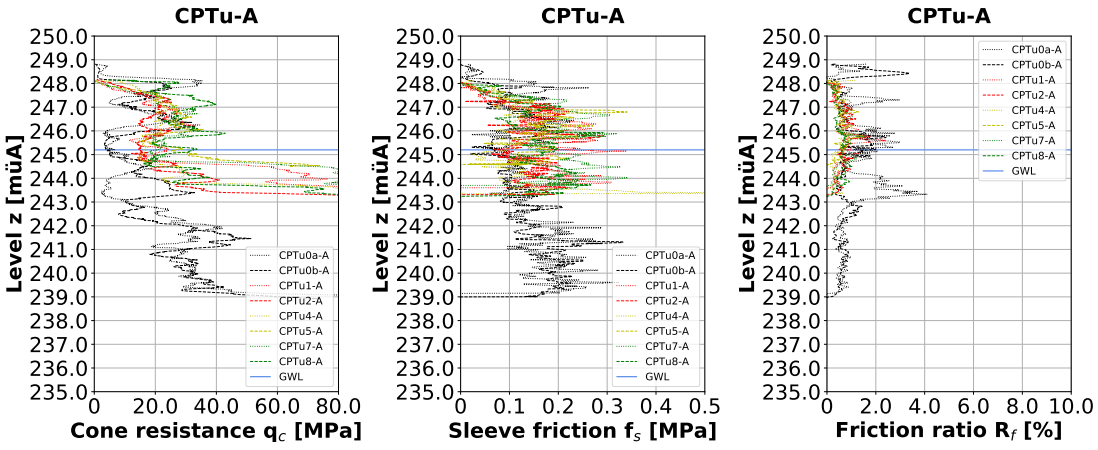

(a) original

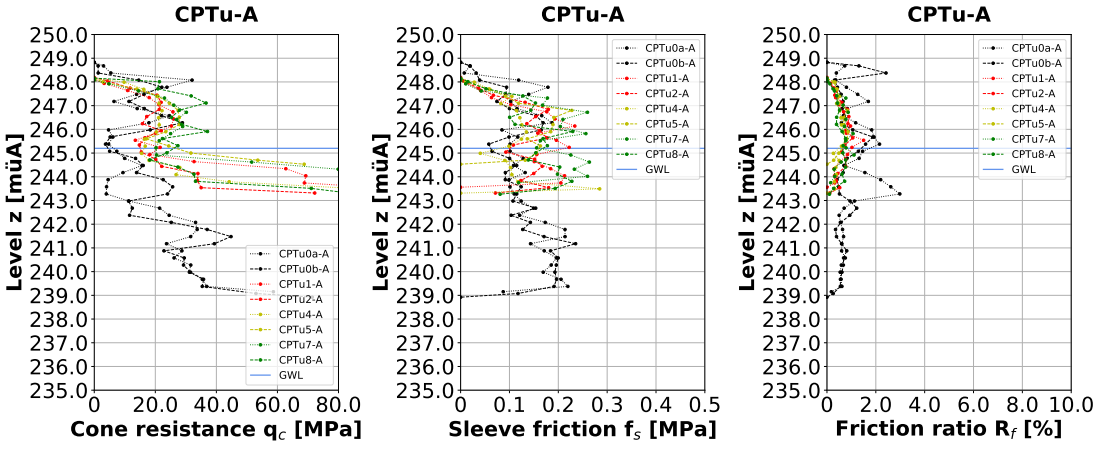

(b) averaged

Figure 3.64: Cone penetration tests with pore water pressure measurement - test area A, between four columns (1)

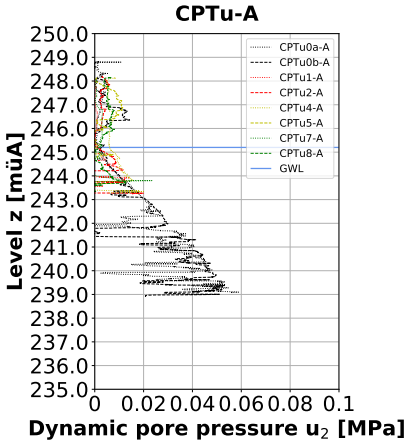

Figure 3.65: Cone penetration tests with pore water pressure measurement - test area A, between four columns (2)

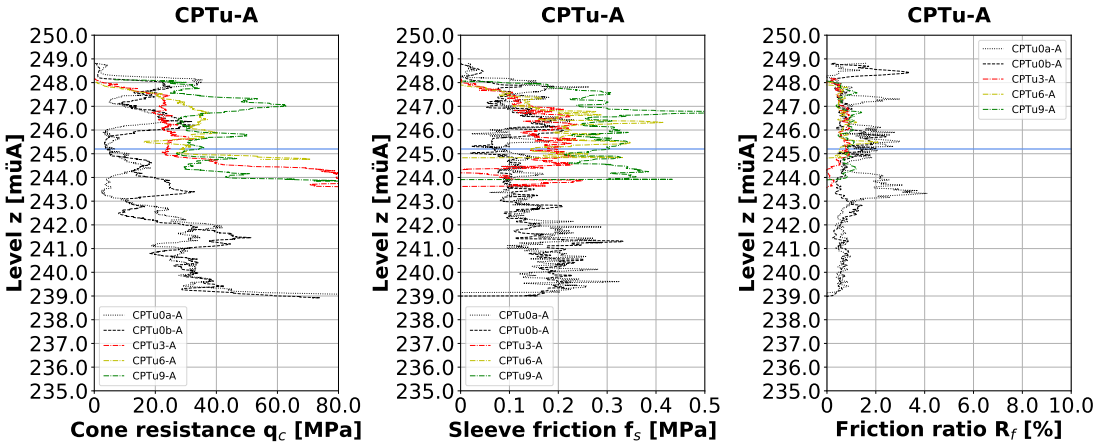

(a) original

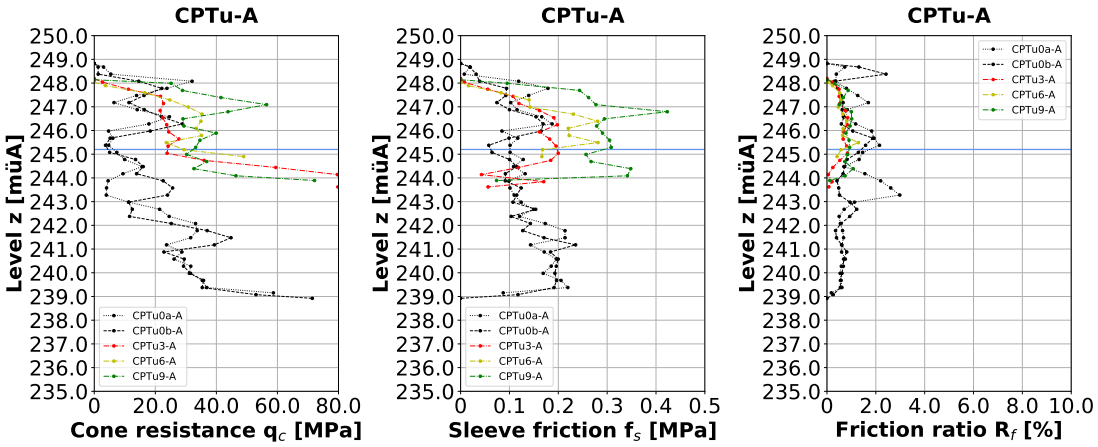

(b) averaged

Figure 3.66: Cone penetration tests with pore water pressure measurement - test area A, between two columns (1)

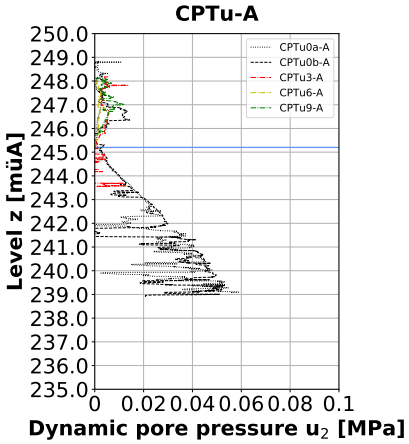

Figure 3.67: Cone penetration tests with pore water pressure measurement - test area A, between two columns (2)

Derived parameters

According to [9, p. 142] the horizontal earth pressure change, caused by the compaction works, can be calculated based on the measured sleeve friction (Eq. (3.4)).

$$\frac{\mathrm{K}_{after}}{\mathrm{K}_{before}} \approx \frac{\mathrm{f}_{s,after} \cdot \tan\varphi'_{before}}{\mathrm{f}_{s,before} \cdot \tan\varphi'_{after}} \approx 0.85 \cdot \frac{\mathrm{f}_{s,after}}{\mathrm{f}_{s,before}} \tag{3.4}$$

K_{after}	lateral earth pressure coefficient after compaction
K_{before}	lateral earth pressure coefficient before compaction
$\mathrm{f}_{s,after}$	sleeve friction after compaction
$\mathrm{f}_{s,before}$	sleeve friction before compaction
φ'_{after}	friction angle after compaction
φ'_{before}	friction angle before compaction

Due to the assumption that the friction angle by the compaction increases by about 3 - 5°, the factor 0.85 in the equation can be introduced.

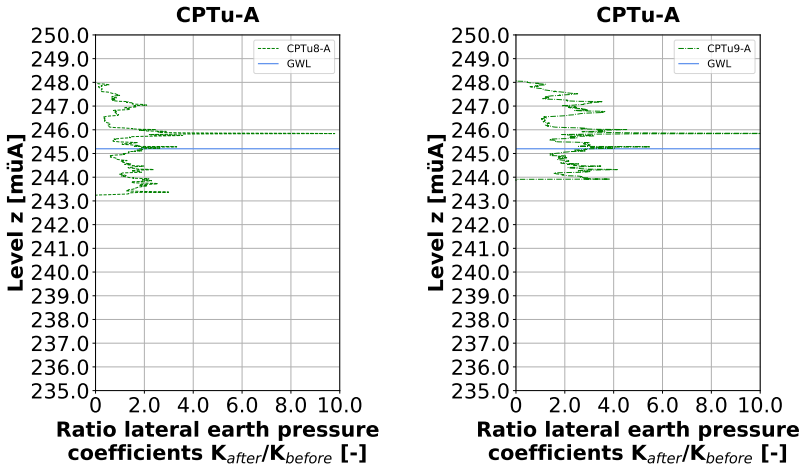

(a) between four columns (b) between two columns

Figure 3.68: Ratio lateral earth pressure coefficients - test area A

According to Eq. (3.4), a change in sleeve friction after compaction leads to a change of the stress increase factor. The cone penetration test results, summarized in Fig. 3.64(b), Fig. 3.66(b), Fig. 3.111(b) and Fig. 3.113(b), show a change in sleeve friction even after compaction. Consequently, the horizontal earth pressure would still change after compaction. The measurement results in Fig. 3.52, Fig. 3.53, Fig. 3.99 and Fig. 3.100 do not indicate this behaviour. After epoch 1 no significant change in ovalization value was recorded. Neither at the inclinometer pipes between two compaction columns.

The overconsolidation ratio is an important design parameter for settlement analyses but also for the assessment of the liquefaction hazard, cf. [10, p. 05019012-8]. According to [9, p. 139] the overconsolidation ratio, caused by the compaction works, can be calculated as follows (Eq. (3.5)).

$$\mathrm{OCR} = \left(\frac{\mathrm{K}_{after}}{\mathrm{K}_{before}} \right)^{\frac{1}{\beta}} \tag{3.5}$$

OCR	overconsolidation ratio
K_{after}	lateral earth pressure coefficient after compaction
K_{before}	lateral earth pressure coefficient before compaction
β	empirically determined exponent

For the empirical exponent the relation $\beta = \sin \varphi'$ was used.

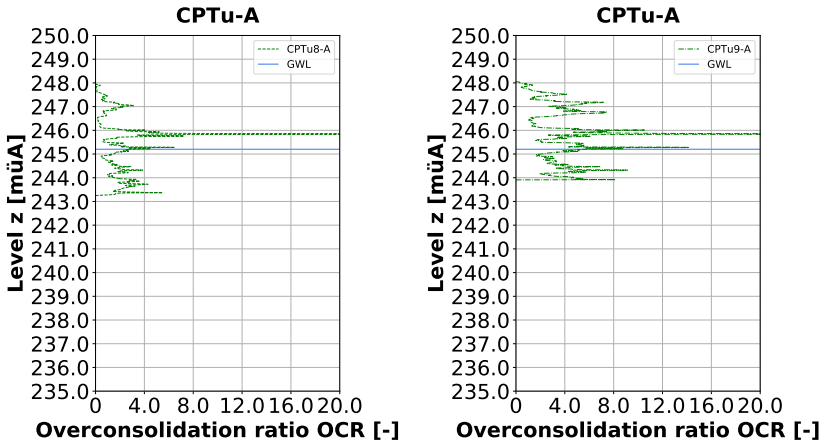

(a) between four columns (b) between two columns

Figure 3.69: Overconsolidation ratio - test area A

It should be noted that the derivation of the overconsolidation ratio from the lateral earth pressure coefficients before and after compaction as shown above is questionable because an increase in horizontal stress is caused by overconsolidation and not vice versa. An increase in horizontal stress is not necessarily an indication for an overconsolidation as it could be forced by other effects too. However, it is possible that compaction leads to overconsolidation but only when the applied method leads to a temporary increase of the vertical stress during compaction. When different effects force the increase in horizontal stress, which is most probable for different compaction methods, one should be careful to calculate the overconsolidation ratio with Eq. (3.5).

According to [9] the reference oedometer modulus can be calculated based on the cone penetration test results as follows (Eq. (3.6)).

$$\mathrm{E}_{oed}^{ref} = \mathrm{m} \cdot \sigma_r \cdot \left(\frac{\sigma'_v}{\sigma_r} \right)^{(1-\mathrm{j})} \tag{3.6}$$

E_{oed}^{ref}	reference oedometer modulus
m	modulus number
σ_r	reference stress (= 100 kPa)
σ'_v	vertical effective stress
j	stress exponent

$$\mathrm{m} = \mathrm{a} \cdot \left(\frac{\mathrm{q}_{cM}}{\sigma_r} \right)^{0.5} \tag{3.7}$$

m	modulus number
a	empirical modulus factor
q_{cM}	stress-adjusted cone resistance
σ_r	reference stress (= 100 kPa)

Table 3.4: Empirical modulus factor a for different soil types according to [9, p. 141]

soil type	empirical modulus factor a
silt, organic, soft	7
silt, loose	12
silt, medium dense	15
silt, dense	20
sand, silty, loose	20
sand, loose	22
sand, medium dense	28
sand, dense	35
gravel, loose	35
gravel, medium dense	40
gravel, dense	45

For the empirical modulus factor before compaction 35 and after compaction 45 was chosen.

$$q_{cM} = q_c \cdot \min\left[\left(\frac{\sigma_r}{\sigma'_m}\right)^{0.5}, 2.5\right] \tag{3.8}$$

q_{cM}	stress-adjusted cone resistance
q_c	cone resistance
σ_r	reference stress (= 100 kPa)
σ'_m	mean effective stress

$$\sigma'_m = \frac{\sigma'_v}{3} \cdot (1 + 2 \cdot K_{before\ or\ after}) \tag{3.9}$$

σ'_m	mean effective stress
σ'_v	vertical effective stress
$K_{before\ or\ after}$	lateral earth pressure coefficient before compaction or after compaction

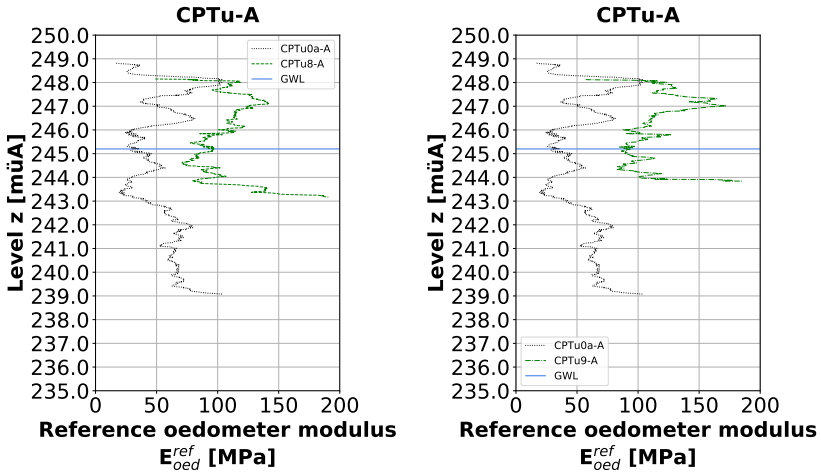

(a) between four columns (b) between two columns

Figure 3.70: Reference oedometer modulus - test area A

Fig. 3.71 shows the normalized soil behaviour type chart (Robertson 2010) with the cone penetration test results CPTu0a-A (black), CPTu0b-A (grey) and CPTu8-A (green). In Fig. 3.72 the cone penetration test results CPTu0a-A (black), CPTu0b-A (grey) and CPTu9-A (green) are represented. For the evaluation the formulas given in [17] were used.

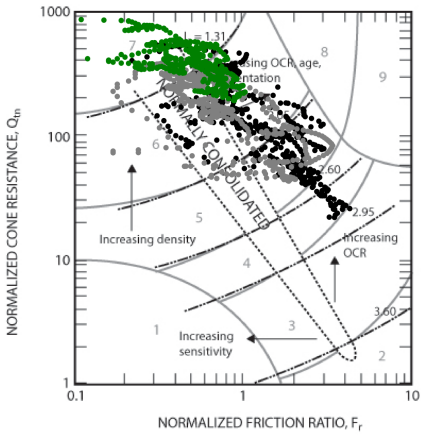

Figure 3.71: Normalized soil behaviour type chart (Robertson 2010) according to [18, p. 27] - test area A, between four columns

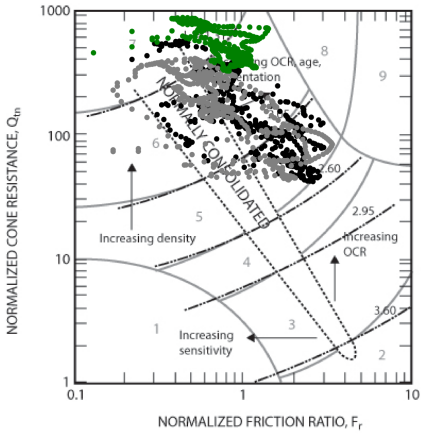

Figure 3.72: Normalized soil behaviour type chart (Robertson 2010) according to [18, p. 27] - test area A, between two columns

1 sensitive, fine grained
2 organic soils - clay
3 clays - silty clay to clay
4 silt mixtures - clayey silt to silty clay
5 sand mixtures - silty sand to sandy silt
6 sands - clean sand to silty sand
7 gravelly sand to dense sand
8 very stiff sand to clayey sand (heavily overconsolidated or cemented)
9 very stiff, fine grained (heavily overconsolidated or cemented)

3.4.1.4 Seismic cone penetration test

After the compaction works no relevant shear wave velocity changes were recorded.

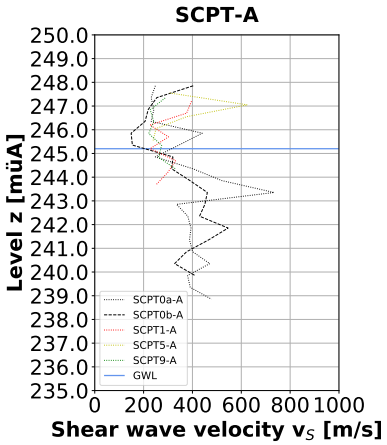

Figure 3.73: Seismic cone penetration tests - test area A, between four columns

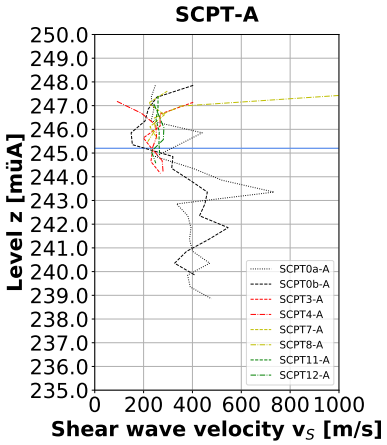

Figure 3.74: Seismic cone penetration tests - test area A, between two columns

3.4.2 Test area B

In this subsection the results of the performed compaction control techniques (inclinodeformeter, dynamic probing heavy, cone penetration test and seismic cone penetration test) on the test area B are documented.

3.4.2.1 Inclinodeformeter

The test evaluation provides information about the diameters, the mean diameter, the ovalization values and the curvatures of the inclinometer pipes including the changes between the epochs.

Diameter

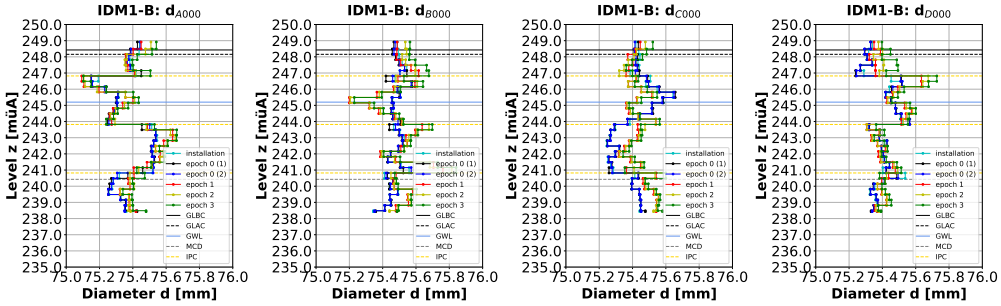

Figure 3.75: Diameters of the inclinometer pipe IDM1-B - 000

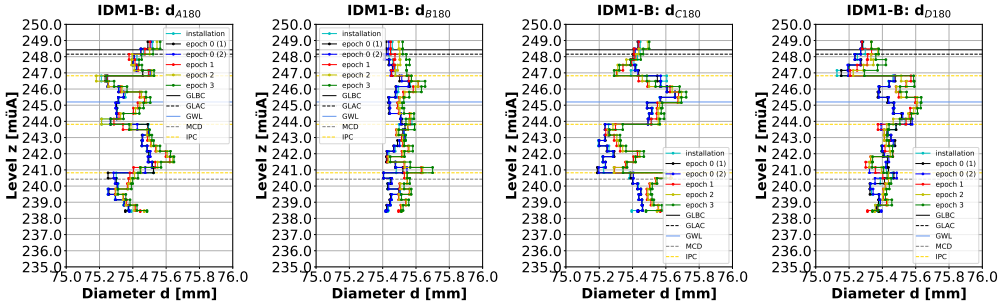

Figure 3.76: Diameters of the inclinometer pipe IDM1-B - 180

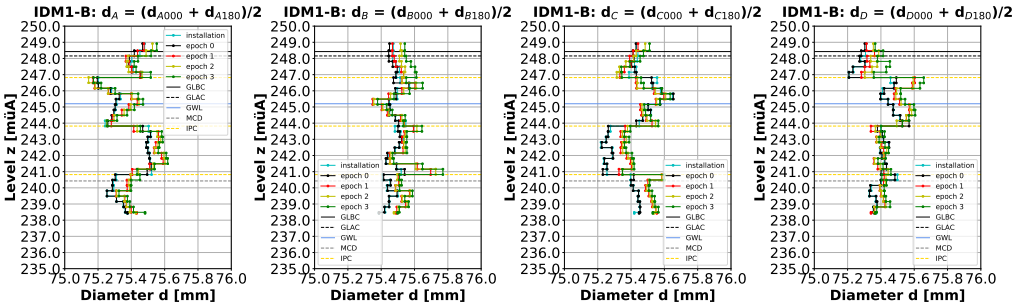

Figure 3.77: Diameters of the inclinometer pipe IDM1-B

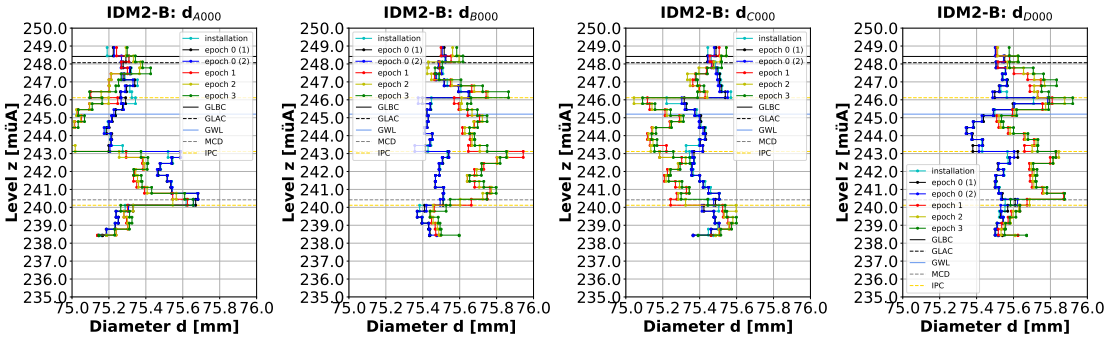

Figure 3.78: Diameters of the inclinometer pipe IDM2-B - 000

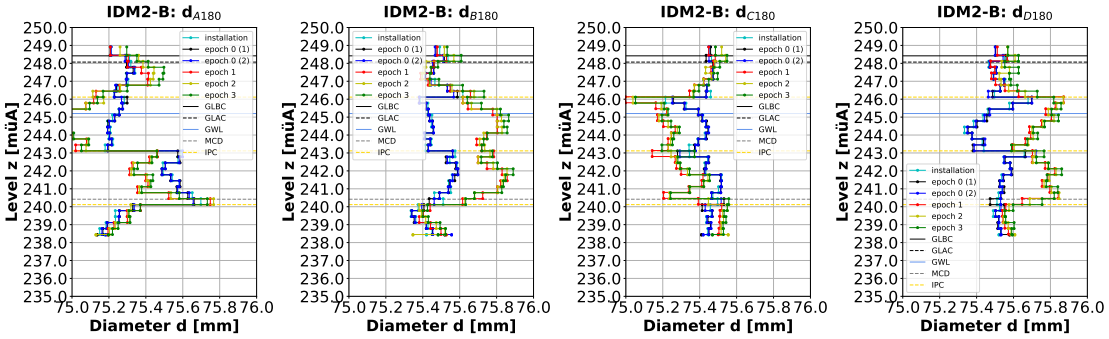

Figure 3.79: Diameters of the inclinometer pipe IDM2-B - 180

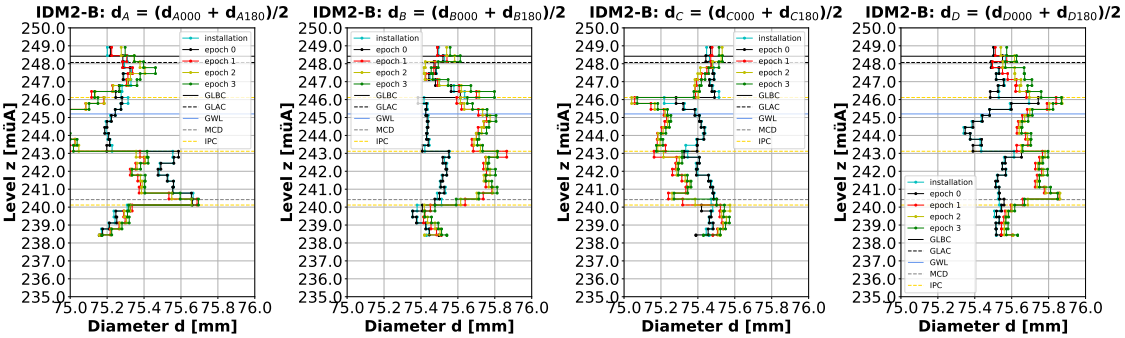

Figure 3.80: Diameters of the inclinometer pipe IDM2-B

Change in diameter

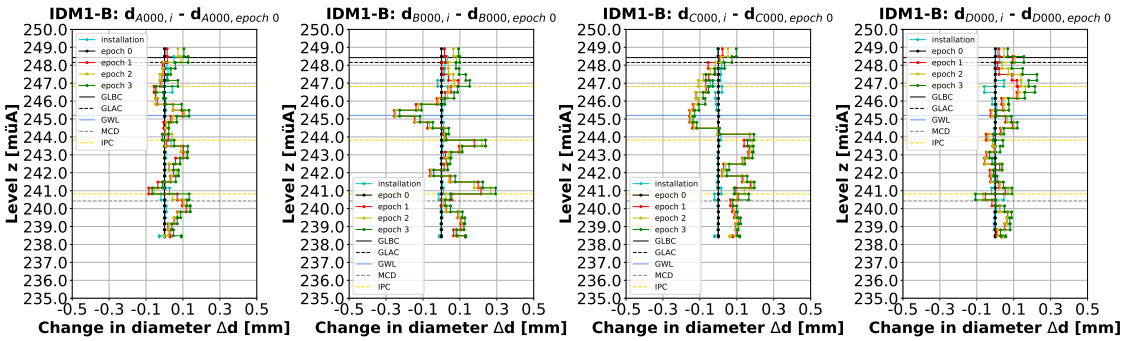

Figure 3.81: Changes in diameter of the inclinometer pipe IDM1-B - 000, epoch 0

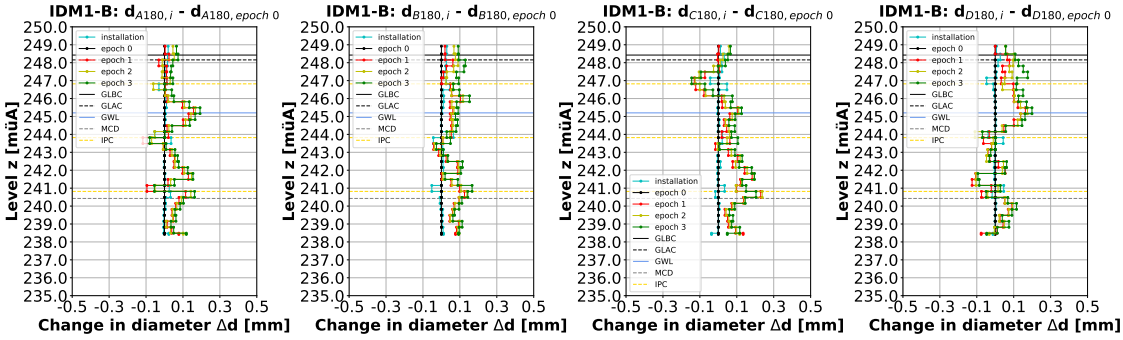

Figure 3.82: Changes in diameter of the inclinometer pipe IDM1-B - 180, epoch 0

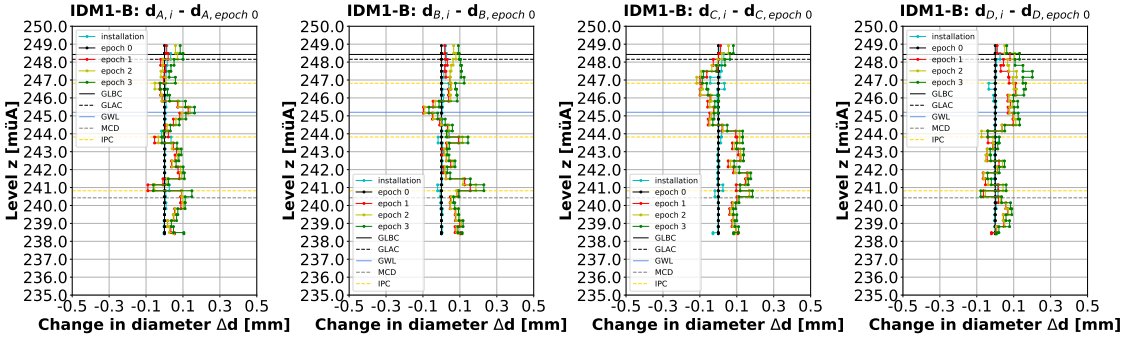

Figure 3.83: Changes in diameter of the inclinometer pipe IDM1-B - epoch 0

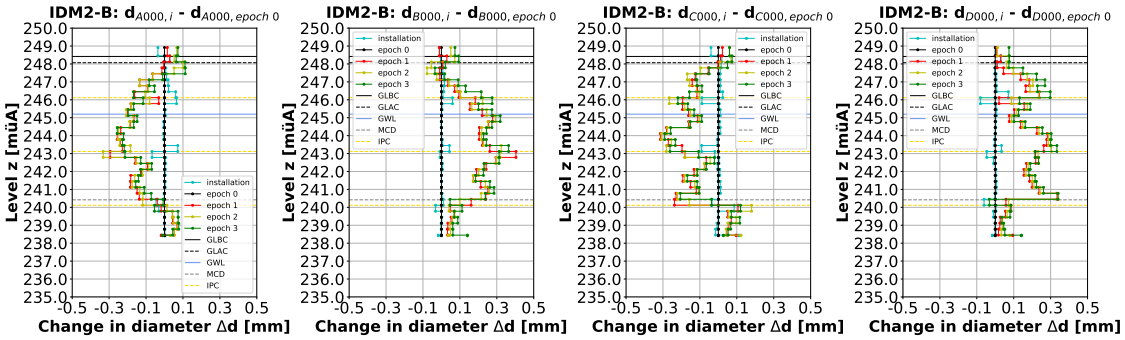

Figure 3.84: Changes in diameter of the inclinometer pipe IDM2-B - 000, epoch 0

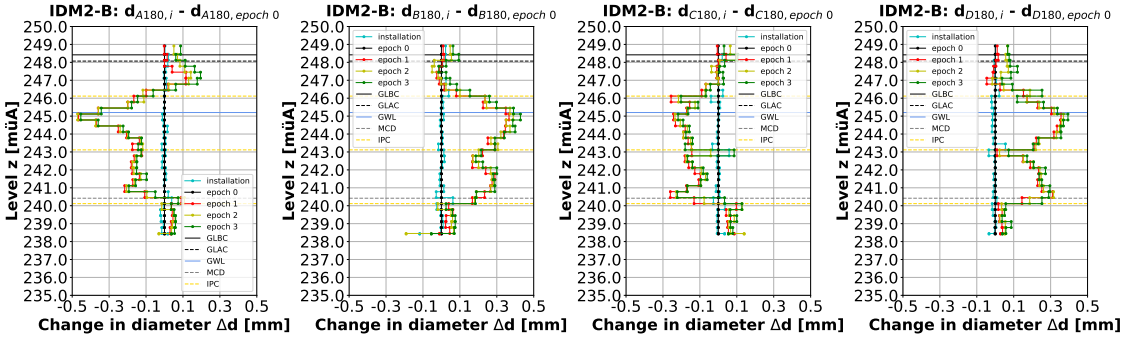

Figure 3.85: Changes in diameter of the inclinometer pipe IDM2-B - 180, epoch 0

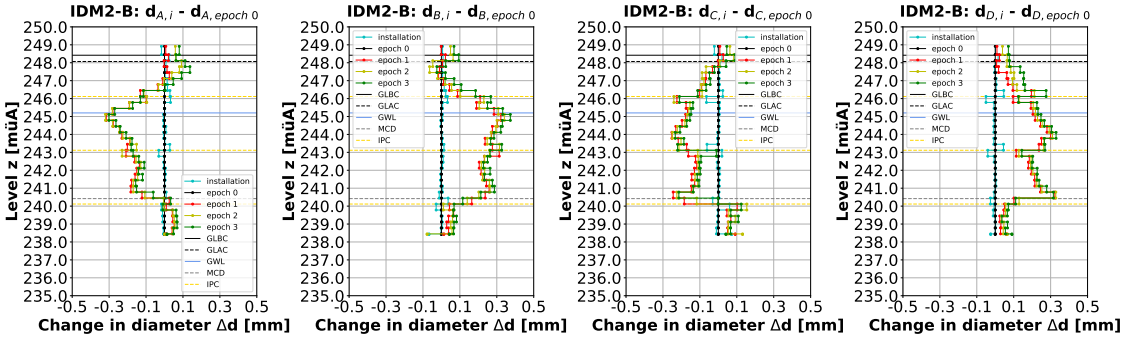

Figure 3.86: Changes in diameter of the inclinometer pipe IDM2-B - epoch 0

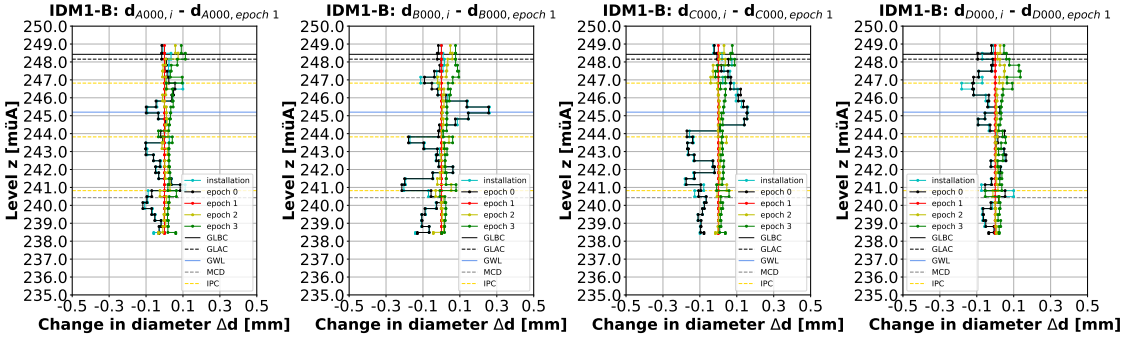

Figure 3.87: Changes in diameter of the inclinometer pipe IDM1-B - 000, epoch 1

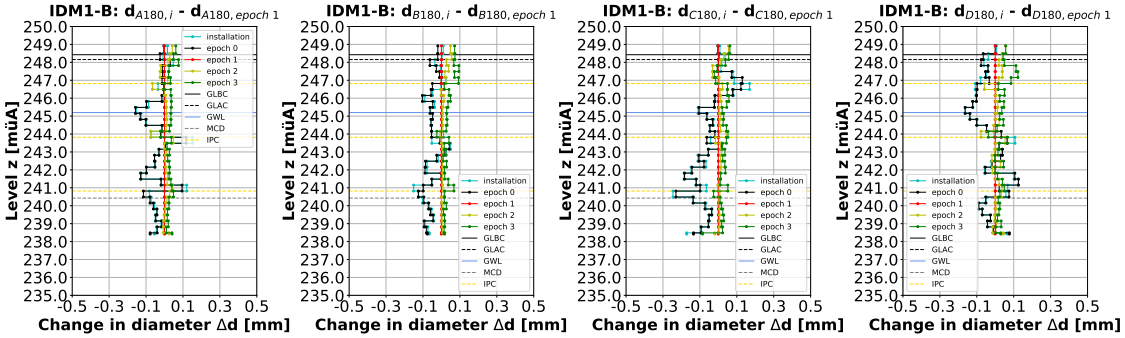

Figure 3.88: Changes in diameter of the inclinometer pipe IDM1-B - 180, epoch 1

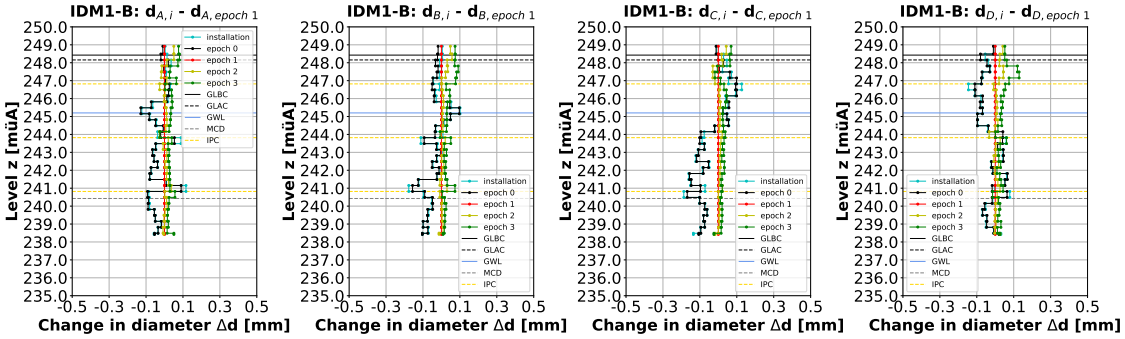

Figure 3.89: Changes in diameter of the inclinometer pipe IDM1-B - epoch 1

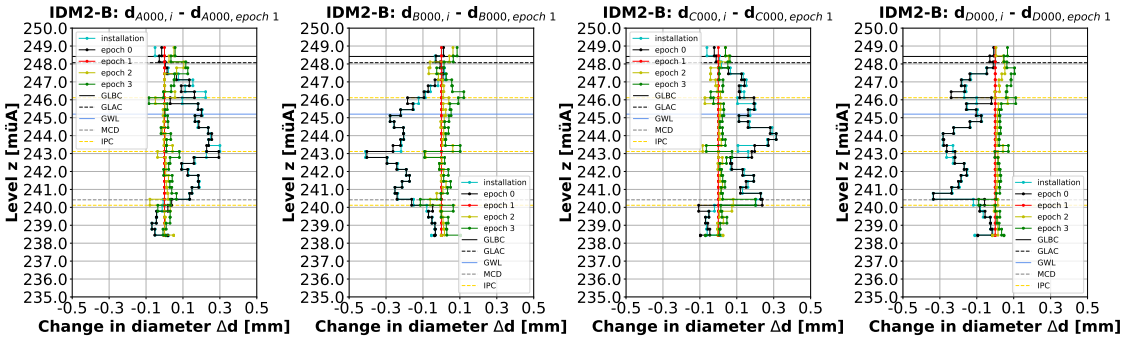

Figure 3.90: Changes in diameter of the inclinometer pipe IDM2-B - 000, epoch 1

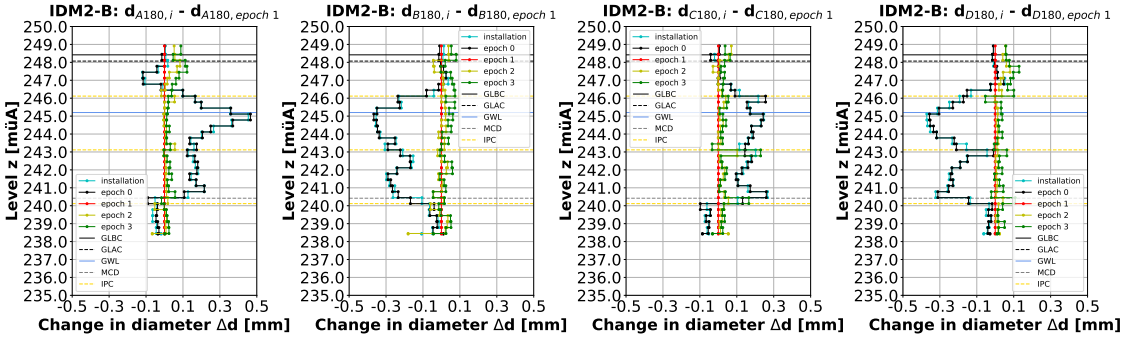

Figure 3.91: Changes in diameter of the inclinometer pipe IDM2-B - 180, epoch 1

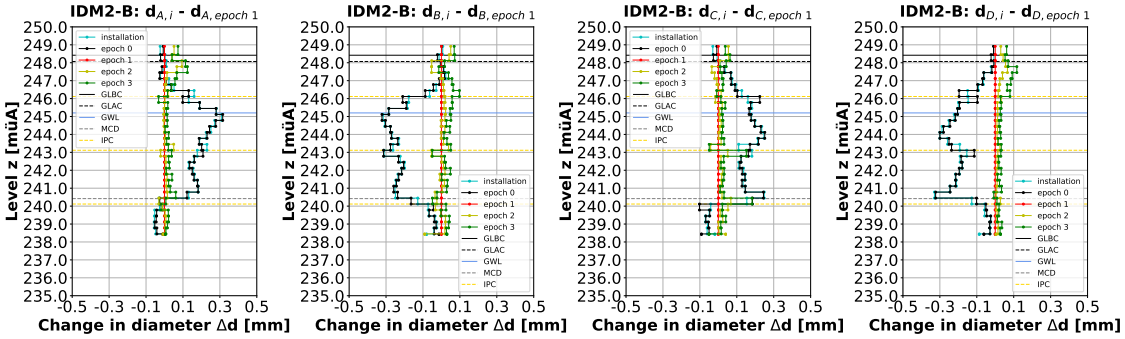

Figure 3.92: Changes in diameter of the inclinometer pipe IDM2-B - epoch 1

Mean diameter and change in mean diameter

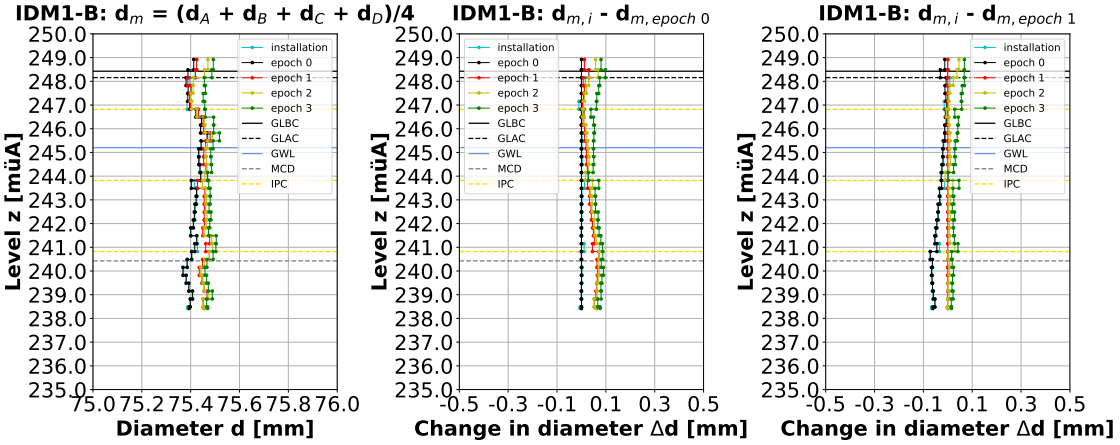

Figure 3.93: Mean diameter and changes in mean diameter of the inclinometer pipe IDM1-B - epoch 0, epoch 1

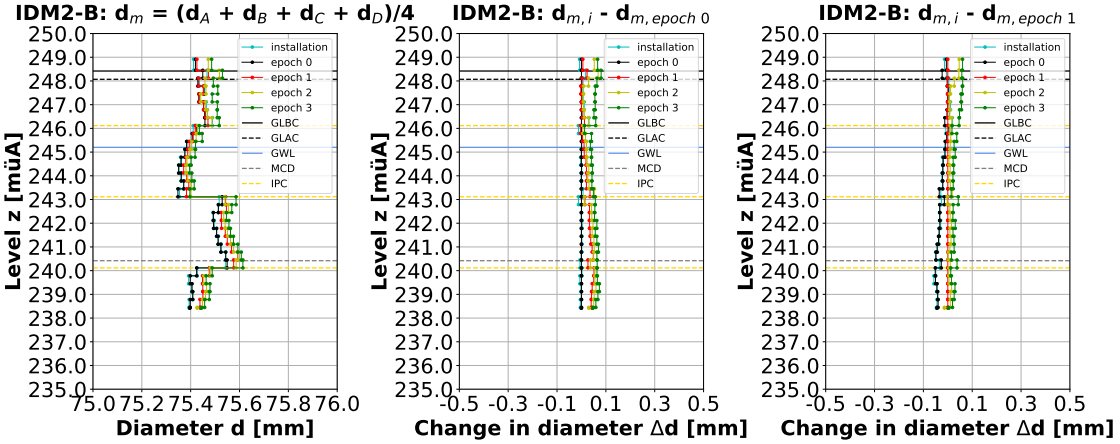

Figure 3.94: Mean diameter and changes in mean diameter of the inclinometer pipe IDM2-B - epoch 0, epoch 1

Ovalization value

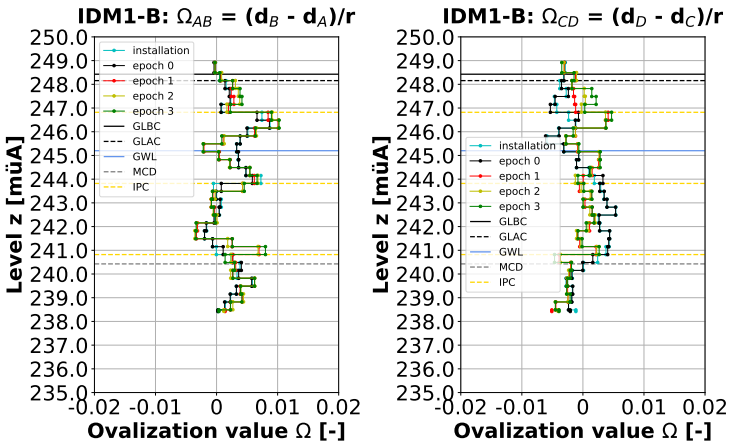

Figure 3.95: Ovalization values of the inclinometer pipe IDM1-B

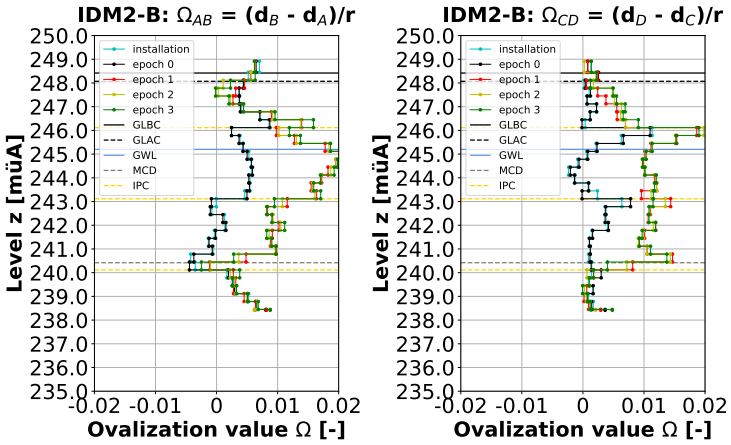

Figure 3.96: Ovalization values of the inclinometer pipe IDM2-B

Change in ovalization value

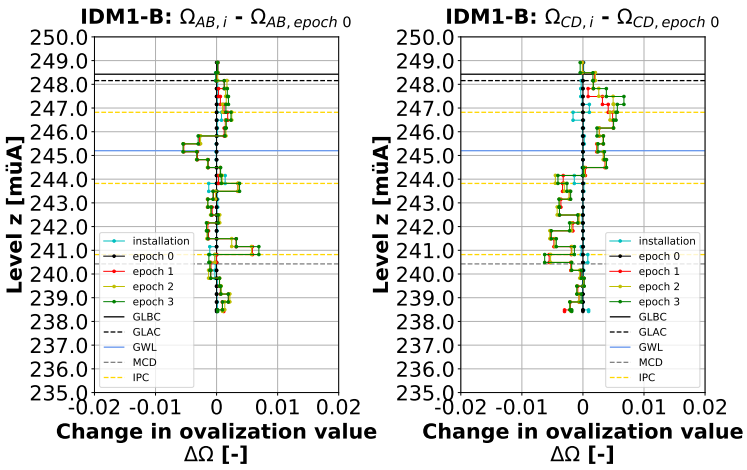

Figure 3.97: Changes in ovalization value of the inclinometer pipe IDM1-B - epoch 0

In Fig. 3.97 an ovalization in the direction CD (above: C - compression, D - extension; below: C - extension, D - compression) after the compaction works can be observed. The ovalization value is below the maximum compaction depth of course almost zero. The ovalization value in the direction AB is generally smaller, changes several times the sign and doesn't represent an obvious ovalization.
Due to the increasing stiffness caused by the ongoing compaction works the inclinometer pipe between four columns should be finally compressed in the direction of the first realized compaction column. For the inclinometer pipe IDM1-B this is only the case near the surface.
Due to the relatively large distance between the inclinometer pipe and the compaction columns the amount of ovalization is comparatively low. The sign change of the ovalization value at the second pipe connection should be a consequence of the relatively large distance.

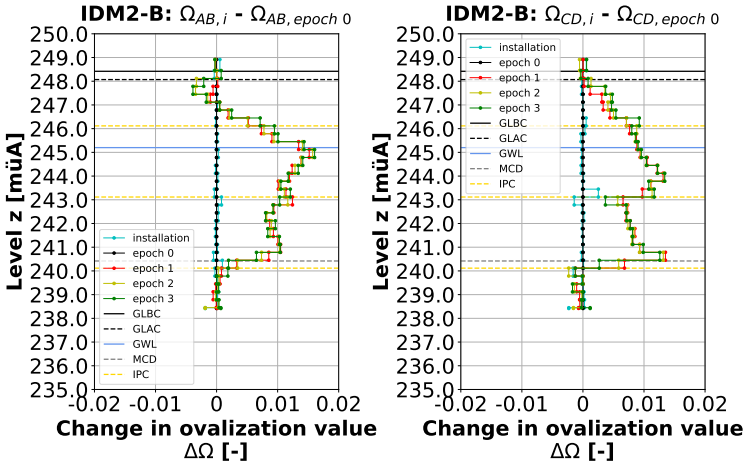

Figure 3.98: Changes in ovalization value of the inclinometer pipe IDM2-B - epoch 0

In Fig. 3.98 an ovalization in the direction AB (A - compression, B - extension) and the direction CD (C - compression, D - extension) after the compaction works can be observed. The ovalization develops with depth and reaches at a specific level a more or less constant value. The ovalization value is below the maximum compaction depth of course almost zero.

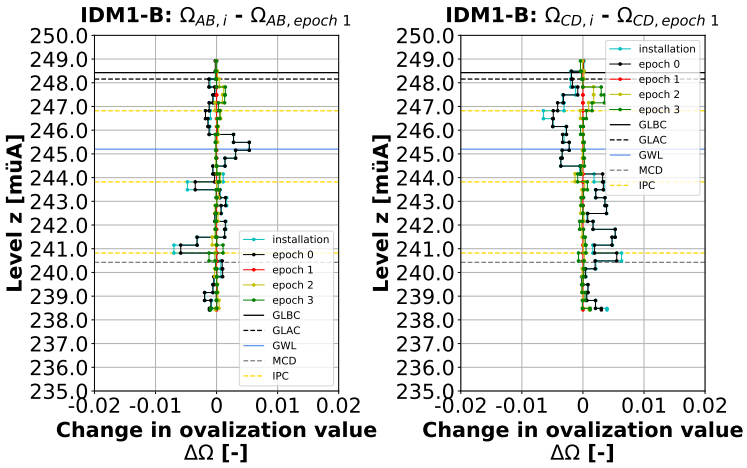

Figure 3.99: Changes in ovalization value of the inclinometer pipe IDM1-B - epoch 1

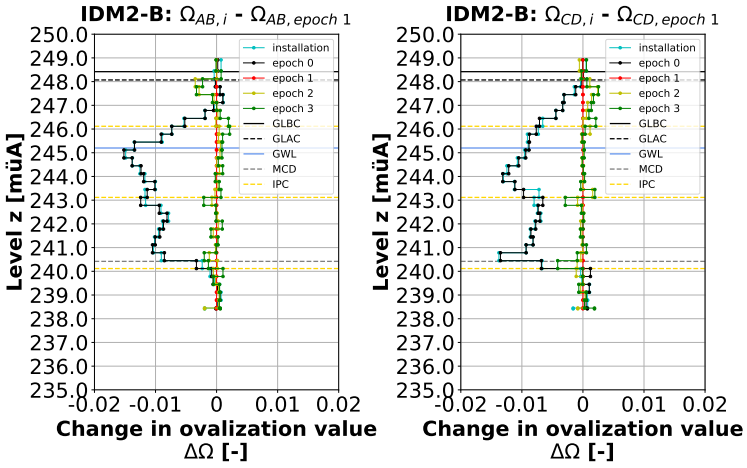

Figure 3.100: Changes in ovalization value of the inclinometer pipe IDM2-B - epoch 1

Curvature

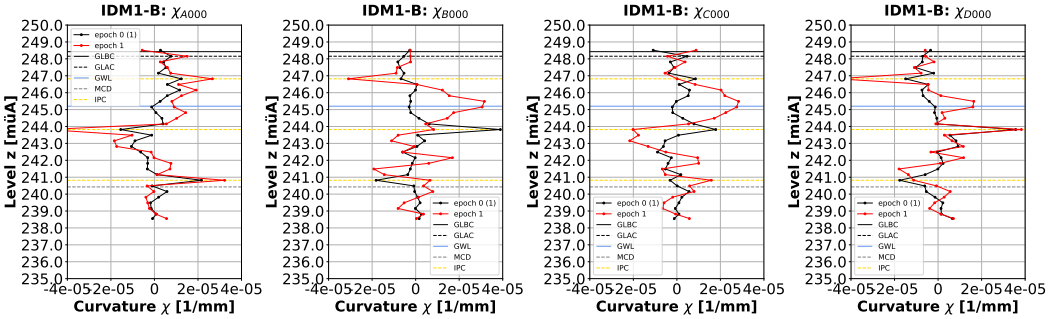

Figure 3.101: Curvatures of the inclinometer pipe IDM1-B - 000

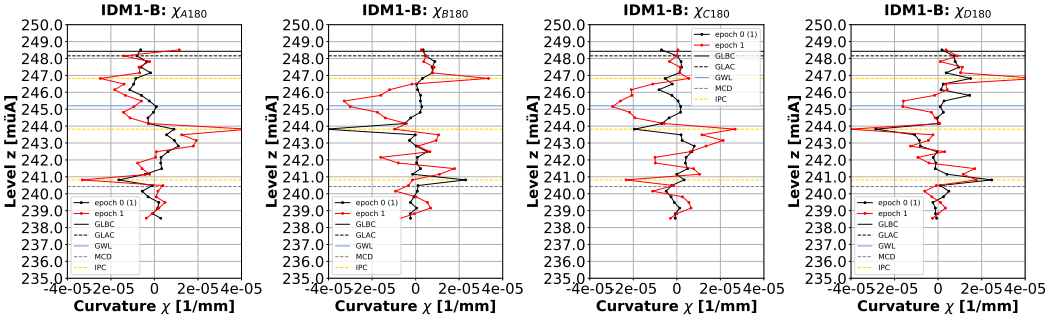

Figure 3.102: Curvatures of the inclinometer pipe IDM1-B - 180

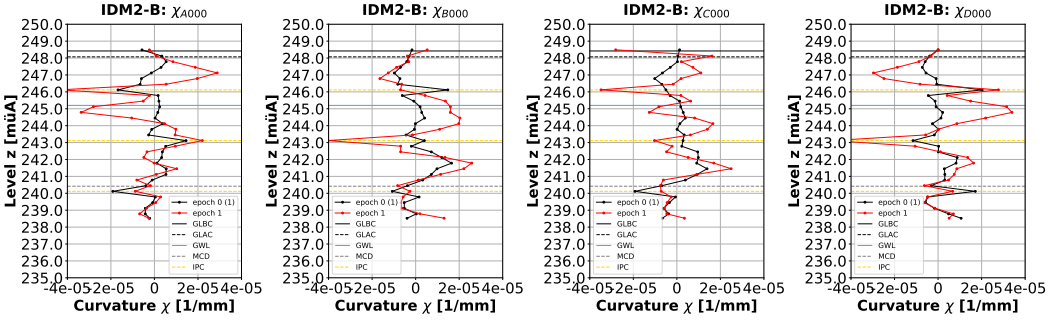

Figure 3.103: Curvatures of the inclinometer pipe IDM2-B - 000

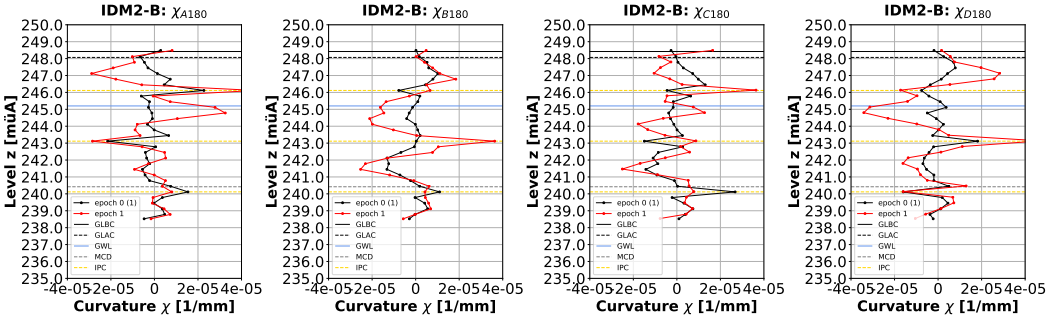

Figure 3.104: Curvatures of the inclinometer pipe IDM2-B - 180

Change in curvature

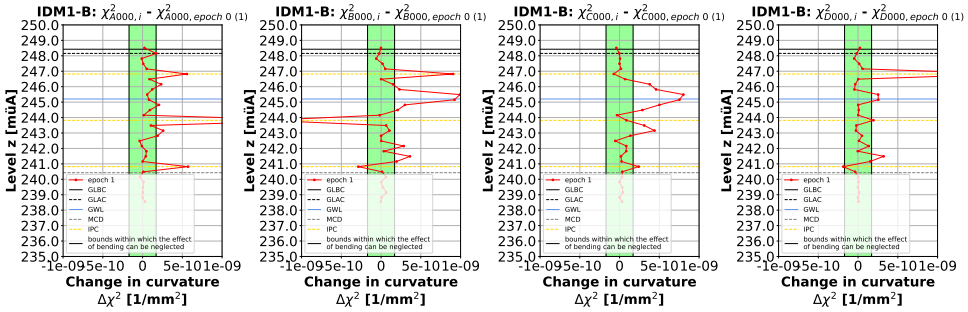

Figure 3.105: Changes in curvature of the inclinometer pipe IDM1-B - 000

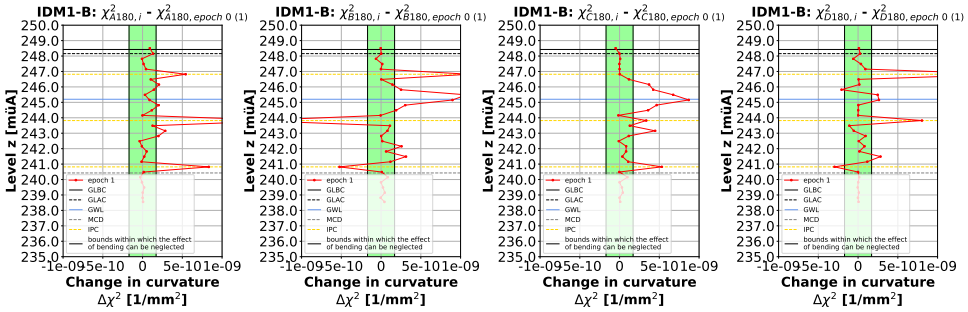

Figure 3.106: Changes in curvature of the inclinometer pipe IDM1-B - 180

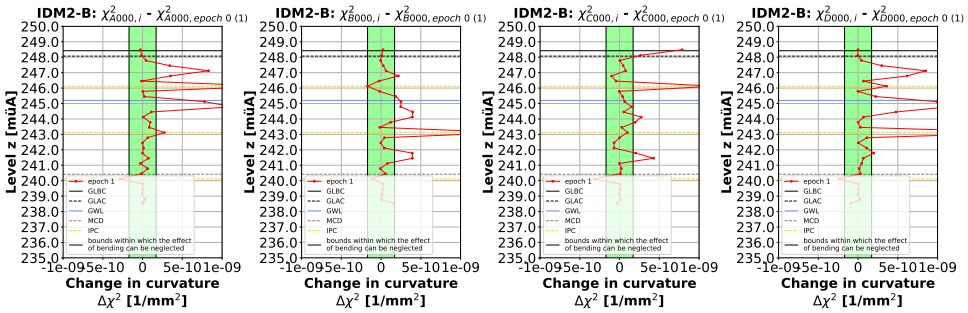

Figure 3.107: Changes in curvature of the inclinometer pipe IDM2-B - 000

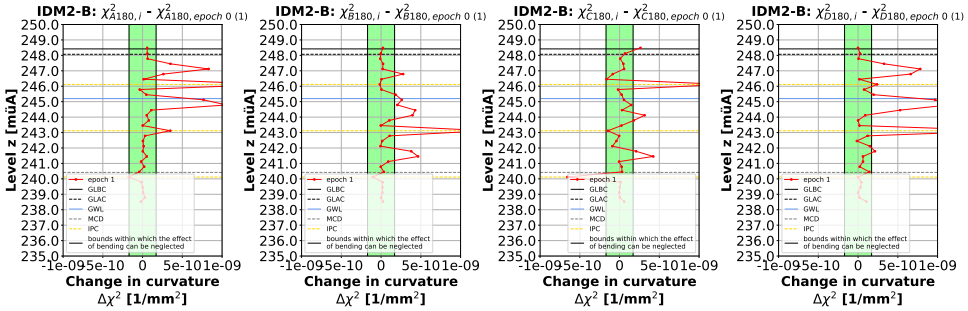

Figure 3.108: Changes in curvature of the inclinometer pipe IDM2-B - 180

3.4.2.2 Dynamic probing heavy

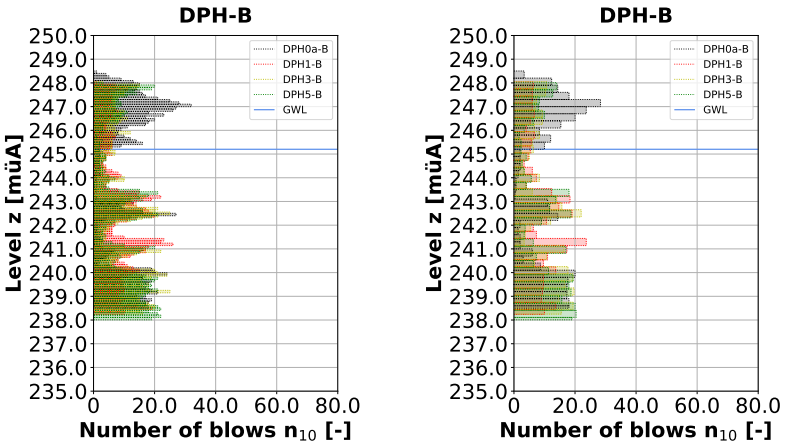

(a) original (b) averaged

Figure 3.109: Heavy dynamic probing tests - test area B, above left

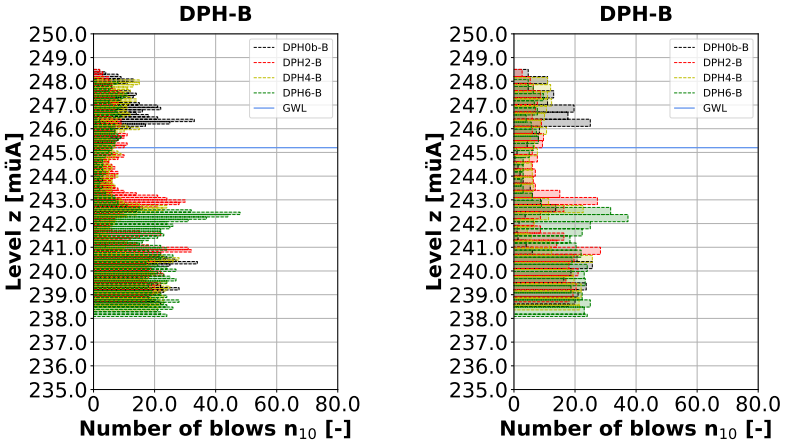

(a) original (b) averaged

Figure 3.110: Heavy dynamic probing tests - test area B, below right

3.4.2.3 Cone penetration test with pore water pressure measurement

In the following first the measurement results are documented and then some derived parameters are described.

Measurement results

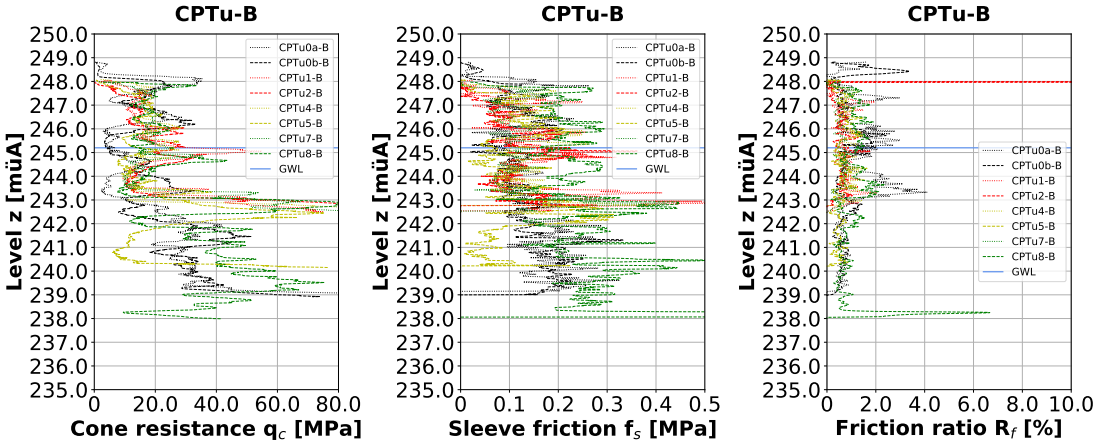

(a) original

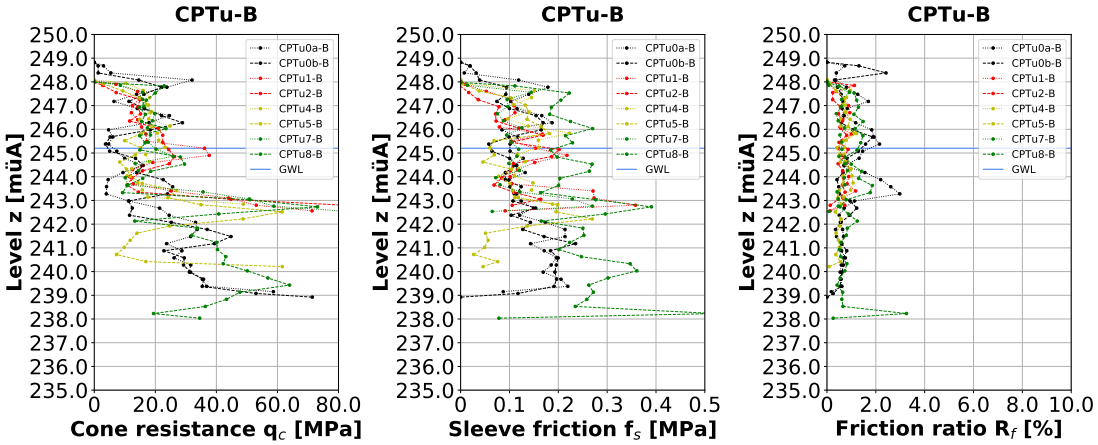

(b) averaged

Figure 3.111: Cone penetration tests with pore water pressure measurement - test area B, between four columns (1)

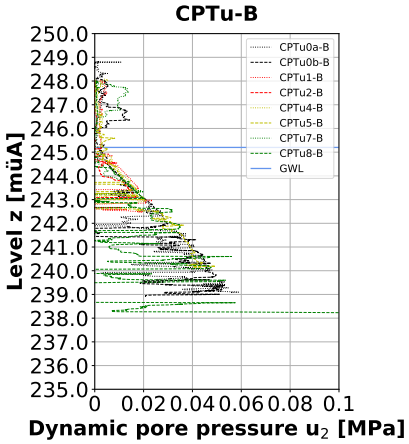

Figure 3.112: Cone penetration tests with pore water pressure measurement - test area B, between four columns (2)

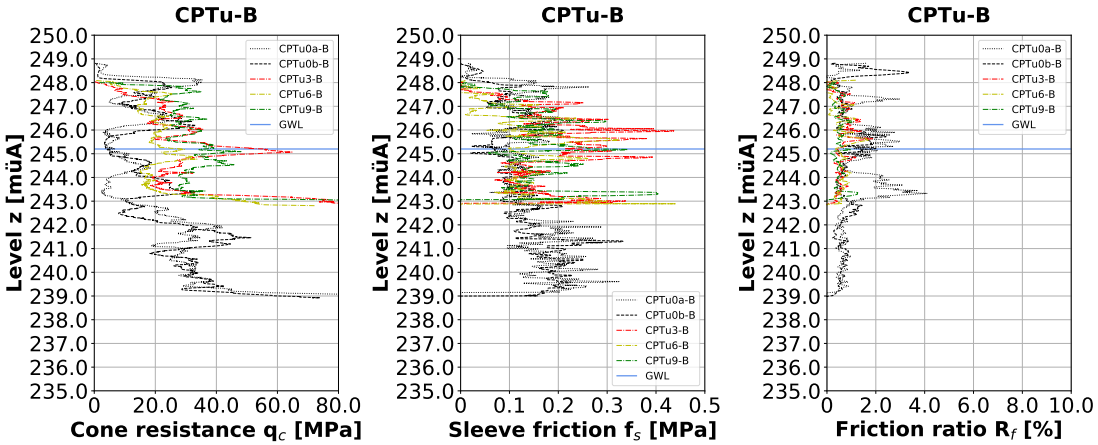

(a) original

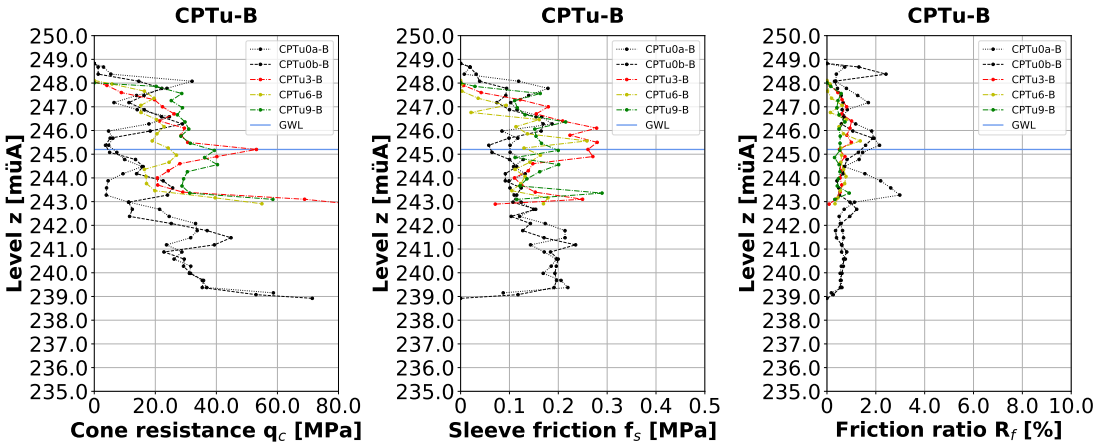

(b) averaged

Figure 3.113: Cone penetration tests with pore water pressure measurement - test area B, between two columns (1)

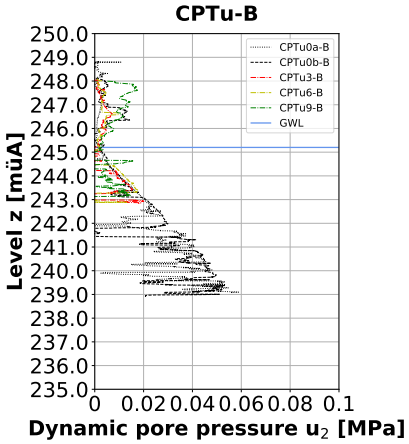

Figure 3.114: Cone penetration tests with pore water pressure measurement - test area B, between two columns (2)

Derived parameters

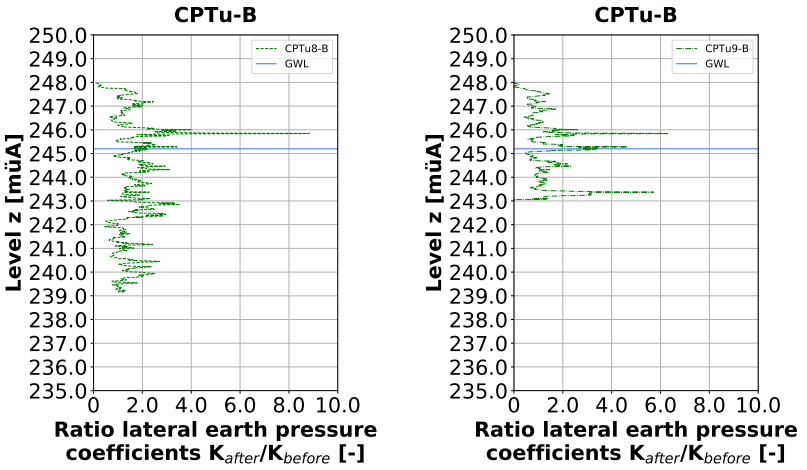

(a) between four columns

(b) between two columns

Figure 3.115: Ratio lateral earth pressure coefficients - test area B

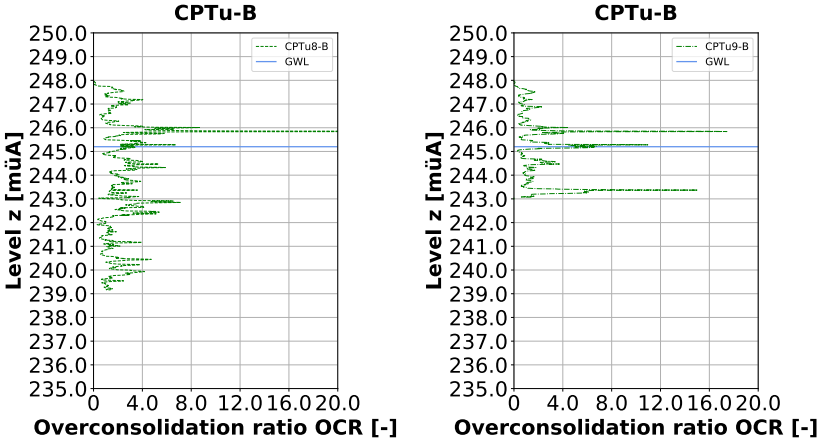

(a) between four columns (b) between two columns

Figure 3.116: Overconsolidation ratio - test area B

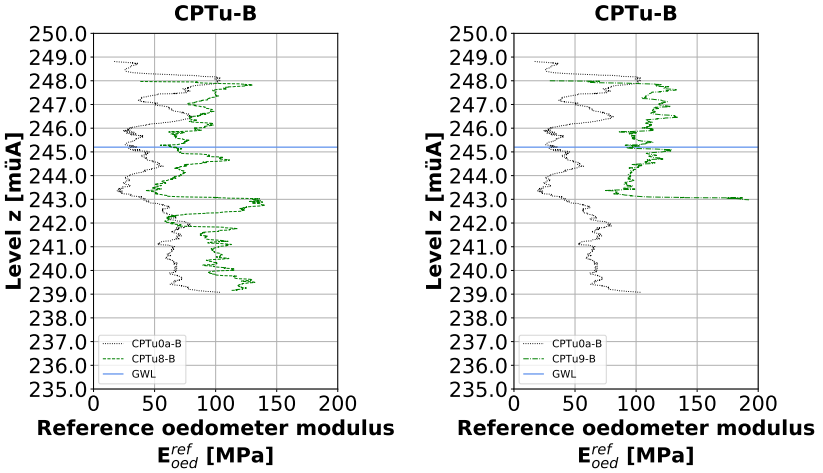

(a) between four columns (b) between two columns

Figure 3.117: Reference oedometer modulus - test area B

Fig. 3.118 shows the normalized soil behaviour type chart (Robertson 2010) with the cone penetration test results CPTu0a-B (black), CPTu0b-B (grey) and CPTu8-B (green). In Fig. 3.119 the cone penetration test results CPTu0a-B (black), CPTu0b-B (grey) and CPTu9-B (green) are represented. For the evaluation the formulas given in [17] were used.

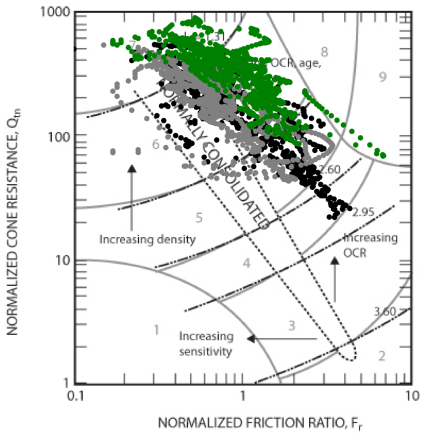

Figure 3.118: Normalized soil behaviour type chart (Robertson 2010) according to [18, p. 27] - test area B, between four columns

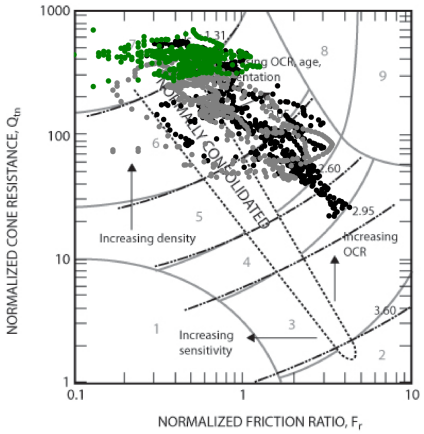

Figure 3.119: Normalized soil behaviour type chart (Robertson 2010) according to [18, p. 27] - test area B, between two columns

1 sensitive, fine grained
2 organic soils - clay
3 clays - silty clay to clay
4 silt mixtures - clayey silt to silty clay
5 sand mixtures - silty sand to sandy silt
6 sands - clean sand to silty sand
7 gravelly sand to dense sand
8 very stiff sand to clayey sand (heavily overconsolidated or cemented)
9 very stiff, fine grained (heavily overconsolidated or cemented)

3.4.2.4 Seismic cone penetration test

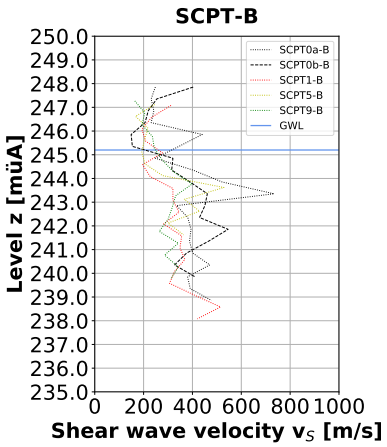

Figure 3.120: Seismic cone penetration tests - test area B, between four columns

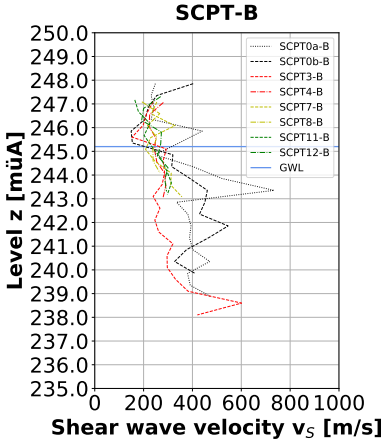

Figure 3.121: Seismic cone penetration tests - test area B, between two columns

4 Numerical studies

This chapter includes all numerical studies regarding the inclinometer pipe as well as the test area A and the test area B.

First, it is necessary to find an appropriate discretization of the inclinometer pipe cross section. Therefore, a preliminary study based on different models in combination with selected load cases was performed. The aim of section 4.2 is a better understanding of the inclinometer pipe deformation behaviour by deep vibro compaction.

4.1 Inclinometer pipe

In this section the geometry and the material properties of the on-site installed inclinometer pipes are described. Furthermore, the modelling of a pipe with channels will be discussed.

4.1.1 Geometry

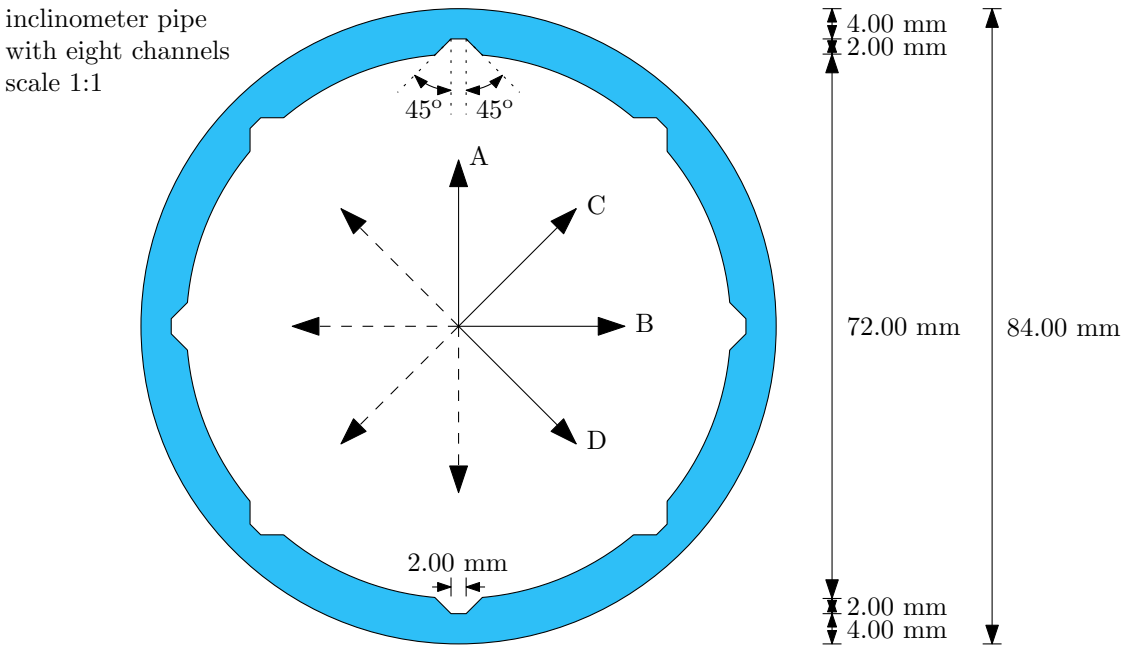

Figure 4.1: Cross section of the inclinometer pipe

The geometry of the cross section of the on-site used inclinometer pipe is shown in Fig. 4.1. Further values can also be found in the product specification sheet of the pipe (see appendix

3). As already mentioned, eight channels are present. This allows the measurement in the four directions A, B, C and D.

4.1.2 Material

The deformation characteristics of the pipe are a crucial component of the boundary value problem for back calculation of earth pressure changes. Thanks to its industrial production, the behaviour of the pipe is less variable than the behaviour of the back-fill material and the soil.

The inclinometer pipe, manufactured by Swiss Environment SA, is made of unplasticized PVC, which is an amorphous thermoplastic polymer. For an ideal thermoplastic material, deformations at constant stress will continuously increase with time. Due to the relative short measurement period on-site, the long-term stiffness of the pipe wasn't further investigated. Unplasticized PVC follows a linear viscoelastic behaviour below the yield point and below the glass transition temperature, which lies within the range of 347 - 353 K (considerably higher than the temperature in the soil), cf. [19, p. 56].

The pipe was modelled in all numerical studies with linear elastic material behaviour. The elastic modulus was determined based on preliminary tests (July 2019) at the geotechnical laboratory. The result of the numerical simulation with good agreement to the measured values (yellow line) is shown in Fig. 4.2. The inclination of both lines is approximately the same. During the preliminary tests, no diameter change was recorded at two specific load intervals. This behaviour was neglected during calibration and is the reason for the distance between both lines. With the software SOFiSTiK the inclinometer pipe was modelled in three dimensions, unconstrained in longitudinal direction with eight channels and at least four elements along the pipe wall. The Poisson's ratio is specified by the producer as 0.34. Due to the chosen model types the unit weight was not of interest.

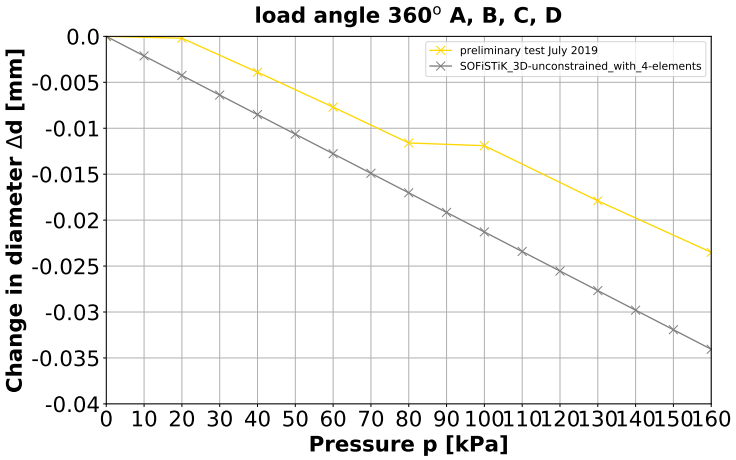

Figure 4.2: Comparison preliminary test and numerical simulation

The material parameters of the inclinometer pipe are summarized in the following table.

Table 4.1: Material parameters of the inclinometer pipe

quantity name	symbol	value	unit
elastic modulus	E	2500000	[kN/m^2]
poisson's ratio	ν	0.34	[-]

4.1.3 Modelling

By using the finite element method in general there are three different types of elements available to discretize the inclinometer pipe: beam elements, surface elements and volume elements. Each of them has advantages and disadvantages. In this subsection the simplest (low computational effort) but also enough accurate method to model the pipe is searched. Therefore, different load cases are considered to ensure realistic results for all investigated types.

4.1.3.1 Discretization

The inclinometer pipe was discretized in two and in three dimensions. The modelling with beam elements is only reasonable if the channels don't have a significant influence on the deformation behaviour. Since this conclusion should be one result of this study, beam elements weren't used yet. The software Plaxis as well as SOFiSTiK, for comparison purposes, was used.

For the models in two dimensions plane strain condition was chosen. To check the results, the models in three dimensions were additionally investigated with constrained deformability in longitudinal direction. In this case the models in two dimensions and in three dimensions should give approximately equivalent results.

To study the influence of the channels on the deformation behaviour, models with and without channels were analysed. The importance of the mesh size was investigated by creating each model with at least two and four elements along the pipe wall.

Plaxis

For the following models plane strain condition was chosen. To discretize the domain (see Fig. 4.3) 15-node triangular elements with 12 gauss points were used.

The geometry of the cross section of the pipe specified in the numerical models is equal to the information in section 4.1.1. The inclinometer pipe was modelled with linear elastic material behaviour using the parameters from Tab. 4.1.

Due to the not perfectly symmetric pipe mesh a so-called dummy layer was necessary around the pipe. The dimension of the layer was specified with 110.00 mm x 110.00 mm. To minimize the influence of the linear elastic modelled dummy layer on the simulation results an elastic modulus of 1 kN/m^2 and a Poisson's ratio of 0.00 were chosen. All outer boundaries of the dummy layer were fully fixed.

The unit weight was for both materials chosen equal 0.00 kN/m^3. Therefore, the generated initial stresses are 0.00 kN/m^2. The applied loads are described in detail in section 4.1.3.2.

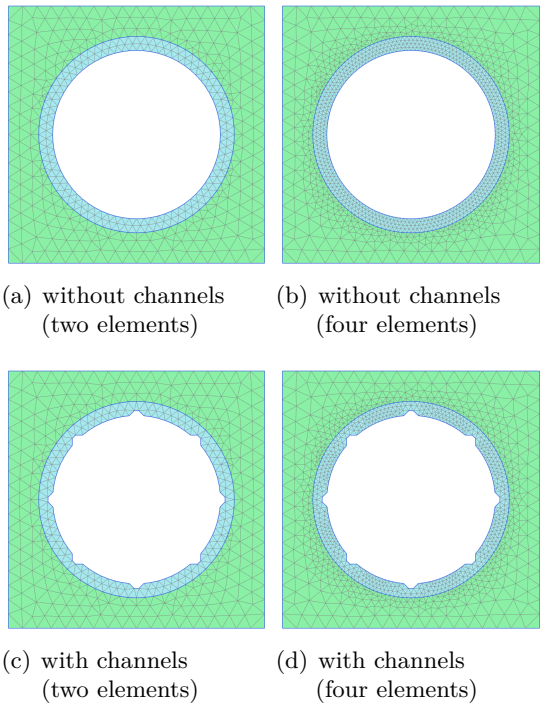

(a) without channels (two elements)
(b) without channels (four elements)
(c) with channels (two elements)
(d) with channels (four elements)

Figure 4.3: Numerical models in two dimensions from Plaxis

SOFiSTiK

For the following numerical models in two dimensions plane strain condition was chosen. To discretize the domain in two dimensions (see Fig. 4.4) 4-node quadrilateral elements with 4 gauss points and in three dimensions (see Fig. 4.5) 8-node hexahedral elements with 8 gauss points were used.

The geometry of the cross section of the pipe specified in the numerical models is equal to the information in section 4.1.1. In three dimensions the inclinometer pipe was modelled with a length of 3.00 m. For the pipe linear elastic material behaviour was chosen. The used material parameters are shown in Tab. 4.1.

Due to the not perfectly symmetric mesh in two dimensions a so-called dummy layer was necessary around the pipe. The dimension of the layer was specified with 110.00 mm x 110.00 mm. To minimize the influence of the linear elastic modelled dummy layer on the simulation results an elastic modulus of 1 kN/m^2 and a Poisson's ratio of 0.00 were chosen. All outer boundaries of the dummy layer were fully fixed. In three dimensions first one eighth of the pipe was modelled and afterwards this was copied by rotation. Thereby, a sufficient symmetry of the pipe mesh is reached and no dummy layer is needed. As already mentioned, the pipe in three dimensions was modelled once with fully fixation at the bottom and the top and once with unconstrained condition in longitudinal direction.

The unit weight was always chosen equal 0.00 kN/m^3. Therefore, the generated initial stresses are 0.00 kN/m^2. The applied loads are described in detail in section 4.1.3.2.

The input data for the models, created with the editor TEDDY, are part of the appendix 6.

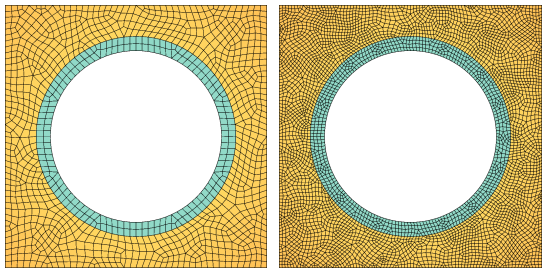

(a) without channels (two elements)

(b) without channels (four elements)

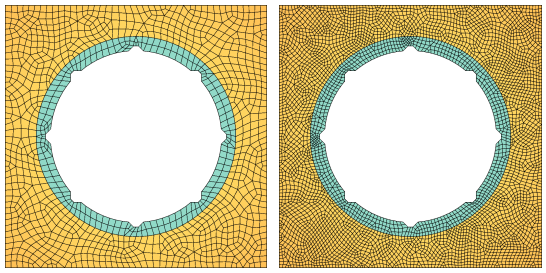

(c) with channels (two elements)

(d) with channels (four elements)

Figure 4.4: Numerical models in two dimensions from SOFiSTiK

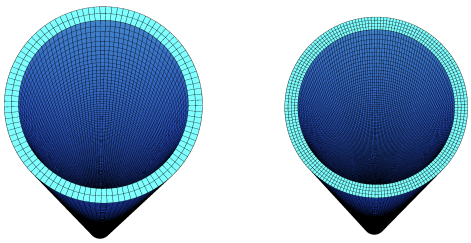

(a) without channels (two elements)

(b) without channels (four elements)

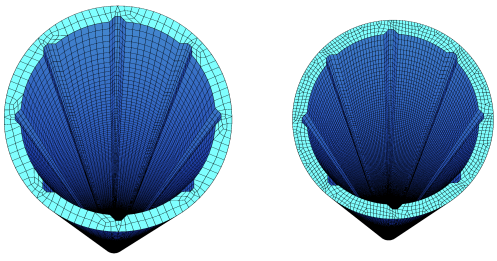

(c) with channels (two elements)

(d) with channels (four elements)

Figure 4.5: Numerical models in three dimensions from SOFiSTiK

4.1.3.2 Load cases

Three different load cases were investigated. In detail they are discussed in the following paragraphs.

Load case 1

First, a load angle of 360° was chosen. Plots of the loaded systems with the resultant deformed mesh are shown in the following figure. The measurement directions are the same as in Fig. 4.1. As expected, in all measurement directions the same compression occurs.

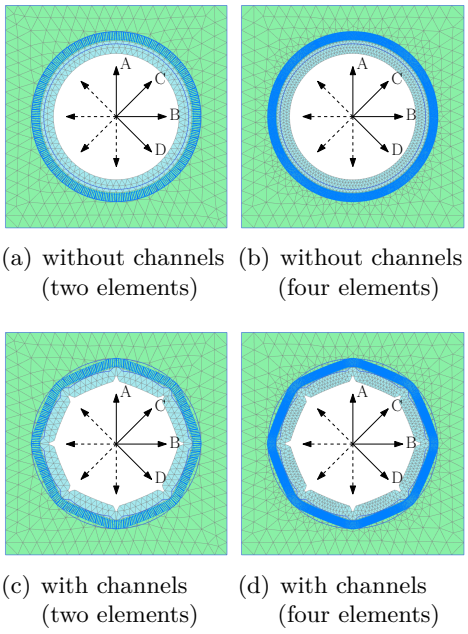

(a) without channels (two elements)

(b) without channels (four elements)

(c) with channels (two elements)

(d) with channels (four elements)

Figure 4.6: Load case 1 (Plaxis)

Load case 2

For load case 2 a load angle of $2 \cdot 90°$ was chosen. Plots of the loaded systems with the resultant deformed mesh are shown in the following figure. The measurement directions are the same as in Fig. 4.1. The resultant force must act for this load case exactly between two channels. As expected, an ovalization occurs with compression in the directions B and D and extension in the directions A and C.

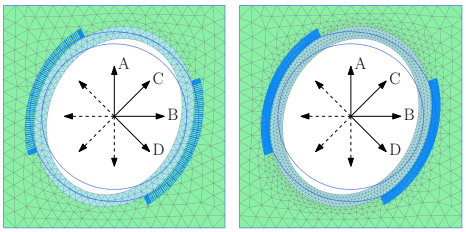

(a) without channels (two elements)

(b) without channels (four elements)

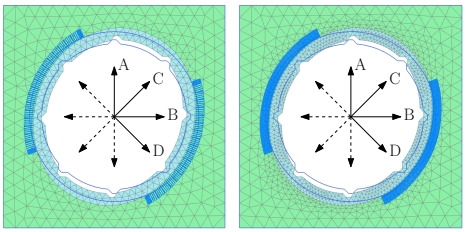

(c) with channels (two elements)

(d) with channels (four elements)

Figure 4.7: Load case 2 (Plaxis)

Load case 3

For load case 3 a load angle of $2 \cdot 45^{o}$ was chosen. Plots of the loaded systems with the resultant deformed mesh are shown in the following figure. The measurement directions are the same as in Fig. 4.1. The resultant force must act for this load case exactly on a channel. As expected, an ovalization occurs with compression in direction B and extension in direction A.

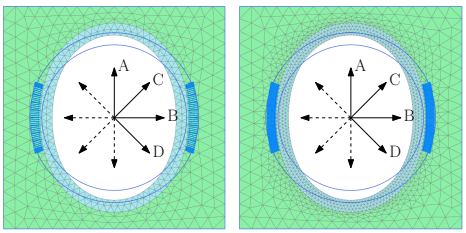

(a) without channels (two elements)

(b) without channels (four elements)

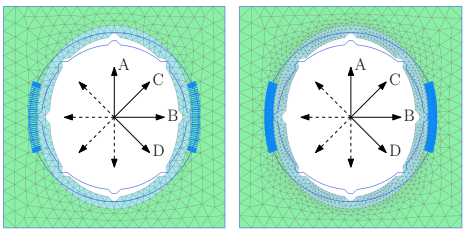

(c) with channels (two elements)

(d) with channels (four elements)

Figure 4.8: Load case 3 (Plaxis)

4.1.4 Simulation results

In the following the simulation results are compared for the different load cases.

4.1.4.1 Load case 1

Both figures provide the following findings:

- For a load angle of 360° the models with plane strain condition predict significant lower deformations than the models with unconstrained deformability in longitudinal direction.
- The models with channels predict slightly lower deformations in the measurement directions than the models without channels.
- The models with channels created with SOFiSTiK show a high sensitivity related to the mesh discretization. This effect is most probably a consequence of the lower order of the elements compared to the 15-node triangular elements used in Plaxis.

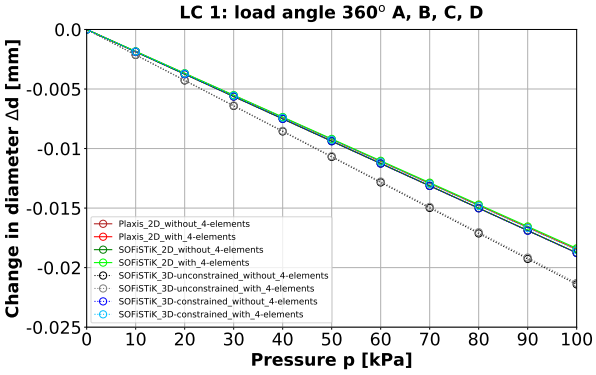

Figure 4.9: Load case 1 (four elements)

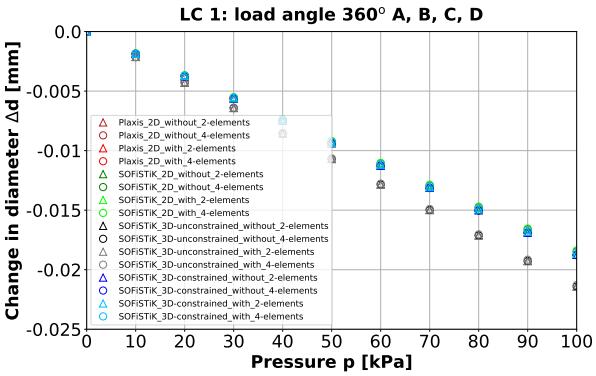

Figure 4.10: Load case 1 (two elements & four elements)

4.1.4.2 Load case 2

Both figures provide the following findings:

- For a load angle of 2 · 90° the models with plane strain condition predict the same deformations than the models with unconstrained deformability in longitudinal direction.
- The models with channels predict much higher deformations in the measurement directions than the models without channels.
- The models with channels created with SOFiSTiK show a high sensitivity related to the mesh discretization. This effect is most probably a consequence of the lower order of the elements compared to the 15-node triangular elements used in Plaxis.

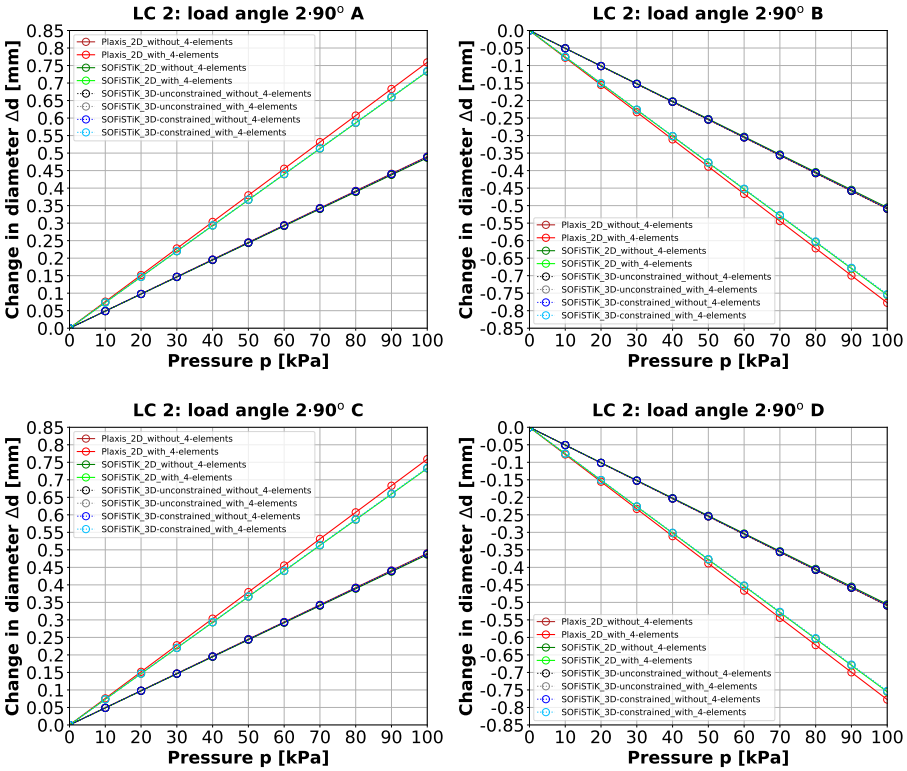

Figure 4.11: Load case 2 (four elements)

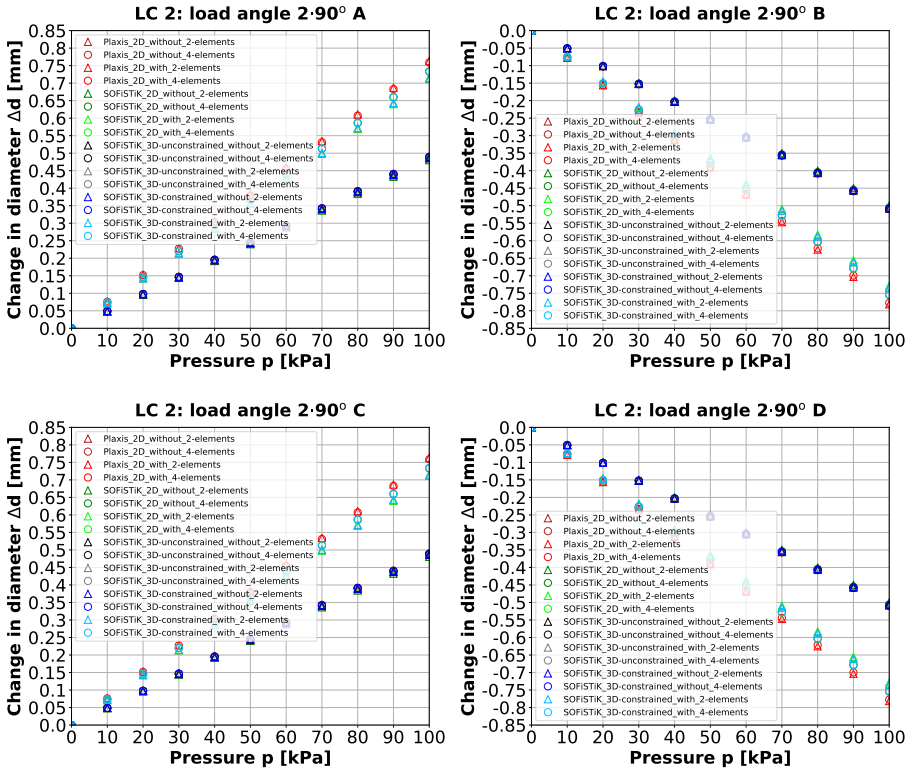

Figure 4.12: Load case 2 (two elements & four elements)

4.1.4.3 Load case 3

Both figures provide the following findings:

- For a load angle of $2 \cdot 45^{o}$ the models with plane strain condition predict the same deformations than the models with unconstrained deformability in longitudinal direction.
- The models with channels predict much higher deformations in the measurement directions than the models without channels.
- The models with channels created with SOFiSTiK show a high sensitivity related to the mesh discretization. This effect is most probably a consequence of the lower order of the elements compared to the 15-node triangular elements used in Plaxis.

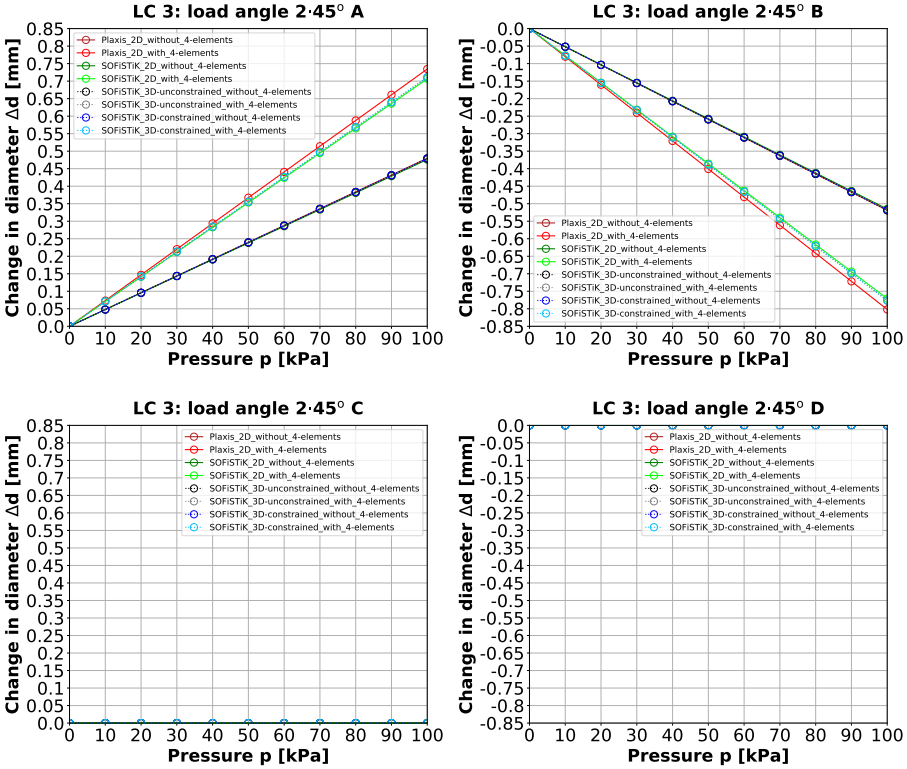

Figure 4.13: Load case 3 (four elements)

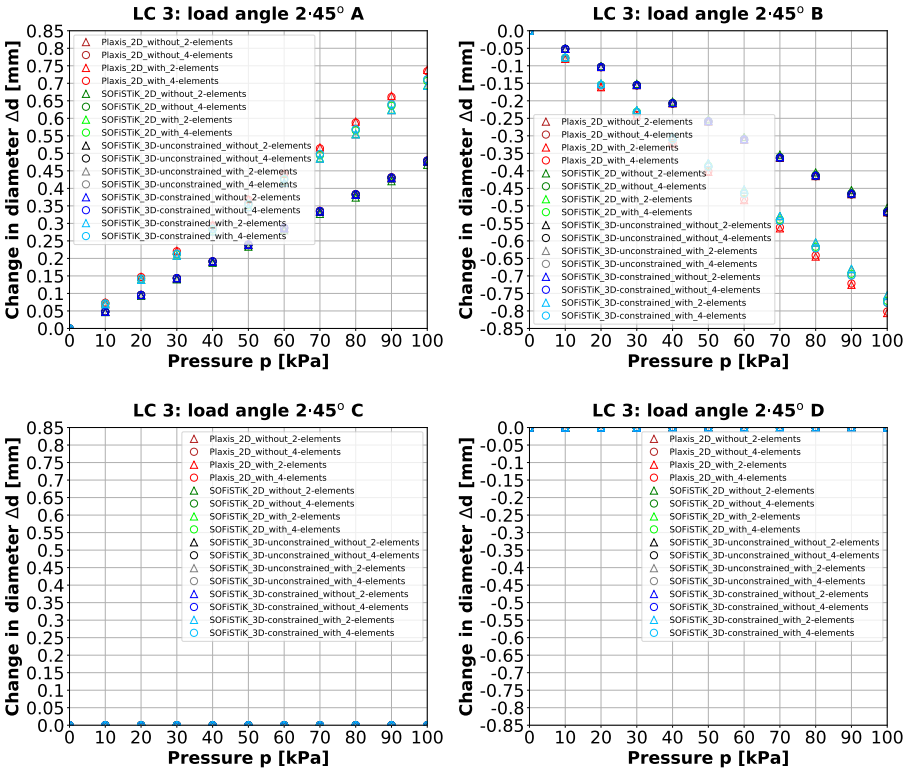

Figure 4.14: Load case 3 (two elements & four elements)

4.1.4.4 Conclusion

Considering the deep vibro compaction a load angle differing from 360° is expected. Thus, the creation of the model in two dimensions with plane strain condition is reasonable. The channels must be modelled necessarily. It is recommended to use the higher order elements in Plaxis (15-node triangular elements) and to discretize the pipe with at least four elements along the pipe wall.

4.2 Test area A & test area B

For a better understanding of the inclinometer pipe deformation behaviour due to deep vibro compaction a numerical study is performed. This study should also provide information regarding the horizontal earth pressure changes next to the inclinometer pipes and the possible overconsolidation in the subsoil. In this section the geometry of the numerical models for the test area A and the test area B, the defined material properties, the modelling approaches 1 to 3 and finally the simulation results are documented.

4.2.1 Geometry

Both test areas were modelled only partially. For a correct system behaviour, according to the symmetry condition, at least a compaction grid of 3 x 2 with both inclinometer pipes inside must be modelled.

The numerical models were created by using the finite element method software Plaxis. The discretization of the domain was performed in two dimensions. The depth position of the modelled horizontal section was specified at 242.00 müA (about 6.20 m below the ground level). For the calculation plane strain condition was chosen. The numerical model for the test area A consists of 32054 15-node triangular elements and the model for the test area B consists of 37004 15-node triangular elements. For the modelling of the inclinometer pipes the results shown in section 4.1 were considered.

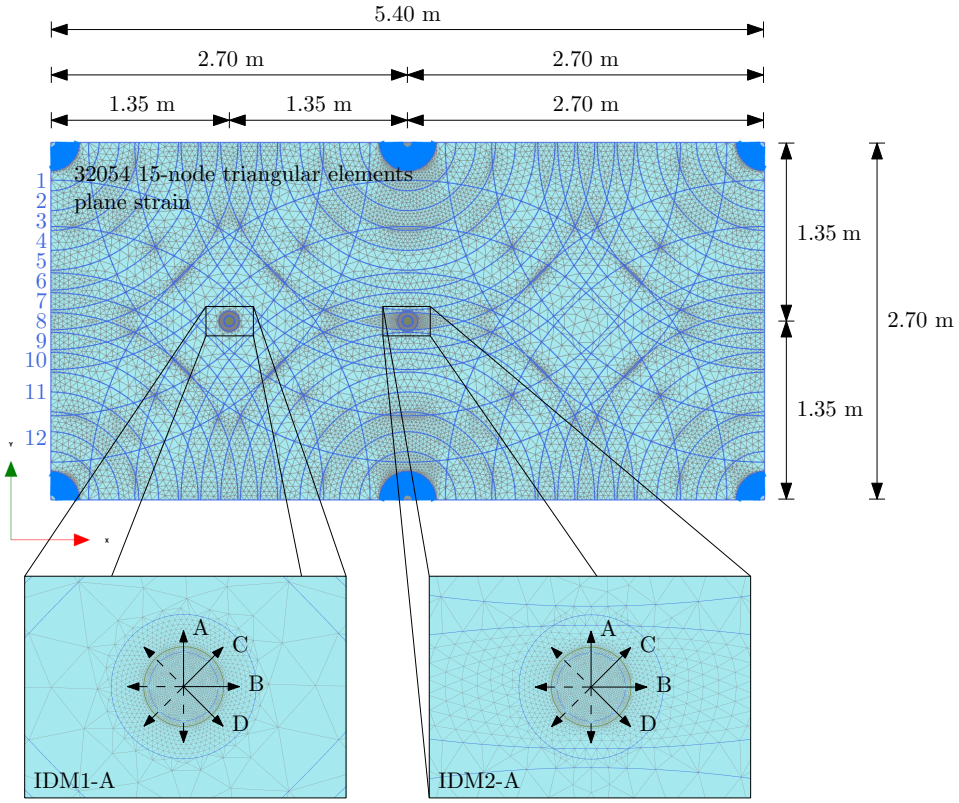

Figure 4.15: Numerical model test area A

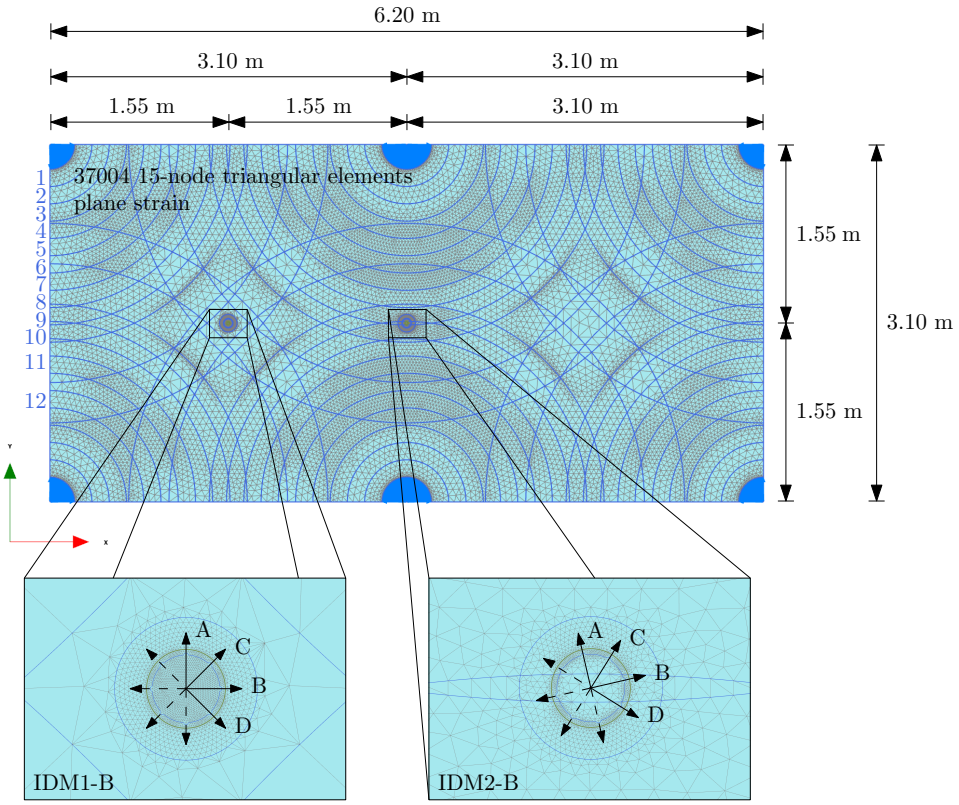

Figure 4.16: Numerical model test area B

The grid spacing for both models is shown in Fig. 4.15 and Fig. 4.16. The geometric dimensions of the inclinometer pipe were chosen according to the specifications in section 4.1.1. The actual orientation of the channels, as documented in Fig. 3.12 and Fig. 3.13, was considered. Around the pipes, clusters corresponding to the drilled boreholes with a diameter of 0.152 m were modelled. Around the centre of each compaction column a cluster with the diameter corresponding to the on-site used depth vibrator model was generated. Due to the dynamic action of the depth vibrator, grain redistribution takes place in the subsoil. This effect is taken into account in a simplified form in approach 3. This requires different zones around the compaction centres. Thus, 12 rings were modelled with a ring thickness of 0.15 m for the first 10 and a ring thickness of 0.35 m for the last 2.

All boundaries were modelled as normally fixed. Additionally, the four model corners were fully fixed.

The numerical model for the test area B differs from the model for test area A only by the grid spacing and the orientation of the inclinometer pipe channels.

4.2.2 Material

The inclinometer pipes were modelled with linear elastic material behaviour considering the parameters in Tab. 4.1. To take the angle of wall friction at the boundary between the pipe and the surrounding soil into account interfaces were generated. For the strength reduction factor 0.46 was chosen, which was considered in the following way according to [2, p. 243].

$$\tan \varphi_i = \mathrm{R}_{inter} \cdot \tan \varphi_{soil} \tag{4.1}$$

φ_i	friction angle (interface)
R_{inter}	strength reduction factor
φ_{soil}	friction angle (associated soil)

$$\mathrm{c}_i = \mathrm{R}_{inter} \cdot \mathrm{c}_{soil} \tag{4.2}$$

c_i	cohesion (interface)
R_{inter}	strength reduction factor
c_{soil}	cohesion (associated soil)

The soil was modelled using the advanced elastic plastic hardening soil model with small-strain stiffness. The estimated material parameters of the soil before compaction are summarized in Tab. 4.2. As can be seen an associated flow rule was used. In all simulations drained material behaviour was considered. The unit weight was only used to calculate the initial stress state. In Plaxis both parameters were set to zero.

Table 4.2: Material parameters of the soil - before compaction

quantity name	symbol	value	unit
unsaturated unit weight	γ_{unsat}	21.00	[kN/m^3]
saturated unit weight	γ_{sat}	21.50	[kN/m^3]
tangent stiffness for primary oedometer loading	E_{oed}^{ref}	40000	[kN/m^2]
secant stiffness in standard drained triaxial test	E_{50}^{ref}	40000	[kN/m^2]
unloading/ reloading stiffness from drained triaxial test	E_{ur}^{ref}	120000	[kN/m^2]
reference stress for stiffnesses	p^{ref}	100	[kN/m^2]
power for stress-level dependency of stiffness	m	0.50	[-]
(effective) cohesion	c'	0.00	[kN/m^2]
(effective) angle of internal friction	φ'	40	[°]
angle of dilatancy	ψ	40	[°]
poisson's ratio for unloading/ reloading	ν_{ur}	0.20	[-]
lateral earth pressure coefficient for normal consolidation	K_0^{nc}	0.3572	[-]
failure ratio	R_f	0.90	[-]
threshold shear strain	$\gamma_{0.7}$	1.50e-04	[-]
unloading/ reloading reference shear modulus	G_{ur}^{ref}	50000	[kN/m^2]
reference shear modulus at very small strains	G_0^{ref}	150000	[kN/m^2]

To avoid the direct load transfer to the support behind the load transmission, a dummy layer was used for the relevant clusters during the loading phases. For the dummy layer the following material parameters were defined. For the sake of simplicity, the material was modelled linear elastic.

Table 4.3: Material parameters of the dummy layer

quantity name	symbol	value	unit
elastic modulus	E	4000	[kN/m^2]
poisson's ratio	ν	0.00	[-]

The stiffness change considered by approach 3 is different at different distances to the compaction centre. The values for the rings 1 to 12 are shown in Tab. 4.4 to Tab. 4.11.

Table 4.4: Material parameters of the soil - after compaction (ring 2, 3, 4 and 5)

quantity name	symbol	value	unit
tangent stiffness for primary oedometer loading	E_{oed}^{ref}	100000	[kN/m^2]
secant stiffness in standard drained triaxial test	E_{50}^{ref}	100000	[kN/m^2]
unloading/ reloading stiffness from drained triaxial test	E_{ur}^{ref}	300000	[kN/m^2]
unloading/ reloading reference shear modulus	G_{ur}^{ref}	125000	[kN/m^2]
reference shear modulus at very small strains	G_{0}^{ref}	375000	[kN/m^2]

Table 4.5: Material parameters of the soil - after compaction (ring 6)

quantity name	symbol	value	unit
tangent stiffness for primary oedometer loading	E_{oed}^{ref}	92000	[kN/m^2]
secant stiffness in standard drained triaxial test	E_{50}^{ref}	92000	[kN/m^2]
unloading/ reloading stiffness from drained triaxial test	E_{ur}^{ref}	276000	[kN/m^2]
unloading/ reloading reference shear modulus	G_{ur}^{ref}	115000	[kN/m^2]
reference shear modulus at very small strains	G_{0}^{ref}	345000	[kN/m^2]

Table 4.6: Material parameters of the soil - after compaction (ring 7)

quantity name	symbol	value	unit
tangent stiffness for primary oedometer loading	E_{oed}^{ref}	84000	[kN/m^2]
secant stiffness in standard drained triaxial test	E_{50}^{ref}	84000	[kN/m^2]
unloading/ reloading stiffness from drained triaxial test	E_{ur}^{ref}	252000	[kN/m^2]
unloading/ reloading reference shear modulus	G_{ur}^{ref}	105000	[kN/m^2]
reference shear modulus at very small strains	G_{0}^{ref}	315000	[kN/m^2]

Table 4.7: Material parameters of the soil - after compaction (ring 8)

quantity name	symbol	value	unit
tangent stiffness for primary oedometer loading	E_{oed}^{ref}	77000	[kN/m^2]
secant stiffness in standard drained triaxial test	E_{50}^{ref}	77000	[kN/m^2]
unloading/ reloading stiffness from drained triaxial test	E_{ur}^{ref}	231000	[kN/m^2]
unloading/ reloading reference shear modulus	G_{ur}^{ref}	96250	[kN/m^2]
reference shear modulus at very small strains	G_{0}^{ref}	288750	[kN/m^2]

Table 4.8: Material parameters of the soil - after compaction (ring 9)

quantity name	symbol	value	unit
tangent stiffness for primary oedometer loading	E_{oed}^{ref}	71000	[kN/m^2]
secant stiffness in standard drained triaxial test	E_{50}^{ref}	71000	[kN/m^2]
unloading/ reloading stiffness from drained triaxial test	E_{ur}^{ref}	213000	[kN/m^2]
unloading/ reloading reference shear modulus	G_{ur}^{ref}	88750	[kN/m^2]
reference shear modulus at very small strains	G_{0}^{ref}	266250	[kN/m^2]

Table 4.9: Material parameters of the soil - after compaction (ring 10 and 1)

quantity name	symbol	value	unit
tangent stiffness for primary oedometer loading	E_{oed}^{ref}	66000	[kN/m^2]
secant stiffness in standard drained triaxial test	E_{50}^{ref}	66000	[kN/m^2]
unloading/ reloading stiffness from drained triaxial test	E_{ur}^{ref}	198000	[kN/m^2]
unloading/ reloading reference shear modulus	G_{ur}^{ref}	82500	[kN/m^2]
reference shear modulus at very small strains	G_{0}^{ref}	247500	[kN/m^2]

Table 4.10: Material parameters of the soil - after compaction (ring 11)

quantity name	symbol	value	unit
tangent stiffness for primary oedometer loading	E_{oed}^{ref}	59000	[kN/m^2]
secant stiffness in standard drained triaxial test	E_{50}^{ref}	59000	[kN/m^2]
unloading/ reloading stiffness from drained triaxial test	E_{ur}^{ref}	177000	[kN/m^2]
unloading/ reloading reference shear modulus	G_{ur}^{ref}	73750	[kN/m^2]
reference shear modulus at very small strains	G_{0}^{ref}	221250	[kN/m^2]

Table 4.11: Material parameters of the soil - after compaction (ring 12)

quantity name	symbol	value	unit
tangent stiffness for primary oedometer loading	E_{oed}^{ref}	50000	[kN/m^2]
secant stiffness in standard drained triaxial test	E_{50}^{ref}	50000	[kN/m^2]
unloading/ reloading stiffness from drained triaxial test	E_{ur}^{ref}	150000	[kN/m^2]
unloading/ reloading reference shear modulus	G_{ur}^{ref}	62500	[kN/m^2]
reference shear modulus at very small strains	G_{0}^{ref}	187500	[kN/m^2]

4.2.3 Modelling

The compaction process is a complex procedure, where a dynamic action is applied to the surrounding soil generated by the depth vibrator.

The vibrator is essentially a cylindrical steel tube, containing internally (as its main feature) an eccentric weight at the bottom, mounted on a vertical shaft which is linked to a motor in the body of the machine above. When set in motion, the eccentric weight rotates around its vertical axis and causes horizontal vibrations that are needed for the vibro compaction method. The dynamic horizontal forces are thus applied directly to the surrounding soil through the tubular casing of the vibrator, cf. [6, p. 31].

The accurate numerical modelling of the mentioned process is time-consuming and complex and requires a huge calculation effort. Especially in connection with both inclinometer pipes and the necessity to model all six compaction columns the problem becomes even more complex.

According to the current state of knowledge the compaction process leads to various effects like stiffness changes, strength changes, changes in stress state, changes in permeability. However, not all effects have a significant influence on the horizontal earth pressure changes. Thus, for the numerical models some simplifications were accepted. Furthermore, assumptions were necessary to solve the problem with reasonable effort:

- The action caused by the depth vibrator was considered as a radial directed uniform static load. The diameter of the loaded quadrant / semi-circle corresponds to the on-site used depth vibrator model. The load is the same at each compaction column. The sequence of loading was considered according to the documentation on-site, shown in Fig. 3.12 and Fig. 3.13.
- The soil was modelled using an advanced elastic plastic hardening soil model with small-strain stiffness [2]. In [4] the use of a hypoplastic constitutive model with intergranular strain is recommended for modelling the deep vibro compaction using the finite element method. The application of such a constitutive model is beyond the scope of this thesis.

4.2.3.1 Approach 1: Uniform load (loading)

In the first calculation phase (initial state) the in situ stress state before compaction was generated. By using the calculation type *field stress* the effective stress in z direction of -99.80 kN/m^2 and the effective stress in x and y direction of -35.65 kN/m^2 could be specified. The mentioned stress state at 242.00 müA can be calculated using the material parameters in Tab. 4.2 and considering the ground level at 248.20 müA. The groundwater level is, as already mentioned, at 245.20 müA.

In the second calculation phase (pipe installation) the material parameters of the clusters representing the inclinometer pipes were changed and the clusters inside the pipes were deactivated. Furthermore, the modelled interfaces were activated. For the phase the calculation type *plastic* was specified.

In the loading phases (DVC04-A to DVC17-A and DVC03-B to DVC16-B) the dummy layer was used, and the uniform load was activated along the relevant compaction column.

For both test areas the compaction sequence was modelled in the correct way. For the phases the calculation type *plastic* was specified.

The measured change in ovalization value in the direction AB of the inclinometer pipe IDM2-A was used to determine the magnitude of the load. During calibration the measured value was compared with the simulated value and the load was changed until both values were equal. This was necessary as the acting uniform static load is unknown. Due to the different stiffness distributions around the inclinometer pipes, considering the three different approaches, unequal load values were used. For approach 1 a load equal to 360 kPa was chosen.

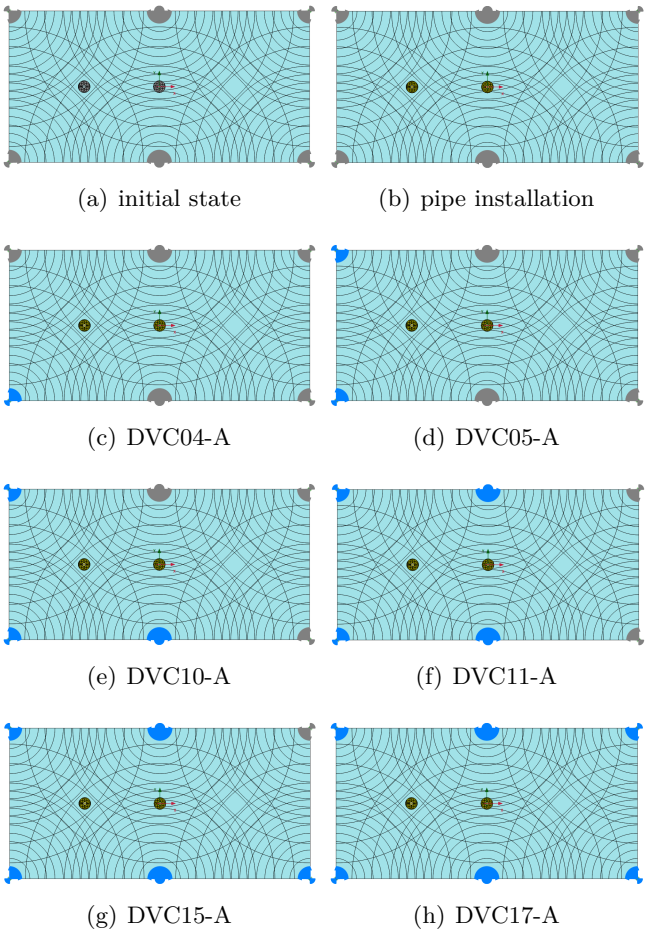

(a) initial state (b) pipe installation

(c) DVC04-A (d) DVC05-A

(e) DVC10-A (f) DVC11-A

(g) DVC15-A (h) DVC17-A

Figure 4.17: Calculation phases test area A (approach 1)

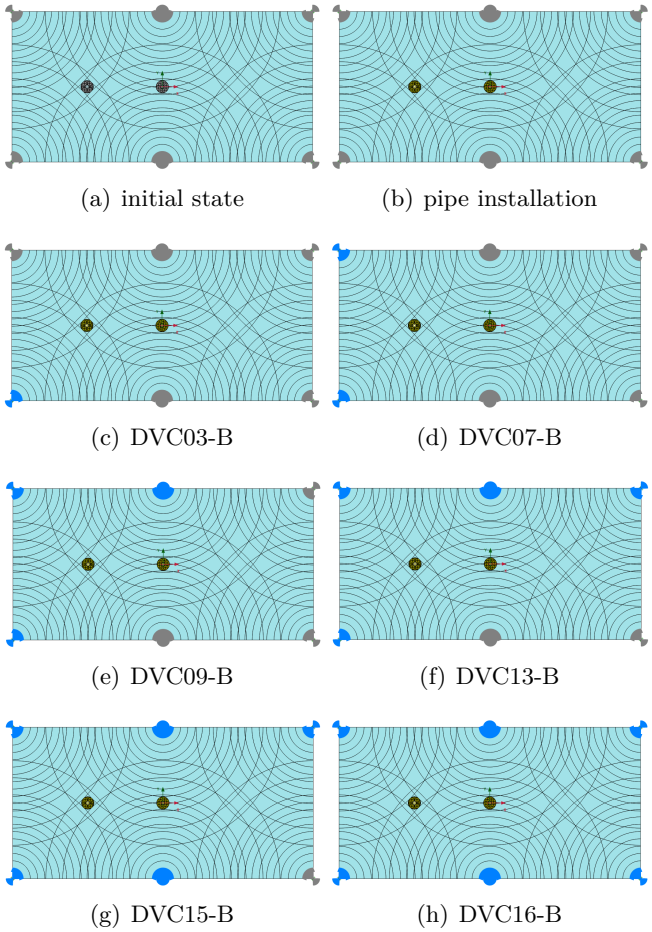

(a) initial state (b) pipe installation

(c) DVC03-B (d) DVC07-B

(e) DVC09-B (f) DVC13-B

(g) DVC15-B (h) DVC16-B

Figure 4.18: Calculation phases test area B (approach 1)

4.2.3.2 Approach 2: Uniform load (loading + unloading)

For approach 2 and 3 an additional unloading phase was considered after the loading phases. In the unloading phases the uniform load was deactivated at the respective compaction column. Furthermore, the material parameters of the cluster with the assigned dummy layer were again changed to the values shown in Tab. 4.2. For all phases the calculation type *plastic* was specified.

The measured change in ovalization value in the direction AB of the inclinometer pipe IDM2-A was used to determine the magnitude of the load. During calibration the measured value was compared with the simulated value and the load was changed until both values were equal. This was necessary as the acting uniform static load is unknown. Due to the different stiffness distributions around the inclinometer pipes, considering the three different approaches, unequal load values were used. For approach 2 a load of 440 kPa was chosen.

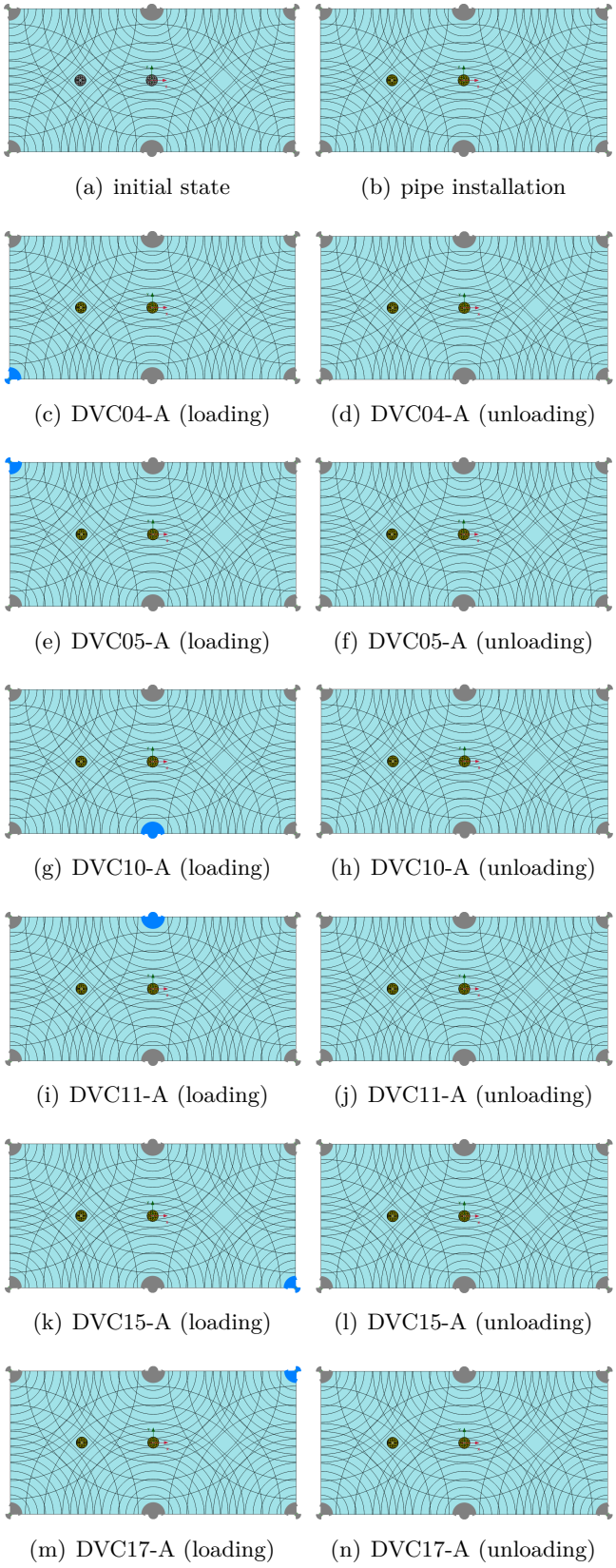

(a) initial state (b) pipe installation

(c) DVC04-A (loading) (d) DVC04-A (unloading)

(e) DVC05-A (loading) (f) DVC05-A (unloading)

(g) DVC10-A (loading) (h) DVC10-A (unloading)

(i) DVC11-A (loading) (j) DVC11-A (unloading)

(k) DVC15-A (loading) (l) DVC15-A (unloading)

(m) DVC17-A (loading) (n) DVC17-A (unloading)

Figure 4.19: Calculation phases test area A (approach 2)

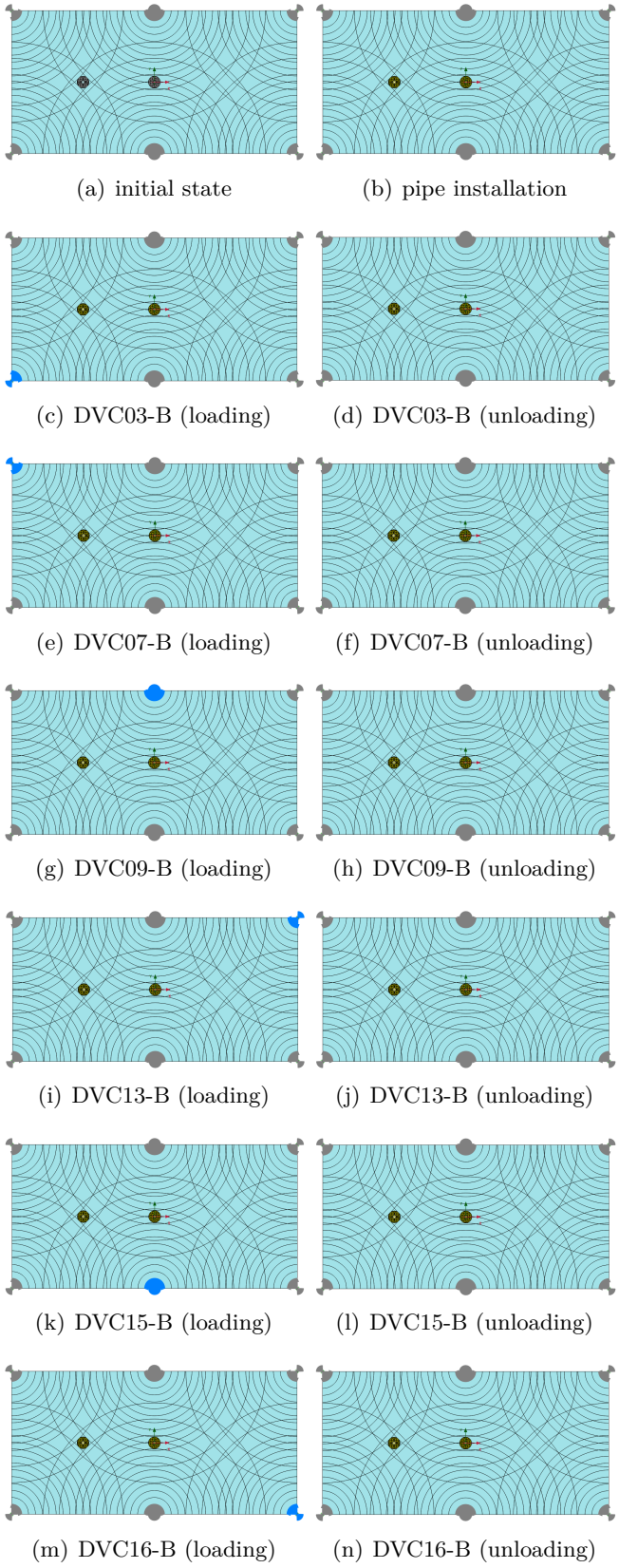

(a) initial state (b) pipe installation

(c) DVC03-B (loading) (d) DVC03-B (unloading)

(e) DVC07-B (loading) (f) DVC07-B (unloading)

(g) DVC09-B (loading) (h) DVC09-B (unloading)

(i) DVC13-B (loading) (j) DVC13-B (unloading)

(k) DVC15-B (loading) (l) DVC15-B (unloading)

(m) DVC16-B (loading) (n) DVC16-B (unloading)

Figure 4.20: Calculation phases test area B (approach 2)

4.2.3.3 Approach 3: Uniform load (loading + unloading) + rings with modified stiffness

For approach 3 the grain redistribution effect was simplified considered by the manual stiffness change of the modelled rings around the compaction centres. The chosen values are shown in Tab. 4.4 to Tab. 4.11 and are illustrated in the following figure. As the stiffness depends, due to the chosen material model, also on the current stress state the maximum manually changed stiffness value is 100000 kN/m^2.

The measured change in ovalization value in the direction AB of the inclinometer pipe IDM2-A was used to determine the magnitude of the load. During calibration the measured value was compared with the simulated value and the load was changed until both values were equal. This was necessary as the acting uniform static load is unknown. Due to the different stiffness distributions around the inclinometer pipes, considering the three different approaches, unequal load values were used. For approach 3 a load of 850 kPa was chosen.

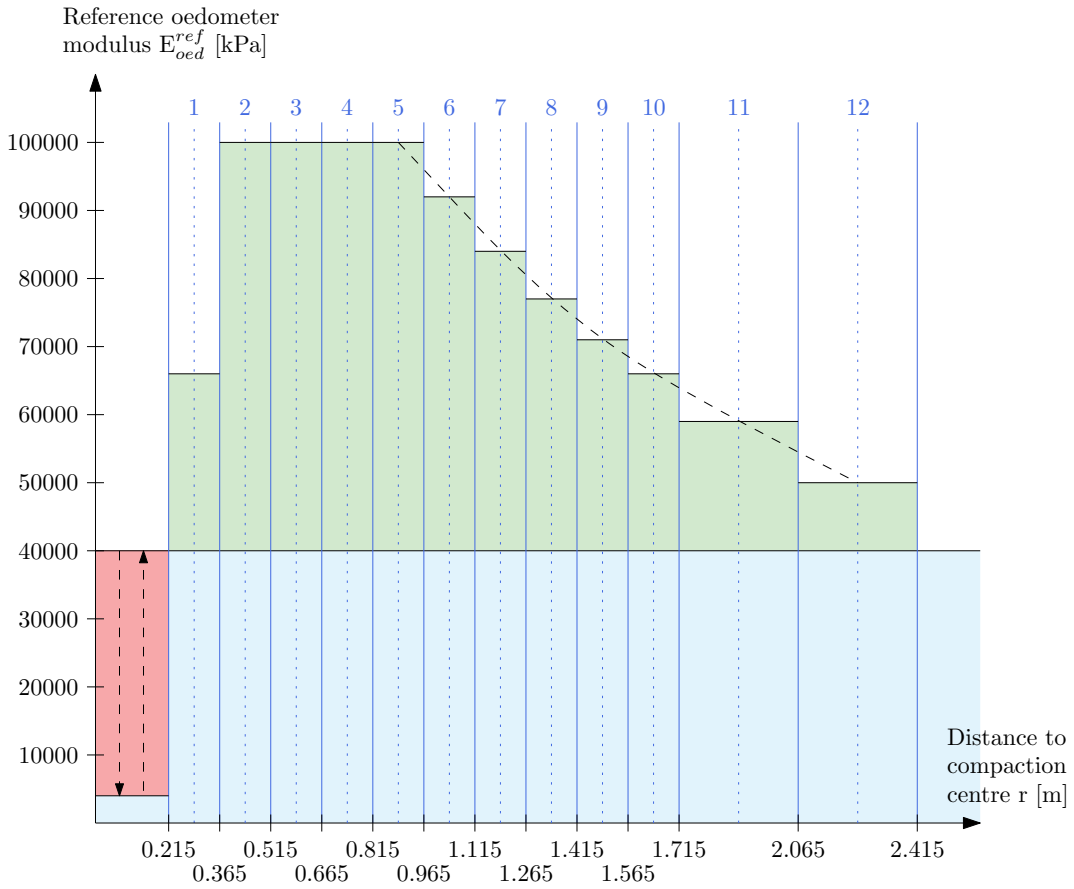

Figure 4.21: Rings with modified stiffness

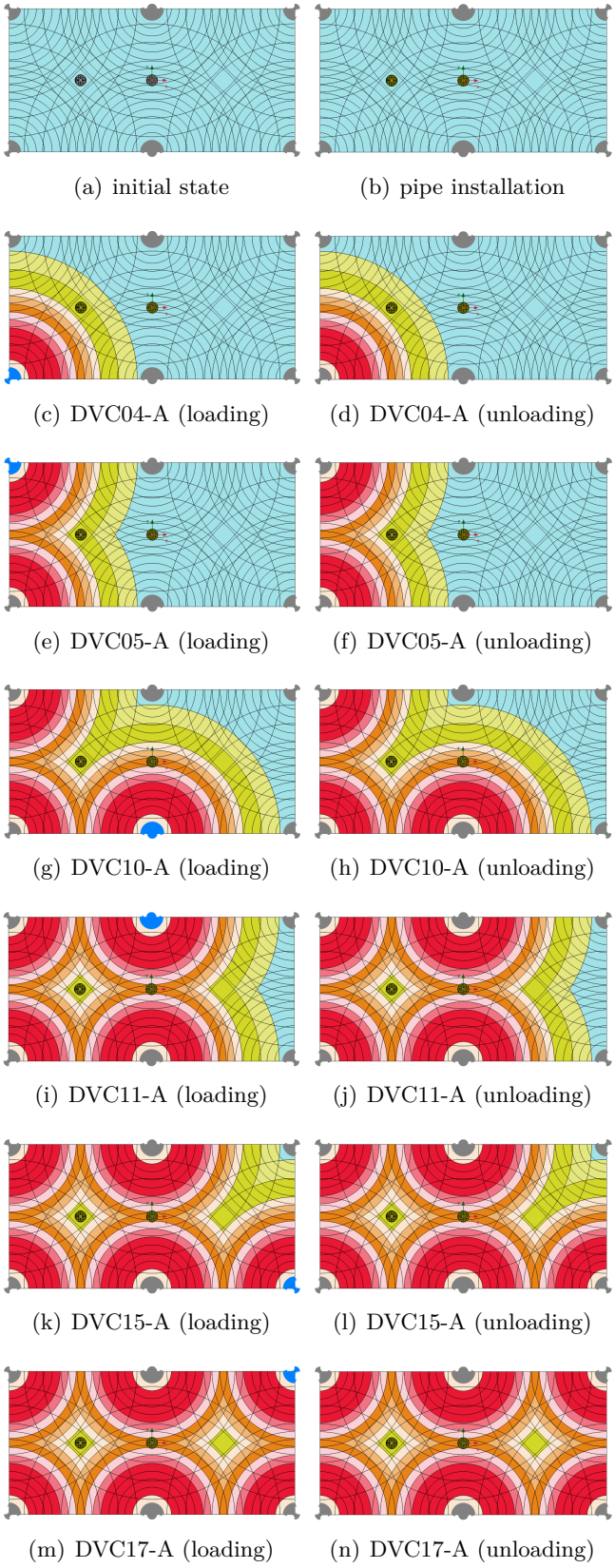

(a) initial state (b) pipe installation

(c) DVC04-A (loading) (d) DVC04-A (unloading)

(e) DVC05-A (loading) (f) DVC05-A (unloading)

(g) DVC10-A (loading) (h) DVC10-A (unloading)

(i) DVC11-A (loading) (j) DVC11-A (unloading)

(k) DVC15-A (loading) (l) DVC15-A (unloading)

(m) DVC17-A (loading) (n) DVC17-A (unloading)

Figure 4.22: Calculation phases test area A (approach 3)

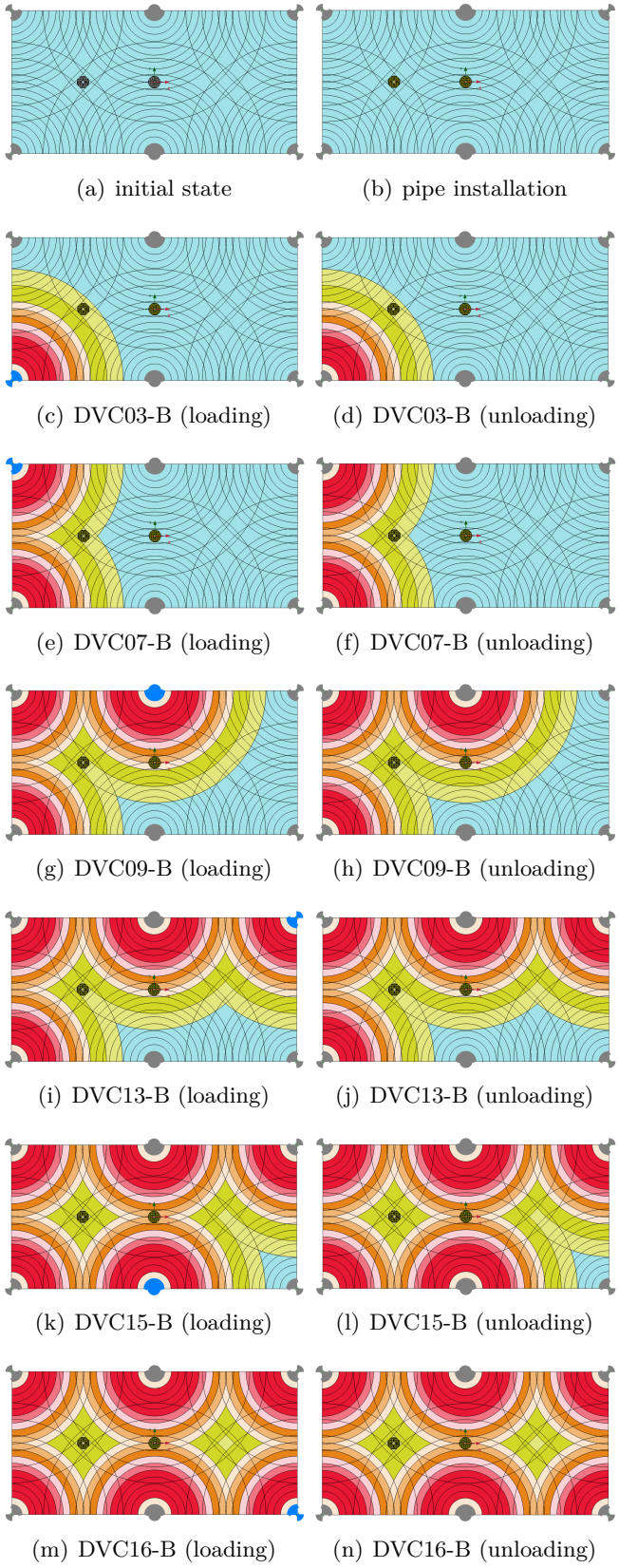

(a) initial state (b) pipe installation

(c) DVC03-B (loading) (d) DVC03-B (unloading)

(e) DVC07-B (loading) (f) DVC07-B (unloading)

(g) DVC09-B (loading) (h) DVC09-B (unloading)

(i) DVC13-B (loading) (j) DVC13-B (unloading)

(k) DVC15-B (loading) (l) DVC15-B (unloading)

(m) DVC16-B (loading) (n) DVC16-B (unloading)

Figure 4.23: Calculation phases test area B (approach 3)

4.2.4 Simulation results

This subsection includes the simulation results of both numerical models: test area A and test area B.

4.2.4.1 Test area A

For all three approaches the changes in diameter and the changes in ovalization value of the inclinometer pipes, the reference oedometer modulus, the change in effective mean normal stress and the change in deviatoric stress of the soil and finally the stress paths and the effective stresses around the inclinometer pipes are shown.

The nodes in the centre of the pipe channels were used for the output of the displacements in x and y direction in each calculation phase. Based on the original coordinates of the mentioned nodes, the coordinates after the phases can be calculated. By using the Pythagorean theorem, the distances between the nodes in all four measurement directions can be determined. The further interpretation was performed according to the explanations in section 3.4.1.1. The simulation results after the second calculation phase (pipe installation) were treated as epoch 0 and the results after the last phase were treated as epoch 1.

Approach 1: Uniform load (loading)

The simulation result is represented by the point of intersection of the red dashed lines. The depth position of the model was specified at 242.00 müA (about 6.20 m below the ground level). In the following figures only the measurement results of epoch 0 and epoch 1 are shown. With approach 1 the pipe deformations can be simulated already qualitatively correct (see Fig. 4.24 and Fig. 4.25).

As discussed in section 3.4.1.1 only the ovalization value is free from errors affecting all diameter measurements. It is therefore neither sensible nor possible to simulate all diameter changes correctly.

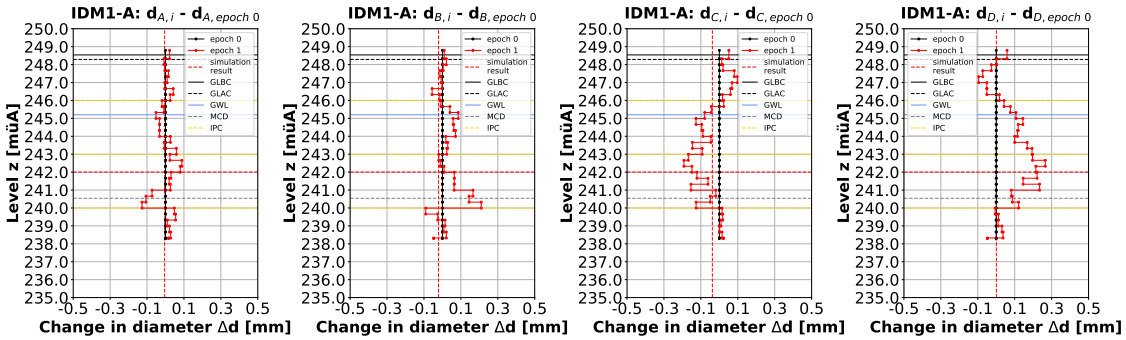

Figure 4.24: Changes in diameter of the inclinometer pipe IDM1-A - epoch 0 (approach 1)

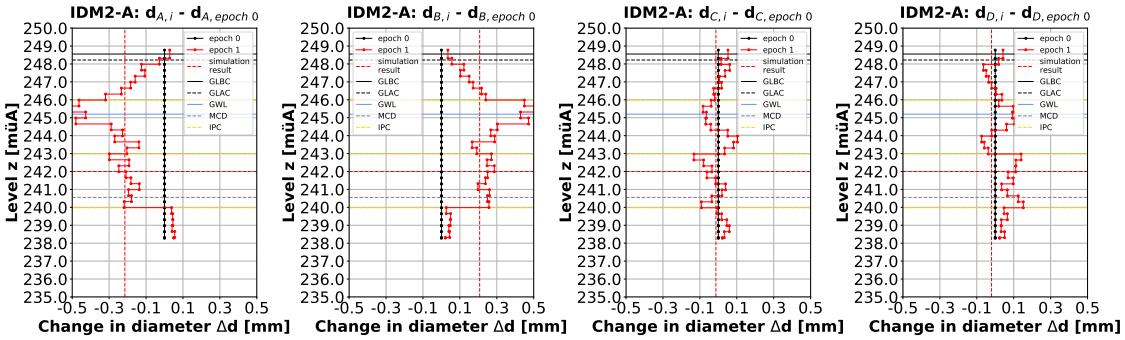

Figure 4.25: Changes in diameter of the inclinometer pipe IDM2-A - epoch 0 (approach 1)

Fig. 4.26 provides the following findings: The simulated change in ovalization value in direction CD is for the inclinometer pipe IDM1-A obviously too small. The change in ovalization value in direction AB is as measured nearly zero.

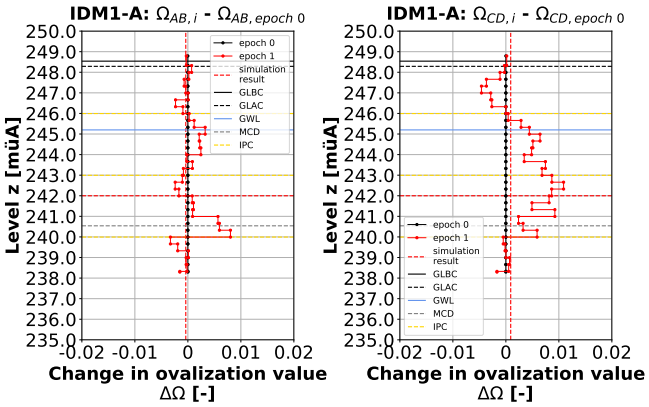

Figure 4.26: Changes in ovalization value of the inclinometer pipe IDM1-A - epoch 0 (approach 1)

Fig. 4.27 provides the following findings: For the inclinometer pipe IDM2-A the simulated change in ovalization value in direction AB is about the same as the measured. This is reasonable as the load was calibrated on this value. In direction CD the simulated change in ovalization value is nearly zero. This is a good agreement as the measurement result is not significant.

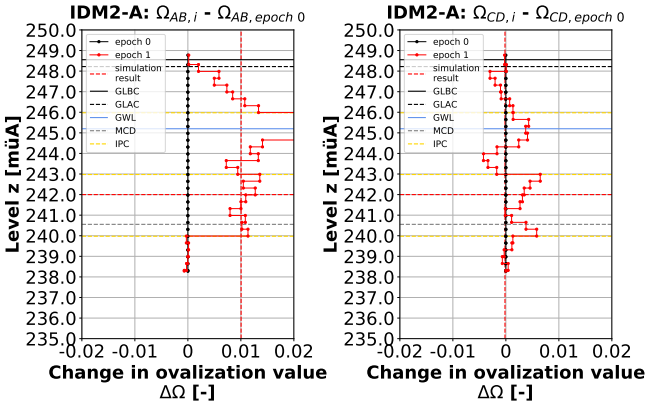

Figure 4.27: Changes in ovalization value of the inclinometer pipe IDM2-A - epoch 0 (approach 1)

Fig. 4.28 shows the reference oedometer modulus after the different calculation phases.

The hardening soil model with small-strain stiffness considers, as the name implies, the increased stiffness of soils at small strains. To calculate the reference shear modulus at very small strains based on the unloading/ reloading reference shear modulus a factor of 3 was used. In the following figures this factor is observable at areas with small strains.

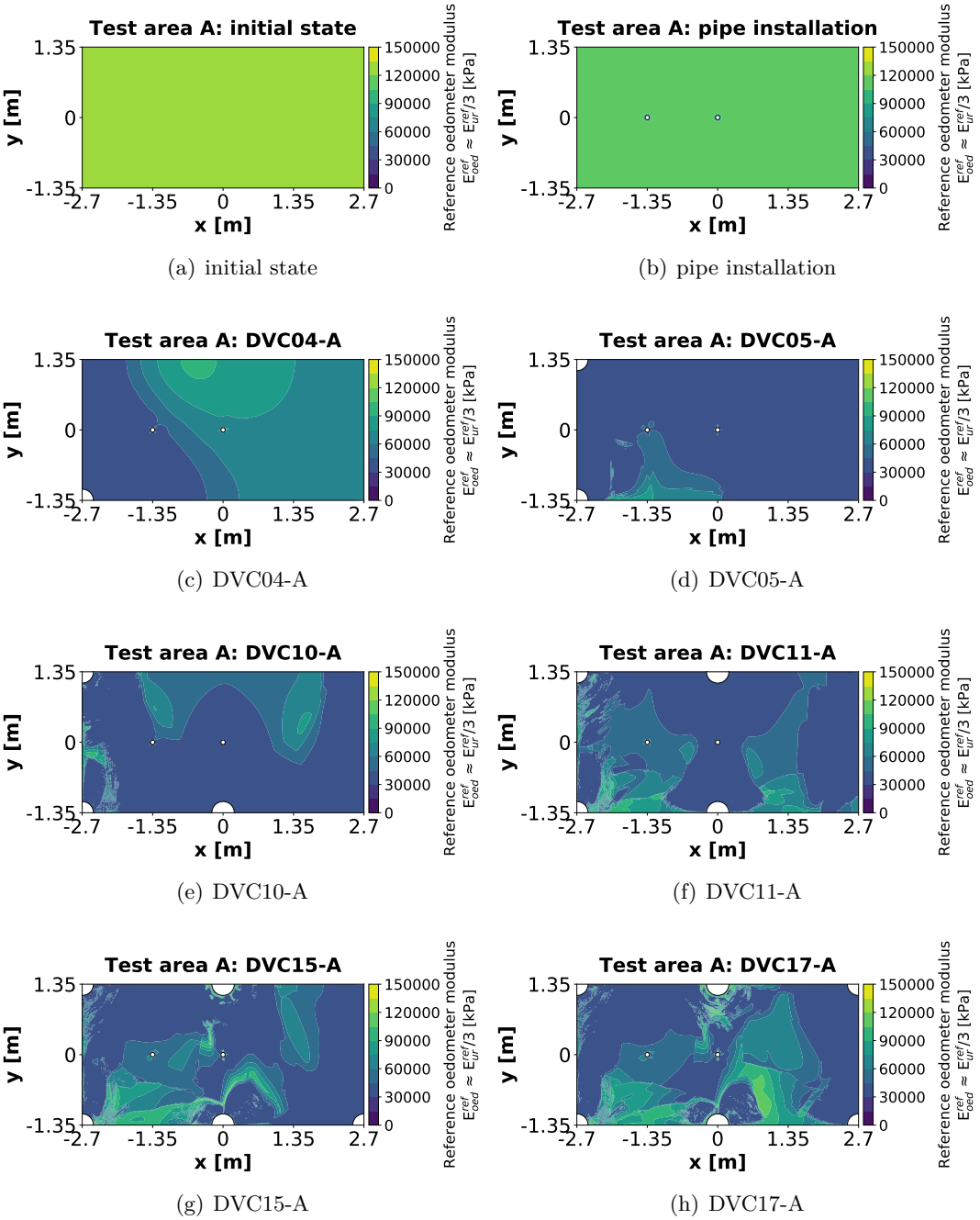

(a) initial state (b) pipe installation

(c) DVC04-A (d) DVC05-A

(e) DVC10-A (f) DVC11-A

(g) DVC15-A (h) DVC17-A

Figure 4.28: Reference oedometer modulus test area A (approach 1)

Fig. 4.29 shows the change in effective mean normal stress between the different calculation phases. During compaction, the value changes significantly around the compaction centre.

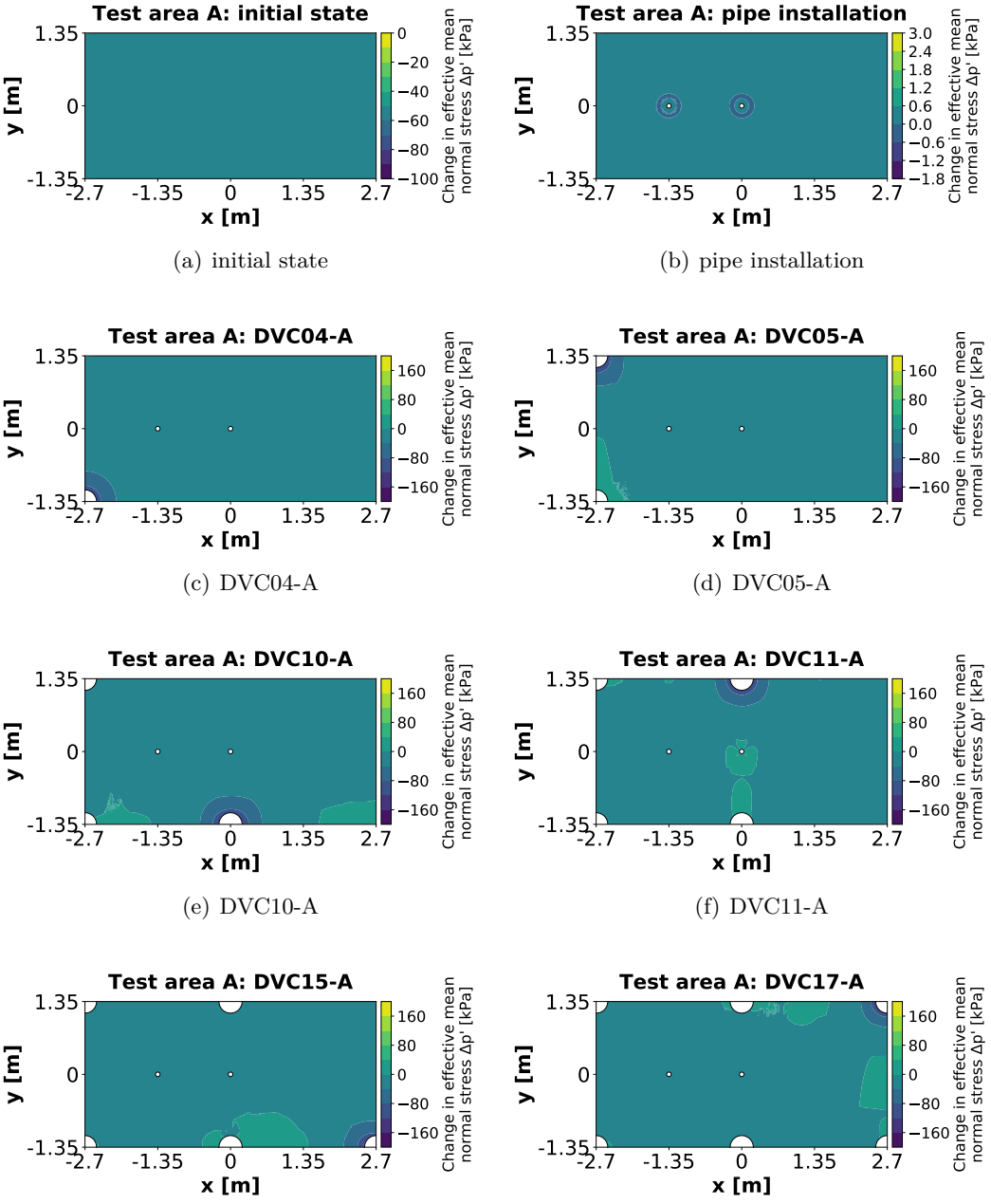

(a) initial state

(b) pipe installation

(c) DVC04-A

(d) DVC05-A

(e) DVC10-A

(f) DVC11-A

(g) DVC15-A

(h) DVC17-A

Figure 4.29: Change in effective mean normal stress test area A (approach 1)

Fig. 4.30 shows the change in deviatoric stress between the different calculation phases. During compaction, the value changes significantly around the compaction centre.

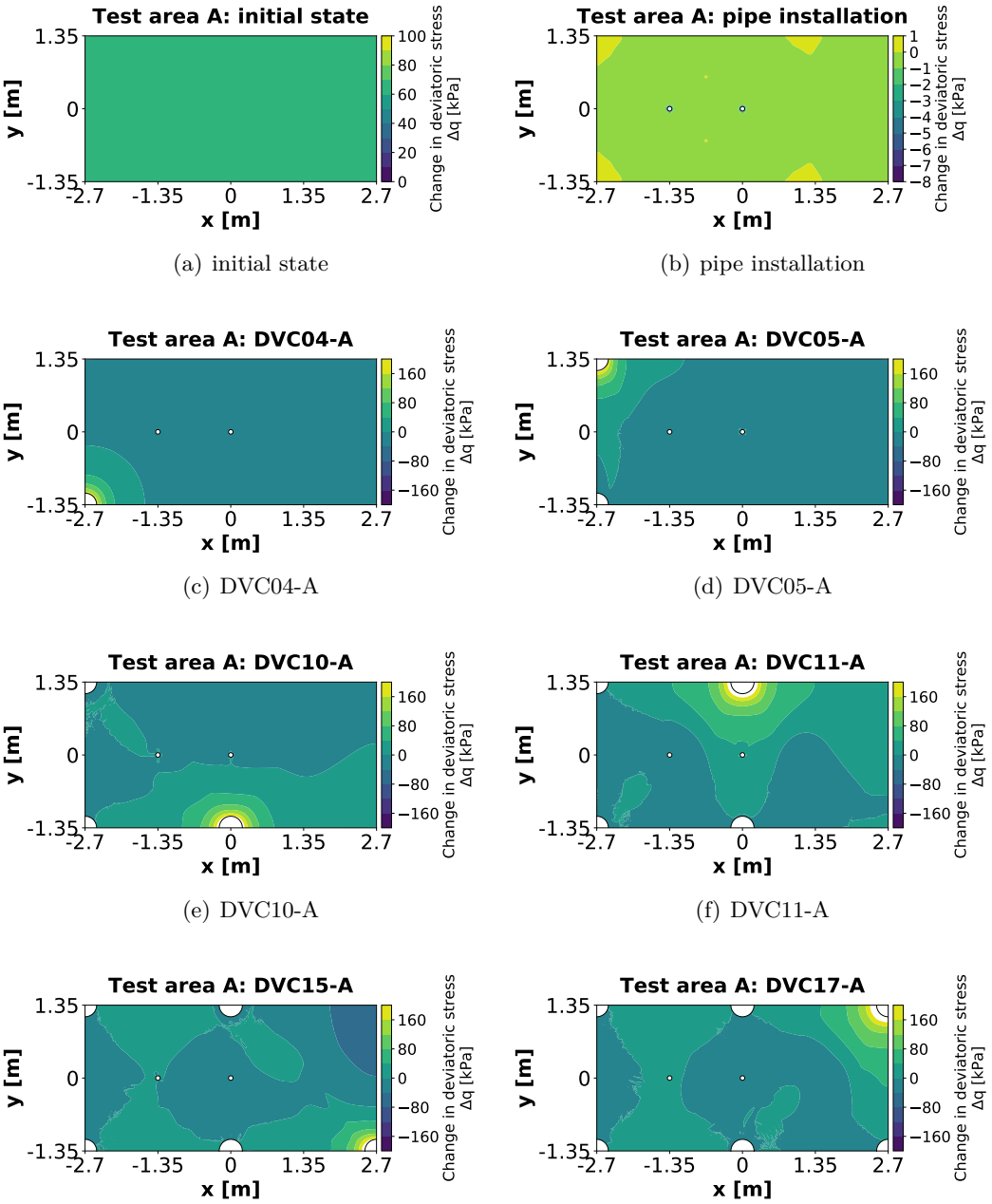

(a) initial state
(b) pipe installation
(c) DVC04-A
(d) DVC05-A
(e) DVC10-A
(f) DVC11-A
(g) DVC15-A
(h) DVC17-A

Figure 4.30: Change in deviatoric stress test area A (approach 1)

The stress paths and effective stresses in x and y direction were evaluated at stress points in all four measurement directions of the inclinometer pipes 0, 5, 15, 30 and 50 cm away from the outer mantel of the pipe. The symbols in the diagrams represent the values at the end of each calculation phase. All stress paths must start on the K_0^{nc}-line.

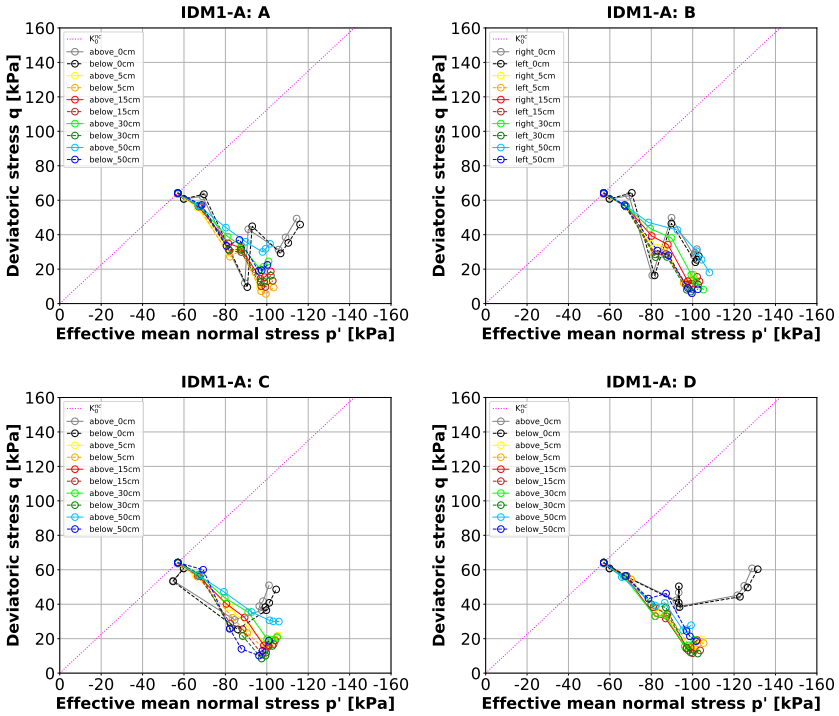

Figure 4.31: Stress paths around the inclinometer pipe IDM1-A (approach 1)

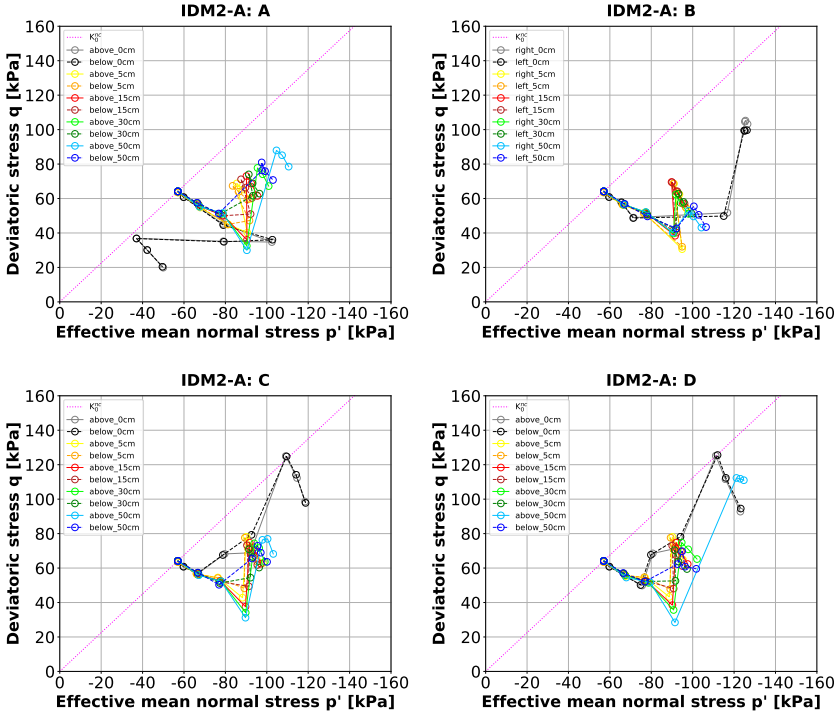

Figure 4.32: Stress paths around the inclinometer pipe IDM2-A (approach 1)

To obtain a result without pipe influence it is recommended to take the values at a specific distance from the pipe mantel. Especially the values 0 cm away from the outer mantel of the pipe deviate from the other values.

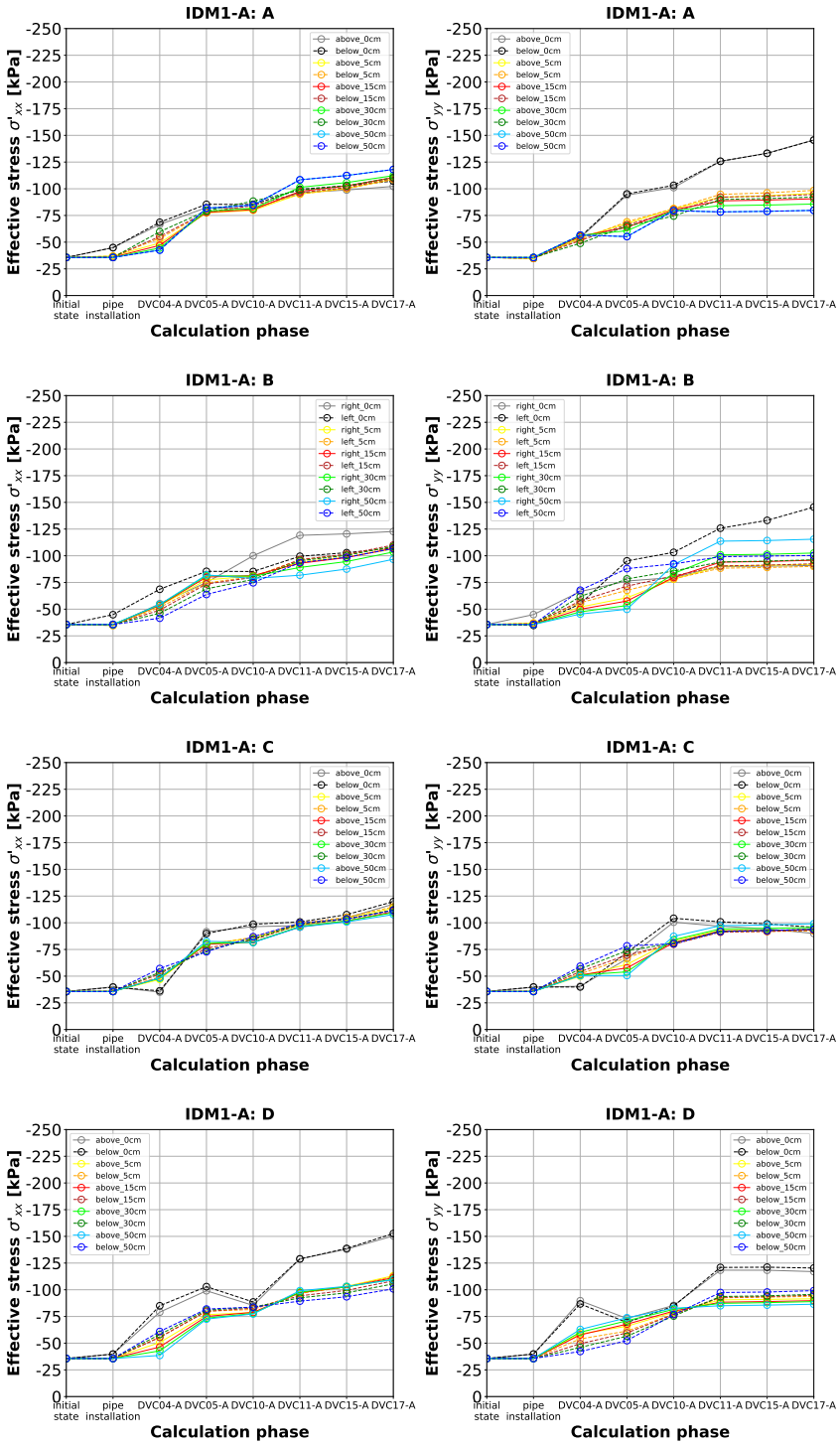

Figure 4.33: Effective stresses around the inclinometer pipe IDM1-A (approach 1)

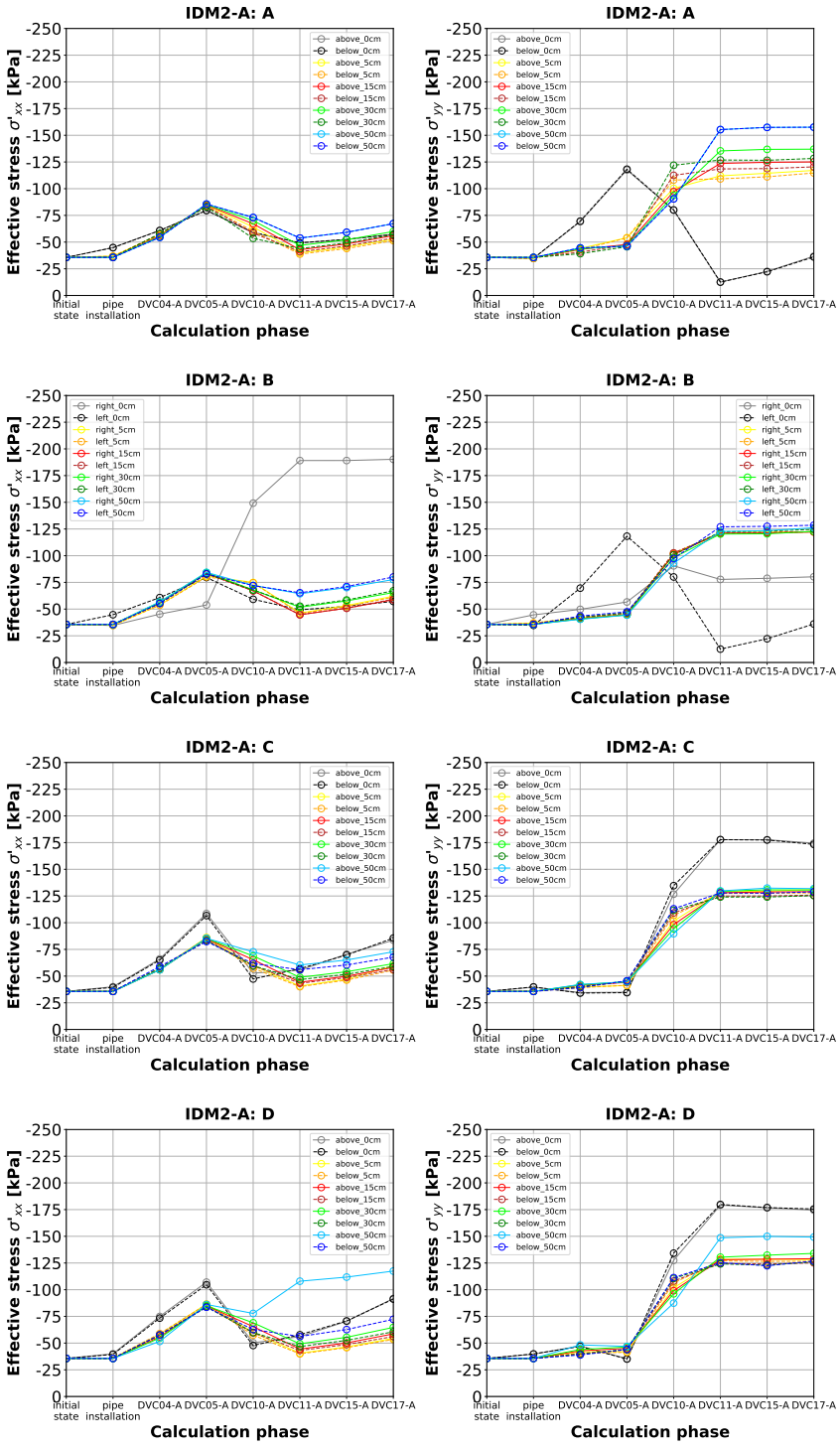

Figure 4.34: Effective stresses around the inclinometer pipe IDM2-A (approach 1)

Approach 2: Uniform load (loading + unloading)

The simulation result is represented by the point of intersection of the red dashed lines. The depth position of the model was specified at 242.00 müA (about 6.20 m below the ground level). In the following figures only the measurement results of epoch 0 and epoch 1 are shown. With approach 2 the pipe deformations can be simulated quantitatively more correct (see Fig. 4.35 and Fig. 4.36).

As discussed in section 3.4.1.1 only the ovalization value is free from errors affecting all diameter measurements. It is therefore neither sensible nor possible to simulate all diameter changes correctly.

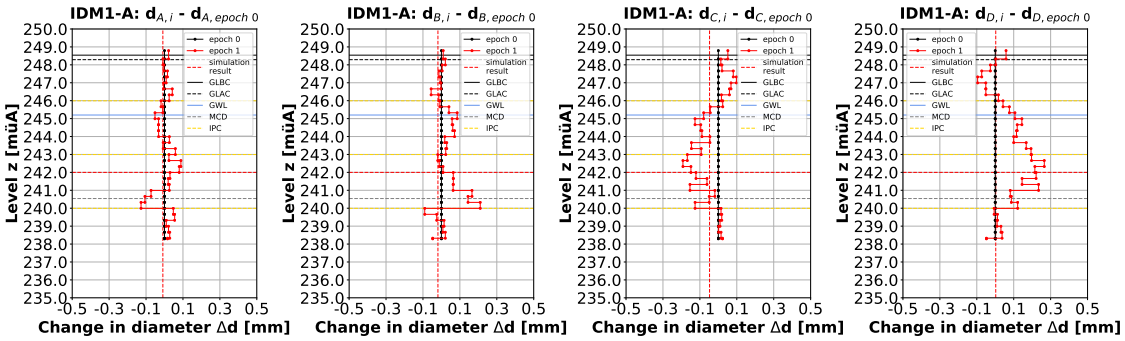

Figure 4.35: Changes in diameter of the inclinometer pipe IDM1-A - epoch 0 (approach 2)

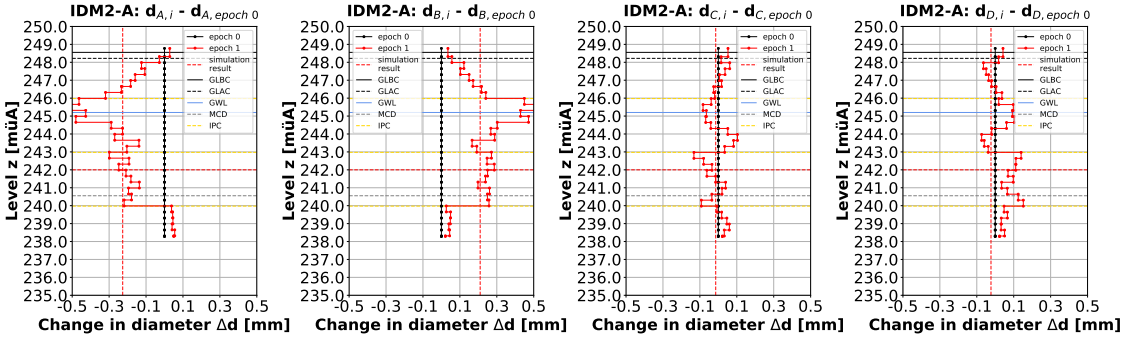

Figure 4.36: Changes in diameter of the inclinometer pipe IDM2-A - epoch 0 (approach 2)

Fig. 4.37 provides the following findings: The simulated change in ovalization value in direction CD is for the inclinometer pipe IDM1-A obviously too small. Nevertheless, the value is bigger as shown in Fig. 4.26. The change in ovalization value in direction AB is as measured nearly zero.

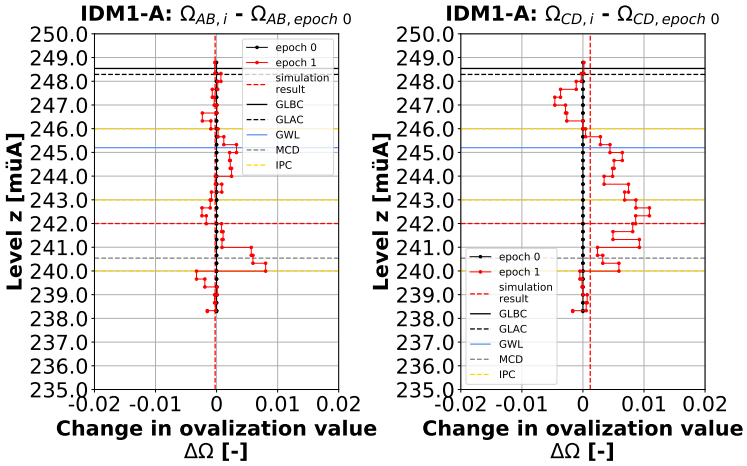

Figure 4.37: Changes in ovalization value of the inclinometer pipe IDM1-A - epoch 0 (approach 2)

Fig. 4.38 provides the following findings: For the inclinometer pipe IDM2-A the simulated change in ovalization value in direction AB is about the same as the measured. This is reasonable as the load was calibrated on this value. In direction CD the simulated change in ovalization value is nearly zero. This is a good agreement as the measurement result is not significant.

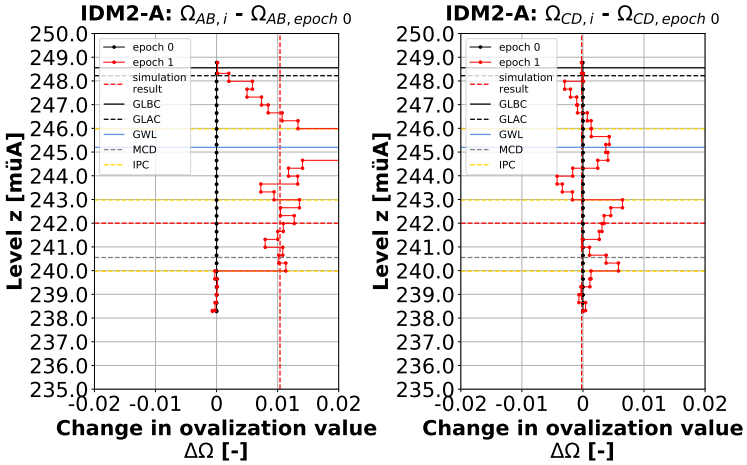

Figure 4.38: Changes in ovalization value of the inclinometer pipe IDM2-A - epoch 0 (approach 2)

Fig. 4.39 shows the reference oedometer modulus after the different calculation phases.

The hardening soil model with small-strain stiffness considers, as the name implies, the increased stiffness of soils at small strains. To calculate the reference shear modulus at very small strains based on the unloading/ reloading reference shear modulus a factor of 3 was used. In the following figures this factor is observable at areas with small strains.

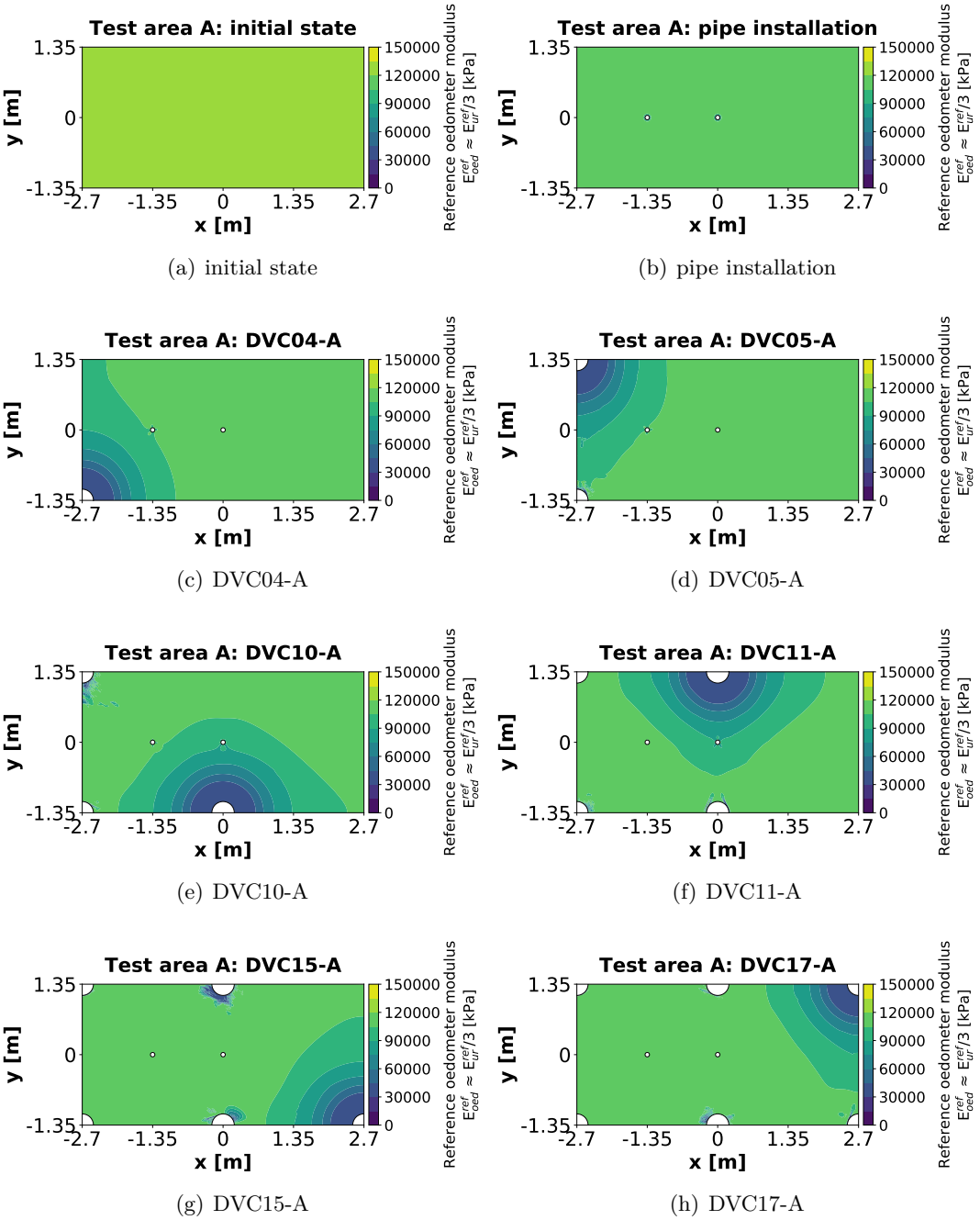

(a) initial state (b) pipe installation

(c) DVC04-A (d) DVC05-A

(e) DVC10-A (f) DVC11-A

(g) DVC15-A (h) DVC17-A

Figure 4.39: Reference oedometer modulus test area A (approach 2)

Fig. 4.40 shows the change in effective mean normal stress between the different calculation phases. During compaction, the value changes significantly around the compaction centre.

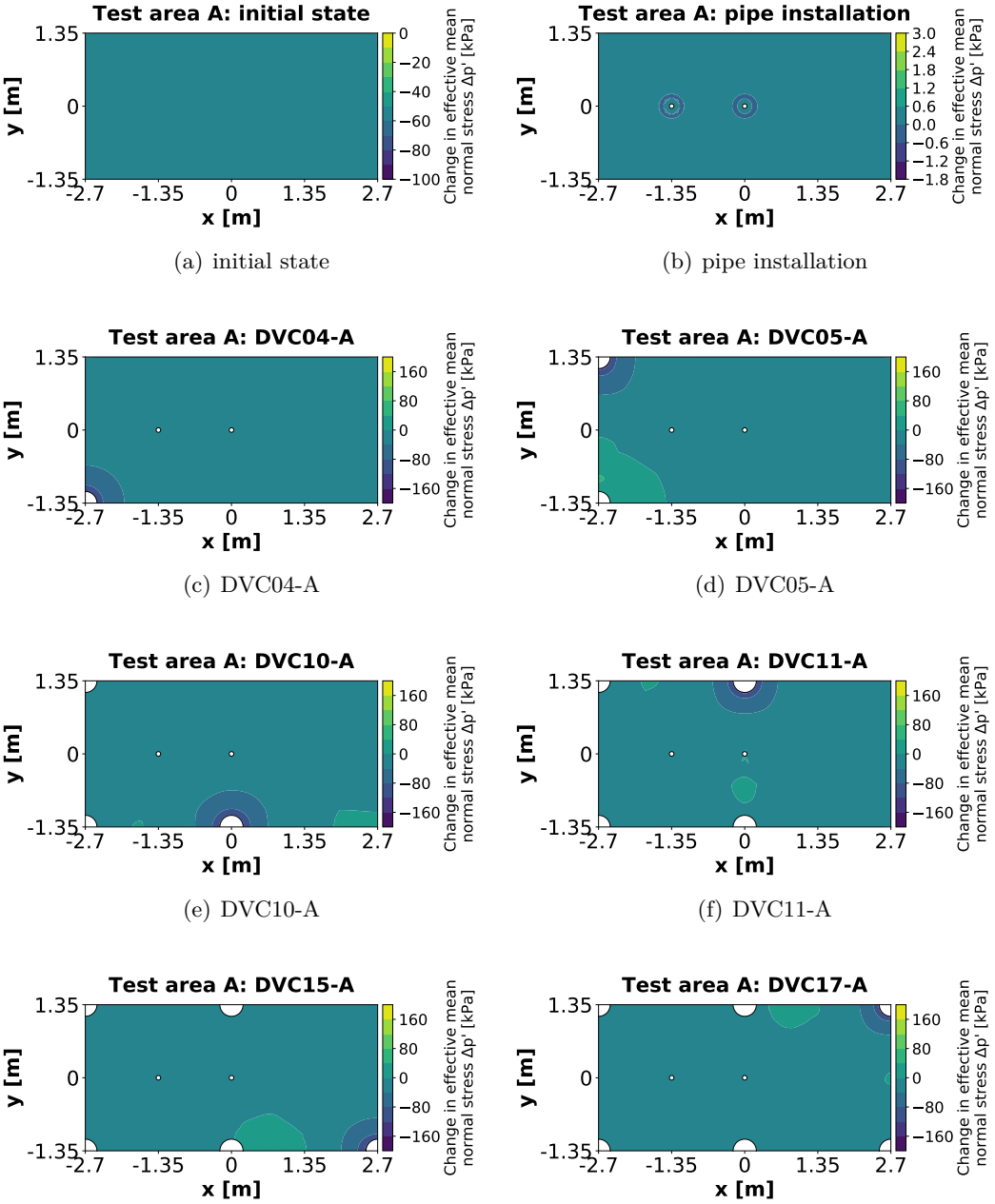

(a) initial state

(b) pipe installation

(c) DVC04-A

(d) DVC05-A

(e) DVC10-A

(f) DVC11-A

(g) DVC15-A

(h) DVC17-A

Figure 4.40: Change in effective mean normal stress test area A (approach 2)

Fig. 4.41 shows the change in deviatoric stress between the different calculation phases. During compaction, the value changes significantly around the compaction centre.

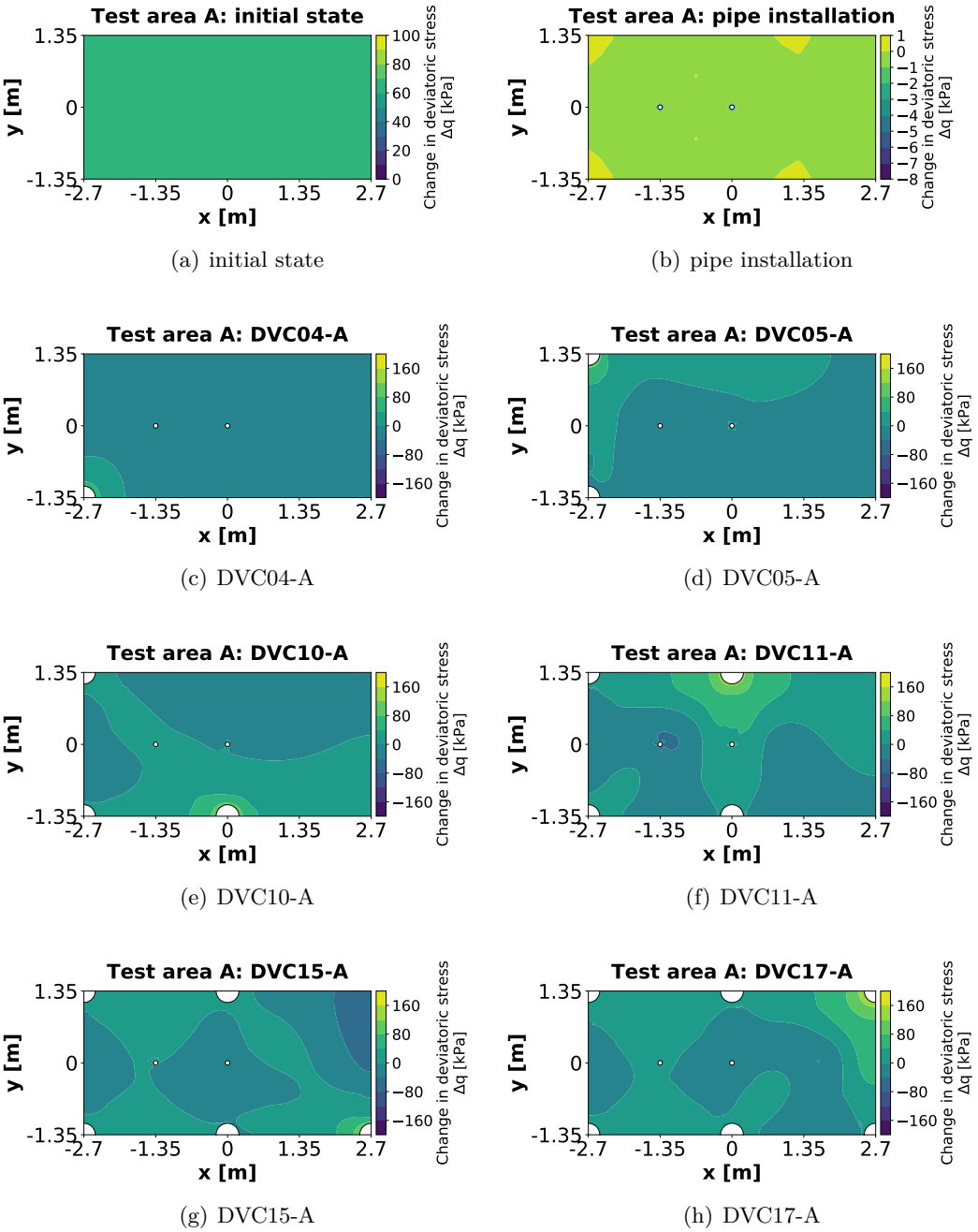

(a) initial state
(b) pipe installation
(c) DVC04-A
(d) DVC05-A
(e) DVC10-A
(f) DVC11-A
(g) DVC15-A
(h) DVC17-A

Figure 4.41: Change in deviatoric stress test area A (approach 2)

The stress paths and effective stresses in x and y direction were evaluated at stress points in all four measurement directions of the inclinometer pipes 0, 5, 15, 30 and 50 cm away from the outer mantel of the pipe. The symbols in the diagrams represent the values at the end of each calculation phase. All stress paths must start on the K_0^{nc}-line.

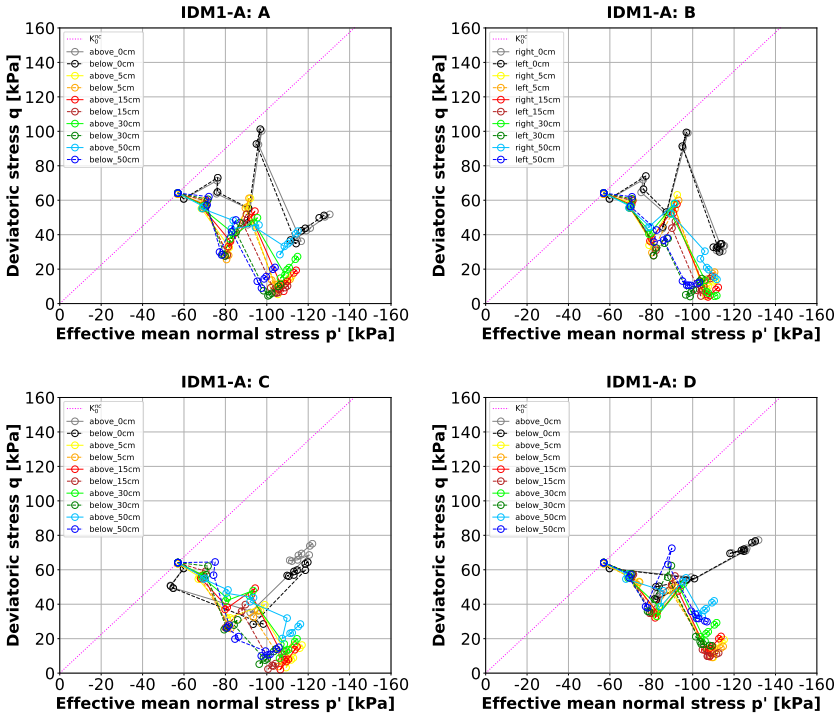

Figure 4.42: Stress paths around the inclinometer pipe IDM1-A (approach 2)

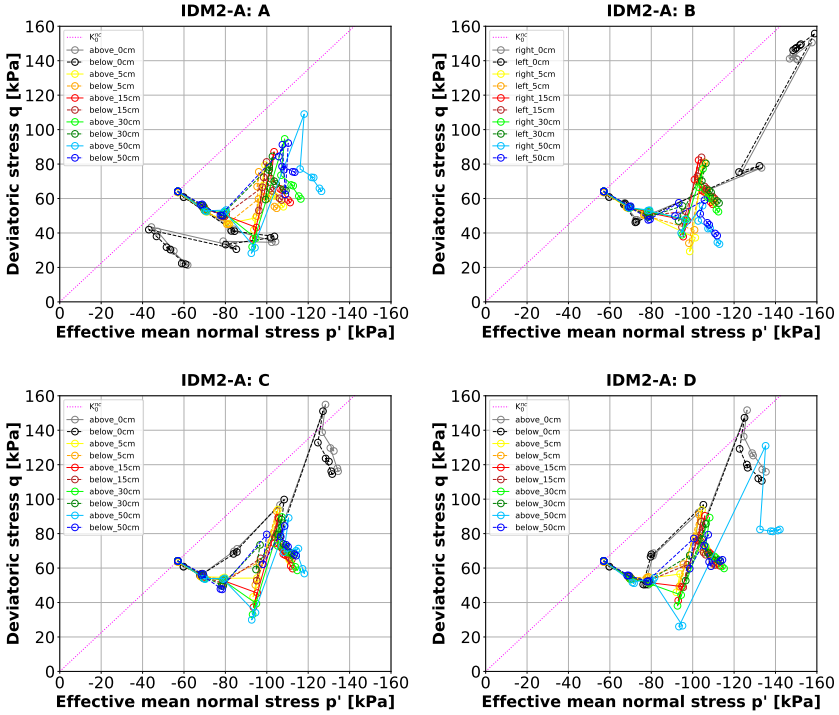

Figure 4.43: Stress paths around the inclinometer pipe IDM2-A (approach 2)

To obtain a result without pipe influence it is recommended to take the values at a specific distance from the pipe mantel. Especially the values 0 cm away from the outer mantel of the pipe deviate from the other values.

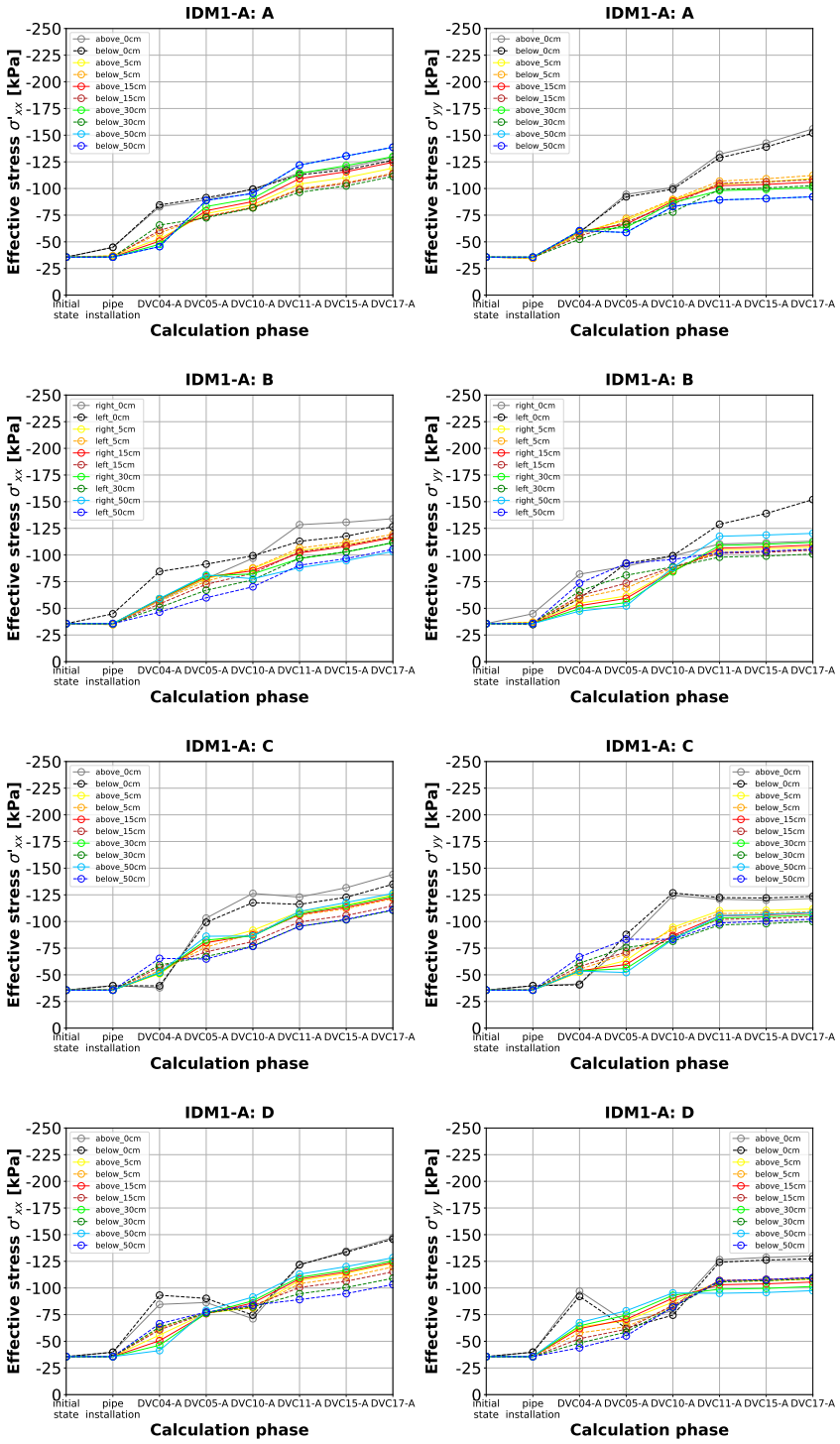

Figure 4.44: Effective stresses around the inclinometer pipe IDM1-A (approach 2)

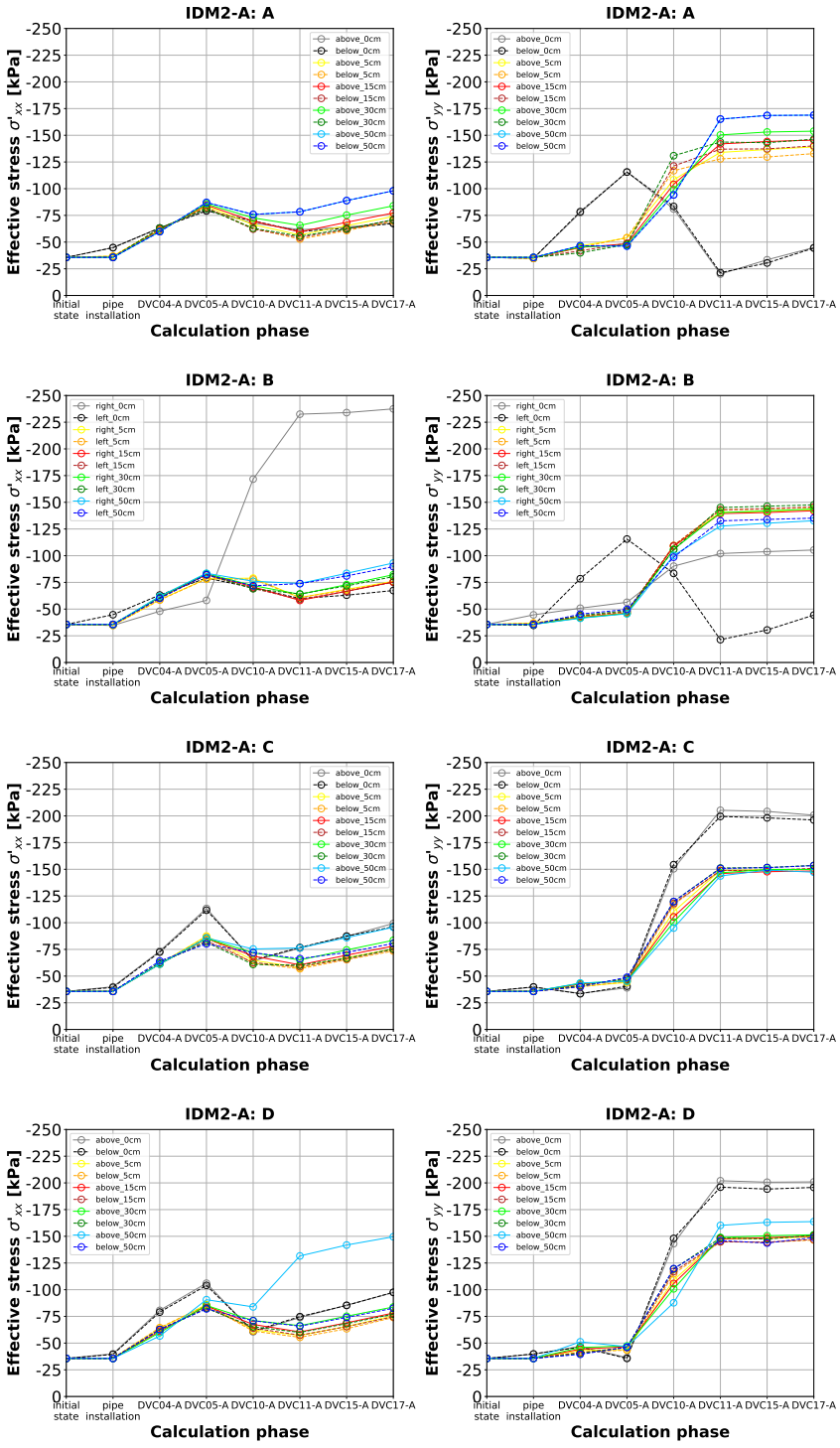

Figure 4.45: Effective stresses around the inclinometer pipe IDM2-A (approach 2)

Approach 3: Uniform load (loading + unloading) + rings with modified stiffness

The simulation result is represented by the point of intersection of the red dashed lines. The depth position of the model was specified at 242.00 müA (about 6.20 m below the ground level). In the following figures only the measurement results of epoch 0 and epoch 1 are shown. With approach 3 the pipe deformations can be simulated qualitatively and quantitatively almost correct (see Fig. 4.46 and Fig. 4.47).

As discussed in section 3.4.1.1 only the ovalization value is free from errors affecting all diameter measurements. It is therefore neither sensible nor possible to simulate all diameter changes correctly.

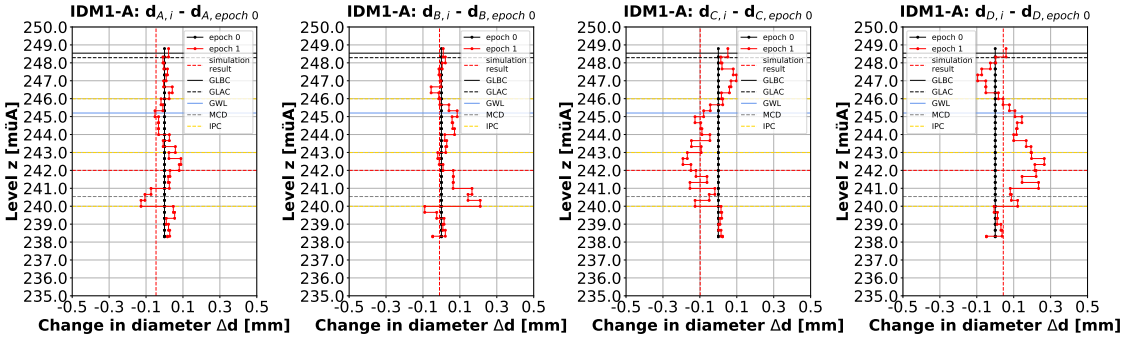

Figure 4.46: Changes in diameter of the inclinometer pipe IDM1-A - epoch 0 (approach 3)

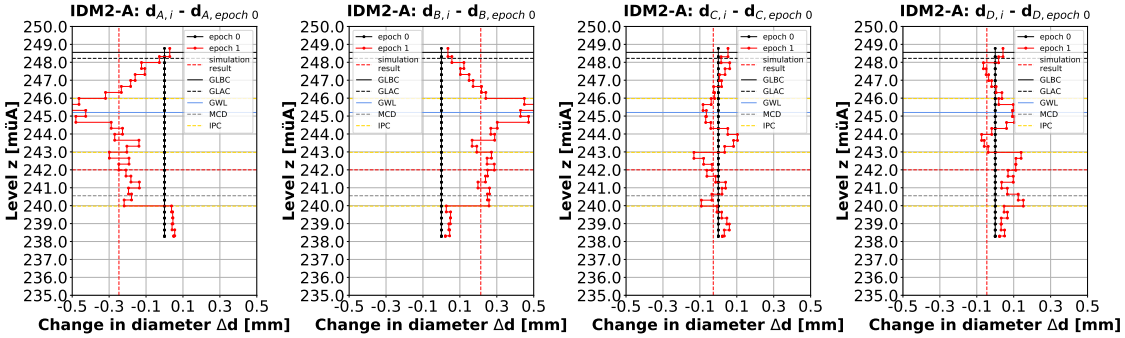

Figure 4.47: Changes in diameter of the inclinometer pipe IDM2-A - epoch 0 (approach 3)

Fig. 4.48 provides the following findings: The simulated change in ovalization value in direction CD is for the inclinometer pipe IDM1-A almost correct. The value is much bigger as shown in Fig. 4.37. The change in ovalization value in direction AB is as measured nearly zero.

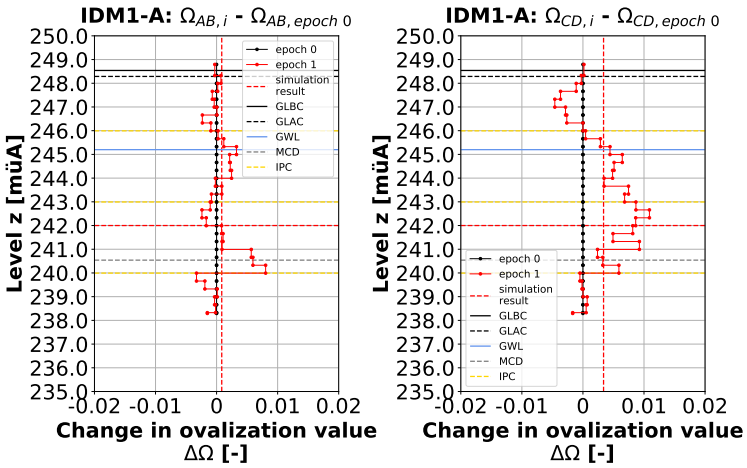

Figure 4.48: Changes in ovalization value of the inclinometer pipe IDM1-A - epoch 0 (approach 3)

Fig. 4.49 provides the following findings: For the inclinometer pipe IDM2-A the simulated change in ovalization value in direction AB is about the same as the measured. This is reasonable as the load was calibrated on this value. In direction CD the simulated change in ovalization value is nearly zero. This is a good agreement as the measurement result is not significant.

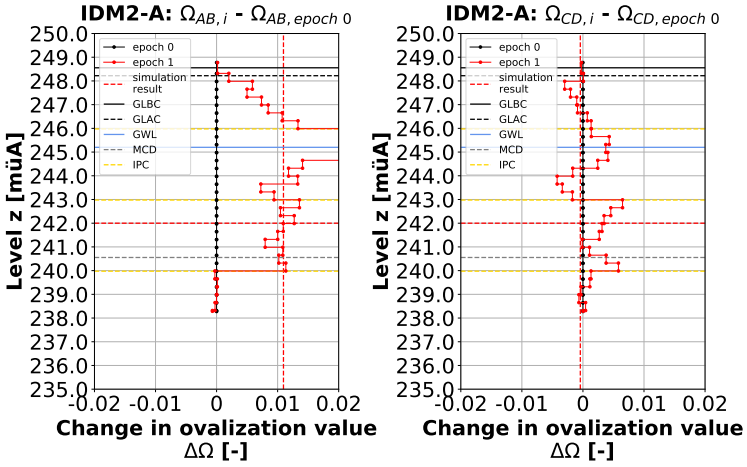

Figure 4.49: Changes in ovalization value of the inclinometer pipe IDM2-A - epoch 0 (approach 3)

Fig. 4.50 shows the reference oedometer modulus after the different calculation phases.

The hardening soil model with small-strain stiffness considers, as the name implies, the increased stiffness of soils at small strains. To calculate the reference shear modulus at very small strains based on the unloading/ reloading reference shear modulus a factor of 3 was used. In the following figures this factor is observable at areas with small strains.

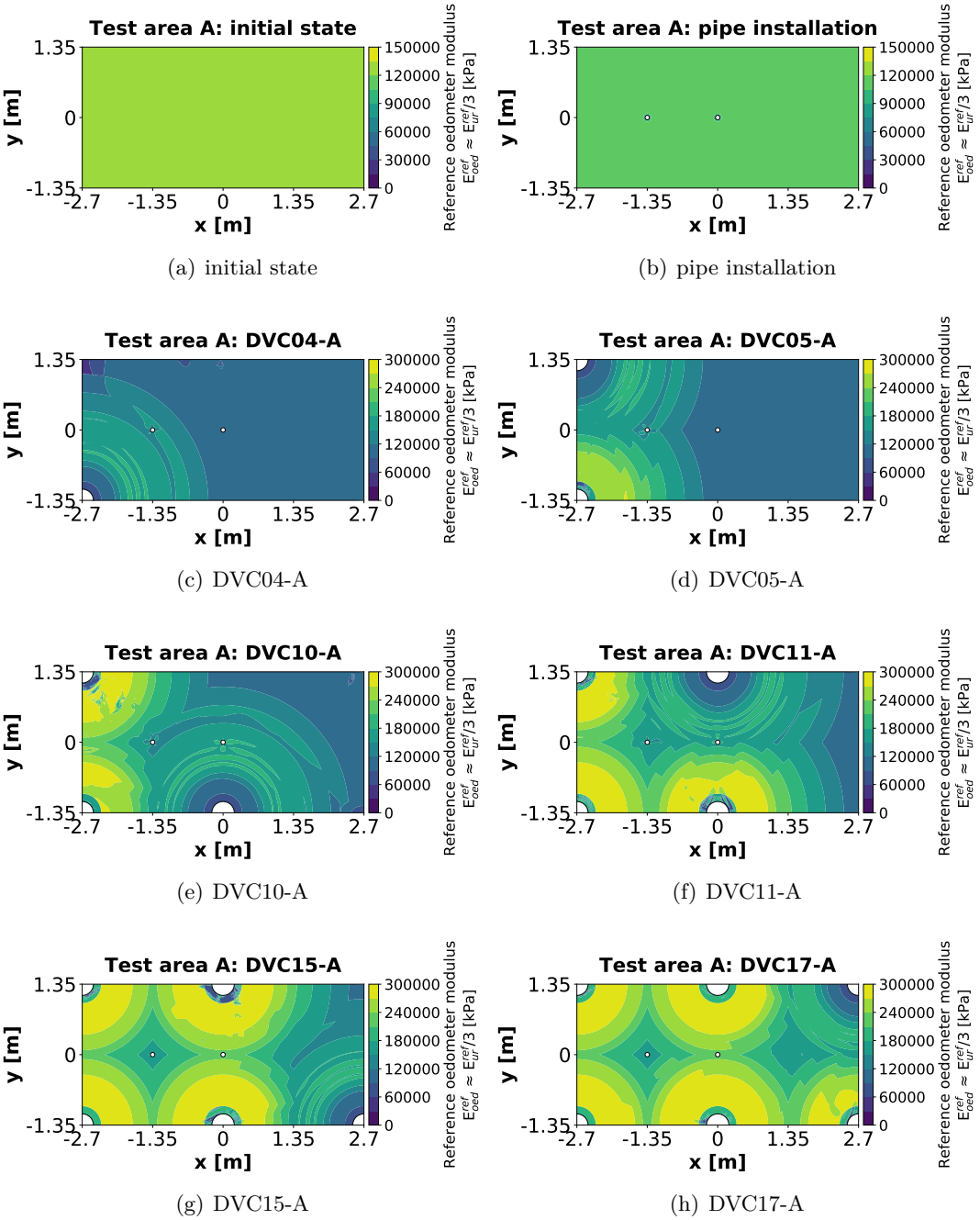

(a) initial state (b) pipe installation

(c) DVC04-A (d) DVC05-A

(e) DVC10-A (f) DVC11-A

(g) DVC15-A (h) DVC17-A

Figure 4.50: Reference oedometer modulus test area A (approach 3)

Fig. 4.51 shows the change in effective mean normal stress between the different calculation phases. During compaction, the value changes significantly around the compaction centre.

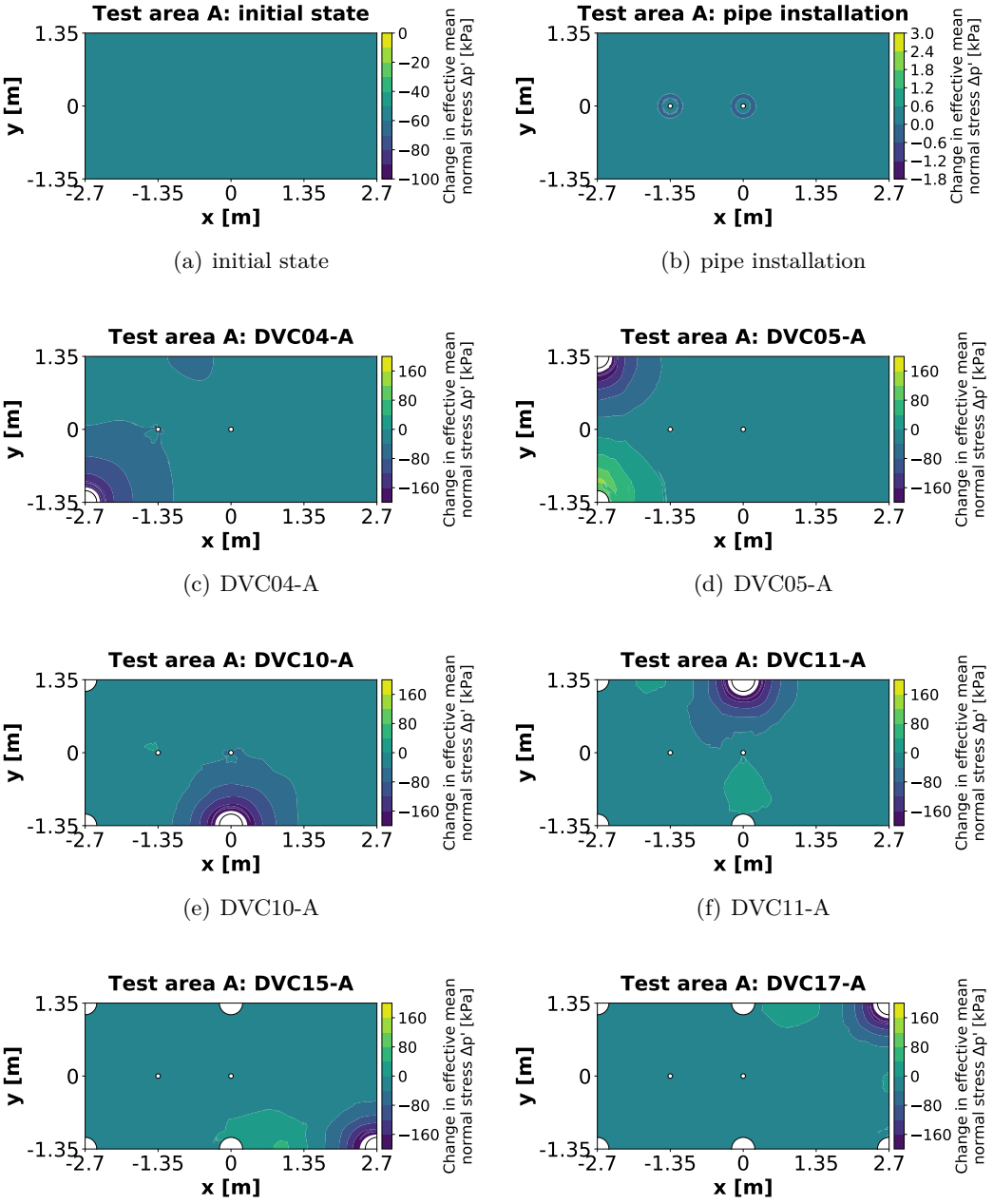

(a) initial state

(b) pipe installation

(c) DVC04-A

(d) DVC05-A

(e) DVC10-A

(f) DVC11-A

(g) DVC15-A

(h) DVC17-A

Figure 4.51: Change in effective mean normal stress test area A (approach 3)

Fig. 4.52 shows the change in deviatoric stress between the different calculation phases. During compaction, the value changes significantly around the compaction centre.

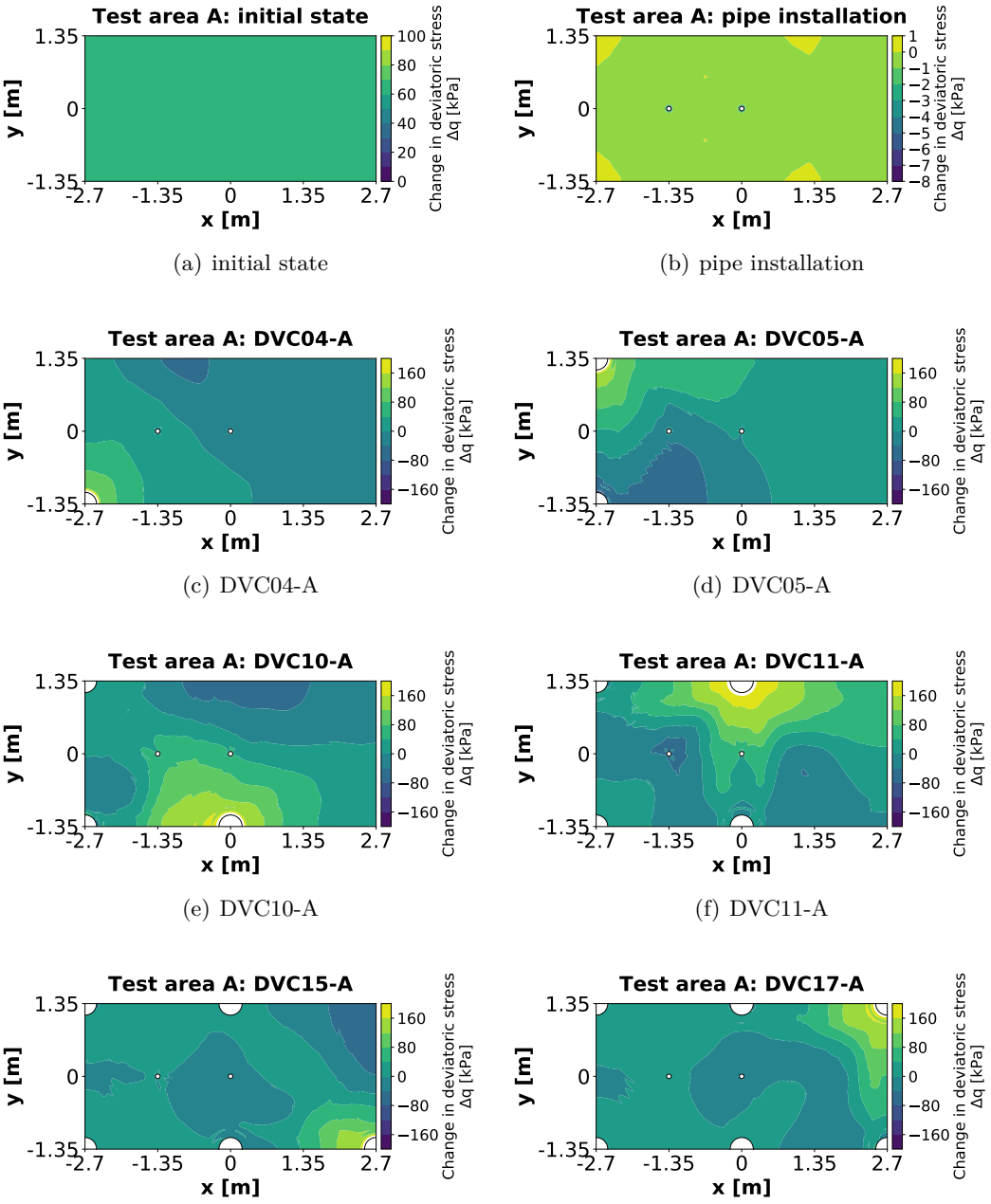

(a) initial state
(b) pipe installation
(c) DVC04-A
(d) DVC05-A
(e) DVC10-A
(f) DVC11-A
(g) DVC15-A
(h) DVC17-A

Figure 4.52: Change in deviatoric stress test area A (approach 3)

The stress paths and effective stresses in x and y direction were evaluated at stress points in all four measurement directions of the inclinometer pipes 0, 5, 15, 30 and 50 cm away from the outer mantel of the pipe. The symbols in the diagrams represent the values at the end of each calculation phase. All stress paths must start on the K_0^{nc}-line.

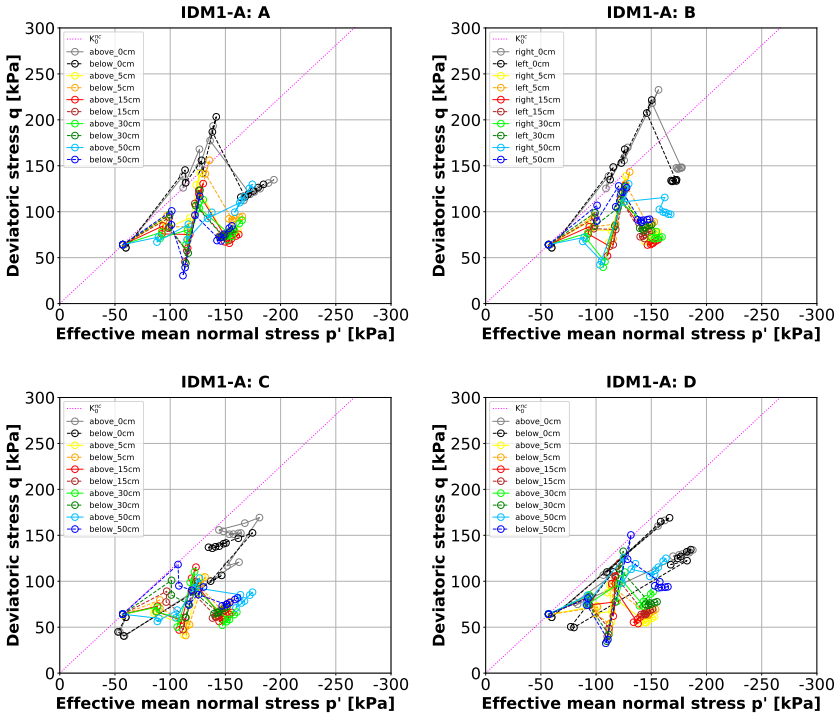

Figure 4.53: Stress paths around the inclinometer pipe IDM1-A (approach 3)

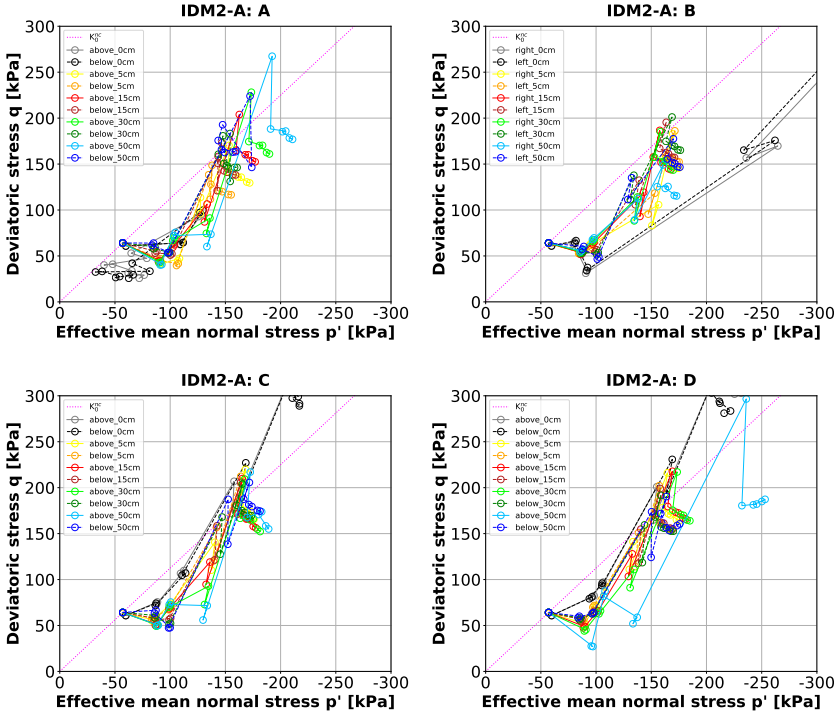

Figure 4.54: Stress paths around the inclinometer pipe IDM2-A (approach 3)

To obtain a result without pipe influence it is recommended to take the values at a specific distance from the pipe mantel. Especially the values 0 cm away from the outer mantel of the pipe deviate from the other values.

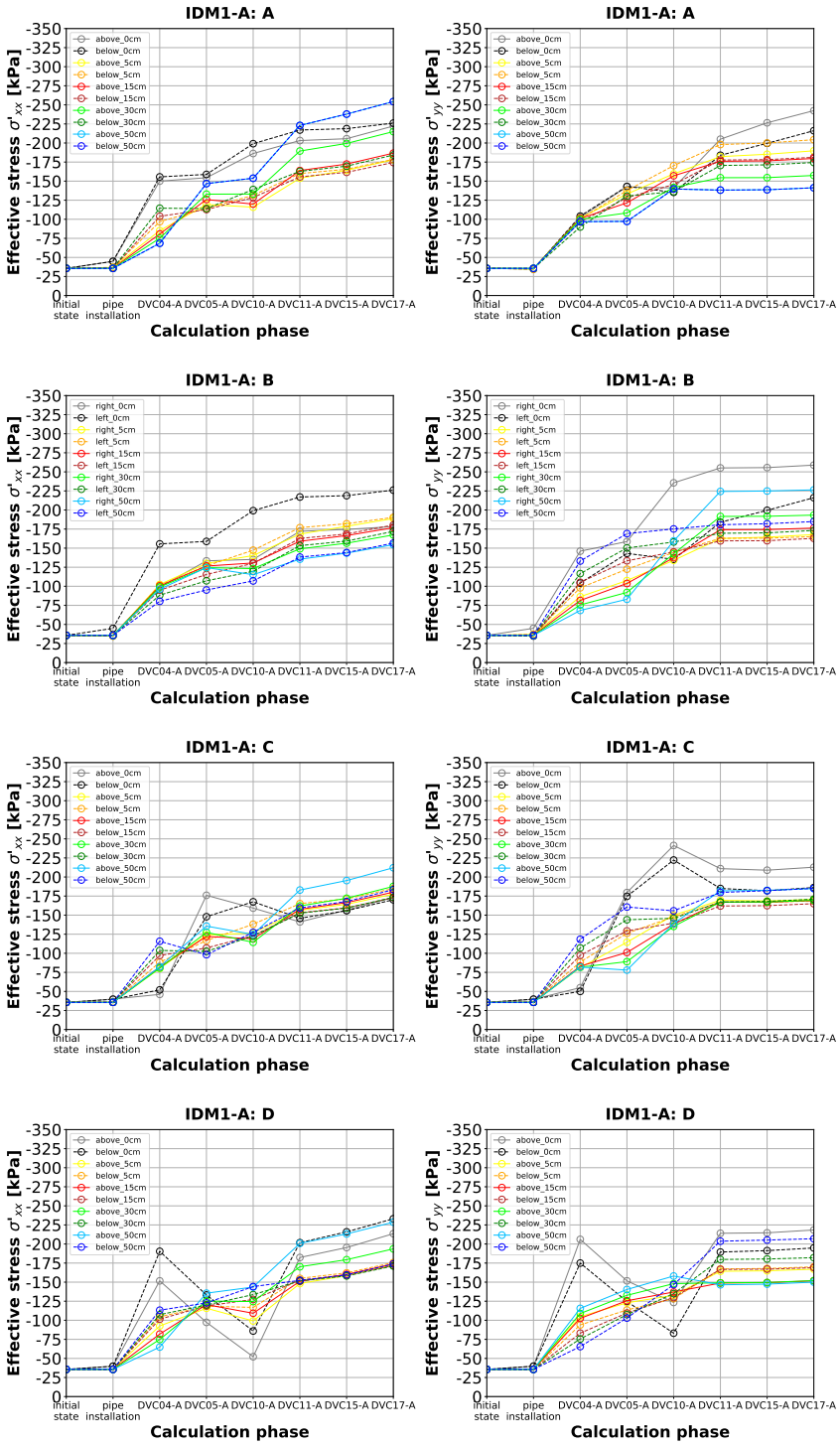

Figure 4.55: Effective stresses around the inclinometer pipe IDM1-A (approach 3)

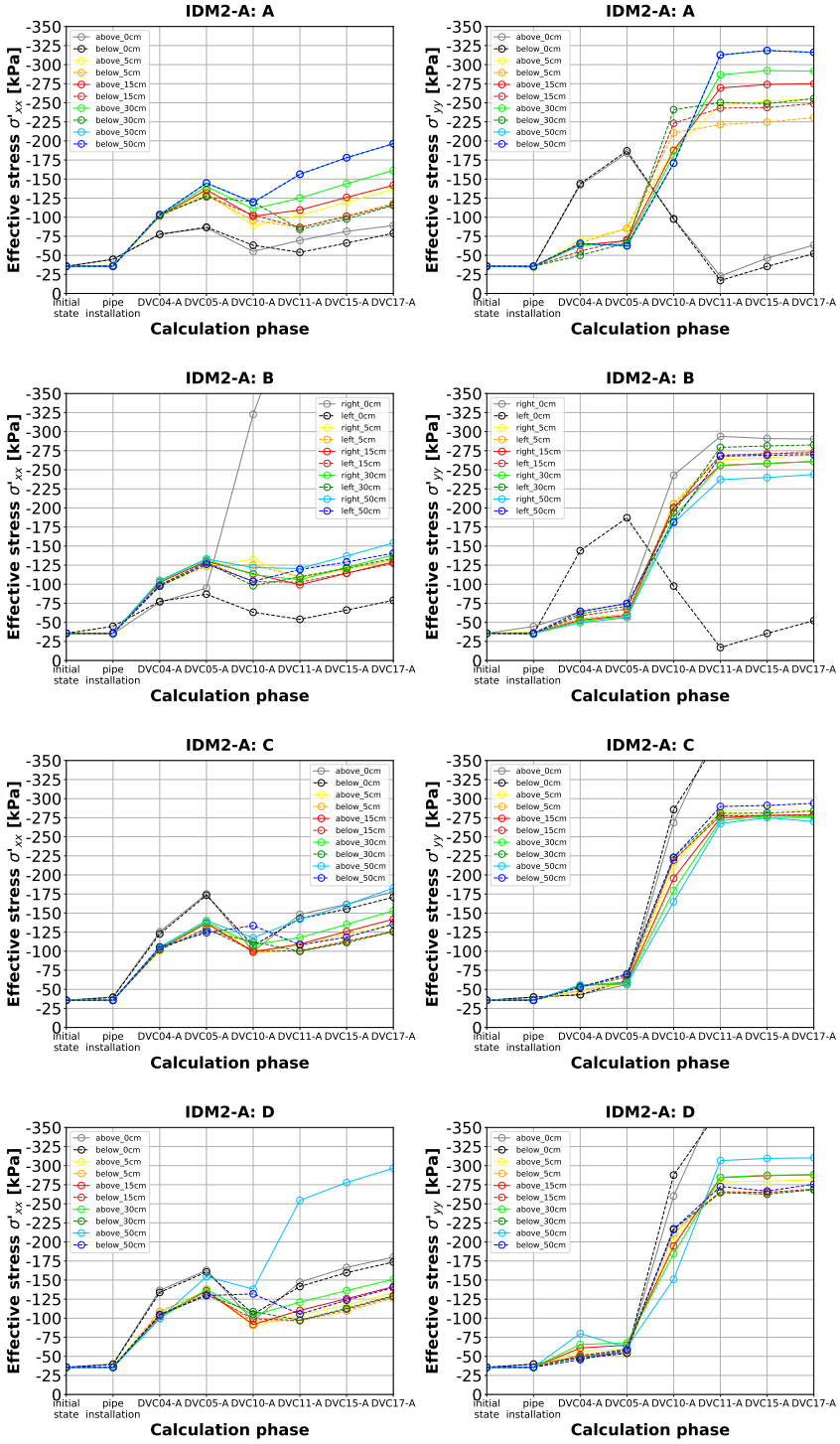

Figure 4.56: Effective stresses around the inclinometer pipe IDM2-A (approach 3)

4.2.4.2 Test area B

For all three approaches the changes in diameter and the changes in ovalization value of the inclinometer pipes, the reference oedometer modulus, the change in effective mean normal stress and the change in deviatoric stress of the soil and finally the stress paths and the effective stresses around the inclinometer pipes are shown.

Approach 1: Uniform load (loading)

The simulation result is represented by the point of intersection of the red dashed lines. The depth position of the model was specified at 242.00 müA (about 6.20 m below the ground level). In the following figures only the measurement results of epoch 0 and epoch 1 are shown. With approach 1 the pipe deformations can be simulated already qualitatively correct (see Fig. 4.57 and Fig. 4.58).

As discussed in section 3.4.1.1 only the ovalization value is free from errors affecting all diameter measurements. It is therefore neither sensible nor possible to simulate all diameter changes correctly.

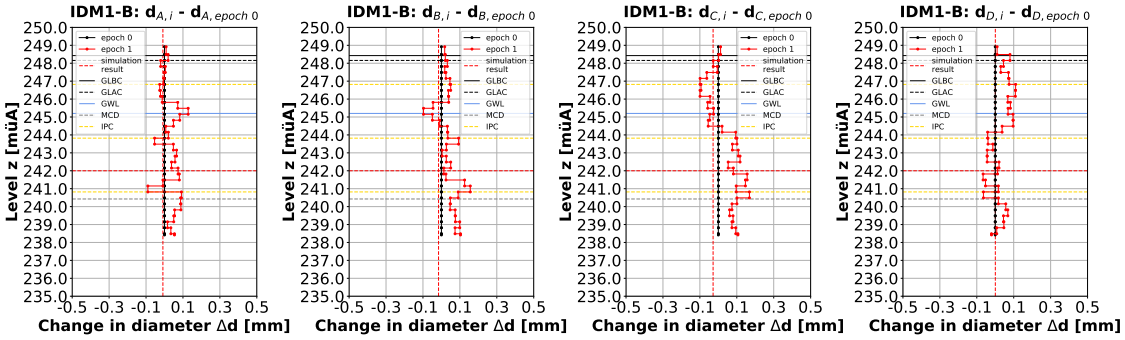

Figure 4.57: Changes in diameter of the inclinometer pipe IDM1-B - epoch 0 (approach 1)

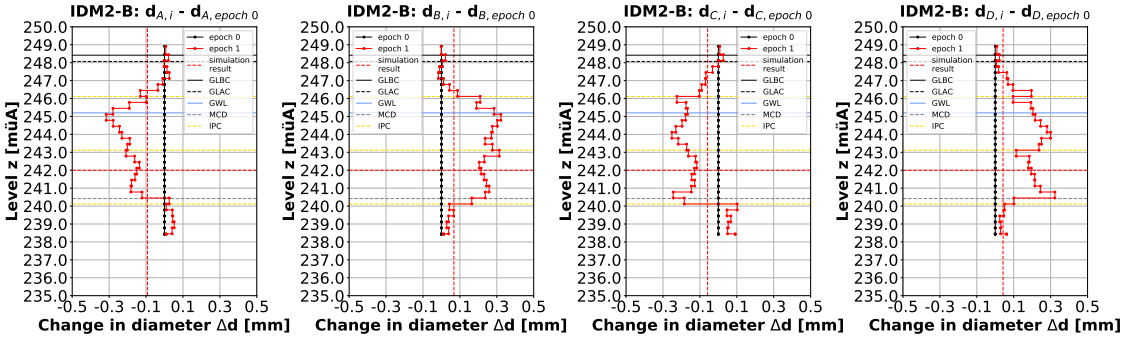

Figure 4.58: Changes in diameter of the inclinometer pipe IDM2-B - epoch 0 (approach 1)

Fig. 4.59 provides the following findings: The simulated change in ovalization value in direction AB and CD is for the inclinometer pipe IDM1-B nearly zero. This is a good agreement as the measurement result is not significant.

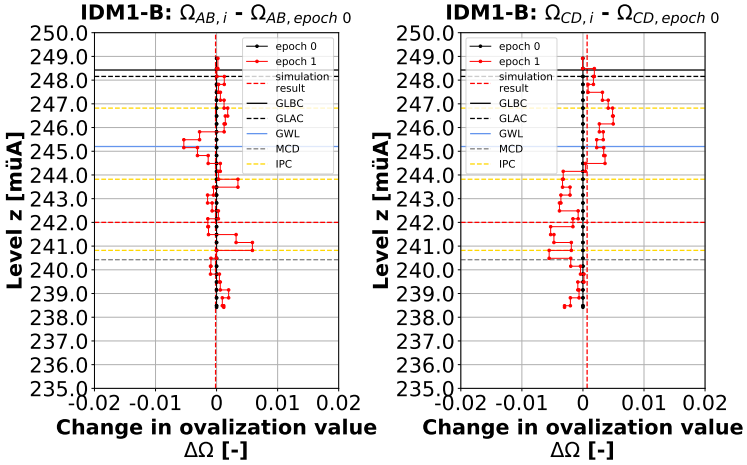

Figure 4.59: Changes in ovalization value of the inclinometer pipe IDM1-B - epoch 0 (approach 1)

Fig. 4.60 provides the following findings: For the inclinometer pipe IDM2-B the simulated change in ovalization value in direction AB and CD is obviously too small.

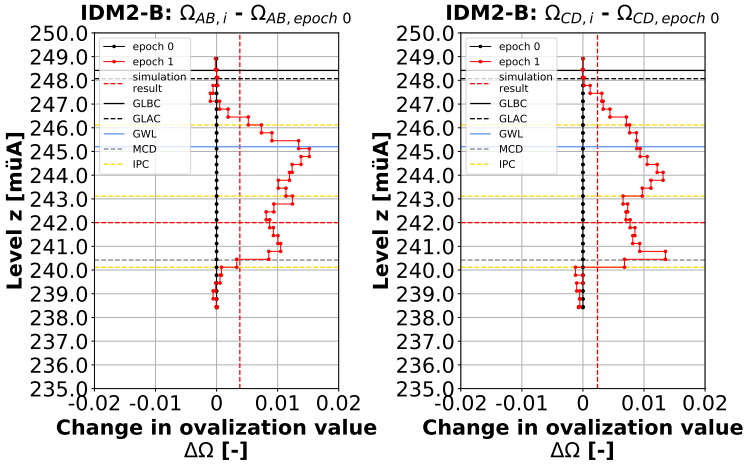

Figure 4.60: Changes in ovalization value of the inclinometer pipe IDM2-B - epoch 0 (approach 1)

Fig. 4.61 shows the reference oedometer modulus after the different calculation phases.

The hardening soil model with small-strain stiffness considers, as the name implies, the increased stiffness of soils at small strains. To calculate the reference shear modulus at very small strains based on the unloading/ reloading reference shear modulus a factor of 3 was used. In the following figures this factor is observable at areas with small strains.

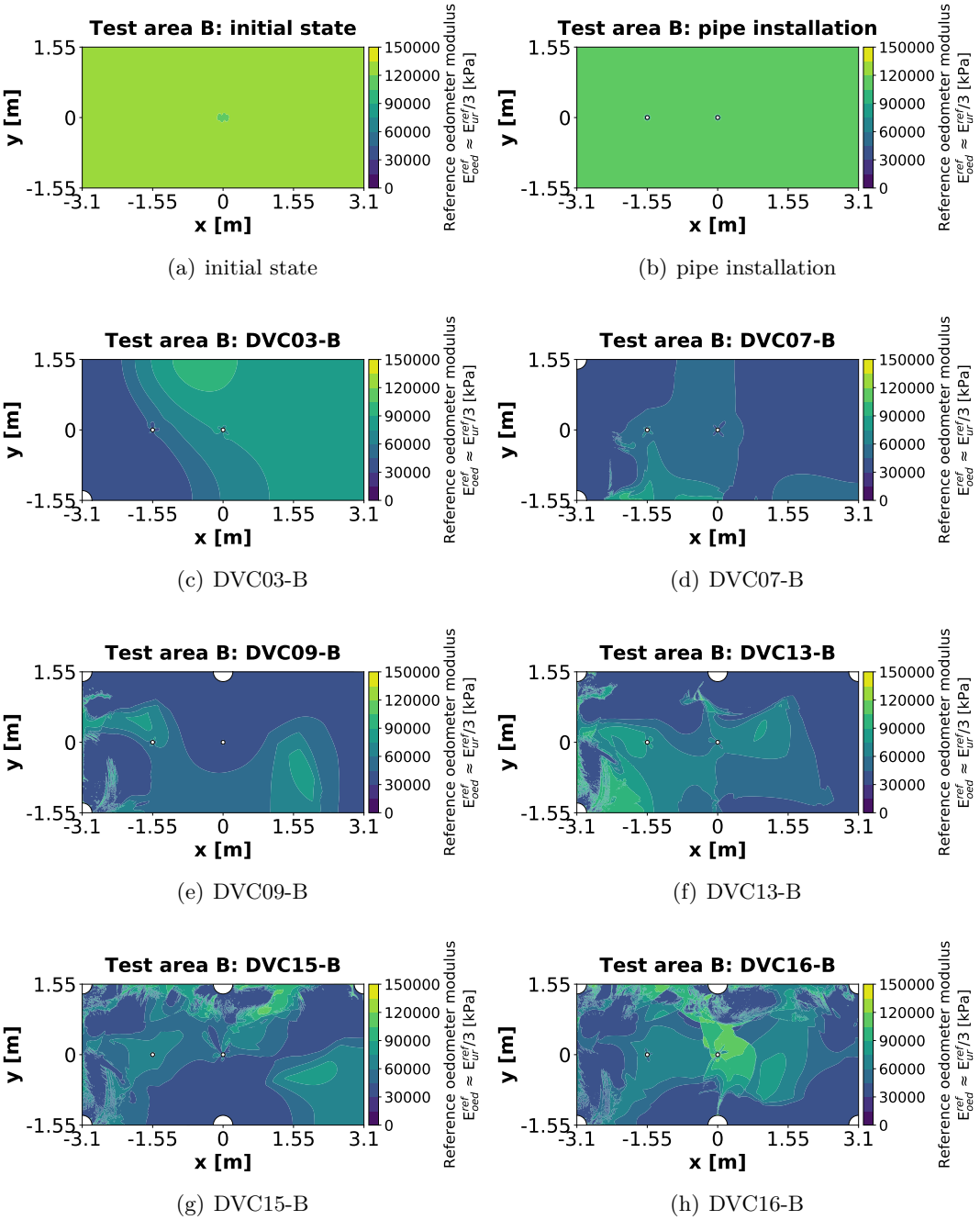

(a) initial state (b) pipe installation

(c) DVC03-B (d) DVC07-B

(e) DVC09-B (f) DVC13-B

(g) DVC15-B (h) DVC16-B

Figure 4.61: Reference oedometer modulus test area B (approach 1)

Fig. 4.62 shows the change in effective mean normal stress between the different calculation phases. During compaction, the value changes significantly around the compaction centre.

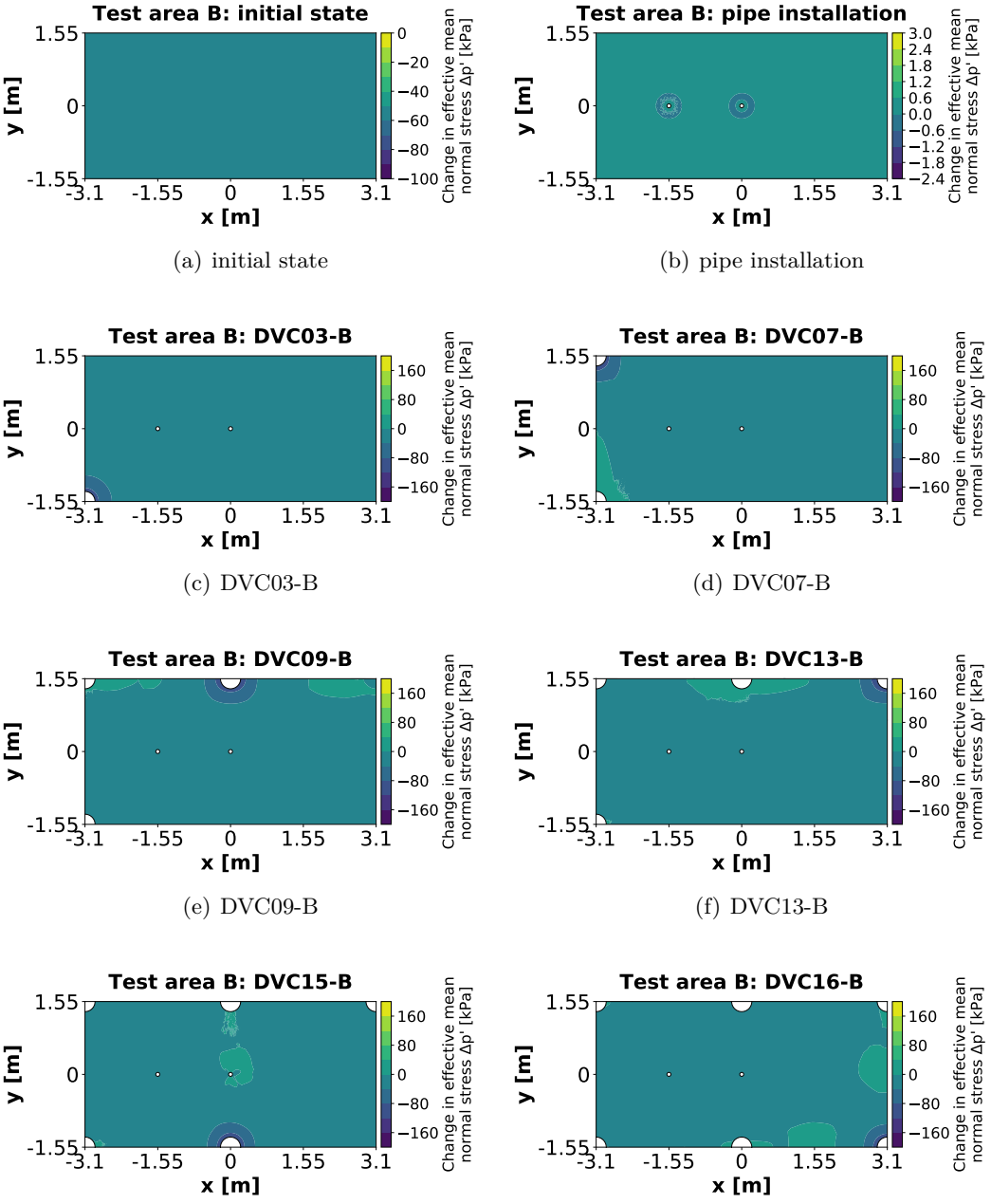

(a) initial state (b) pipe installation

(c) DVC03-B (d) DVC07-B

(e) DVC09-B (f) DVC13-B

(g) DVC15-B (h) DVC16-B

Figure 4.62: Change in effective mean normal stress test area B (approach 1)

Fig. 4.63 shows the change in deviatoric stress between the different calculation phases. During compaction, the value changes significantly around the compaction centre.

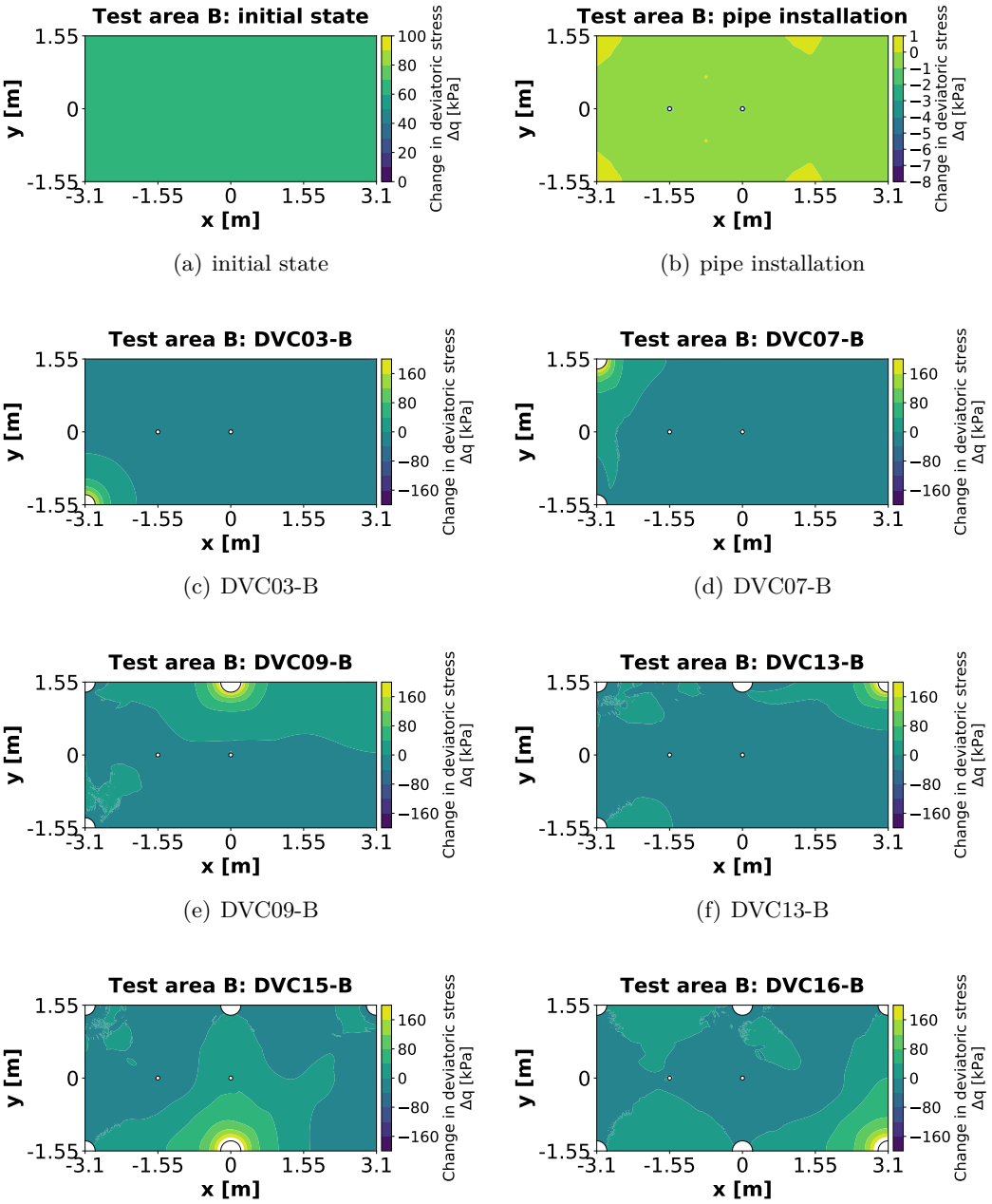

(a) initial state (b) pipe installation

(c) DVC03-B (d) DVC07-B

(e) DVC09-B (f) DVC13-B

(g) DVC15-B (h) DVC16-B

Figure 4.63: Change in deviatoric stress test area B (approach 1)

The stress paths and effective stresses in x and y direction were evaluated at stress points in all four measurement directions of the inclinometer pipes 0, 5, 15, 30 and 50 cm away from the outer mantel of the pipe. The symbols in the diagrams represent the values at the end of each calculation phase. All stress paths must start on the K_0^{nc}-line.

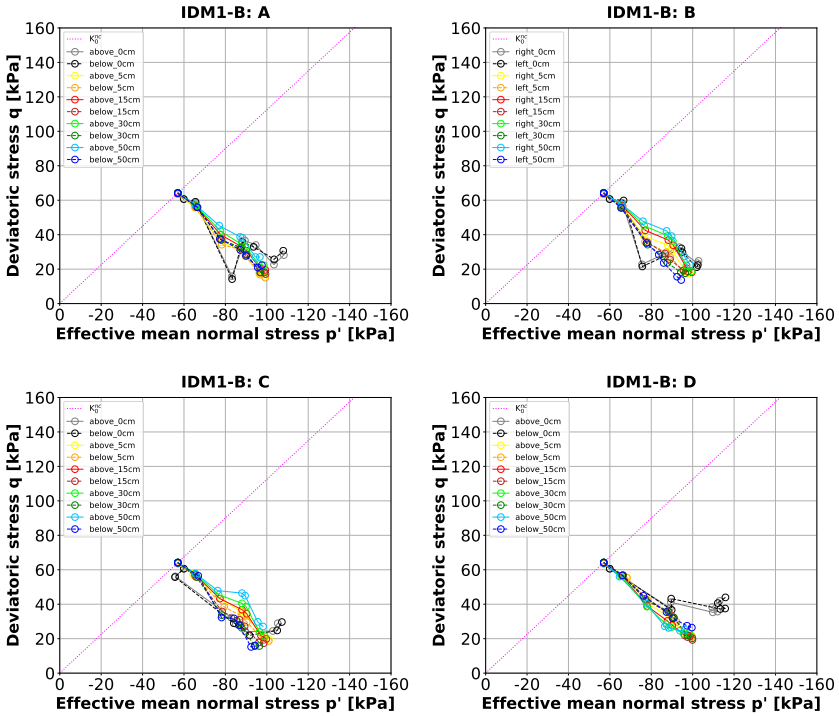

Figure 4.64: Stress paths around the inclinometer pipe IDM1-B (approach 1)

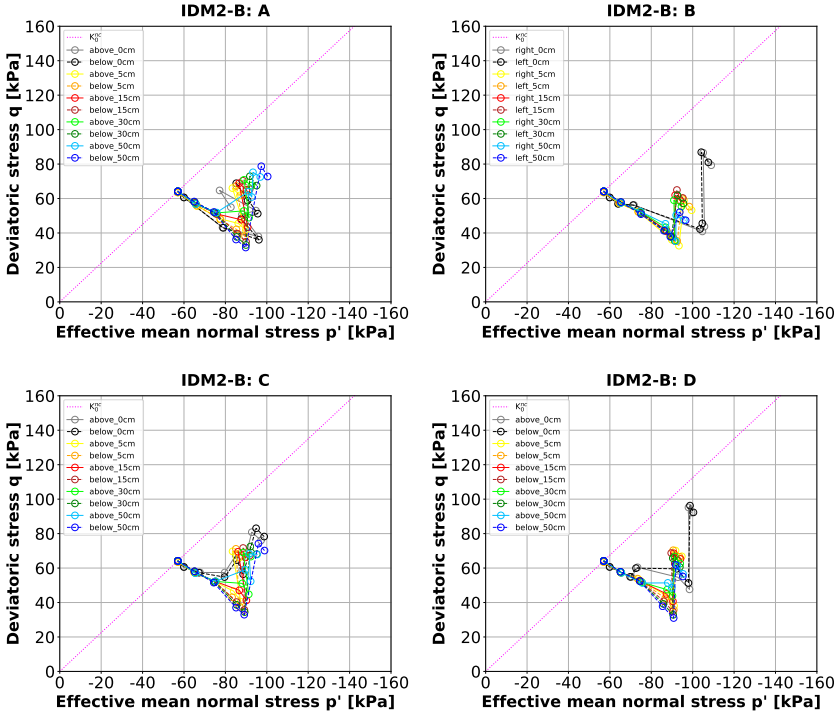

Figure 4.65: Stress paths around the inclinometer pipe IDM2-B (approach 1)

To obtain a result without pipe influence it is recommended to take the values at a specific distance from the pipe mantel. Especially the values 0 cm away from the outer mantel of the pipe deviate from the other values.

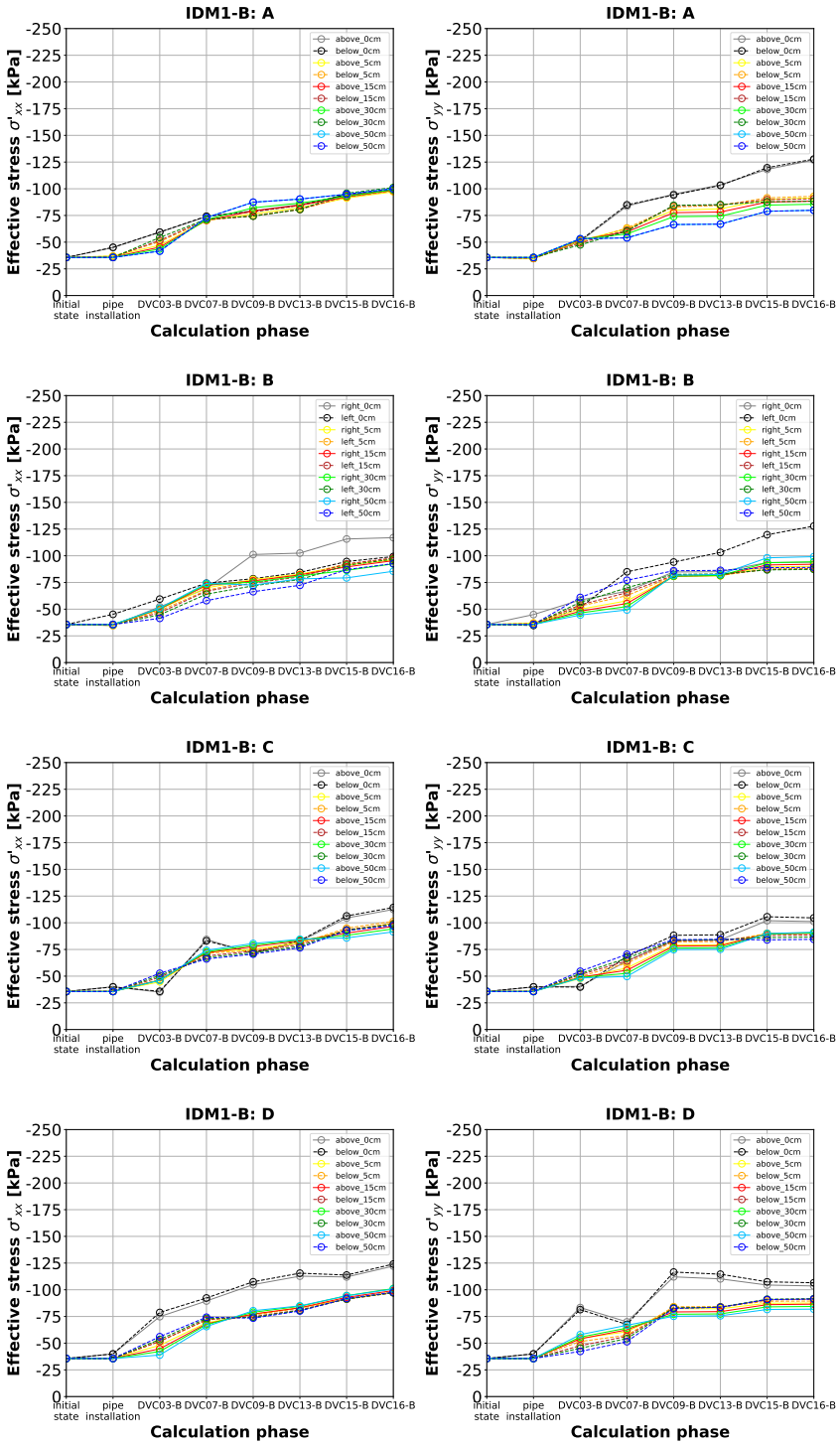

Figure 4.66: Effective stresses around the inclinometer pipe IDM1-B (approach 1)

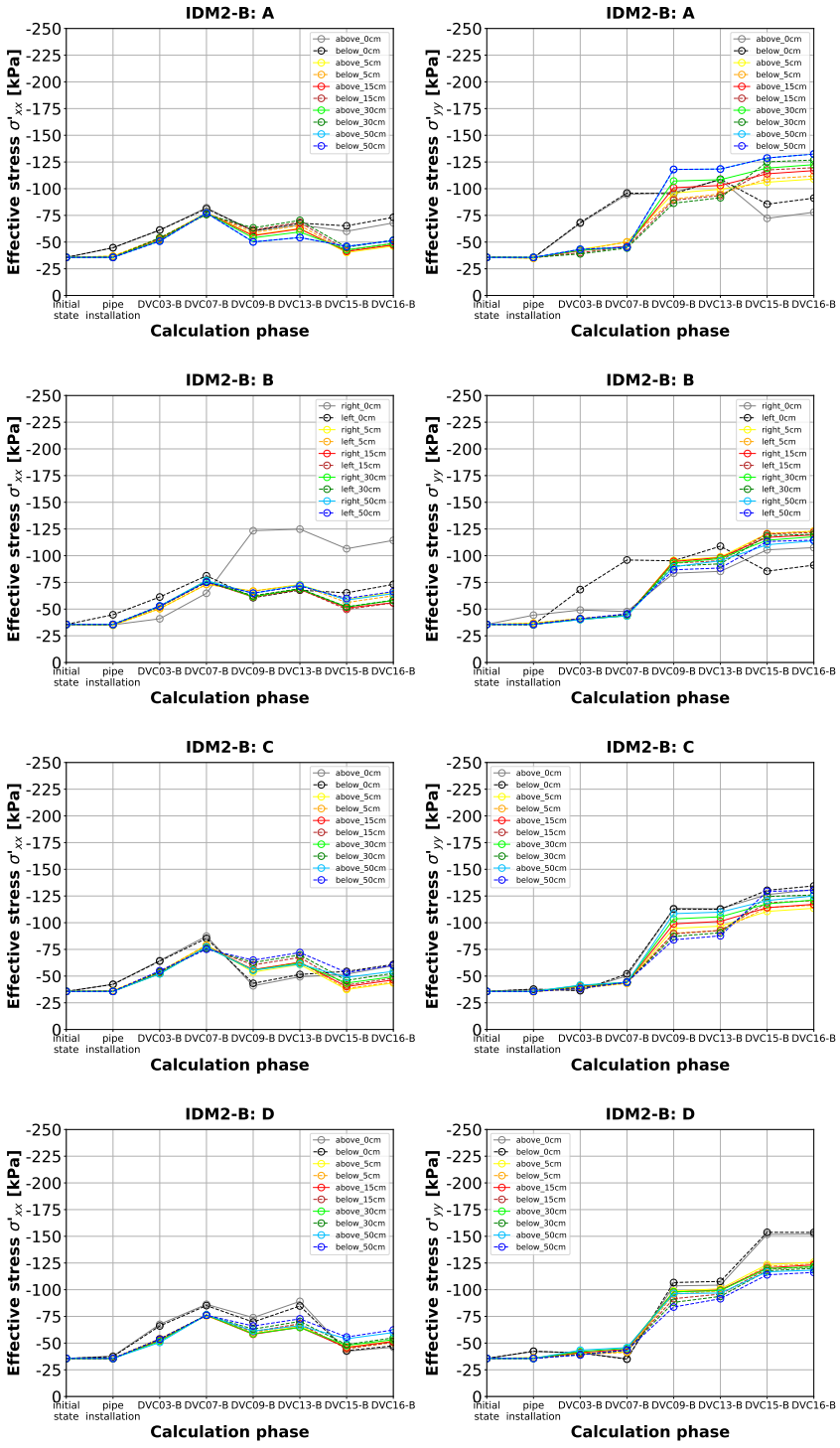

Figure 4.67: Effective stresses around the inclinometer pipe IDM2-B (approach 1)

Approach 2: Uniform load (loading + unloading)

The simulation result is represented by the point of intersection of the red dashed lines. The depth position of the model was specified at 242.00 müA (about 6.20 m below the ground level). In the following figures only the measurement results of epoch 0 and epoch 1 are shown. With approach 2 the pipe deformations can be simulated quantitatively more correct (see Fig. 4.68 and Fig. 4.69).

As discussed in section 3.4.1.1 only the ovalization value is free from errors affecting all diameter measurements. It is therefore neither sensible nor possible to simulate all diameter changes correctly.

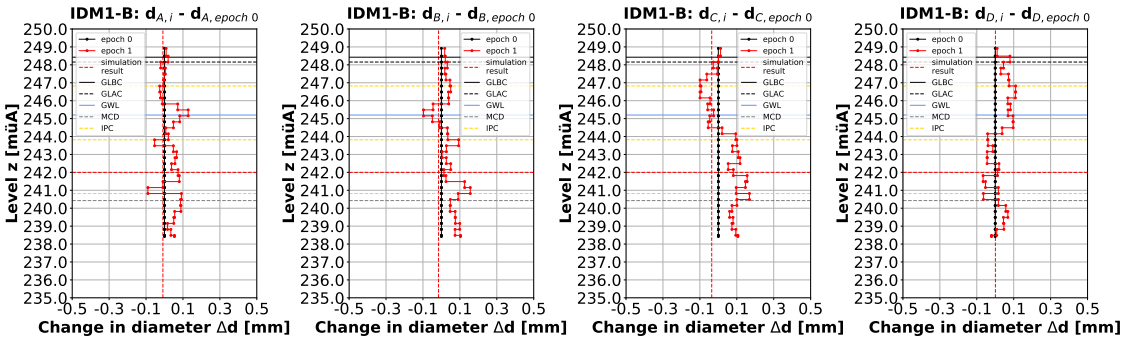

Figure 4.68: Changes in diameter of the inclinometer pipe IDM1-B - epoch 0 (approach 2)

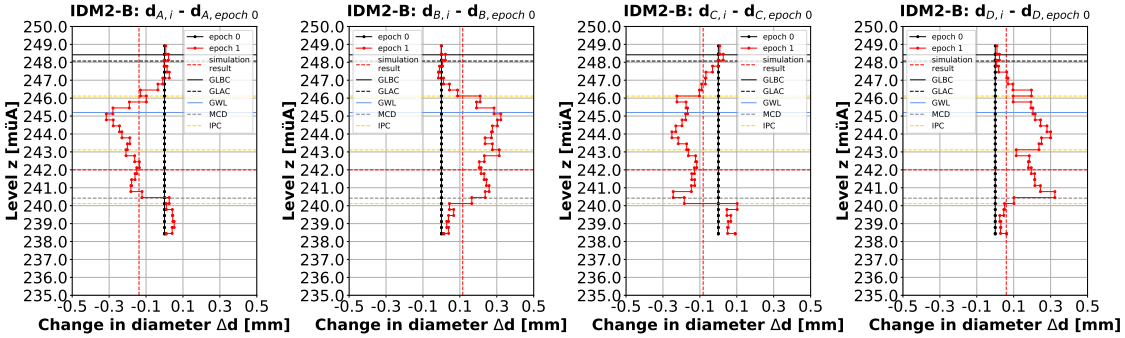

Figure 4.69: Changes in diameter of the inclinometer pipe IDM2-B - epoch 0 (approach 2)

Fig. 4.70 provides the following findings: The simulated change in ovalization value in direction AB and CD is for the inclinometer pipe IDM1-B nearly zero. This is a good agreement as the measurement result is not significant.

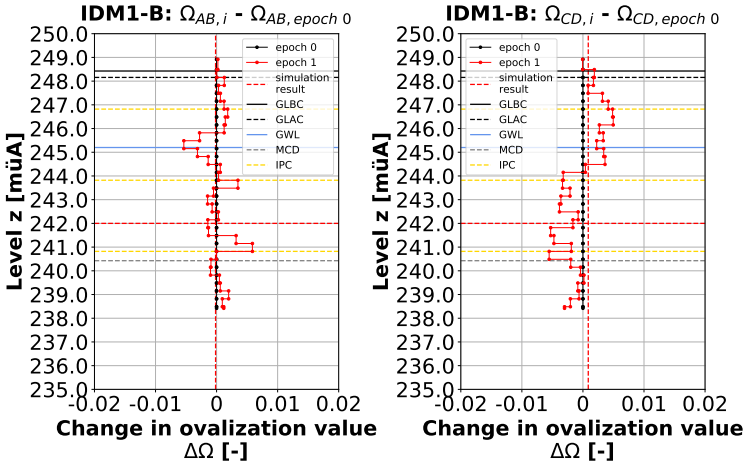

Figure 4.70: Changes in ovalization value of the inclinometer pipe IDM1-B - epoch 0 (approach 2)

Fig. 4.71 provides the following findings: For the inclinometer pipe IDM2-B the simulated change in ovalization value in direction AB and CD is obviously too small. Nevertheless, the values are bigger as shown in Fig. 4.60.

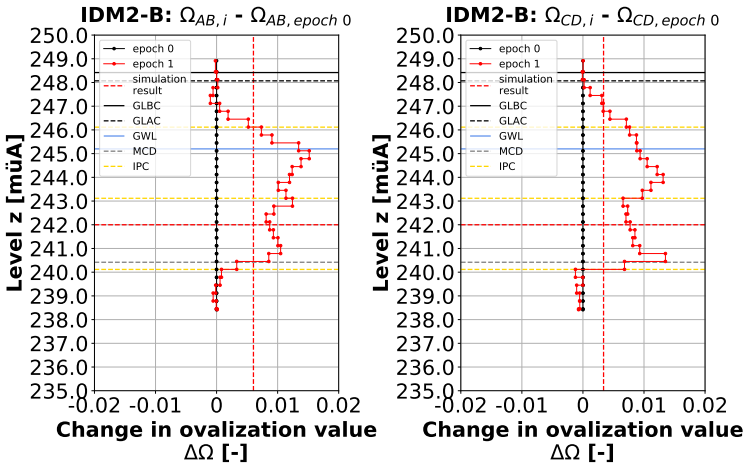

Figure 4.71: Changes in ovalization value of the inclinometer pipe IDM2-B - epoch 0 (approach 2)

Fig. 4.72 shows the reference oedometer modulus after the different calculation phases.

The hardening soil model with small-strain stiffness considers, as the name implies, the increased stiffness of soils at small strains. To calculate the reference shear modulus at very small strains based on the unloading/ reloading reference shear modulus a factor of 3 was used. In the following figures this factor is observable at areas with small strains.

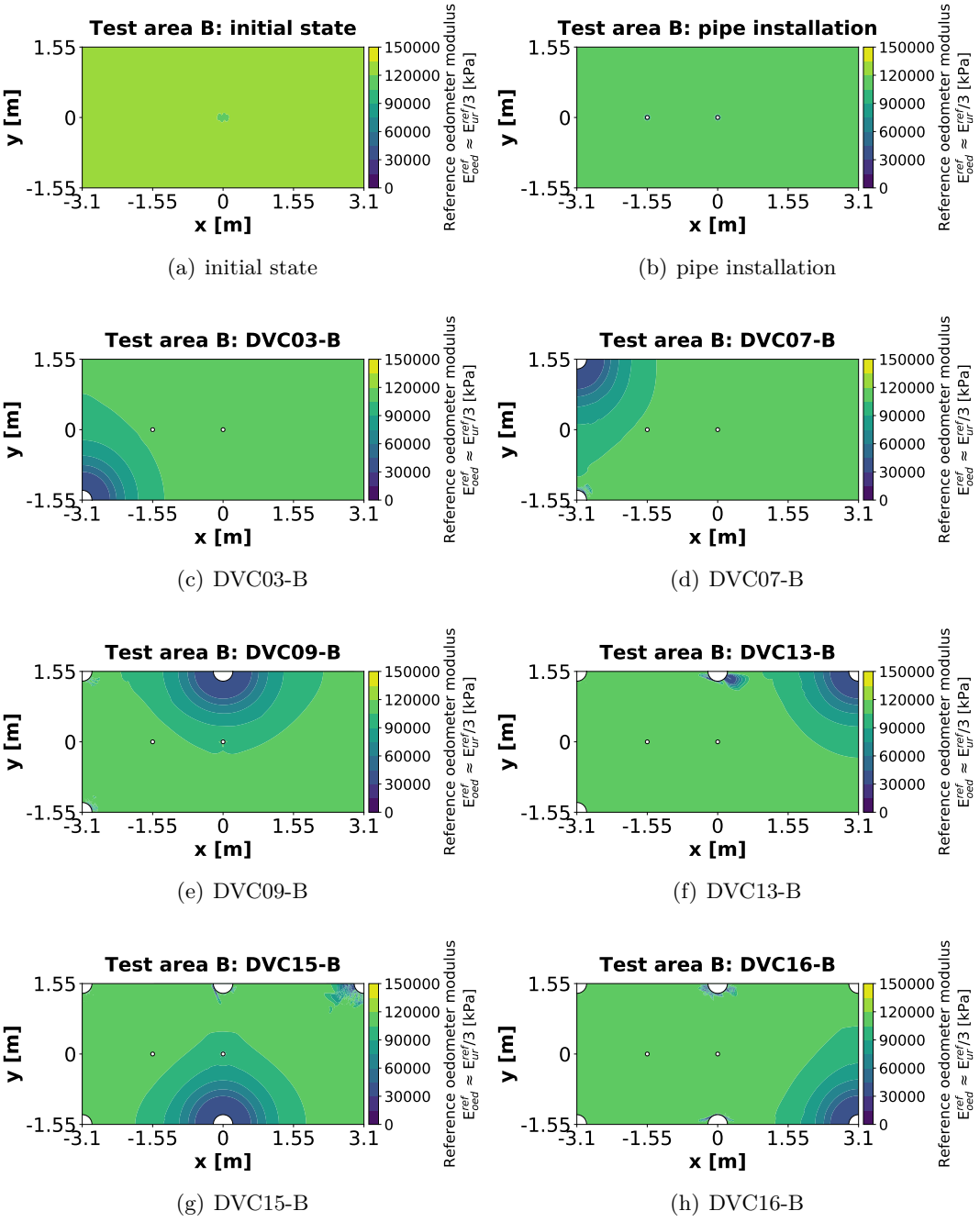

(a) initial state (b) pipe installation

(c) DVC03-B (d) DVC07-B

(e) DVC09-B (f) DVC13-B

(g) DVC15-B (h) DVC16-B

Figure 4.72: Reference oedometer modulus test area B (approach 2)

Fig. 4.73 shows the change in effective mean normal stress between the different calculation phases. During compaction, the value changes significantly around the compaction centre.

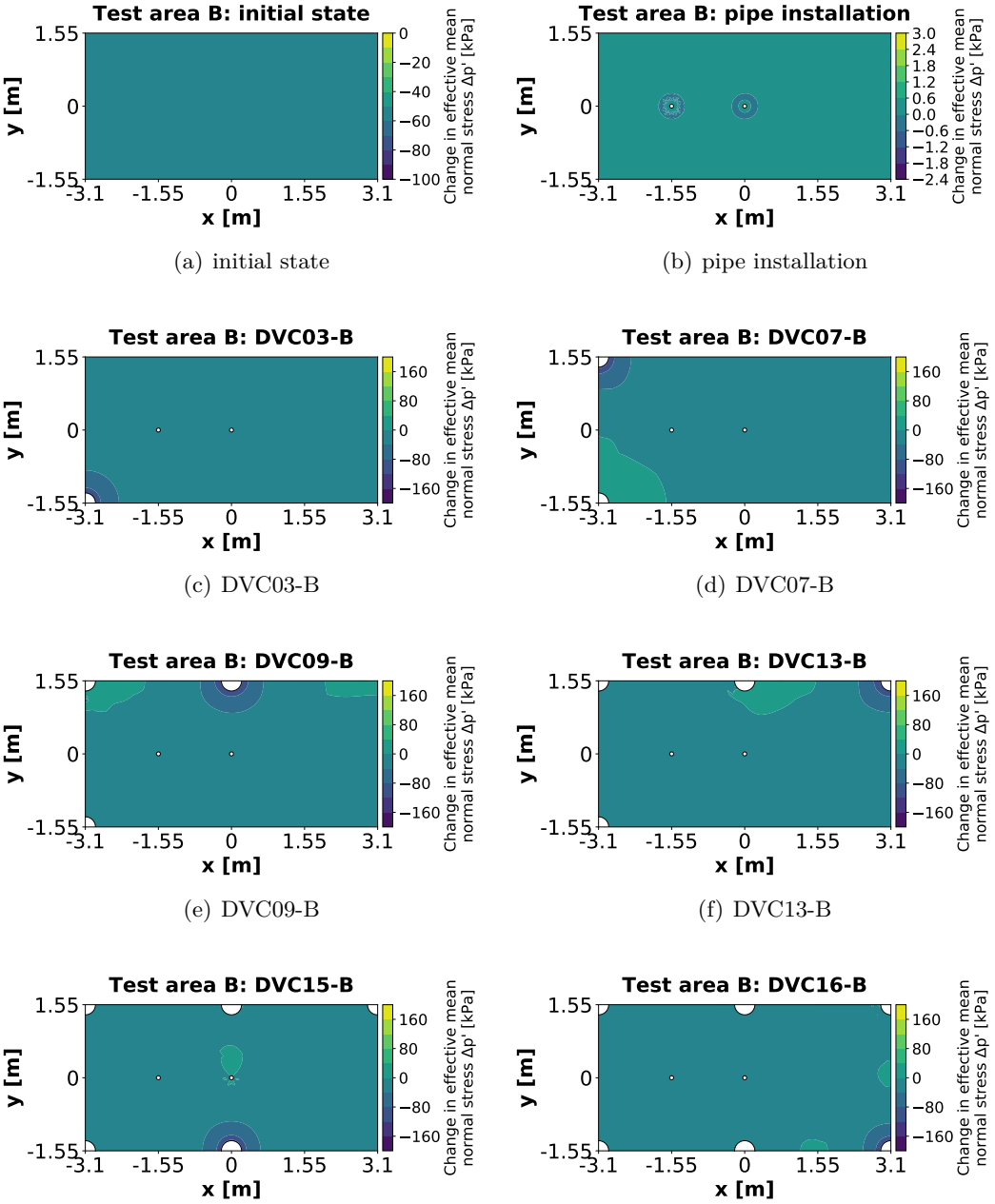

(a) initial state (b) pipe installation

(c) DVC03-B (d) DVC07-B

(e) DVC09-B (f) DVC13-B

(g) DVC15-B (h) DVC16-B

Figure 4.73: Change in effective mean normal stress test area B (approach 2)

Fig. 4.74 shows the change in deviatoric stress between the different calculation phases. During compaction, the value changes significantly around the compaction centre.

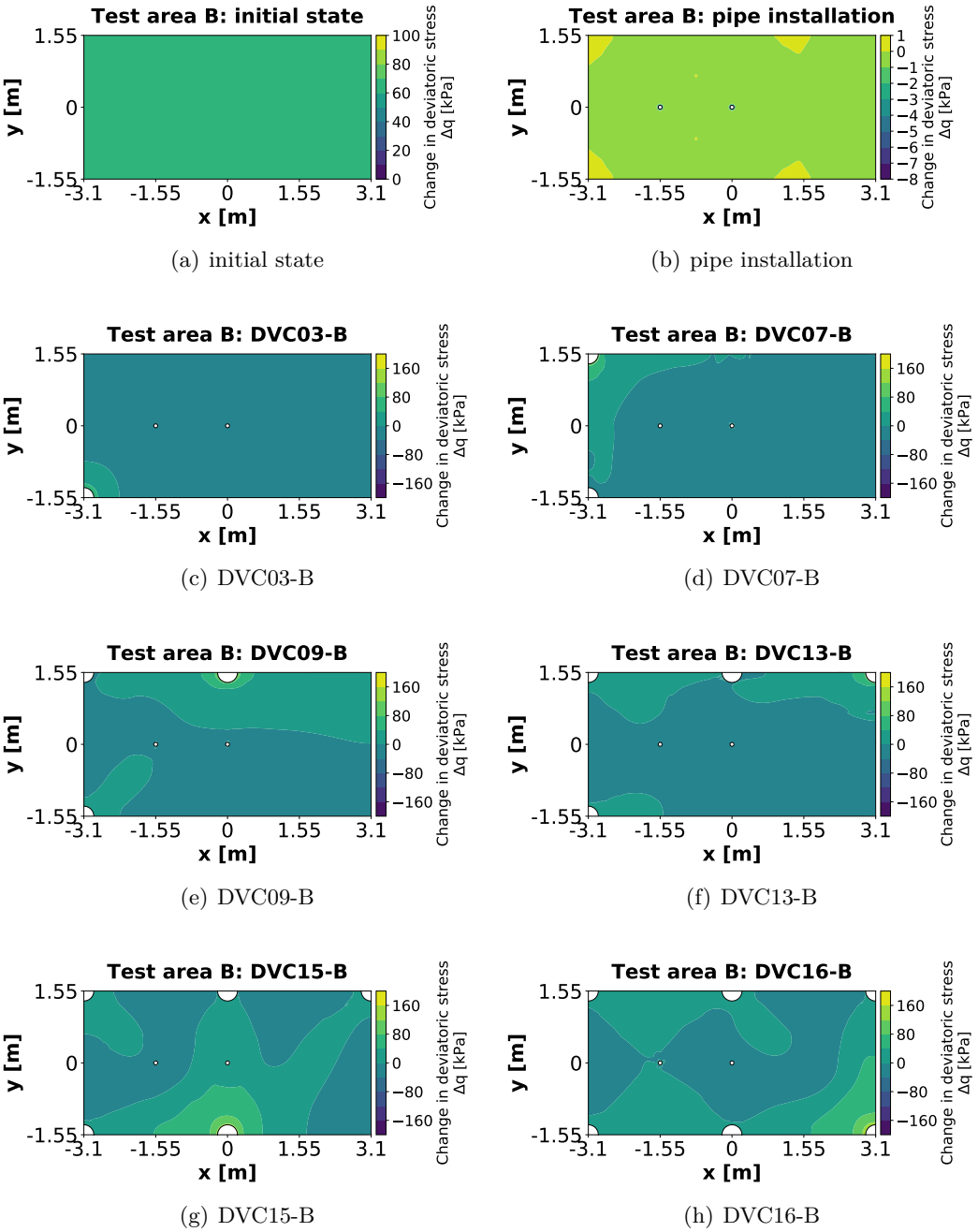

(a) initial state (b) pipe installation

(c) DVC03-B (d) DVC07-B

(e) DVC09-B (f) DVC13-B

(g) DVC15-B (h) DVC16-B

Figure 4.74: Change in deviatoric stress test area B (approach 2)

The stress paths and effective stresses in x and y direction were evaluated at stress points in all four measurement directions of the inclinometer pipes 0, 5, 15, 30 and 50 cm away from the outer mantel of the pipe. The symbols in the diagrams represent the values at the end of each calculation phase. All stress paths must start on the K_0^{nc}-line.

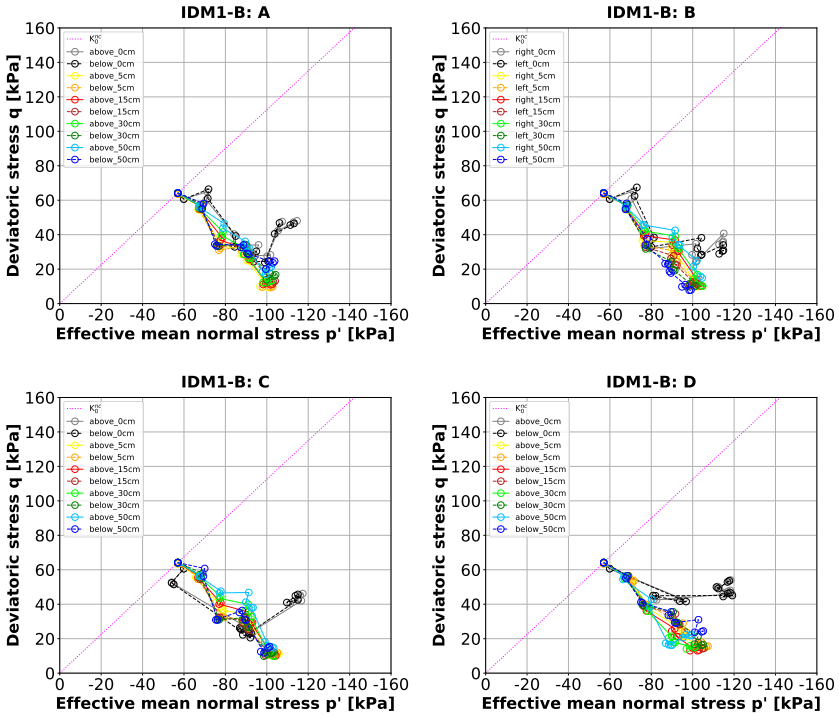

Figure 4.75: Stress paths around the inclinometer pipe IDM1-B (approach 2)

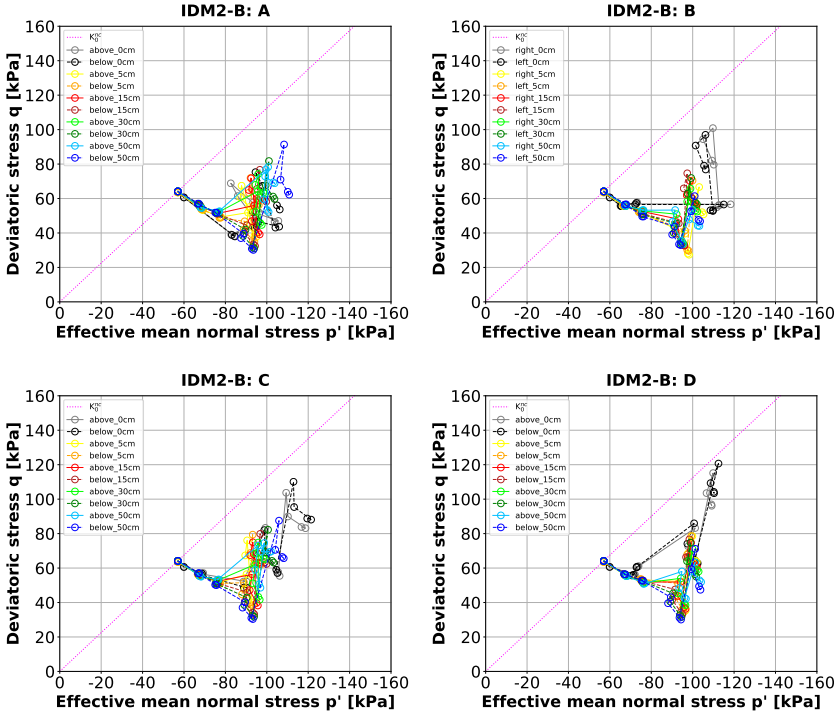

Figure 4.76: Stress paths around the inclinometer pipe IDM2-B (approach 2)

To obtain a result without pipe influence it is recommended to take the values at a specific distance from the pipe mantel. Especially the values 0 cm away from the outer mantel of the pipe deviate from the other values.

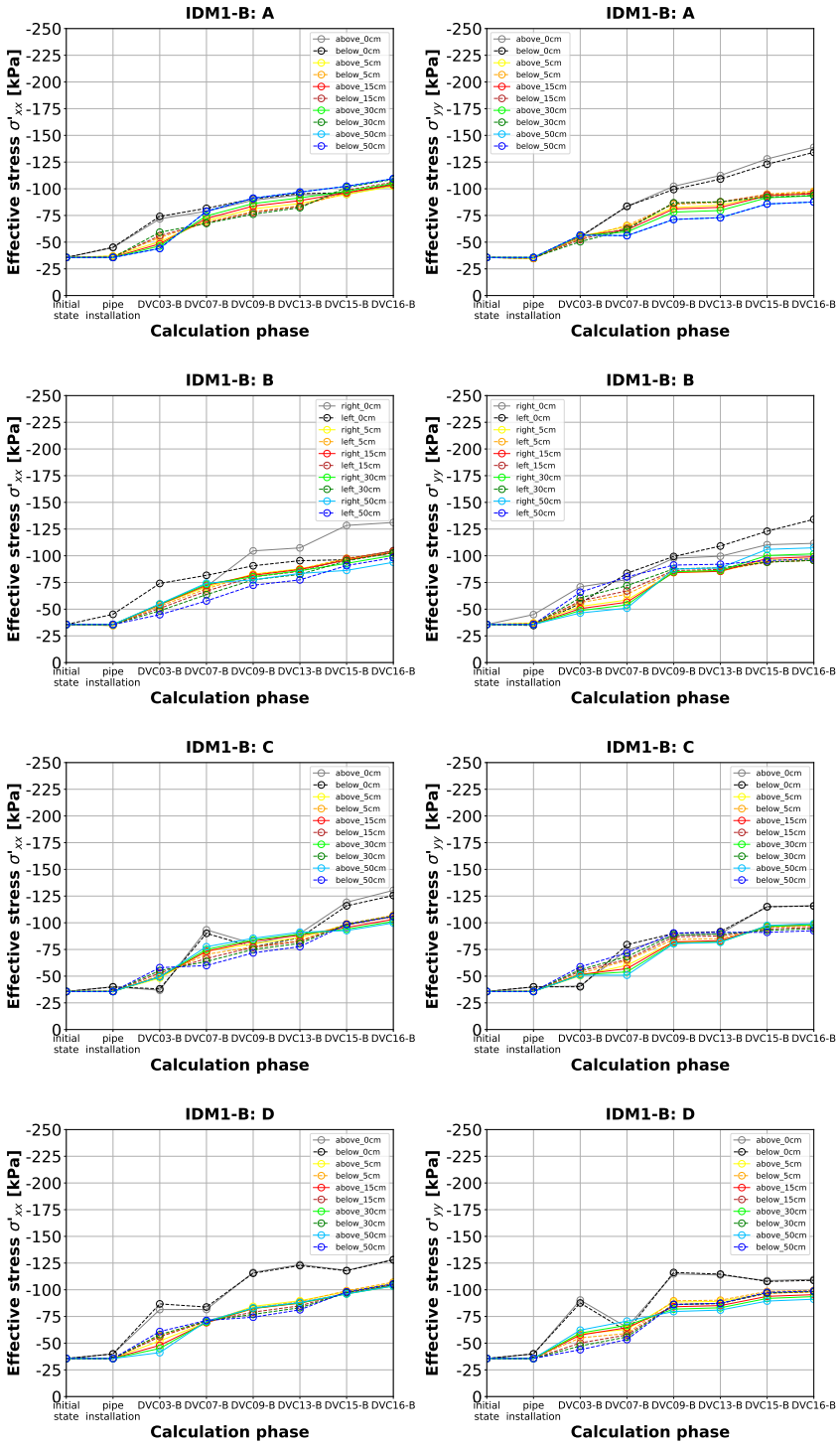

Figure 4.77: Effective stresses around the inclinometer pipe IDM1-B (approach 2)

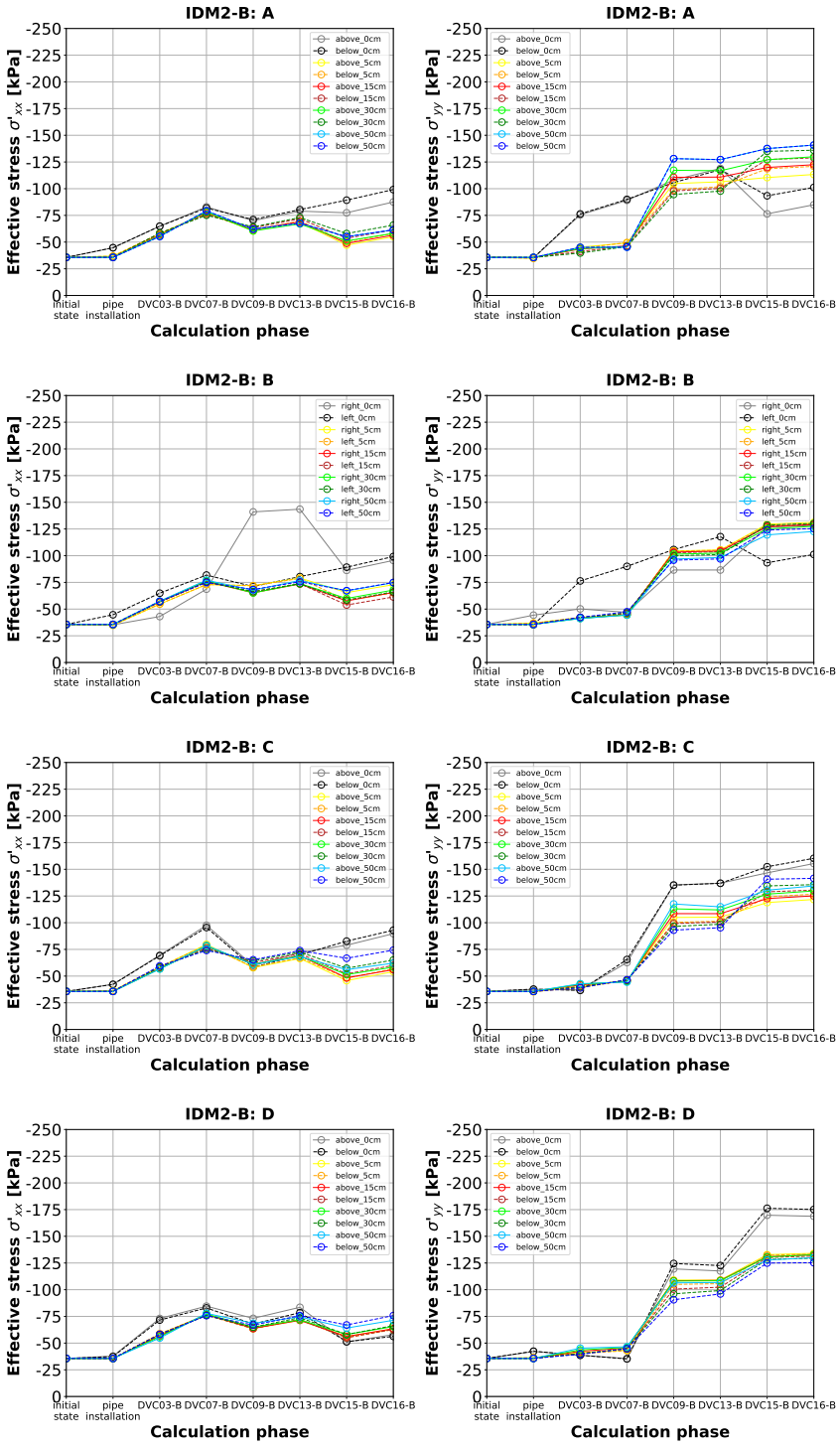

Figure 4.78: Effective stresses around the inclinometer pipe IDM2-B (approach 2)

Approach 3: Uniform load (loading + unloading) + rings with modified stiffness

The simulation result is represented by the point of intersection of the red dashed lines. The depth position of the model was specified at 242.00 müA (about 6.20 m below the ground level). In the following figures only the measurement results of epoch 0 and epoch 1 are shown. With approach 3 the pipe deformations can be simulated qualitatively and quantitatively almost correct (see Fig. 4.79 and Fig. 4.80).

As discussed in section 3.4.1.1 only the ovalization value is free from errors affecting all diameter measurements. It is therefore neither sensible nor possible to simulate all diameter changes correctly.

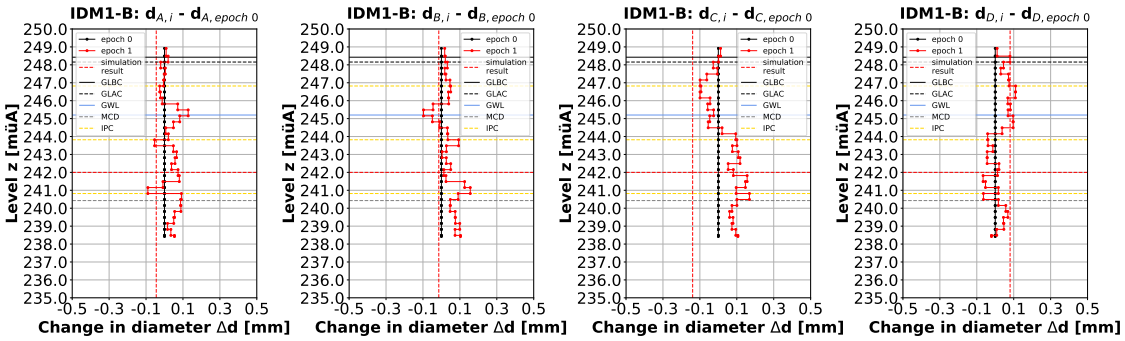

Figure 4.79: Changes in diameter of the inclinometer pipe IDM1-B - epoch 0 (approach 3)

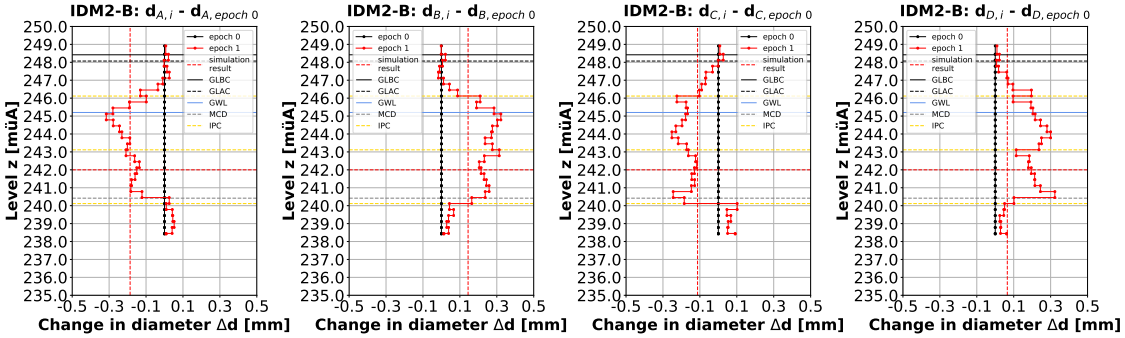

Figure 4.80: Changes in diameter of the inclinometer pipe IDM2-B - epoch 0 (approach 3)

Fig. 4.81 provides the following findings: The simulated change in ovalization value in direction AB is for the inclinometer pipe IDM1-B nearly zero. This is a good agreement as the measurement result is not significant. The judgement of the simulated change in ovalization value in direction CD is difficult due to the sign change of the measurement results at the second pipe connection.

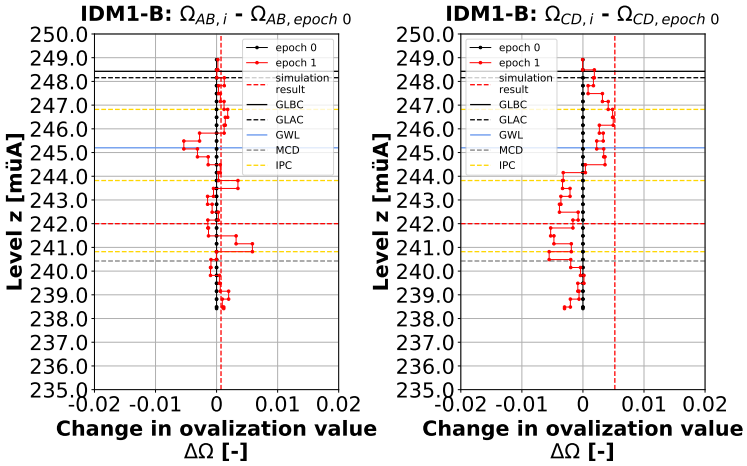

Figure 4.81: Changes in ovalization value of the inclinometer pipe IDM1-B - epoch 0 (approach 3)

Fig. 4.82 provides the following findings: For the inclinometer pipe IDM2-B the simulated change in ovalization value in direction AB and CD is almost correct. The values are much bigger as shown in Fig. 4.71.

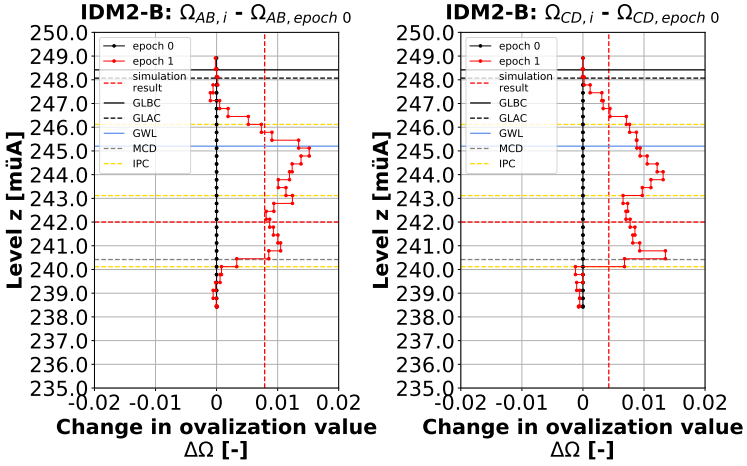

Figure 4.82: Changes in ovalization value of the inclinometer pipe IDM2-B - epoch 0 (approach 3)

Fig. 4.83 shows the reference oedometer modulus after the different calculation phases.

The hardening soil model with small-strain stiffness considers, as the name implies, the increased stiffness of soils at small strains. To calculate the reference shear modulus at very small strains based on the unloading/ reloading reference shear modulus a factor of 3 was used. In the following figures this factor is observable at areas with small strains.

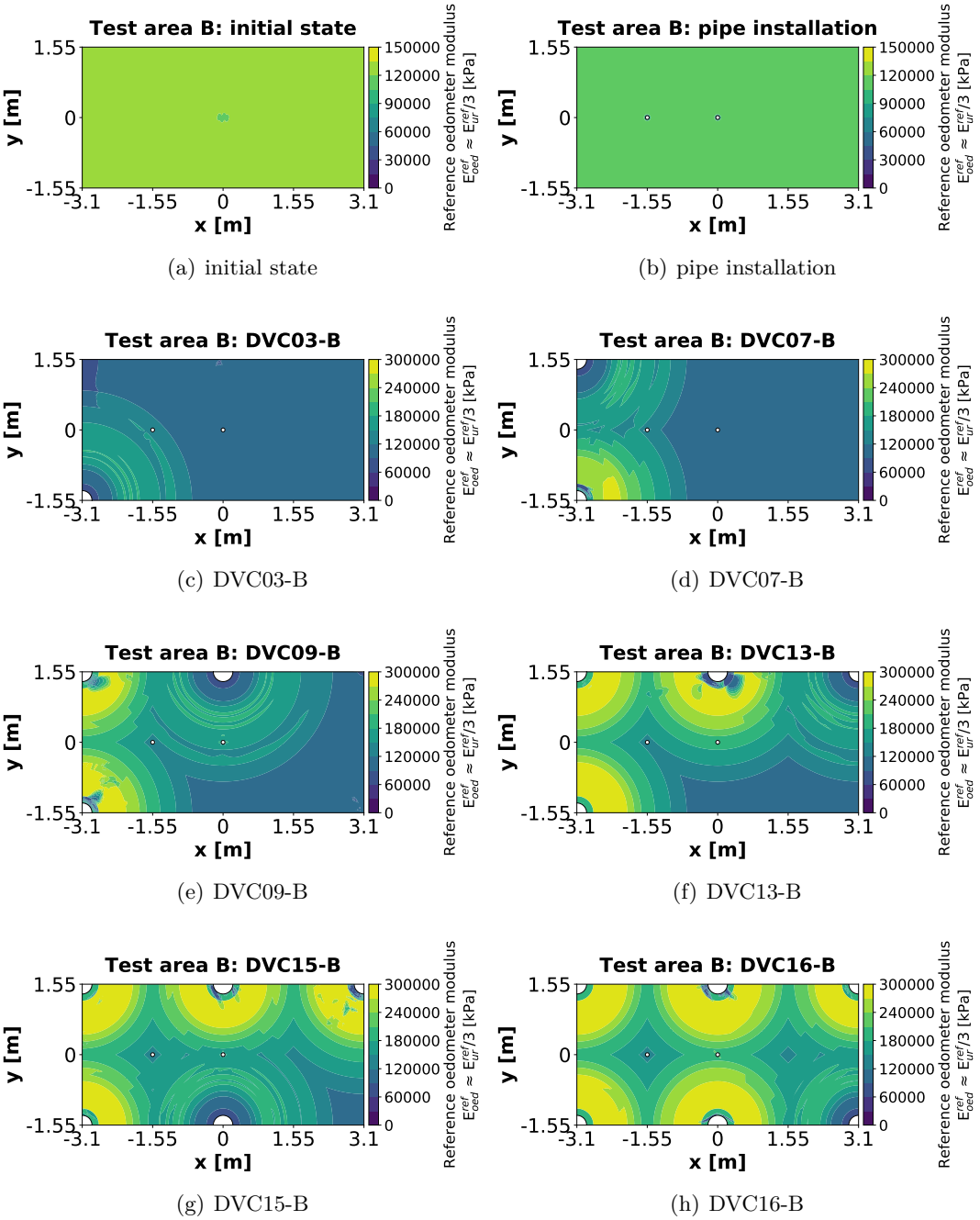

(a) initial state (b) pipe installation

(c) DVC03-B (d) DVC07-B

(e) DVC09-B (f) DVC13-B

(g) DVC15-B (h) DVC16-B

Figure 4.83: Reference oedometer modulus test area B (approach 3)

Fig. 4.84 shows the change in effective mean normal stress between the different calculation phases. During compaction, the value changes significantly around the compaction centre.

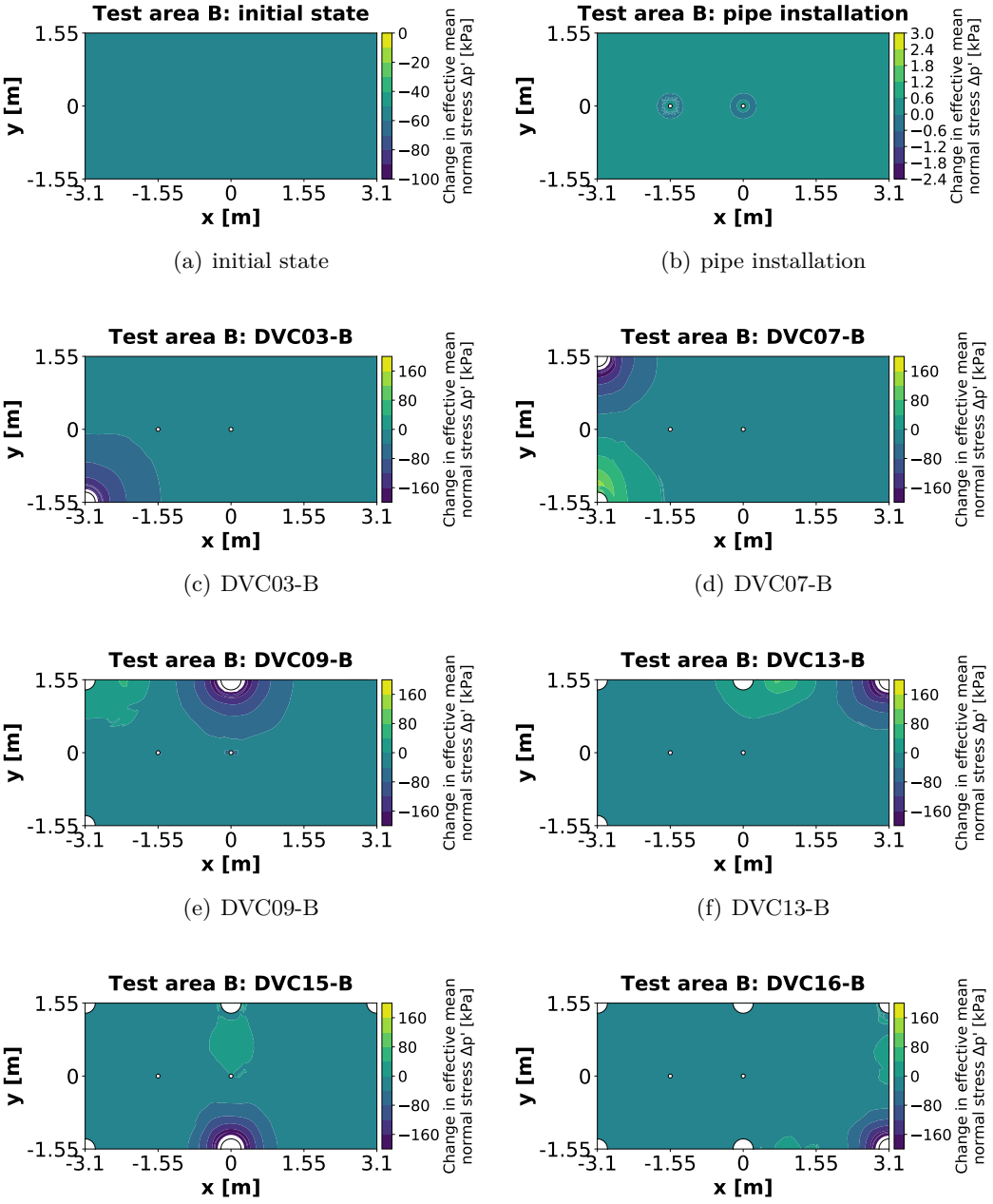

(a) initial state (b) pipe installation

(c) DVC03-B (d) DVC07-B

(e) DVC09-B (f) DVC13-B

(g) DVC15-B (h) DVC16-B

Figure 4.84: Change in effective mean normal stress test area B (approach 3)

Fig. 4.85 shows the change in deviatoric stress between the different calculation phases. During compaction, the value changes significantly around the compaction centre.

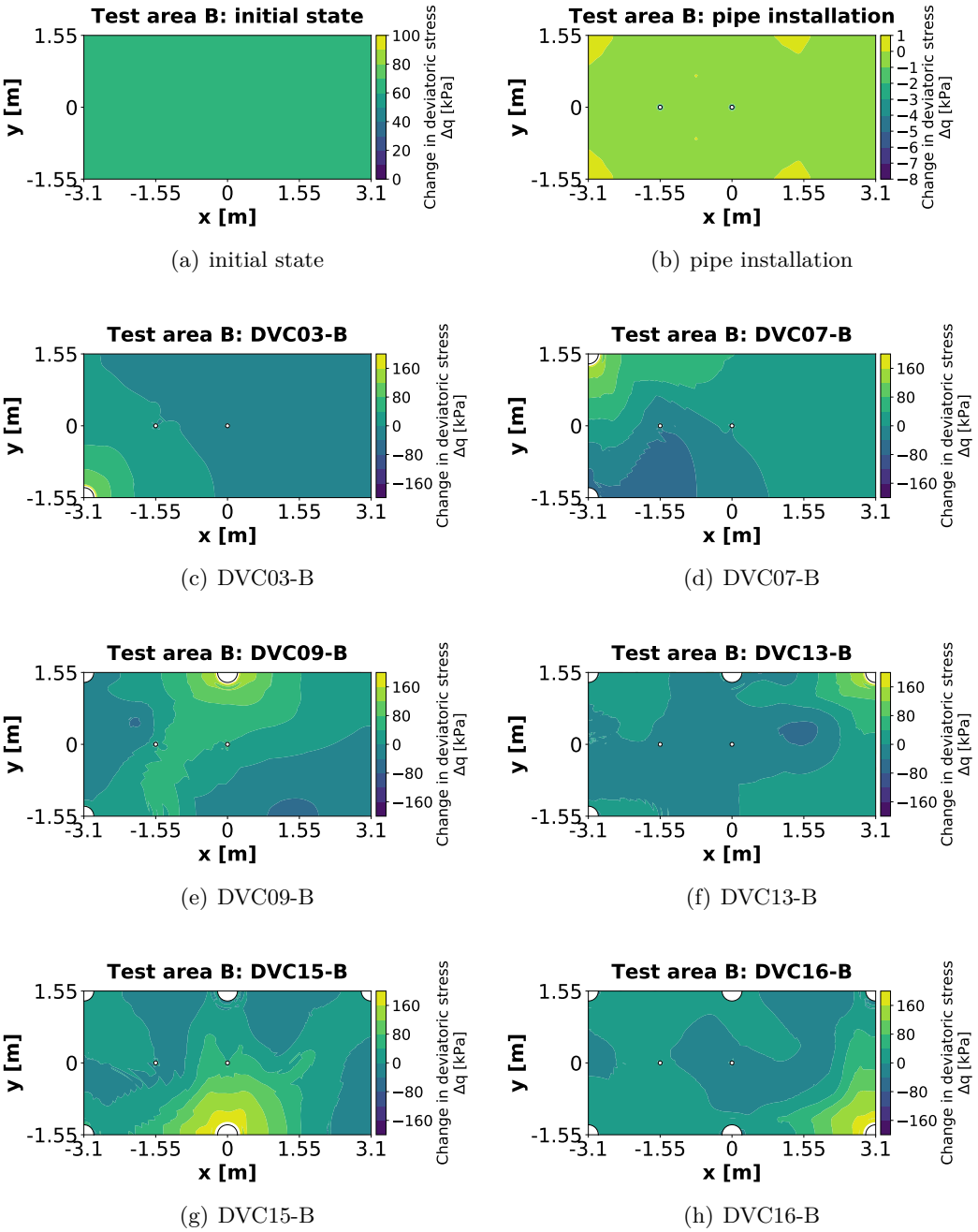

(a) initial state (b) pipe installation

(c) DVC03-B (d) DVC07-B

(e) DVC09-B (f) DVC13-B

(g) DVC15-B (h) DVC16-B

Figure 4.85: Change in deviatoric stress test area B (approach 3)

The stress paths and effective stresses in x and y direction were evaluated at stress points in all four measurement directions of the inclinometer pipes 0, 5, 15, 30 and 50 cm away from the outer mantel of the pipe. The symbols in the diagrams represent the values at the end of each calculation phase. All stress paths must start on the K_0^{nc}-line.

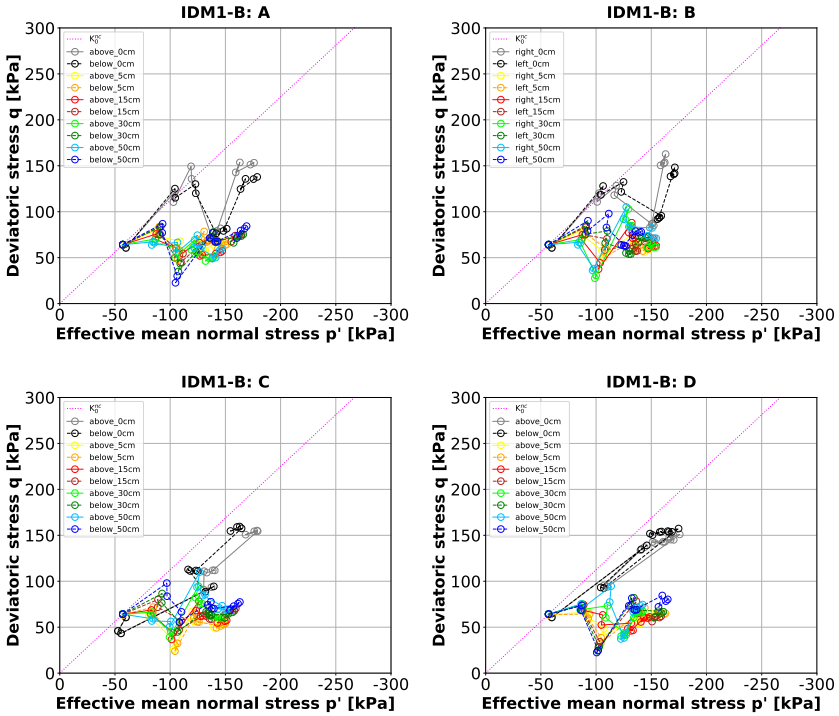

Figure 4.86: Stress paths around the inclinometer pipe IDM1-B (approach 3)

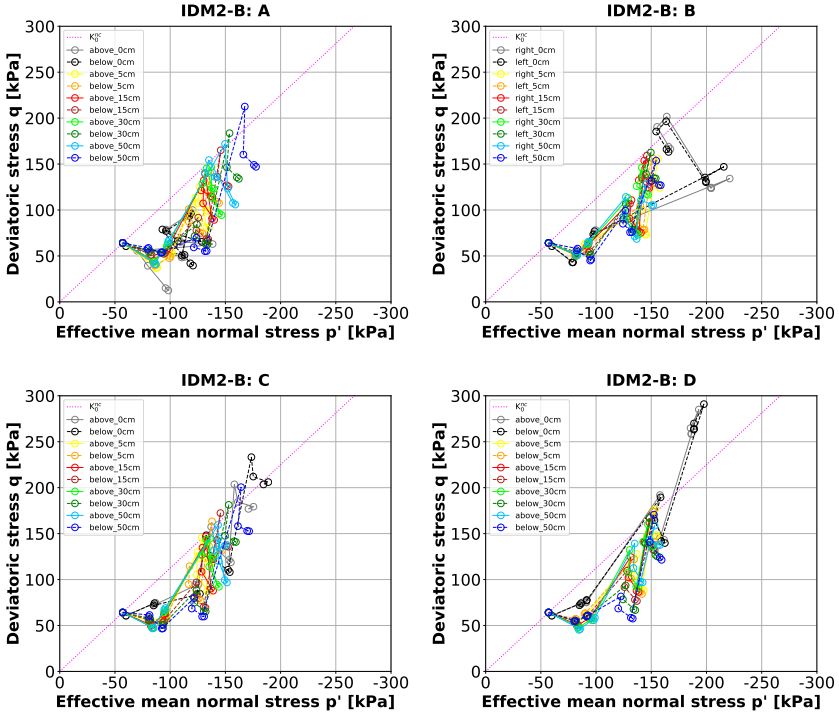

Figure 4.87: Stress paths around the inclinometer pipe IDM2-B (approach 3)

To obtain a result without pipe influence it is recommended to take the values at a specific distance from the pipe mantel. Especially the values 0 cm away from the outer mantel of the pipe deviate from the other values.

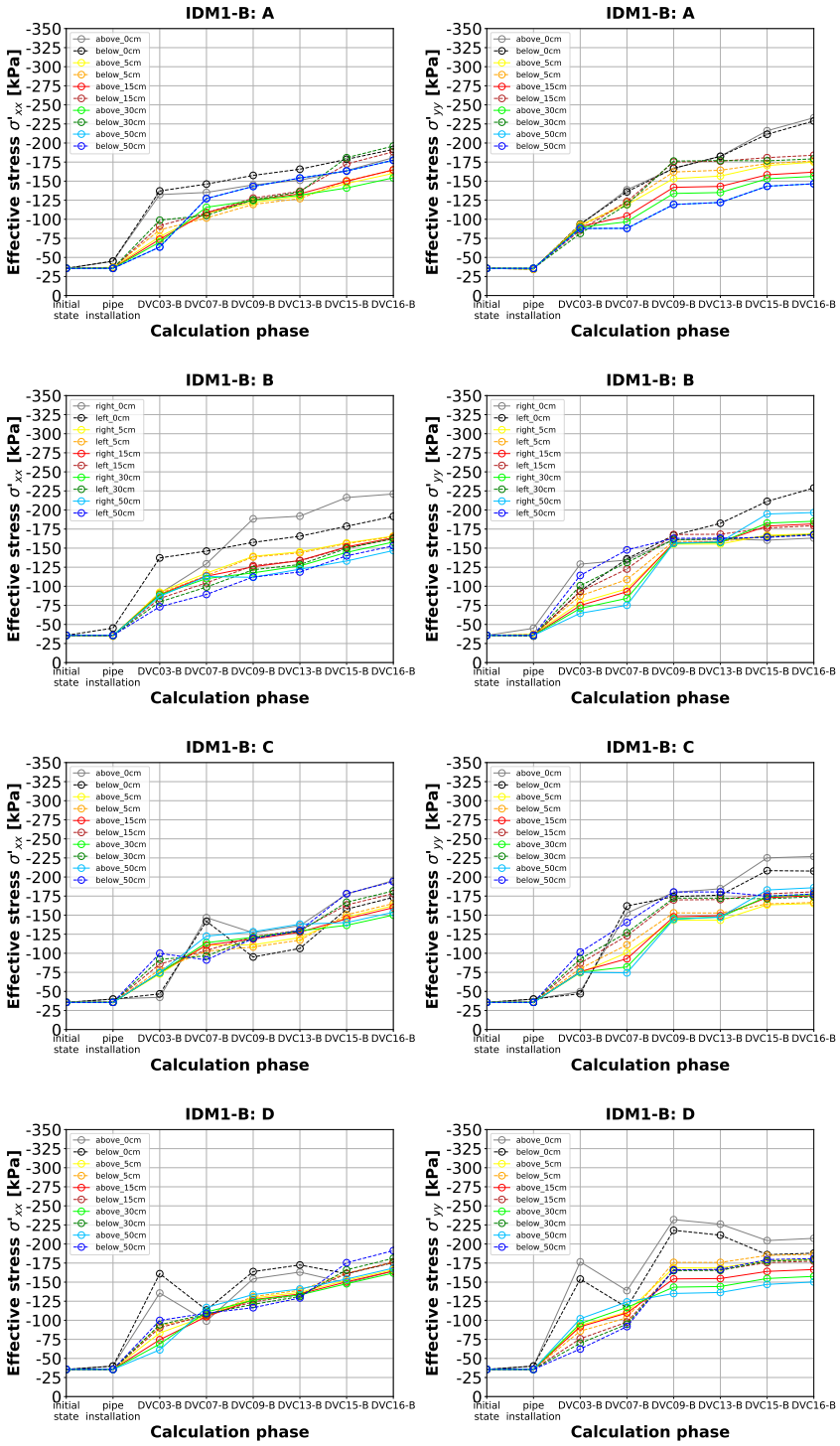

Figure 4.88: Effective stresses around the inclinometer pipe IDM1-B (approach 3)

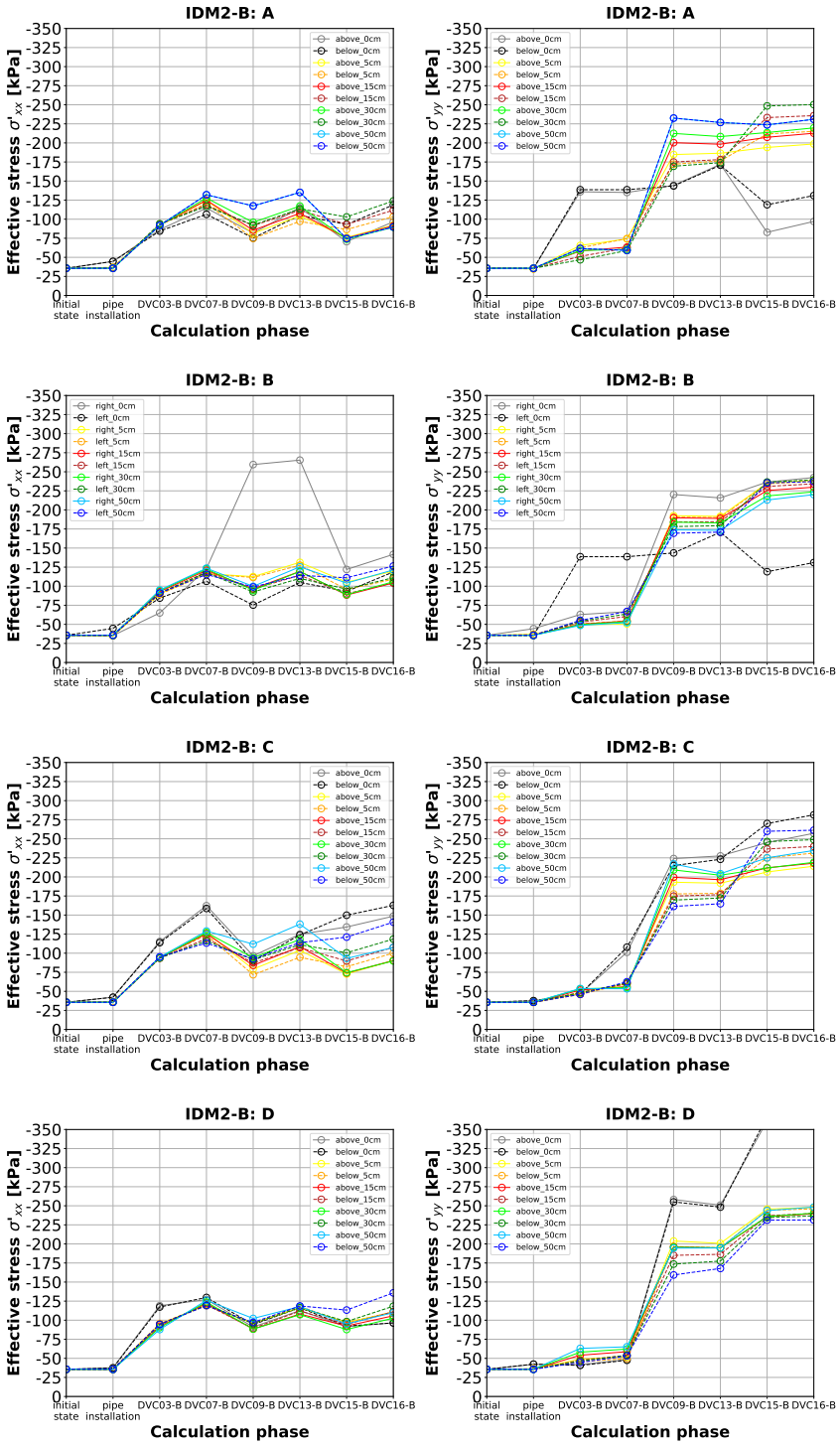

Figure 4.89: Effective stresses around the inclinometer pipe IDM2-B (approach 3)

4.2.4.3 Conclusion

The three approaches always lead to a stress increase around the inclinometer pipes after the last calculation phase. Due to the smaller grid spacing at test area A, the increase there is larger compared to test area B.

In Tab. 4.12, Tab. 4.13 and Tab. 4.14 for all three approaches the effective stresses after the last calculation phase in x and y direction 15 cm away from the outer mantel of the pipes are summarized. The values were determined by using Fig. 4.34, Fig. 4.45 and Fig. 4.56 for the inclinometer pipe IDM2-A, Fig. 4.67, Fig. 4.78 and Fig. 4.89 for the inclinometer pipe IDM2-B, Fig. 4.33, Fig. 4.44 and Fig. 4.55 for the inclinometer pipe IDM1-A and Fig. 4.66, Fig. 4.77 and Fig. 4.88 for the inclinometer pipe IDM1-B. To obtain a result without pipe influence it is recommended to take the value at a specific distance from the pipe mantel.

The rows of the tables are sorted according to the distance of the inclinometer pipes to the nearest compaction centres. The inclinometer pipe IDM2-A has the shortest distance (see Tab. 3.2).

Considering the initial stress (before compaction) in x and y direction of -35.65 kN/m^2, the stress increase factors could be calculated. In addition, Fig. 3.68(b), Fig. 3.115(b), Fig. 3.68(a) and Fig. 3.115(a) were used to determine the stress increase factors based on the cone penetration test results. If possible, the values were taken at 242.00 müA.

Table 4.12: Effective stresses and stress increase factors - approach 1 and CPTu

	approach 1				CPTu
inclinometer pipe	$\sigma'_{xx,15cm}$ [kPa]	$\sigma'_{xx,15cm}$/ -35.65 [-]	$\sigma'_{yy,15cm}$ [kPa]	$\sigma'_{yy,15cm}$/ -35.65 [-]	K_{after}/ K_{before} [-]
IDM2-A	approx. -60	1.7	approx. -120	3.4	3.0
IDM2-B	approx. -50	1.4	approx. -115	3.2	1.2
IDM1-A	approx. -110	3.1	approx. -90	2.5	2.0
IDM1-B	approx. -100	2.8	approx. -85	2.4	1.0

Table 4.13: Effective stresses and stress increase factors - approach 2 and CPTu

	approach 2				CPTu
inclinometer pipe	$\sigma'_{xx,15cm}$ [kPa]	$\sigma'_{xx,15cm}$/ -35.65 [-]	$\sigma'_{yy,15cm}$ [kPa]	$\sigma'_{yy,15cm}$/ -35.65 [-]	K_{after}/ K_{before} [-]
IDM2-A	approx. -75	2.1	approx. -140	3.9	3.0
IDM2-B	approx. -60	1.7	approx. -125	3.5	1.2
IDM1-A	approx. -120	3.4	approx. -110	3.1	2.0
IDM1-B	approx. -105	2.9	approx. -95	2.7	1.0

Table 4.14: Effective stresses and stress increase factors - approach 3 and CPTu

	approach 3				CPTu
inclinometer pipe	$\sigma'_{xx,15cm}$ [kPa]	$\sigma'_{xx,15cm}$/ -35.65 [-]	$\sigma'_{yy,15cm}$ [kPa]	$\sigma'_{yy,15cm}$/ -35.65 [-]	K_{after}/ K_{before} [-]
IDM2-A	approx. -130	3.6	approx. -270	7.6	3.0
IDM2-B	approx. -100	2.8	approx. -230	6.5	1.2
IDM1-A	approx. -175	4.9	approx. -170	4.8	2.0
IDM1-B	approx. -165	4.6	approx. -170	4.8	1.0

Approach 3 leads to the largest effective stresses. This is reasonable, due to the largest chosen static load. To reach the required ovalization, despite the huge soil stiffness around the pipes, the load was necessary.

The effective stress values reflect the grid spacing. The smaller the distance between the inclinometer pipe and the nearest compaction centre, the larger the stress after the last calculation phase.

In the centre between four compaction columns the effective stresses in x and y direction are approximately the same. Thus, also the stress increase factors are approximately the same in both directions. In the centre between two compaction columns the effective stresses in x and y direction are different. The ratio between the value in y direction and the value in x direction is approximately 2. Consequently, the stress increase factors differ in both directions.

The stress increase factors based on the cone penetration tests differ from the simulated values. The empirical factors are smaller, especially in comparison to the values of approach 3. It should be noted that the empirical value at position IDM2-B is relatively small compared to the value at position IDM1-A. With the cone penetration test result it is only possible to determine one single value, independent of the direction. This is due to the measuring principle. The flat dilatometer test would be more appropriate for determining the influence of direction. Due to the coarse grain size distribution on-site the latter test could not be performed.

To evaluate the potential overconsolidation in the subsoil, the stress paths shown in Fig. 4.31, Fig. 4.32, Fig. 4.42, Fig. 4.43, Fig. 4.53, Fig. 4.54, Fig. 4.64, Fig. 4.65, Fig. 4.75, Fig. 4.76, Fig. 4.86 and Fig. 4.87 were used. The symbols in the diagrams represent the values at the end of each calculation phase. Only approach 2 and 3 lead to an overconsolidation around the inclinometer pipe between two compaction columns due to the considered unloading phase (after the loading phase). Because of the missing unloading phases in approach 1, no overconsolidation can be identified. The inclinometer pipe between four compaction columns is too far away from the nearest compaction centre. The stress path does not move back to the elastic range.

5 Conclusion

5.1 Summary

The inclinometer pipes installed at both test areas showed significant deformations after deep vibro compaction. The deformations could be measured by using the inclinodeformeter device. The mean diameter was not suitable to evaluate the horizontal earth pressure changes in the subsoil. Nevertheless, the ovalization value provided insightful findings. The qualitative horizontal stress distribution over depth after compaction is one result. Furthermore, the grid spacing is reflected by the measurement results. The smaller the distance between the inclinometer pipe and the nearest compaction centre, the larger the change in ovalization after compaction. It was found that the final pipe deformation is determined by the sequence of the compaction columns.

Dynamic probing and cone penetration test results were suitable for evaluating the compaction success. Using existing empirical relationships, soil properties could be estimated before and after compaction. The correlations were critically questioned. The cone penetration tests predict different horizontal stresses in the subsoil over time (even after compaction). This stress changes could not be confirmed based on the inclinodeformeter measurement results.

Due to the ovalization of the inclinometer pipes after compaction, the horizontal stress increase is with certainty one effect of the vibroflotation method on the subsoil. The ovalization of the pipes was extensively discussed.

The back calculation of the changes in lateral earth pressure based on the measured pipe deformations was challenging. Main problem was the correct assessment of the soil stiffness (step 10) around the pipes during the compaction process. Different stiffness distributions lead to remarkably different horizontal stresses.

The behaviour of the inclinometer pipe cross section at different model approaches and load scenarios was investigated. Considering the order of magnitude of the measurement results the pipe channels were for the simulations not negligible.

A part of both test areas at a specific depth was modelled. Simplifications were made for the load application and the stiffness distribution. For three different approaches the pipe deformations and the horizontal stresses around the inclinometer pipes were simulated. Furthermore, the stress paths around the inclinometer pipes were evaluated. It was found that between two compaction columns the horizontal stress after compaction is directional. The horizontal stress increase differs for all three approaches. The simulated stress increase factors were always larger than the empirical values. It has been shown that the stress path is dependent on the model approach. Considering additional unloading phases after the loading phases an overconsolidation was achieved in some areas.

5.2 Outlook

The following is recommended for further experimental investigations with the inclinodeformeter probe on vibratory compaction fields:

- homogeneous, sandy subsoil
  A homogeneous subsoil should lead to more uniform measurement results with less outliers. A sandy subsoil would allow additional measurements with the flat dilatometer.
- simplification of the boundary value problem
  The number of compaction columns should be reduced to a minimum. Furthermore, the pipe deformations should be measured after each compaction column.
- recording of the stiffness changes around the compaction centres
  The use of additional measurement systems could reduce the uncertainties.

Both the horizontal stress increase and the possible overconsolidation are advantageous in the settlement analysis. The effect of the horizontal stress increase on the settlement analysis for different load types (single foundation, strip foundation and surface foundation) would be a possible further research topic.

Bibliography

[1] Adam, Dietmar ; Paulmichl, Ivan ; Kopf, Fritz ; Erdmann, Peter: Integrierte Verdichtungskontrollen bei dynamischen Verdichtungsverfahren. In: Adam, Dietmar (Hrsg.) ; Herrmann, Richard A. (Hrsg.): *Symposium Baugrundverbesserung in der Geotechnik, Siegen*, Eigenverlag des Institut für Geotechnik, 2010

[2] Bentley Systems: *Plaxis Material Models Manual*. V20.04, 2020

[3] Franki Foundations: *https://www.ffgb.be*. Website, 2020. – Accessed: 23.10.2020

[4] Heins, Evelyn ; Grabe, Jürgen ; Hamann, Thorben: Numerische Simulation einer Bodenverbesserungsmaßnahme infolge Rütteldruckverdichtung. In: *BAWMitteilungen Nr. 98 Numerische Methoden in der Geotechnik* Bd. 98. Bundesanstalt für Wasserbau (BAW), Karlsruhe, 2015, S. 59 – 68

[5] Keller Grundbau Ges.mbH: *Deep Vibro Techniques*. 2011. – Brochure 10-02E

[6] Kirsch, Klaus ; Kirsch, Fabian: *Ground Improvement by Deep Vibratory Methods*. 1st Edition. Spon Press, Taylor & Francis Group, New York, 2010

[7] Massarsch, Karl R.: Settlement Analysis of Compacted Fill. In: Publications Committee 13th ICSMFE (Hrsg.): *Proceedings of the 13th International Conference on Soil Mechanics and Foundation Engineering, New Delhi, India* Bd. 1, Taylor & Francis, London, 1994, S. 325 – 328

[8] Massarsch, Karl R.: Effects of Vibratory Compaction. In: *TRANSVIB 2002 International Conference on Vibratory Pile Driving and Deep Soil Compaction, Louvain-la-Neuve*, A.A. Balkema, Lisse, 2002, S. 33 – 42

[9] Massarsch, Karl R.: Das Setzungsverhalten von vibrationsverdichteten, rolligen Böden. In: *geotechnik* 42 (2019), Nr. 3, S. 134 – 150

[10] Massarsch, Karl R. ; Fellenius, Bengt H.: Evaluation of Vibratory Compaction by In Situ Tests. In: *Journal of Geotechnical and Geoenvironmental Engineering* 145 (2019), Nr. 12, S. 05019012–1 – 05019012–14

[11] Massarsch, Karl R. ; Wersäll, Carl ; Fellenius, Bengt H. ; Bałachowski, Lech ; Kurek, Norbert ; Konkol, Jakub: Discussion: Horizontal stress increase induced by deep vibratory compaction. In: *Proceedings of the Institution of Civil Engineers - Geotechnical Engineering* 173 (2020), Nr. 4, S. 370 – 375

[12] Menard Group: *https://www.menard-group.com*. Website, 2020. – Accessed: 23.10.2020

[13] Nagy, Péter: *Rütteldruckverdichtung (Dynamische Verdichtungskontrolle auf Basis der Rüttlerbewegung)*, Technische Universität Wien, Dissertation, 2018

[14] ÖNORM EN 14731: *Ausführung von besonderen geotechnischen Arbeiten (Spezialtiefbau) - Baugrundverbesserung durch Tiefenrüttelverfahren.* Österreichisches Normungsinstitut, Wien, 2006. – Ausgabe: 2006-10-01

[15] ÖNORM EN 1997-2: *Eurocode 7: Geotechnical design - Part 2: Ground investigation and testing.* Austrian Standards Institute, Wien, 2010. – Edition: 2010-08-15

[16] Robertson, Peter K.: CPT-DMT Correlations. In: *Journal of Geotechnical and Geoenvironmental Engineering* 135 (2009), Nr. 11, S. 1762 – 1771

[17] Robertson, Peter K.: Cone penetration test (CPT)-based soil behaviour type (SBT) classification system - an update. In: *Canadian Geotechnical Journal* 53 (2016), Nr. 12, S. 1910 – 1927

[18] Robertson, Peter K. ; (Robertson), K. L. C.: *Guide to Cone Penetration Testing for Geotechnical Engineering.* 6th Edition. Gregg Drilling & Testing, Inc., Signal Hill, 2014

[19] Schwager, Markus V.: *Development, analysis and applications of an 'inclinodeformeter' device for earth pressure measurements*, ETH Zurich, Dissertation, 2013

[20] Studio Marchetti: *https://www.marchetti-dmt.it.* Website, 2020. – Accessed: 22.10.2020

[21] Wachter, Barbara: *Untersuchungen zur Messgenauigkeit und Weiterentwicklung der IDM-Sonde*, Technische Universität Graz, Institut für Bodenmechanik und Grundbau, Diplomarbeit, 2016

[22] Witt, Karl J.: *Grundbau-Taschenbuch.* Bd. 2: *Grundbau-Taschenbuch Teil 2: Geotechnische Verfahren.* 8. vollständig überarbeitete und aktualisierte Auflage. Wilhelm Ernst & Sohn, Verlag für Architektur und technische Wissenschaften GmbH & Co. KG, Berlin, 2018

List of Figures

List of Tables

Appendix

1 Technical report preliminary test July 2019

Ermittlung der Änderung des mittleren Rohrdurchmesser unter hydrostatischer Belastung auf das IDM-Rohr

(Kleinversuch IBG - TU Graz als Vorbereitung auf einen möglichen In-situ Versuch zur Ermittlung der Horizontalspannungsänderung im Zuge einer Rütteldruckverdichtung)

Juli 2019

Als Vorbereitung für ein mögliches kleines Forschungsprojekt (IBG, Keller Grundbau, Dr. Schwager) zur Untersuchung der Horizontalspannungsänderung im Zuge einer Rütteldruckverdichtung wurde im Labor für Bodenmechanik und Grundbau der TU Graz ein kleiner Versuchsstand aufgebaut, mittels welchem unterschiedliche hydrostatische Drücke auf das IDM-Messrohr aufgebracht werden können. Die unterschiedlichen Drücke führen zu Änderungen des mittleren Rohrdurchmessers.

Der Versuchsaufbau besteht aus einem stabilen Außenrohr, welches durch Fußplatte und Kopfabschluss abgedichtet ist und in welchem ein IDM-Rohr (gegen das Außenrohr abgedichtet) eingebaut wurde. Über Wasseranschluss und Druckanzeige kann der Ringraum zwischen dem Außenrohr und dem IDM-Rohr mit Wasser befüllt und mit unterschiedlichen Wasserdrücken beaufschlagt werden. Der Versuchsaufbau ist im Nachfolgenden ersichtlich.

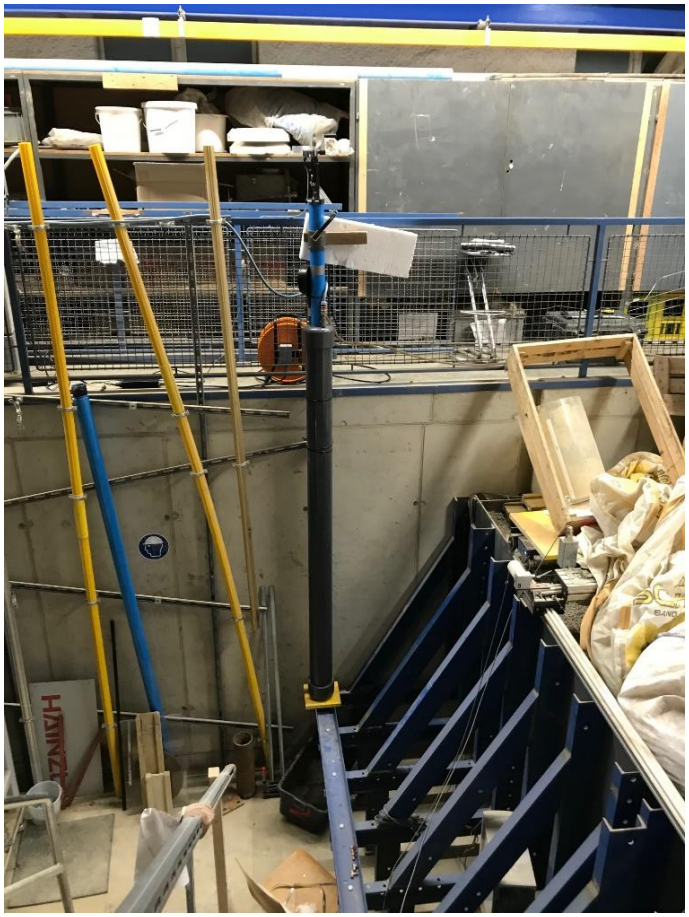

Abb. 1 Versuchsstand: Außenrohr (grau) mit eingebautem IDM-Messrohr (blau)

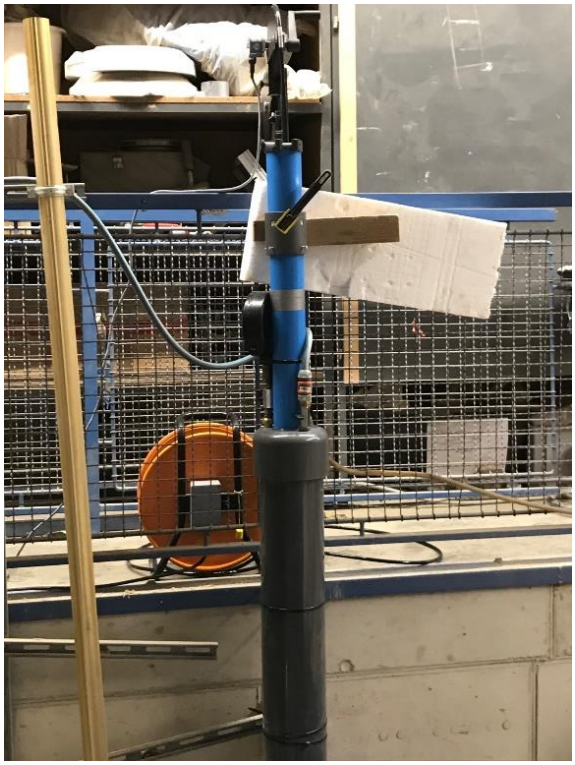

Abb. 2 Kopfbereich Versuchsstand: IDM-Messrohr, abgedichtetes und mit Wasseranschluss ausgestattetes Außenrohr

Abb. 3 Messvorgang IDM, Druckanzeige für Wasserdruck im Ringraum Außenrohr - IDM-Messrohr

Im durchgeführten Vorversuch wurden für unterschiedliche Druckstufen IDM-Messungen in Richtung A0, Umschlagsmessung A180 sowie in Richtung B0 und Umschlagsmessung B180 durchgeführt. Das IDM-Rohr weist eine Länge von 3,0 m, das Druckrohr eine Länge von ca. 2,5 m auf. Im IDM-Rohr wurde für die Ermittlung des mittleren Durchmessers vorerst die Messstrecke von ca. 1,0 bis 1,8 m Tiefe ausgewertet, um Randeinflüsse einzugrenzen. Für die Ermittlung des mittleren Durchmessers (zwischen 1,0 und 1,8 m) wurden die Messwerte in den jeweiligen Tiefenstufen gemittelt (aus A0, A180, B0 und B180) - wobei die Tiefenzuordnung aufgrund einer ersten vereinfachten Auswertung mittels Excel nicht exakt erfolgte - und dann aus den ca. 2850 Datensätzen (für die unterschiedlichen Tiefen) ein einziger gemittelter Durchmesser errechnet.

Es wurden 2 Nullmessungen ohne Wasserbefüllung durchgeführt, sodann eine Messung mit Wasserbefüllung (hydrostatisch) und schließlich bei befülltem Rohr eine Druckbeaufschlagung mit 0,2, 0,4, 0,6, 0,8, 1,0, 1,3 sowie 1,6 bar vorgenommen. Die Ergebnisse sind nachfolgend zusammengefasst.

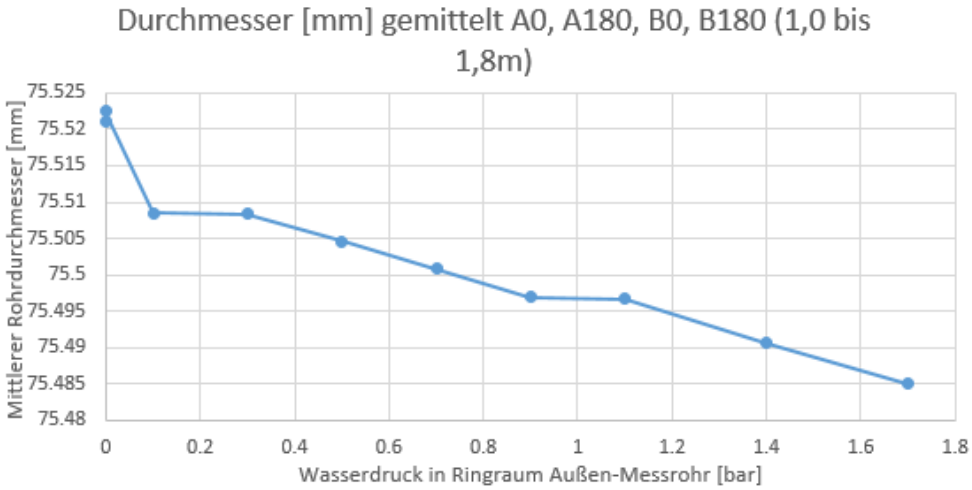

Abb. 4 Ergebnisse des Vorversuchs

Auf der Abszisse sind die jeweiligen Wasserdrücke (in ca. 1,4 m Tiefe) im Ringraum zwischen dem Außenrohr und dem IDM-Messrohr und auf der Ordinate der mittlere Rohrdurchmesser aufgetragen. Die beiden Messwerte bei 0 bar stellen die Nullmessung (ohne Wasserbefüllung), die restlichen Daten die mittleren Durchmesser bei den entsprechenden Wasserdrücken bis max. ca. 1,7 bar dar.

Grundsätzlich ist eine Abnahme des Rohrdurchmessers mit zunehmendem Wasserdruck gut erkennbar, wobei die Größenordnung der Durchmesseränderung von z.B. 0,4 bar (40 kPa) auf ca. 1,4 bar (140 kPa) bei knapp 0,02 mm (20 µm) liegt. Das Messsystem IDM erlaubt eine Auflösung im Bereich von ca. 2 bis 3 µm was aus obigen Unstetigkeiten in etwa erkennbar ist.

Betrachtet man nun z.B. einen nicht bindigen Boden in 5 m Tiefe (Annahme ohne Grundwasser) ergibt sich eine Vertikalspannung von ca. 100 kPa in dieser Tiefe und bei einem K_0 von ca. 0,5 eine Horizontalspannung von ca. 50 kPa. Wird bei einer Rütteldruckverdichtung eine Horizontalspannungserhöhung von z.B. 2 erwirkt (laut Massarsch teilweise deutlich höhere Werte möglich), ergibt sich eine Steigerung von 50 auf ca. 100 kPa, was nach obigen Voruntersuchungen gut auflösbar sein sollte.

Zudem sollte der Versuch In-situ so durchgeführt werden, dass nach jeder neu hergestellten Säule um einen Messpunkt eine IDM-Messung durchgeführt wird. Durch diesen Vorgang wird der Rohrquerschnitt nicht durch eine hydrostatische Druckänderung beansprucht, sondern mit jeder neuen Säule um das Messrohr kommt es (im Vergleich zur vorigen Messung) zu einer Ovalisierung. Erst nach Fertigstellung aller Rüttelsäulen um das Messrohr haben wir einen mehr oder weniger gleichmäßigen Druck um das Messrohr. Der Weg hierhin führt aber über eine veränderliche Ovalisierung des Rohres. Diese Versuchsdurchführung ist zwar zeitaufwändiger aber im Hinblick auf die Aussagekraft interessanter (und „sicherer“).

Roman Marte, Andreas Hasawend

2 Layout test area A and test area B

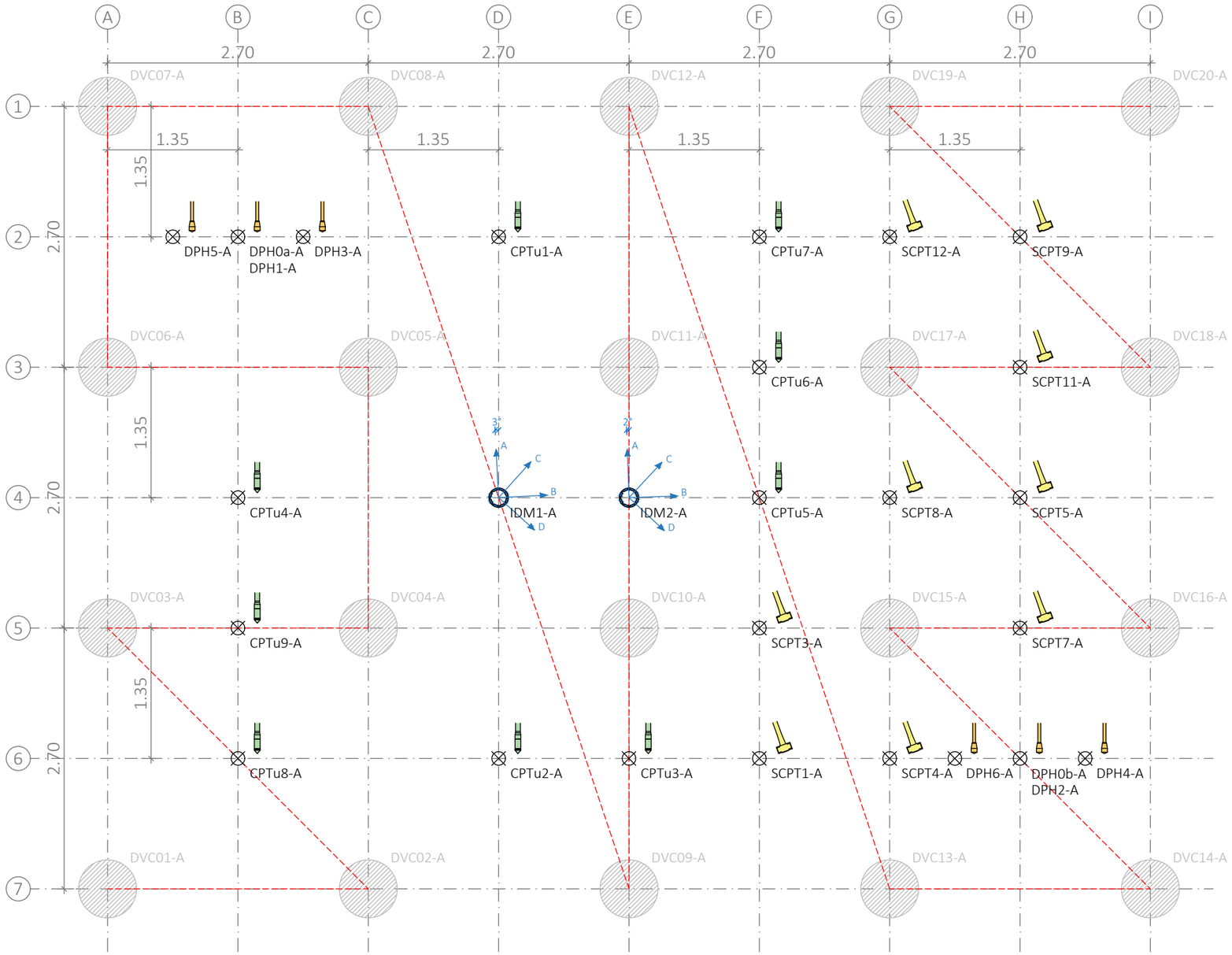

Designation	before DVC	after DVC		
	Epoch 0 (21.02.2020)	Epoch 1 (27.02.2020)	Epoch 2 (10.03.2020)	Epoch 3 (21.04.2020)
IDM1-A	X	X	X	X
IDM2-A	X	X	X	X
DPH0a-A	X			
DPH0b-A	X			
DPH1-A		X		
DPH2-A		X		
DPH3-A			X	
DPH4-A			X	
DPH5-A				X
DPH6-A				X
CPTu0a-A	X	(just outside the test area)		
CPTu0b-A	X	(just outside the test area)		
CPTu1-A		X		
CPTu2-A		X		
CPTu3-A		X		
CPTu4-A			X	
CPTu5-A			X	
CPTu6-A			X	
CPTu7-A				X
CPTu8-A				X
CPTu9-A				X
SCPT0a-A	X	(just outside the test area)		
SCPT0b-A	X	(just outside the test area)		
SCPT1-A		X		
SCPT3-A		X		
SCPT4-A		X		
SCPT5-A			X	
SCPT7-A			X	
SCPT8-A			X	
SCPT9-A				X
SCPT11-A				X
SCPT12-A				X

LEGEND

IDMx-A — Inclinodeformeter

DPHx-A — Dynamic Probing Heavy

CPTux-A — Cone Penetration Test

SCPTx-A — Seismic Cone Penetration Test

Graz University of Technology

Investigations on the horizontal stress state of non-cohesive soils due to deep vibro compaction
Experimental investigations

Institute of Soil Mechanics, Foundation Engineering and Computational Geotechnics

Test area - Deep vibro compaction - A (2.70 m x 2.70 m)

Grid with measurement points

Index	Date	Description
a	06.02.2020	Creation
b	13.02.2020	Nomenclature measurement points
c	28.03.2020	Translation and actualization
d	07.05.2020	Measurement directions Inclinodeformeter

Date	Draughtsman	Inspector	Dimension	Scale	Number
07.05.2020	Gasser	Marte	A3	1:50	TA-DVC-A_d

C:\Users\DanielGasser\MEGA\04_Messung\01_Pläne\TA-DVC-A.dwg

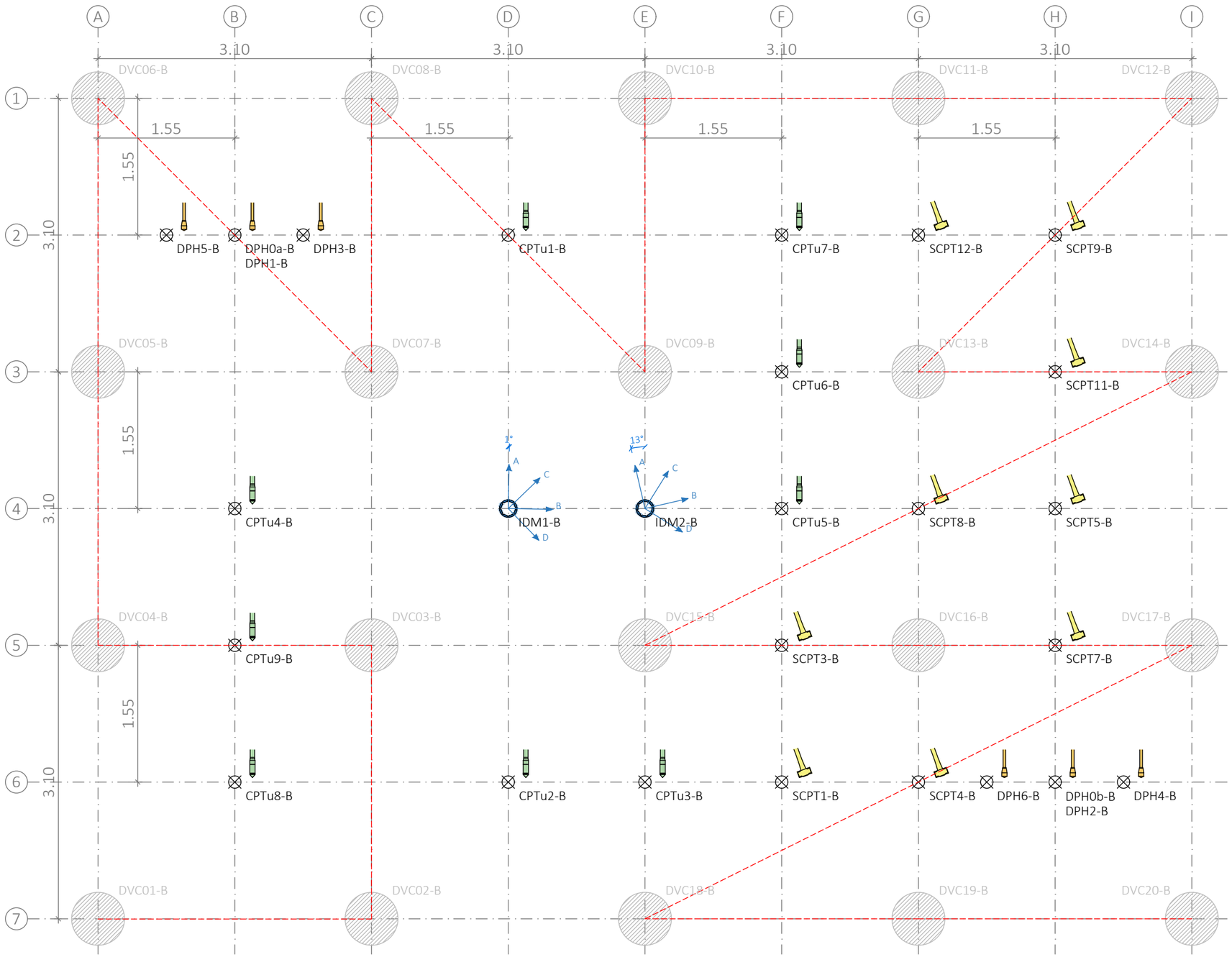

Designation	before DVC	after DVC		
	Epoch 0 (21.02.2020)	Epoch 1 (27.02.2020)	Epoch 2 (10.03.2020)	Epoch 3 (21.04.2020)
IDM1-B	X	X	X	X
IDM2-B	X	X	X	X
DPH0a-B	X			
DPH0b-B	X			
DPH1-B		X		
DPH2-B		X		
DPH3-B			X	
DPH4-B			X	
DPH5-B				X
DPH6-B				X
CPTu0a-B	X	(just outside the test area)		
CPTu0b-B	X	(just outside the test area)		
CPTu1-B		X		
CPTu2-B		X		
CPTu3-B		X		
CPTu4-B			X	
CPTu5-B			X	
CPTu6-B			X	
CPTu7-B				X
CPTu8-B				X
CPTu9-B				X
SCPT0a-B	X	(just outside the test area)		
SCPT0b-B	X	(just outside the test area)		
SCPT1-B		X		
SCPT3-B		X		
SCPT4-B		X		
SCPT5-B			X	
SCPT7-B			X	
SCPT8-B			X	
SCPT9-B				X
SCPT11-B				X
SCPT12-B				X

LEGEND

- IDMx-B — Inclinodeformeter
- DPHx-B — Dynamic Probing Heavy
- CPTux-B — Cone Penetration Test
- SCPTx-B — Seismic Cone Penetration Test

Graz University of Technology

Investigations on the horizontal stress state of non-cohesive soils due to deep vibro compaction
Experimental investigations

Institute of Soil Mechanics, Foundation Engineering and Computational Geotechnics

Test area - Deep vibro compaction - B (3.10 m x 3.10 m)

Grid with measurement points

Index	Date	Description
a	06.02.2020	Creation
b	13.02.2020	Nomenclature measurement points
c	28.03.2020	Translation and actualization
d	07.05.2020	Measurement directions Inclinodeformeter

Date	Draughtsman	Inspector	Dimension	Scale	Number
07.05.2020	Gasser	Marte	A3	1:50	TA-DVC-B_d

C:\Users\DanielGasser\MEGA\04_Messung\01_Pläne\TA-DVC-B.dwg

3 Product specification sheet inclinometer pipe

info@se-ch.biz
www.swissenvironment.ch


1

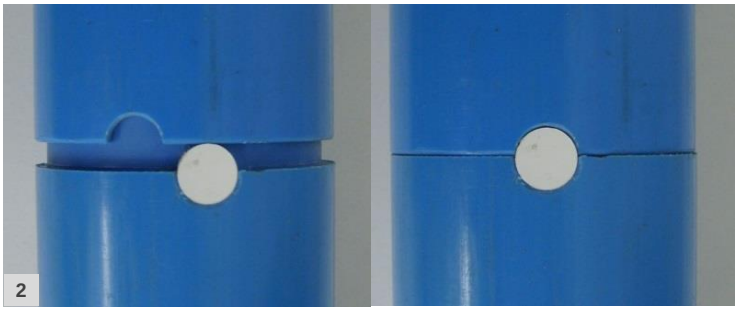
2


3


4

Messrohre «SwissEnvironment»
für Setzungsmessungen

- SE (Settlement-Hook USBR)
- Inkrex (Inkremental-Extensometer)

- Installation in Bohrlöchern, Einbau in Auffüllungen, Eingiessen in Beton oder Befestigung an Strukturen (z.B. Spundwände)
- Hergestellt aus schlagfestem PVC
- Kupplungen ins Rohr gefräst (keine zusätzliche Muffe nötig)
- Sicherer Zusammenbau durch Führungshilfe (Aussparung & Knopf)
- Präzise Bearbeitung der Führungsrillen (Rillen nicht extrudiert sondern von Hand gezogen)
- Verdrehung unter 0.5° auf 10m
- Zusätzlich zu den Setzungsmessungen auch für Inklinometer-messungen verwendbar.

Zubehör

- Abschlussdeckel und Böden aus Kunststoff
- Fussstahlbecher für den Einbau von grösseren Rohrlängen
- Anker zur Auftriebssicherung bei der Injektion
- Wasserdichte Deckel
- Umlenkrollen für Messung mit Zugseil
- Klebstoff, Nieten usw.

Für den korrekten Einbau bitte die Einbauanleitung beachten


5

1) Kupplungsseite
2) Einfaches Zusammenbauen (Aussparung & Knopf)
3) SE-Rohr mit Haftungsrillen für Injektion (Setzungsmessung)
4) SE-Rohrkupplungen 75mm & 120mm
5) Inkrex-Rohr (Inkremental-Extensometer), Länge 3.0m

Fortsetzung Rückseite

info@se-ch.biz
www.swissenvironment.ch

Technische Daten

			NW 71 SE und Inkrex	**NW 84** nur SE
Rohr	Innendurchmesser		58 mm	72 mm
	Aussendurchmesser		71 mm	84 mm
	Rillentiefe		2.0 mm	
	Wandstärke		6.5 mm	6 mm
	Gewicht		1.8 kg/m Inkrex 2.1 kg/m	2.5 kg/m
	Verdrehung der Rillen		< 0.5° / 10m	
	Zugbelastung (geklebt & vernietet)		> 700kg	
	Widerstandsfähigkeit bez. Injektionsdruck		15 bar	12 bar
	Temperaturbereich		-30~+80°C	
	Material		schlagfestes PVC	
Längen	Inkrex		3.00 m	
	SE		0.95 m	0.95 m
Boden	Masse		65 - 70 mm x 50 mm	78 - 83 mm x 50 mm
	Material		schlagfestes PVC	
	Gewicht		96 g	120 g
Deckel	Masse		58 - 70 mm x 50 mm	71 - 83 mm x 50 mm
	Material		schlagfestes PVC	
	Gewicht		40 g	54 g
Inkrex-Messring	Material		Messing	
	Aussendurchmesser		80 mm	
SE-Muffen	Länge	Variante kurz	75 mm	
		Variante lang	120 mm	
	Messbereich	Variante kurz	max. 35 mm	
		Variante lang	max. 80 mm	

4 Extended MATLAB code

```
function IDM_Deformations;
clear all;

%%%%%%%%%% Eingabewerte Auswertung %%%%%%%%%%
span=3000           % Spannweite des gleitenden Mittelwertes für Savitzky-Golay-Filter für ungemittelte Darstellung der Messwerte
degree=2;           % Polynomgrad für Savitzky-Golay-Filter für ungemittelte Darstellung der Messwerte
mean=1/3            % Prozent von einem Meter (Abschnittslänge für die Mittelwertbildung)
Ignore1=0.25        % Bereich in Meter, welcher nach dem Rohranfang für die Mittelwertbildung vernachlässigt wird
Ignore=0.25         % Bereich in Meter, welcher vor und nach jedem Stoß (Verbindung Rohrelement) für die Mittelwertbidlung vernachlässigt wird
Percent=0;          % Prozent der Messwerte, welche als Ausreißer ausgeschlossen werden
BohrlochTiefe=0     % BohrlochTiefe=0: Auswertung bis zmax
                    % BohrlochTiefe=z: Auswertung bis z
Cutoff=0;           % Anzahl an Messwerten, welche am Rohrende vernachlässigt werden
check='no'          % 'no': übliche Auswertung
                    % 'NS'/'NR': Auswertung um die Messungen bezüglich Neigung Sonde oder Neigung Rad zu überprüfen

%%%%%%%%%% Eingabewerte Bohrloch %%%%%%%%%%
% Messdaten müssen im Ordner Ort wie folgt abgelegt sein:
%       Bezeichnung_ddmmyyyy_A000.dat
%       Bezeichnung_ddmmyyyy_B000.dat
%       Bezeichnung_ddmmyyyy_A180.dat
%       Bezeichnung_ddmmyyyy_B180.dat

Ort='Ordner';                       % Name des Ordners am Computer, welcher die abgspeicherten Messdaten enthält
Inklinometer='001';                 % Bezeichnung der Bohrung bzw. des Inklinometerrohres
Typ=['000';'000'];                  % Messrichtungen '000' oder '180'
AnzahlMessungen=2                   % Anzahl an auszuwertenden Messungen
Messdaten=['21022020';'27022020']   % Datum der Messungen
Rohrverschnitt=2.8                  % Länge des Rohrstückes in Meter (Abstand Rohranfang bis zum ersten Rohrelement)

%%%%%%%%%% Geometrie %%%%%%%%%%
% Wert für 84er Rohr: X=19.3671
% Wert für 71er Rohr: X=6.371
Meter=3567;     % Anzahl an Messungen pro Meter Rohr
d=56            % Durchmesser der Räder der Messsonde
Y=10            % Basislänge des Hebels
X=19.3671       % Abstand zur Bestimmung der Lage des Rotationszentrums des Hebels

G(1)=d;
G(2)=X;
G(3)=Y;

%%%%%%%%%% Messdaten einlesen %%%%%%%%%%
n=AnzahlMessungen;
global mDA;
global mDB;
global mZ;
global w;

```

```
 50 for i=1:1:n
 51 TiefeBohrloch=BohrlochTiefe;
 52 clear mDA;
 53 clear mDB;
 54 clear mZ;
 55 w=0;
 56
 57 % Einlesen der Messrichtung A0 oder A180
 58 PfadA=['\',Ort,'\',Inklinometer,'_',Messdaten(i,:),'_A',Typ(i,:),'.dat']
 59 [tA URA USA UQA TempA DruckA zA_readin NSA NQA NRA DA] = textread(PfadA,'%f %f %f↙
%f %f %f %f %f %f %f %f','headerlines',2);
 60
 61 % Einlesen der Messrichtung B0 oder B180
 62 PfadB=['\',Ort,'\',Inklinometer,'_',Messdaten(i,:),'_B',Typ(i,:),'.dat']
 63 [tB URB USB UQB TempB DruckB zB_readin NSB NQB NRB DB] = textread(PfadB,'%f %f %f↙
%f %f %f %f %f %f %f %f','headerlines',2);
 64
 65 % relativer Abstand zwischen Erst- und Folgewerten in Messrichtung A und B
 66 zA=zA_readin-zA_readin(1);
 67 zB=zB_readin-zB_readin(1);
 68
 69 if (TiefeBohrloch>0) && (i==1)
 70     Depth=Meter*TiefeBohrloch;
 71 end
 72 if TiefeBohrloch==0
 73     [TiefeBohrloch,Depth]=max(zA);
 74     TiefeBohrloch
 75 end
 76 DepthCut=floor((Depth-Cutoff)/2)*2
 77 Anzahl3m=floor((TiefeBohrloch-roundn(Cutoff/Meter,3)-Rohrverschnitt)/3)
 78
 79 % Anzahl an Messwerten an den Punkten Start, erster Stoß, letzter Stoß und Ende in↙
Messrichtung A und B
 80 StartA=1;
 81 StartB=1;
 82 ErsterStossA=round(Rohrverschnitt*Meter);
 83 ErsterStossB=round(Rohrverschnitt*Meter);
 84 LetzterStossA=round(ErsterStossA+Anzahl3m*3*Meter);
 85 LetzterStossB=round(ErsterStossB+Anzahl3m*3*Meter);
 86 EndeA=DepthCut;
 87 EndeB=DepthCut;
 88
 89 %%%%%%%%%% Querneigungskorrektur %%%%%%%%%%
 90 switch check
 91     case {'NS'}          % Überprüfung Messungen bezüglich Neigung Sonde
 92         DAkor=NSA;
 93         DBkor=NSB;
 94     case {'NR'}          % Überprüfung Messungen bezüglich Neigung Rad
 95         DAkor=NRA;
 96         DBkor=NRB;
 97     otherwise            % übliche Auswertung mit Querneigungskorrektur
 98         DAkor=Kor(USA,URA,UQA,G);
 99         DBkor=Kor(USB,URB,UQB,G);
100 end
101
102 %%%%%%%%%% Filter %%%%%%%%%%
103 % Glättung der Messdaten mittels Savitzky-Golay-Filter
104 DAA(1:DepthCut)=smooth(DAkor(1:DepthCut),span,'sgolay',degree);
105 DBB(1:DepthCut)=smooth(DBkor(1:DepthCut),span,'sgolay',degree);
106 zAA(1:DepthCut)=zA(1:DepthCut);
```

```
107 zBB(1:DepthCut)=zB(1:DepthCut);
108
109 %%%%%%%%%% Messwerte mitteln %%%%%%%%%%
110 if check=='no'
111 IgnoreM1=floor(Meter*Ignore1);
112 IgnoreM=floor(Meter*Ignore);
113
114 % Rohrstück
115 anzahlA=floor(ErsterStossA/(mean*Meter));
116 Ara=ErsterStossA-anzahlA*mean*Meter;
117 ZAra=0;
118 while Ara<=IgnoreM1
119     ZAra=ZAra+1;
120     Ara=Ara+mean*Meter;
121 end
122 Are=mean*Meter;
123 ZAre=1;
124 while Are<=IgnoreM
125     ZAre=ZAre+1;
126     Are=Are+mean*Meter;
127 end
128 zAAV(floor(StartA):floor(ErsterStossA))=zA(floor(StartA):floor(ErsterStossA));
129 zBAV(floor(StartB):floor(ErsterStossB))=zB(floor(StartB):floor(ErsterStossB));
130
131 DAAV(floor(StartA):floor(Ara))=trimmean(DAkor(floor(StartA+IgnoreM1):floor(Ara)),↙
Percent);
132 DBAV(floor(StartB):floor(Ara))=trimmean(DBkor(floor(StartB+IgnoreM1):floor(Ara)),↙
Percent);
133 sv(DAAV(floor(StartA)),DBAV(floor(StartB)),zAAV(floor(StartA)));
134 sv(DAAV(floor(Ara)),DBAV(floor(Ara)),zAAV(floor(Ara)));
135 for k=1:1:(anzahlA-ZAra-ZAre)
136     DAAV(floor(Ara+(k-1)*mean*Meter):floor(Ara+k*mean*Meter))=trimmean(DAkor(floor↙
(Ara+(k-1)*mean*Meter):floor(Ara+k*mean*Meter)),Percent);
137     DBAV(floor(Ara+(k-1)*mean*Meter):floor(Ara+k*mean*Meter))=trimmean(DBkor(floor↙
(Ara+(k-1)*mean*Meter):floor(Ara+k*mean*Meter)),Percent);
138     sv(DAAV(floor(Ara+(k-1)*mean*Meter)),DBAV(floor(Ara+(k-1)*mean*Meter)),zAAV↙
(floor(Ara+(k-1)*mean*Meter)));
139     sv(DAAV(floor(Ara+k*mean*Meter)),DBAV(floor(Ara+k*mean*Meter)),zAAV(floor↙
(Ara+k*mean*Meter)));
140 end
141 DAAV(floor(ErsterStossA-Are):floor(ErsterStossA))=trimmean(DAkor(floor↙
(ErsterStossA-Are):floor(ErsterStossA-IgnoreM)),Percent);
142 DBAV(floor(ErsterStossB-Are):floor(ErsterStossB))=trimmean(DBkor(floor↙
(ErsterStossB-Are):floor(ErsterStossB-IgnoreM)),Percent);
143 sv(DAAV(floor(ErsterStossA-Are)),DBAV(floor(ErsterStossB-Are)),zAAV(floor↙
(ErsterStossA-Are)));
144 sv(DAAV(floor(ErsterStossA)),DBAV(floor(ErsterStossB)),zAAV(floor(ErsterStossA)));
145
146 % für alle außer dem letzten Rohrelement
147 for j=1:1:Anzahl3m
148     anzahlA=floor(3*Meter/(mean*Meter));
149     Ara=mean*Meter;
150     ZAra=1;
151     while Ara<=IgnoreM
152         ZAra=ZAra+1;
153         Ara=Ara+mean*Meter;
154     end
155     Are=mean*Meter;
156     ZAre=1;
157     while Are<=IgnoreM
```

```
158         ZAre=ZAre+1;
159         Are=Are+mean*Meter;
160     end
161     zAAV(floor(ErsterStossA+(j-1)*3*Meter):floor(ErsterStossA+j*3*Meter))=zA(floor↙
(ErsterStossA+(j-1)*3*Meter):floor(ErsterStossA+j*3*Meter));
162     zBAV(floor(ErsterStossB+(j-1)*3*Meter):floor(ErsterStossB+j*3*Meter))=zB(floor↙
(ErsterStossB+(j-1)*3*Meter):floor(ErsterStossB+j*3*Meter));
163
164     DAAV(floor(ErsterStossA+(j-1)*3*Meter):floor(ErsterStossA+(j-1)*3*Meter+Ara)) ↙
=trimmean(DAkor(floor(ErsterStossA+(j-1)*3*Meter+IgnoreM):floor(ErsterStossA+(j-1) ↙
*3*Meter+Ara)),Percent);
165     DBAV(floor(ErsterStossB+(j-1)*3*Meter):floor(ErsterStossB+(j-1)*3*Meter+Ara)) ↙
=trimmean(DBkor(floor(ErsterStossB+(j-1)*3*Meter+IgnoreM):floor(ErsterStossB+(j-1) ↙
*3*Meter+Ara)),Percent);
166     sv(DAAV(floor(ErsterStossA+(j-1)*3*Meter)),DBAV(floor(ErsterStossB+(j-1) ↙
*3*Meter)),zAAV(floor(ErsterStossA+(j-1)*3*Meter)));
167     sv(DAAV(floor(ErsterStossA+(j-1)*3*Meter+Ara)),DBAV(floor(ErsterStossB+(j-1) ↙
*3*Meter+Ara)),zAAV(floor(ErsterStossA+(j-1)*3*Meter+Ara)));
168     for k=1:1:(anzahlA-ZAra-ZAre)
169         DAAV(floor(ErsterStossA+(j-1)*3*Meter+Ara+(k-1)*mean*Meter):floor ↙
(ErsterStossA+(j-1)*3*Meter+Ara+k*mean*Meter))=trimmean(DAkor(floor(ErsterStossA+(j-1) ↙
*3*Meter+Ara+(k-1)*mean*Meter):floor(ErsterStossA+(j-1)*3*Meter+Ara+k*mean*Meter)), ↙
Percent);
170         DBAV(floor(ErsterStossB+(j-1)*3*Meter+Ara+(k-1)*mean*Meter):floor ↙
(ErsterStossB+(j-1)*3*Meter+Ara+k*mean*Meter))=trimmean(DBkor(floor(ErsterStossB+(j-1) ↙
*3*Meter+Ara+(k-1)*mean*Meter):floor(ErsterStossB+(j-1)*3*Meter+Ara+k*mean*Meter)), ↙
Percent);
171         sv(DAAV(floor(ErsterStossA+(j-1)*3*Meter+Ara+(k-1)*mean*Meter)),DBAV(floor ↙
(ErsterStossB+(j-1)*3*Meter+Ara+(k-1)*mean*Meter)),zAAV(floor(ErsterStossA+(j-1) ↙
*3*Meter+Ara+(k-1)*mean*Meter)));
172         sv(DAAV(floor(ErsterStossA+(j-1)*3*Meter+Ara+k*mean*Meter)),DBAV(floor ↙
(ErsterStossB+(j-1)*3*Meter+Ara+k*mean*Meter)),zAAV(floor(ErsterStossA+(j-1) ↙
*3*Meter+Ara+k*mean*Meter)));
173     end
174     DAAV(floor(ErsterStossA+j*3*Meter-Are):floor(ErsterStossA+j*3*Meter))=trimmean ↙
(DAkor(floor(ErsterStossA+j*3*Meter-Are):floor(ErsterStossA+j*3*Meter-IgnoreM)), ↙
Percent);
175     DBAV(floor(ErsterStossB+j*3*Meter-Are):floor(ErsterStossB+j*3*Meter))=trimmean ↙
(DBkor(floor(ErsterStossB+j*3*Meter-Are):floor(ErsterStossB+j*3*Meter-IgnoreM)), ↙
Percent);
176     sv(DAAV(floor(ErsterStossA+j*3*Meter-Are)),DBAV(floor(ErsterStossB+j*3*Meter- ↙
Are)),zAAV(floor(ErsterStossA+j*3*Meter-Are)));
177     sv(DAAV(floor(ErsterStossA+j*3*Meter)),DBAV(floor(ErsterStossB+j*3*Meter)), ↙
zAAV(floor(ErsterStossA+j*3*Meter)));
178 end
179
180 % letztes Rohrelement
181 anzahlA=floor((EndeA-LetzterStossA)/(mean*Meter));
182 Are=(EndeA-LetzterStossA)-anzahlA*mean*Meter;
183 Ara=mean*Meter;
184 ZAra=1;
185 while Ara<=IgnoreM
186     ZAra=ZAra+1;
187     Ara=Ara+mean*Meter;
188 end
189 zAAV(floor(LetzterStossA):floor(EndeA))=zA(floor(LetzterStossA):floor(EndeA));
190 zBAV(floor(LetzterStossB):floor(EndeB))=zB(floor(LetzterStossB):floor(EndeB));
191
192 DAAV(floor(LetzterStossA):floor(LetzterStossA+Ara))=trimmean(DAkor(floor ↙
(LetzterStossA+IgnoreM):floor(LetzterStossA+Ara)),Percent);
```

```
193 DBAV(floor(LetzterStossB):floor(LetzterStossB+Ara))=trimmean(DBkor(floor↙
(LetzterStossB+IgnoreM):floor(LetzterStossB+Ara)),Percent);
194 sv(DAAV(floor(LetzterStossA)),DBAV(floor(LetzterStossB)),zAAV(floor↙
(LetzterStossA)));
195 sv(DAAV(floor(LetzterStossA+Ara)),DBAV(floor(LetzterStossB+Ara)),zAAV(floor↙
(LetzterStossA+Ara)));
196 for k=1:1:(anzahlA-ZAra)
197     DAAV(floor(LetzterStossA+Ara+(k-1)*mean*Meter):floor↙
(LetzterStossA+Ara+k*mean*Meter))=trimmean(DAkor(floor(LetzterStossA+Ara+(k-1)↙
*mean*Meter):floor(LetzterStossA+Ara+k*mean*Meter)),Percent);
198     DBAV(floor(LetzterStossB+Ara+(k-1)*mean*Meter):floor↙
(LetzterStossB+Ara+k*mean*Meter))=trimmean(DBkor(floor(LetzterStossB+Ara+(k-1)↙
*mean*Meter):floor(LetzterStossB+Ara+k*mean*Meter)),Percent);
199     sv(DAAV(floor(LetzterStossA+Ara+(k-1)*mean*Meter)),DBAV(floor↙
(LetzterStossB+Ara+(k-1)*mean*Meter)),zAAV(floor(LetzterStossA+Ara+(k-1)↙
*mean*Meter)));
200     sv(DAAV(floor(LetzterStossA+Ara+k*mean*Meter)),DBAV(floor↙
(LetzterStossB+Ara+k*mean*Meter)),zAAV(floor(LetzterStossA+Ara+k*mean*Meter)));
201 end
202 DAAV(floor(EndeA-Are):floor(EndeA))=trimmean(DAkor(floor(EndeA-Are):floor(EndeA)),↙
Percent);
203 DBAV(floor(EndeB-Are):floor(EndeB))=trimmean(DBkor(floor(EndeB-Are):floor(EndeB)),↙
Percent);
204 sv(DAAV(floor(EndeA-Are)),DBAV(floor(EndeB-Are)),zAAV(floor(EndeA-Are)));
205 sv(DAAV(floor(EndeA)),DBAV(floor(EndeB)),zAAV(floor(EndeA)));
206
207 %%%%%%%%%% Resultate abspeichern %%%%%%%%%%
208 if i==1
209     M=[Messdaten];
210     dlmwrite([Inklinometer,'_',Ort,'_Dates.dat'], M, 'delimiter', '', 'precision',↙
6);
211     M=[mZ];
212     dlmwrite([Inklinometer,'_',Ort,'_DiameterA.dat'], M, 'delimiter', '\t',↙
'precision', 6);
213     dlmwrite([Inklinometer,'_',Ort,'_DiameterB.dat'], M, 'delimiter', '\t',↙
'precision', 6);
214     M=[mDA];
215     dlmwrite([Inklinometer,'_',Ort,'_DiameterA.dat'], M, '-append', 'delimiter',↙
'\t', 'precision', 6);
216     M=[mDB];
217     dlmwrite([Inklinometer,'_',Ort,'_DiameterB.dat'], M, '-append', 'delimiter',↙
'\t', 'precision', 6);
218 else
219     M=[mZ];
220     dlmwrite([Inklinometer,'_',Ort,'_DiameterA.dat'], M, '-append', 'delimiter',↙
'\t', 'precision', 6);
221     dlmwrite([Inklinometer,'_',Ort,'_DiameterB.dat'], M, '-append', 'delimiter',↙
'\t', 'precision', 6);
222     M=[mDA];
223     dlmwrite([Inklinometer,'_',Ort,'_DiameterA.dat'], M, '-append', 'delimiter',↙
'\t', 'precision', 6);
224     M=[mDB];
225     dlmwrite([Inklinometer,'_',Ort,'_DiameterB.dat'], M, '-append', 'delimiter',↙
'\t', 'precision', 6);
226 end
227 end
228
229 %%%%%%%%%% Abbildungen %%%%%%%%%%
230 colour=['k';'g';'c';'b';'m';'r';'y'];
231 if i==1
```

```
232     f1=figure('Name',[Inklinometer,'_',Typ↙
(n,:),'_DiameterA'],'NumberTitle','off');
233 else
234     figure(f1);
235 end
236 plot(DAA,zAA,colour(i),'LineWidth',2)
237 title(['Field measurement: ',Ort,', borehole ',Inklinometer])
238 switch check
239     case {'NS'}
240         xlabel('Sensor inclination {\alpha}PA [°]')
241     case {'NR'}
242         xlabel('Wheel inclination {\alpha}LA [°]')
243     otherwise
244         xlabel('Diameter DA [mm]')
245 end
246 ylabel('Position in the borehole z [m]')
247 ylim([0 inf])
248 axis ij
249 hold on
250 legendenvektor(i,:)=[Messdaten(i,:)];
251 if i==1
252     grid on
253     grid minor
254     box on
255 end
256 legend(legendenvektor(:,:))
257 saveas(gcf,[Inklinometer,'_',Typ(n,:),'_DiameterA.fig'])
258
259 colour=['k';'g';'c';'b';'m';'r';'y'];
260 if i==1
261     f2=figure('Name',[Inklinometer,'_',Typ↙
(n,:),'_DiameterB'],'NumberTitle','off');
262 else
263     figure(f2);
264 end
265 plot(DBB,zBB,colour(i),'LineWidth',2)
266 title(['Field measurement: ',Ort,', borehole ',Inklinometer])
267 switch check
268     case {'NS'}
269         xlabel('Sensor inclination {\alpha}PB [°]')
270     case {'NR'}
271         xlabel('Wheel inclination {\alpha}LB [°]')
272     otherwise
273         xlabel('Diameter DB [mm]')
274 end
275 ylabel('Position in the borehole z [m]')
276 ylim([0 inf])
277 axis ij
278 hold on
279 legendenvektor(i,:)=[Messdaten(i,:)];
280 if i==1
281     grid on
282     grid minor
283     box on
284 end
285 legend(legendenvektor(:,:))
286 saveas(gcf,[Inklinometer,'_',Typ(n,:),'_DiameterB.fig'])
287
288 %%%%%%%%%% Krümmungen berechnen und abspeichern %%%%%%%%%%
289 if i==2 || i==4
```

```
290     zKA=zA(1:(DepthCut-1))+diff(zA(1:DepthCut))/2;
291     KA=((diff(NSA(1:DepthCut)))/180*pi)./(diff(zA(1:DepthCut))*1000);
292     if i==2
293         M=[zKA.'];
294         dlmwrite([Inklinometer,'_',Ort,'_CurvatureA.dat'], M, 'delimiter', '\t',↙
'precision', 6);
295     else
296         M=[zKA.'];
297         dlmwrite([Inklinometer,'_',Ort,'_CurvatureA.dat'], M, '-append',↙
'delimiter', '\t', 'precision', 6);
298     end
299     M=[KA.'];
300     dlmwrite([Inklinometer,'_',Ort,'_CurvatureA.dat'], M, '-append', 'delimiter',↙
'\t', 'precision', 6);
301
302     zKB=zB(1:(DepthCut-1))+diff(zB(1:DepthCut))/2;
303     KB=((diff(NSB(1:DepthCut)))/180*pi)./(diff(zB(1:DepthCut))*1000);
304     if i==2
305         M=[zKB.'];
306         dlmwrite([Inklinometer,'_',Ort,'_CurvatureB.dat'], M, 'delimiter', '\t',↙
'precision', 6);
307     else
308         M=[zKB.'];
309         dlmwrite([Inklinometer,'_',Ort,'_CurvatureB.dat'], M, '-append',↙
'delimiter', '\t', 'precision', 6);
310     end
311     M=[KB.'];
312     dlmwrite([Inklinometer,'_',Ort,'_CurvatureB.dat'], M, '-append', 'delimiter',↙
'\t', 'precision', 6);
313 end
314
315 end
316
317 %%%%%%%%%% Werte in Matrix schreiben %%%%%%%%%%
318 function [sv]=sv(mDAe,mDBe,mZe)
319 w=w+1;
320
321 mDA(w)=mDAe;
322 mDB(w)=mDBe;
323 mZ(w)=mZe;
324 end
325
326 end
```

```
function IDM_Deformations;
clear all;

%%%%%%%%%% Eingabewerte Auswertung %%%%%%%%%%
span=3000           % Spannweite des gleitenden Mittelwertes für Savitzky-Golay-Filter für ungemittelte Darstellung der Messwerte
degree=2;           % Polynomgrad für Savitzky-Golay-Filter für ungemittelte Darstellung der Messwerte
mean=1/3            % Prozent von einem Meter (Abschnittslänge für die Mittelwertbildung)
Ignore1=0.25        % Bereich in Meter, welcher nach dem Rohranfang für die Mittelwertbildung vernachlässigt wird
Ignore=0.25         % Bereich in Meter, welcher vor und nach jedem Stoß (Verbindung Rohrelement) für die Mittelwertbidlung vernachlässigt wird
Percent=0;          % Prozent der Messwerte, welche als Ausreißer ausgeschlossen werden
BohrlochTiefe=0     % BohrlochTiefe=0: Auswertung bis zmax
                    % BohrlochTiefe=z: Auswertung bis z
Cutoff=0;           % Anzahl an Messwerten, welche am Rohrende vernachlässigt werden
check='no'          % 'no': übliche Auswertung
                    % 'NS'/'NR': Auswertung um die Messungen bezüglich Neigung Sonde oder Neigung Rad zu überprüfen

%%%%%%%%%% Eingabewerte Bohrloch %%%%%%%%%%
% Messdaten müssen im Ordner Ort wie folgt abgelegt sein:
%       Bezeichnung_ddmmyyyy_A000.dat
%       Bezeichnung_ddmmyyyy_B000.dat
%       Bezeichnung_ddmmyyyy_A180.dat
%       Bezeichnung_ddmmyyyy_B180.dat

Ort='Ordner';                       % Name des Ordners am Computer, welcher die abgspeicherten Messdaten enthält
Inklinometer='001';                 % Bezeichnung der Bohrung bzw. des Inklinometerrohres
Typ=['000';'000'];                  % Messrichtungen '000' oder '180'
AnzahlMessungen=2                   % Anzahl an auszuwertenden Messungen
Messdaten=['21022020';'27022020']   % Datum der Messungen
Rohrverschnitt=2.8                  % Länge des Rohrstückes in Meter (Abstand Rohranfang bis zum ersten Rohrelement)

%%%%%%%%%% Geometrie %%%%%%%%%%
% Wert für 84er Rohr: X=19.3671
% Wert für 71er Rohr: X=6.371
Meter=3567;     % Anzahl an Messungen pro Meter Rohr
d=56            % Durchmesser der Räder der Messsonde
Y=10            % Basislänge des Hebels
X=19.3671       % Abstand zur Bestimmung der Lage des Rotationszentrums des Hebels

G(1)=d;
G(2)=X;
G(3)=Y;

%%%%%%%%%% Messdaten einlesen %%%%%%%%%%
n=AnzahlMessungen;
global mDA;
global mDB;
global mNSA;
global mNSB;
global mZ;
```

```
 50 global w;
 51
 52 for i=1:1:n
 53 TiefeBohrloch=BohrlochTiefe;
 54 clear mDA;
 55 clear mDB;
 56 clear mNSA;
 57 clear mNSB;
 58 clear mZ;
 59 w=0;
 60
 61 % Einlesen der Messrichtung A0 oder A180
 62 PfadA=['\',Ort,'\',Inklinometer,'_',Messdaten(i,:),'_A',Typ(i,:),'.dat']
 63 [tA URA USA UQA TempA DruckA zA_readin NSA NQA NRA DA] = textread(PfadA,'%f %f %f↙
%f %f %f %f %f %f %f %f %f','headerlines',2);
 64
 65 % Einlesen der Messrichtung B0 oder B180
 66 PfadB=['\',Ort,'\',Inklinometer,'_',Messdaten(i,:),'_B',Typ(i,:),'.dat']
 67 [tB URB USB UQB TempB DruckB zB_readin NSB NQB NRB DB] = textread(PfadB,'%f %f %f↙
%f %f %f %f %f %f %f %f %f','headerlines',2);
 68
 69 % relativer Abstand zwischen Erst- und Folgewerten in Messrichtung A und B
 70 zA=zA_readin-zA_readin(1);
 71 zB=zB_readin-zB_readin(1);
 72
 73 if (TiefeBohrloch>0) && (i==1)
 74     Depth=Meter*TiefeBohrloch;
 75 end
 76 if TiefeBohrloch==0
 77     [TiefeBohrloch,Depth]=max(zA);
 78     TiefeBohrloch
 79 end
 80 DepthCut=floor((Depth-Cutoff)/2)*2
 81 Anzahl3m=floor((TiefeBohrloch-roundn(Cutoff/Meter,3)-Rohrverschnitt)/3)
 82
 83 % Anzahl an Messwerten an den Punkten Start, erster Stoß, letzter Stoß und Ende in↙
Messrichtung A und B
 84 StartA=1;
 85 StartB=1;
 86 ErsterStossA=round(Rohrverschnitt*Meter);
 87 ErsterStossB=round(Rohrverschnitt*Meter);
 88 LetzterStossA=round(ErsterStossA+Anzahl3m*3*Meter);
 89 LetzterStossB=round(ErsterStossB+Anzahl3m*3*Meter);
 90 EndeA=DepthCut;
 91 EndeB=DepthCut;
 92
 93 %%%%%%%%%% Querneigungskorrektur %%%%%%%%%%
 94 switch check
 95     case {'NS'}         % Überprüfung Messungen bezüglich Neigung Sonde
 96         DAkor=NSA;
 97         DBkor=NSB;
 98     case {'NR'}         % Überprüfung Messungen bezüglich Neigung Rad
 99         DAkor=NRA;
100         DBkor=NRB;
101     otherwise           % übliche Auswertung mit Querneigungskorrektur
102         DAkor=Kor(USA,URA,UQA,G);
103         DBkor=Kor(USB,URB,UQB,G);
104 end
105
106 %%%%%%%%%% Filter %%%%%%%%%%
```

```
% Glättung der Messdaten mittels Savitzky-Golay-Filter
DAA(1:DepthCut)=smooth(DAkor(1:DepthCut),span,'sgolay',degree);
DBB(1:DepthCut)=smooth(DBkor(1:DepthCut),span,'sgolay',degree);
zAA(1:DepthCut)=zA(1:DepthCut);
zBB(1:DepthCut)=zB(1:DepthCut);

%%%%%%%%%% Messwerte mitteln %%%%%%%%%%
if check=='no'
IgnoreM1=floor(Meter*Ignore1);
IgnoreM=floor(Meter*Ignore);

% Rohrstück
anzahlA=floor(ErsterStossA/(mean*Meter));
Ara=ErsterStossA-anzahlA*mean*Meter;
ZAra=0;
while Ara<=IgnoreM1
    ZAra=ZAra+1;
    Ara=Ara+mean*Meter;
end
Are=mean*Meter;
ZAre=1;
while Are<=IgnoreM
    ZAre=ZAre+1;
    Are=Are+mean*Meter;
end
zAAV(floor(StartA):floor(ErsterStossA))=zA(floor(StartA):floor(ErsterStossA));
zBAV(floor(StartB):floor(ErsterStossB))=zB(floor(StartB):floor(ErsterStossB));

DAAV(floor(StartA):floor(Ara))=trimmean(DAkor(floor(StartA+IgnoreM1):floor(Ara)),↙
Percent);
DBAV(floor(StartB):floor(Ara))=trimmean(DBkor(floor(StartB+IgnoreM1):floor(Ara)),↙
Percent);
NSAAV(floor(StartA):floor(Ara))=trimmean(NSA(floor(StartA+IgnoreM1):floor(Ara)),↙
Percent);
NSBAV(floor(StartB):floor(Ara))=trimmean(NSB(floor(StartB+IgnoreM1):floor(Ara)),↙
Percent);
sv(DAAV(floor(StartA)),DBAV(floor(StartB)),NSAAV(floor(StartA)),NSBAV(floor↙
(StartB)),(zAAV(floor(StartA))+zAAV(floor(Ara)))/2);
for k=1:1:(anzahlA-ZAra-ZAre)
    DAAV(floor(Ara+(k-1)*mean*Meter):floor(Ara+k*mean*Meter))=trimmean(DAkor(floor↙
(Ara+(k-1)*mean*Meter):floor(Ara+k*mean*Meter)),Percent);
    DBAV(floor(Ara+(k-1)*mean*Meter):floor(Ara+k*mean*Meter))=trimmean(DBkor(floor↙
(Ara+(k-1)*mean*Meter):floor(Ara+k*mean*Meter)),Percent);
    NSAAV(floor(Ara+(k-1)*mean*Meter):floor(Ara+k*mean*Meter))=trimmean(NSA(floor↙
(Ara+(k-1)*mean*Meter):floor(Ara+k*mean*Meter)),Percent);
    NSBAV(floor(Ara+(k-1)*mean*Meter):floor(Ara+k*mean*Meter))=trimmean(NSB(floor↙
(Ara+(k-1)*mean*Meter):floor(Ara+k*mean*Meter)),Percent);
    sv(DAAV(floor(Ara+(k-1)*mean*Meter)),DBAV(floor(Ara+(k-1)*mean*Meter)),NSAAV↙
(floor(Ara+(k-1)*mean*Meter)),NSBAV(floor(Ara+(k-1)*mean*Meter)),(zAAV(floor(Ara+(k-1)↙
*mean*Meter))+zAAV(floor(Ara+k*mean*Meter)))/2);
end
DAAV(floor(ErsterStossA-Are):floor(ErsterStossA))=trimmean(DAkor(floor↙
(ErsterStossA-Are):floor(ErsterStossA-IgnoreM)),Percent);
DBAV(floor(ErsterStossB-Are):floor(ErsterStossB))=trimmean(DBkor(floor↙
(ErsterStossB-Are):floor(ErsterStossB-IgnoreM)),Percent);
NSAAV(floor(ErsterStossA-Are):floor(ErsterStossA))=trimmean(NSA(floor↙
(ErsterStossA-Are):floor(ErsterStossA-IgnoreM)),Percent);
NSBAV(floor(ErsterStossB-Are):floor(ErsterStossB))=trimmean(NSB(floor↙
(ErsterStossB-Are):floor(ErsterStossB-IgnoreM)),Percent);
sv(DAAV(floor(ErsterStossA-Are)),DBAV(floor(ErsterStossB-Are)),NSAAV(floor↙
```

```
(ErsterStossA-Are)),NSBAV(floor(ErsterStossB-Are)),(zAAV(floor(ErsterStossA-Are))+zAAV
(floor(ErsterStossA)))/2);
152
153 % für alle außer dem letzten Rohrelement
154 for j=1:1:Anzahl3m
155     anzahlA=floor(3*Meter/(mean*Meter));
156     Ara=mean*Meter;
157     ZAra=1;
158     while Ara<=IgnoreM
159         ZAra=ZAra+1;
160         Ara=Ara+mean*Meter;
161     end
162     Are=mean*Meter;
163     ZAre=1;
164     while Are<=IgnoreM
165         ZAre=ZAre+1;
166         Are=Are+mean*Meter;
167     end
168     zAAV(floor(ErsterStossA+(j-1)*3*Meter):floor(ErsterStossA+j*3*Meter))=zA(floor
(ErsterStossA+(j-1)*3*Meter):floor(ErsterStossA+j*3*Meter));
169     zBAV(floor(ErsterStossB+(j-1)*3*Meter):floor(ErsterStossB+j*3*Meter))=zB(floor
(ErsterStossB+(j-1)*3*Meter):floor(ErsterStossB+j*3*Meter));
170
171     DAAV(floor(ErsterStossA+(j-1)*3*Meter):floor(ErsterStossA+(j-1)*3*Meter+Ara))
=trimmean(DAkor(floor(ErsterStossA+(j-1)*3*Meter+IgnoreM):floor(ErsterStossA+(j-1)
*3*Meter+Ara)),Percent);
172     DBAV(floor(ErsterStossB+(j-1)*3*Meter):floor(ErsterStossB+(j-1)*3*Meter+Ara))
=trimmean(DBkor(floor(ErsterStossB+(j-1)*3*Meter+IgnoreM):floor(ErsterStossB+(j-1)
*3*Meter+Ara)),Percent);
173     NSAAV(floor(ErsterStossA+(j-1)*3*Meter):floor(ErsterStossA+(j-1)*3*Meter+Ara))
=trimmean(NSA(floor(ErsterStossA+(j-1)*3*Meter+IgnoreM):floor(ErsterStossA+(j-1)
*3*Meter+Ara)),Percent);
174     NSBAV(floor(ErsterStossB+(j-1)*3*Meter):floor(ErsterStossB+(j-1)*3*Meter+Ara))
=trimmean(NSB(floor(ErsterStossB+(j-1)*3*Meter+IgnoreM):floor(ErsterStossB+(j-1)
*3*Meter+Ara)),Percent);
175     sv(DAAV(floor(ErsterStossA+(j-1)*3*Meter)),DBAV(floor(ErsterStossB+(j-1)
*3*Meter)),NSAAV(floor(ErsterStossA+(j-1)*3*Meter)),NSBAV(floor(ErsterStossB+(j-1)
*3*Meter)),(zAAV(floor(ErsterStossA+(j-1)*3*Meter))+zAAV(floor(ErsterStossA+(j-1)
*3*Meter+Ara)))/2);
176     for k=1:1:(anzahlA-ZAra-ZAre)
177         DAAV(floor(ErsterStossA+(j-1)*3*Meter+Ara+(k-1)*mean*Meter):floor
(ErsterStossA+(j-1)*3*Meter+Ara+k*mean*Meter))=trimmean(DAkor(floor(ErsterStossA+(j-1)
*3*Meter+Ara+(k-1)*mean*Meter):floor(ErsterStossA+(j-1)*3*Meter+Ara+k*mean*Meter)),
Percent);
178         DBAV(floor(ErsterStossB+(j-1)*3*Meter+Ara+(k-1)*mean*Meter):floor
(ErsterStossB+(j-1)*3*Meter+Ara+k*mean*Meter))=trimmean(DBkor(floor(ErsterStossB+(j-1)
*3*Meter+Ara+(k-1)*mean*Meter):floor(ErsterStossB+(j-1)*3*Meter+Ara+k*mean*Meter)),
Percent);
179         NSAAV(floor(ErsterStossA+(j-1)*3*Meter+Ara+(k-1)*mean*Meter):floor
(ErsterStossA+(j-1)*3*Meter+Ara+k*mean*Meter))=trimmean(NSA(floor(ErsterStossA+(j-1)
*3*Meter+Ara+(k-1)*mean*Meter):floor(ErsterStossA+(j-1)*3*Meter+Ara+k*mean*Meter)),
Percent);
180         NSBAV(floor(ErsterStossB+(j-1)*3*Meter+Ara+(k-1)*mean*Meter):floor
(ErsterStossB+(j-1)*3*Meter+Ara+k*mean*Meter))=trimmean(NSB(floor(ErsterStossB+(j-1)
*3*Meter+Ara+(k-1)*mean*Meter):floor(ErsterStossB+(j-1)*3*Meter+Ara+k*mean*Meter)),
Percent);
181         sv(DAAV(floor(ErsterStossA+(j-1)*3*Meter+Ara+(k-1)*mean*Meter)),DBAV(floor
(ErsterStossB+(j-1)*3*Meter+Ara+(k-1)*mean*Meter)),NSAAV(floor(ErsterStossA+(j-1)
*3*Meter+Ara+(k-1)*mean*Meter)),NSBAV(floor(ErsterStossB+(j-1)*3*Meter+Ara+(k-1)
*mean*Meter)),(zAAV(floor(ErsterStossA+(j-1)*3*Meter+Ara+(k-1)*mean*Meter))+zAAV(floor
```

```
(ErsterStossA+(j-1)*3*Meter+Ara+k*mean*Meter)))/2);
182     end
183     DAAV(floor(ErsterStossA+j*3*Meter-Are):floor(ErsterStossA+j*3*Meter))=trimmean ↙
(DAkor(floor(ErsterStossA+j*3*Meter-Are):floor(ErsterStossA+j*3*Meter-IgnoreM)), ↙
Percent);
184     DBAV(floor(ErsterStossB+j*3*Meter-Are):floor(ErsterStossB+j*3*Meter))=trimmean ↙
(DBkor(floor(ErsterStossB+j*3*Meter-Are):floor(ErsterStossB+j*3*Meter-IgnoreM)), ↙
Percent);
185     NSAAV(floor(ErsterStossA+j*3*Meter-Are):floor(ErsterStossA+j*3*Meter)) ↙
=trimmean(NSA(floor(ErsterStossA+j*3*Meter-Are):floor(ErsterStossA+j*3*Meter- ↙
IgnoreM)),Percent);
186     NSBAV(floor(ErsterStossB+j*3*Meter-Are):floor(ErsterStossB+j*3*Meter)) ↙
=trimmean(NSB(floor(ErsterStossB+j*3*Meter-Are):floor(ErsterStossB+j*3*Meter- ↙
IgnoreM)),Percent);
187     sv(DAAV(floor(ErsterStossA+j*3*Meter-Are)),DBAV(floor(ErsterStossB+j*3*Meter- ↙
Are)),NSAAV(floor(ErsterStossA+j*3*Meter-Are)),NSBAV(floor(ErsterStossB+j*3*Meter- ↙
Are)),(zAAV(floor(ErsterStossA+j*3*Meter-Are))+zAAV(floor(ErsterStossA+j*3*Meter))) ↙
/2);
188 end
189
190 % letztes Rohrelement
191 anzahlA=floor((EndeA-LetzterStossA)/(mean*Meter));
192 Are=(EndeA-LetzterStossA)-anzahlA*mean*Meter;
193 Ara=mean*Meter;
194 ZAra=1;
195 while Ara<=IgnoreM
196     ZAra=ZAra+1;
197     Ara=Ara+mean*Meter;
198 end
199 zAAV(floor(LetzterStossA):floor(EndeA))=zA(floor(LetzterStossA):floor(EndeA));
200 zBAV(floor(LetzterStossB):floor(EndeB))=zB(floor(LetzterStossB):floor(EndeB));
201
202 DAAV(floor(LetzterStossA):floor(LetzterStossA+Ara))=trimmean(DAkor(floor ↙
(LetzterStossA+IgnoreM):floor(LetzterStossA+Ara)),Percent);
203 DBAV(floor(LetzterStossB):floor(LetzterStossB+Ara))=trimmean(DBkor(floor ↙
(LetzterStossB+IgnoreM):floor(LetzterStossB+Ara)),Percent);
204 NSAAV(floor(LetzterStossA):floor(LetzterStossA+Ara))=trimmean(NSA(floor ↙
(LetzterStossA+IgnoreM):floor(LetzterStossA+Ara)),Percent);
205 NSBAV(floor(LetzterStossB):floor(LetzterStossB+Ara))=trimmean(NSB(floor ↙
(LetzterStossB+IgnoreM):floor(LetzterStossB+Ara)),Percent);
206 sv(DAAV(floor(LetzterStossA)),DBAV(floor(LetzterStossB)),NSAAV(floor ↙
(LetzterStossA)),NSBAV(floor(LetzterStossB)),(zAAV(floor(LetzterStossA))+zAAV(floor ↙
(LetzterStossA+Ara)))/2);
207 for k=1:1:(anzahlA-ZAra)
208     DAAV(floor(LetzterStossA+Ara+(k-1)*mean*Meter):floor ↙
(LetzterStossA+Ara+k*mean*Meter))=trimmean(DAkor(floor(LetzterStossA+Ara+(k-1) ↙
*mean*Meter):floor(LetzterStossA+Ara+k*mean*Meter)),Percent);
209     DBAV(floor(LetzterStossB+Ara+(k-1)*mean*Meter):floor ↙
(LetzterStossB+Ara+k*mean*Meter))=trimmean(DBkor(floor(LetzterStossB+Ara+(k-1) ↙
*mean*Meter):floor(LetzterStossB+Ara+k*mean*Meter)),Percent);
210     NSAAV(floor(LetzterStossA+Ara+(k-1)*mean*Meter):floor ↙
(LetzterStossA+Ara+k*mean*Meter))=trimmean(NSA(floor(LetzterStossA+Ara+(k-1) ↙
*mean*Meter):floor(LetzterStossA+Ara+k*mean*Meter)),Percent);
211     NSBAV(floor(LetzterStossB+Ara+(k-1)*mean*Meter):floor ↙
(LetzterStossB+Ara+k*mean*Meter))=trimmean(NSB(floor(LetzterStossB+Ara+(k-1) ↙
*mean*Meter):floor(LetzterStossB+Ara+k*mean*Meter)),Percent);
212     sv(DAAV(floor(LetzterStossA+Ara+(k-1)*mean*Meter)),DBAV(floor ↙
(LetzterStossB+Ara+(k-1)*mean*Meter)),NSAAV(floor(LetzterStossA+Ara+(k-1) ↙
*mean*Meter)),NSBAV(floor(LetzterStossB+Ara+(k-1)*mean*Meter)),(zAAV(floor ↙
(LetzterStossA+Ara+(k-1)*mean*Meter))+zAAV(floor(LetzterStossA+Ara+k*mean*Meter)))/2);
```

```
end
DAAV(floor(EndeA-Are):floor(EndeA))=trimmean(DAkor(floor(EndeA-Are):floor(EndeA)),Percent);
DBAV(floor(EndeB-Are):floor(EndeB))=trimmean(DBkor(floor(EndeB-Are):floor(EndeB)),Percent);
NSAAV(floor(EndeA-Are):floor(EndeA))=trimmean(NSA(floor(EndeA-Are):floor(EndeA)),Percent);
NSBAV(floor(EndeB-Are):floor(EndeB))=trimmean(NSB(floor(EndeB-Are):floor(EndeB)),Percent);
sv(DAAV(floor(EndeA-Are)),DBAV(floor(EndeB-Are)),NSAAV(floor(EndeA-Are)),NSBAV(floor(EndeB-Are)),(zAAV(floor(EndeA-Are))+zAAV(floor(EndeA)))/2);

%%%%%%%%%% Resultate abspeichern %%%%%%%%%%
if i==1
    M=[Messdaten];
    dlmwrite([Inklinometer,'_',Ort,'_Dates.dat'], M, 'delimiter', '', 'precision', 6);
    M=[mZ];
    dlmwrite([Inklinometer,'_',Ort,'_DiameterA.dat'], M, 'delimiter', '\t', 'precision', 6);
    dlmwrite([Inklinometer,'_',Ort,'_DiameterB.dat'], M, 'delimiter', '\t', 'precision', 6);
    M=[mDA];
    dlmwrite([Inklinometer,'_',Ort,'_DiameterA.dat'], M, '-append', 'delimiter', '\t', 'precision', 6);
    M=[mDB];
    dlmwrite([Inklinometer,'_',Ort,'_DiameterB.dat'], M, '-append', 'delimiter', '\t', 'precision', 6);
else
    M=[mZ];
    dlmwrite([Inklinometer,'_',Ort,'_DiameterA.dat'], M, '-append', 'delimiter', '\t', 'precision', 6);
    dlmwrite([Inklinometer,'_',Ort,'_DiameterB.dat'], M, '-append', 'delimiter', '\t', 'precision', 6);
    M=[mDA];
    dlmwrite([Inklinometer,'_',Ort,'_DiameterA.dat'], M, '-append', 'delimiter', '\t', 'precision', 6);
    M=[mDB];
    dlmwrite([Inklinometer,'_',Ort,'_DiameterB.dat'], M, '-append', 'delimiter', '\t', 'precision', 6);
end
end

%%%%%%%%%% Abbildungen %%%%%%%%%%
colour=['k';'g';'c';'b';'m';'r';'y'];
if i==1
    f1=figure('Name',[Inklinometer,'_',Typ(n,:),'_DiameterA'],'NumberTitle','off');
else
    figure(f1);
end
plot(DAA,zAA,colour(i),'LineWidth',2)
title(['Field measurement: ',Ort,', borehole ',Inklinometer])
switch check
    case {'NS'}
        xlabel('Sensor inclination {\alpha}PA [°]')
    case {'NR'}
        xlabel('Wheel inclination {\alpha}LA [°]')
    otherwise
        xlabel('Diameter DA [mm]')
```

```
end
ylabel('Position in the borehole z [m]')
ylim([0 inf])
axis ij
hold on
legendenvektor(i,:)=[Messdaten(i,:)];
if i==1
    grid on
    grid minor
    box on
end
legend(legendenvektor(:,:))
saveas(gcf,[Inklinometer,'_',Typ(n,:),'_DiameterA.fig'])

colour=['k';'g';'c';'b';'m';'r';'y'];
if i==1
    f2=figure('Name',[Inklinometer,'_',Typ
(n,:),'_DiameterB'],'NumberTitle','off');
else
    figure(f2);
end
plot(DBB,zBB,colour(i),'LineWidth',2)
title(['Field measurement: ',Ort,', borehole ',Inklinometer])
switch check
    case {'NS'}
        xlabel('Sensor inclination {\alpha}PB [°]')
    case {'NR'}
        xlabel('Wheel inclination {\alpha}LB [°]')
    otherwise
        xlabel('Diameter DB [mm]')
end
ylabel('Position in the borehole z [m]')
ylim([0 inf])
axis ij
hold on
legendenvektor(i,:)=[Messdaten(i,:)];
if i==1
    grid on
    grid minor
    box on
end
legend(legendenvektor(:,:))
saveas(gcf,[Inklinometer,'_',Typ(n,:),'_DiameterB.fig'])

%%%%%%%%%% Krümmungen berechnen und abspeichern %%%%%%%%%%
if i==2 || i==4
    zKA=mZ(1:(numel(mZ)-1))+diff(mZ)/2;
    KA=((diff(mNSA))/180*pi)./(diff(mZ)*1000);
    if i==2
        M=[zKA];
        dlmwrite([Inklinometer,'_',Ort,'_CurvatureA.dat'], M, 'delimiter', '\t',
'precision', 6);
    else
        M=[zKA];
        dlmwrite([Inklinometer,'_',Ort,'_CurvatureA.dat'], M, '-append',
'delimiter', '\t', 'precision', 6);
    end
    M=[KA];
    dlmwrite([Inklinometer,'_',Ort,'_CurvatureA.dat'], M, '-append', 'delimiter',
'\t', 'precision', 6);
```

```
314
315     zKB=zKA;
316     KB=((diff(mNSB))/180*pi)./(diff(mZ)*1000);
317     if i==2
318         M=[zKB];
319         dlmwrite([Inklinometer,'_',Ort,'_CurvatureB.dat'], M, 'delimiter', '\t',↙
'precision', 6);
320     else
321         M=[zKB];
322         dlmwrite([Inklinometer,'_',Ort,'_CurvatureB.dat'], M, '-append',↙
'delimiter', '\t', 'precision', 6);
323     end
324     M=[KB];
325     dlmwrite([Inklinometer,'_',Ort,'_CurvatureB.dat'], M, '-append', 'delimiter',↙
'\t', 'precision', 6);
326 end
327
328 end
329
330 %%%%%%%%%% Werte in Matrix schreiben %%%%%%%%%%
331 function [sv]=sv(mDAe,mDBe,mNSAe,mNSBe,mZe)
332 w=w+1;
333
334 mDA(w)=mDAe;
335 mDB(w)=mDBe;
336 mNSA(w)=mNSAe;
337 mNSB(w)=mNSBe;
338 mZ(w)=mZe;
339 end
340
341 end
```

```
function Dkor=Kor(US,UR,UQ,G);
% Korrektur des Einflusses der Querneigung

% Korrekturkoeffizienten
A1=-0.0001585921;
A2=0.0001507314937;
A3=3.746651009e-006;
C1=-0.0002042935516;
C2=0.0002858638645;
C3=-0.001690189367;

NQ0=-0.43       % Neigung aus der Ebene einer vertikalen Messsonde
Sensitivity=16;

NS=asind(-US/Sensitivity);      % Neigung der Sonde
NR=asind(-UR/Sensitivity);      % Neigung des Hebels
NQ=asind(-UQ/Sensitivity);      % Neigung aus der Ebene

CF=1.0
% Differenzterm
NDif=NR-NS;
% Korrekturterm hinsichtlich Neigung aus der Ebene einer vertikalen Messsonde
NDifKor0=(A1*NR+A2*NS+A3).*(NQ0^2)+(C1*NR+C2*NS+C3).*NQ0;
% Korrekturterm hinsichtlich Neigung aus der Ebene
NDifKor=(A1*NR+A2*NS+A3).*(NQ.*NQ)+(C1*NR+C2*NS+C3).*NQ;

% korrigierte Innendurchmesser
Dkor=(G(1)+G(2)+sind(NDif-(NDifKor-NDifKor0))*G(3))/CF;

end
```

5 Test results

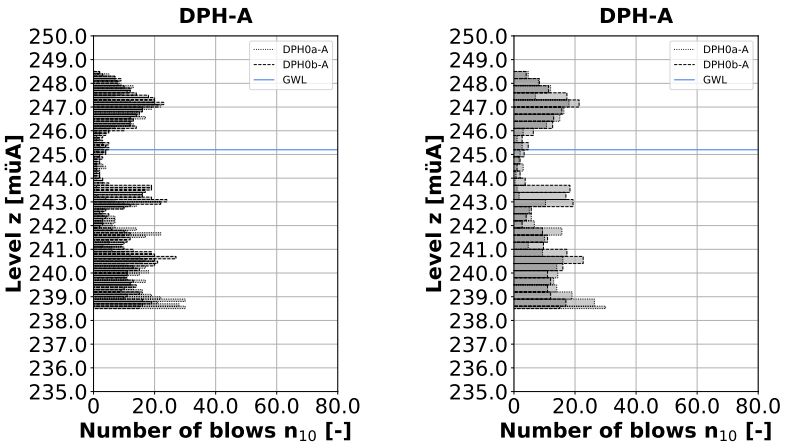

(a) original (b) averaged

Figure 1: Heavy dynamic probing tests - test area A, epoch 0

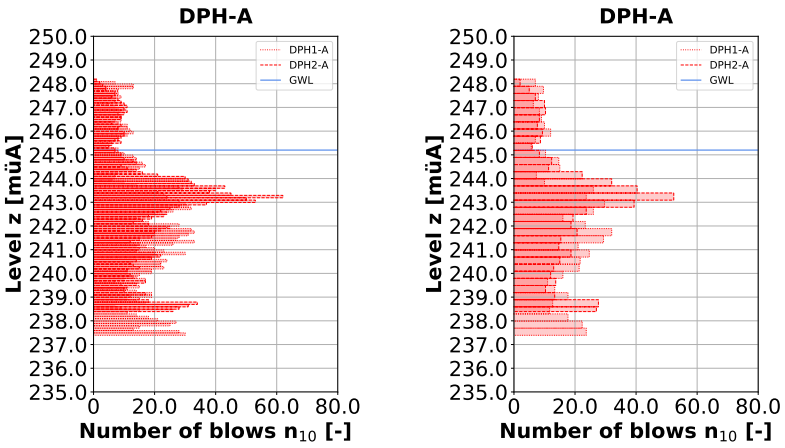

(a) original (b) averaged

Figure 2: Heavy dynamic probing tests - test area A, epoch 1

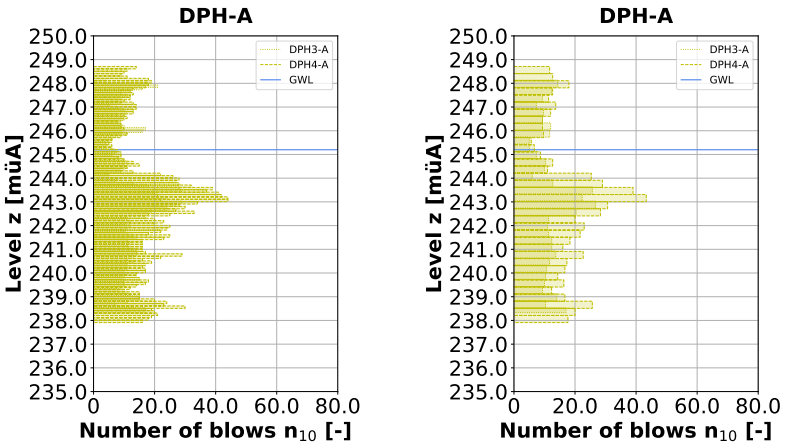

(a) original (b) averaged

Figure 3: Heavy dynamic probing tests - test area A, epoch 2

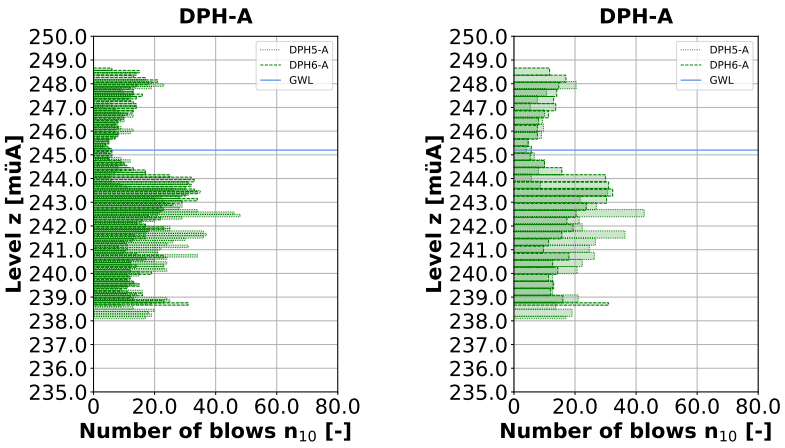

(a) original (b) averaged

Figure 4: Heavy dynamic probing tests - test area A, epoch 3

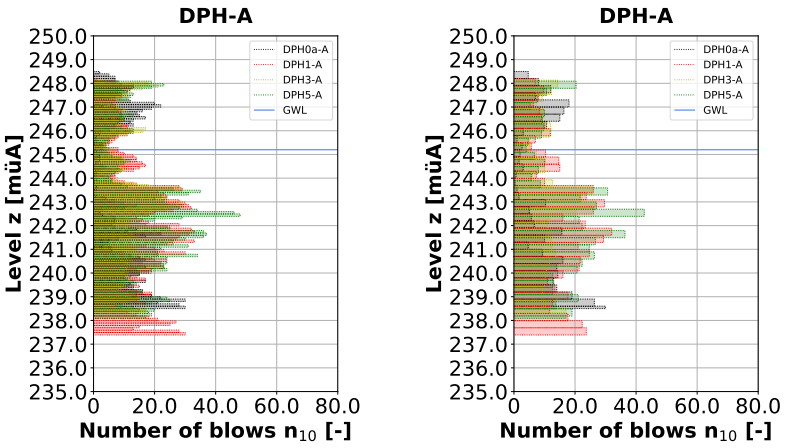

(a) original (b) averaged

Figure 5: Heavy dynamic probing tests - test area A, above left

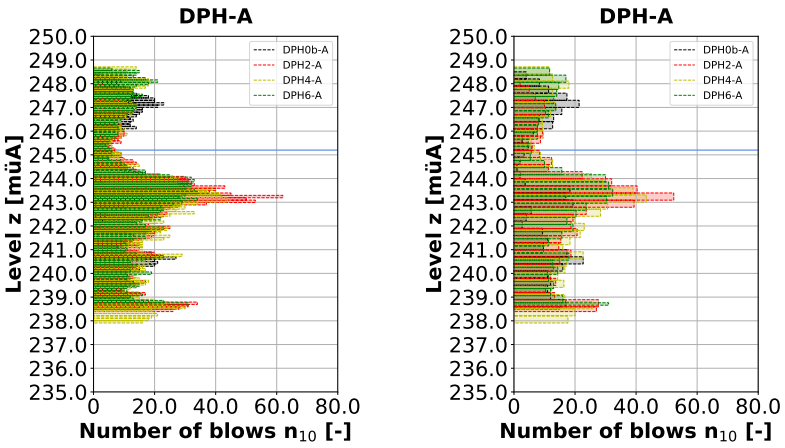

(a) original (b) averaged

Figure 6: Heavy dynamic probing tests - test area A, below right

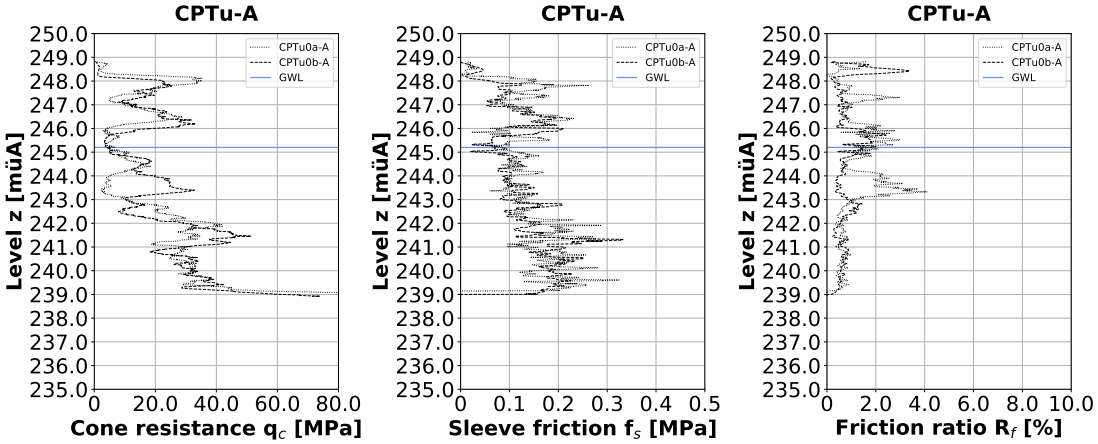

(a) original

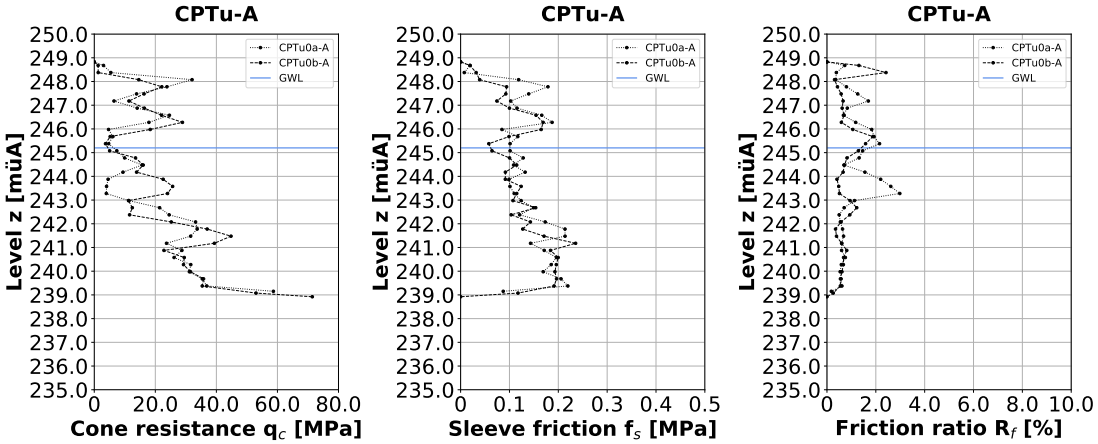

(b) averaged

Figure 7: Cone penetration tests with pore water pressure measurement - test area A, epoch 0 (1)

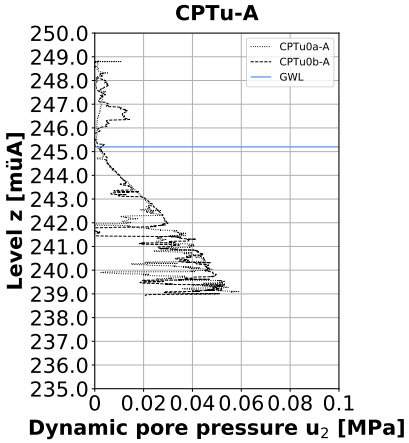

Figure 8: Cone penetration tests with pore water pressure measurement - test area A, epoch 0 (2)

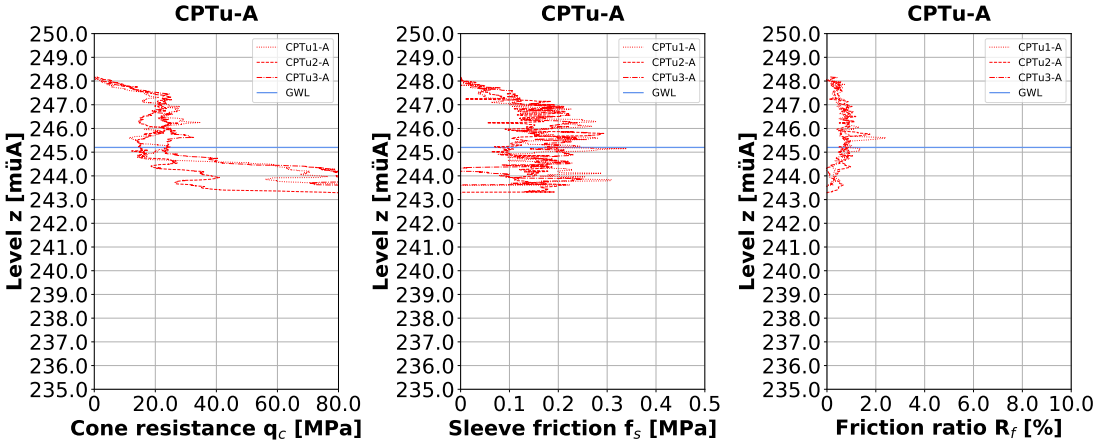

(a) original

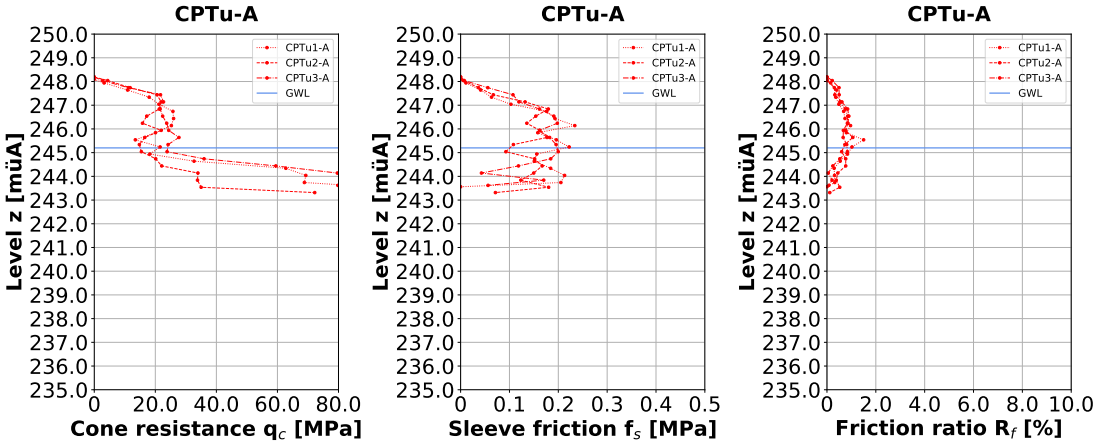

(b) averaged

Figure 9: Cone penetration tests with pore water pressure measurement - test area A, epoch 1 (1)

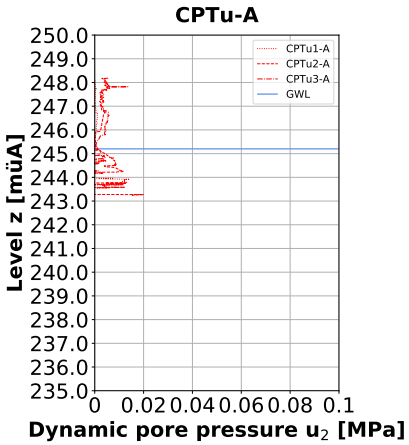

Figure 10: Cone penetration tests with pore water pressure measurement - test area A, epoch 1 (2)

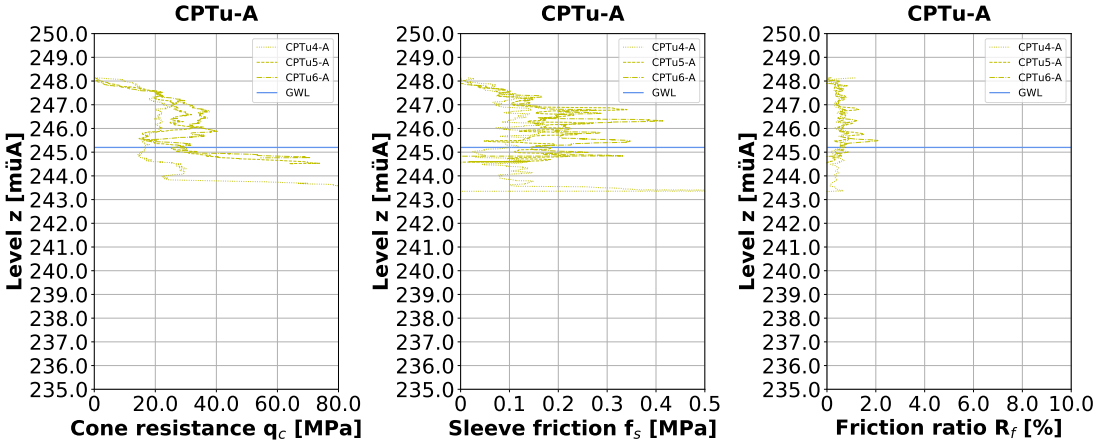

(a) original

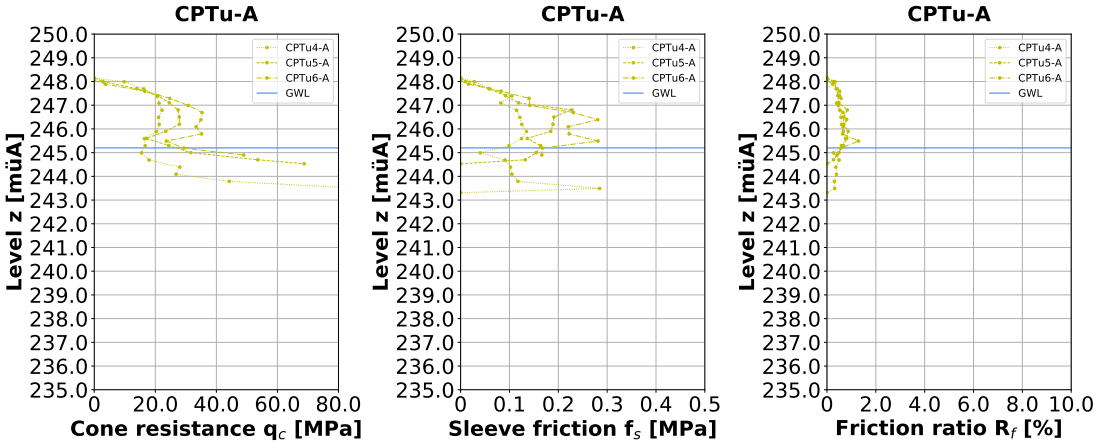

(b) averaged

Figure 11: Cone penetration tests with pore water pressure measurement - test area A, epoch 2 (1)

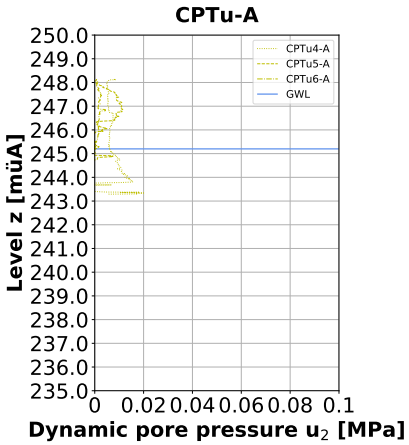

Figure 12: Cone penetration tests with pore water pressure measurement - test area A, epoch 2 (2)

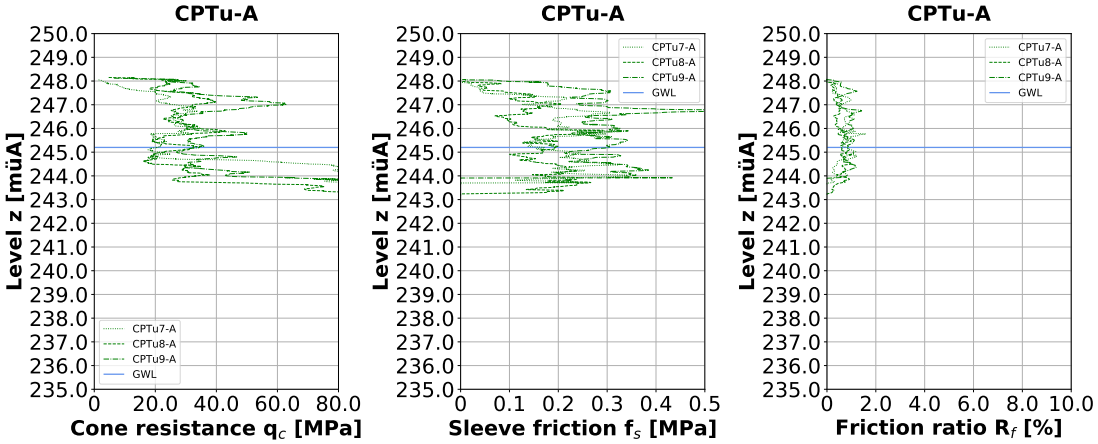

(a) original

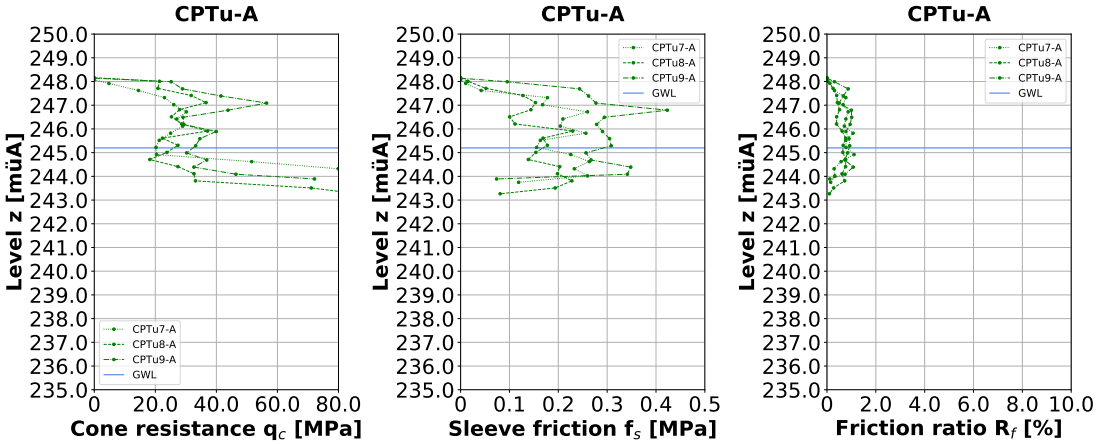

(b) averaged

Figure 13: Cone penetration tests with pore water pressure measurement - test area A, epoch 3 (1)

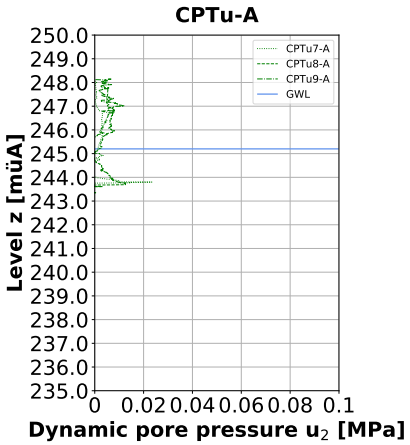

Figure 14: Cone penetration tests with pore water pressure measurement - test area A, epoch 3 (2)

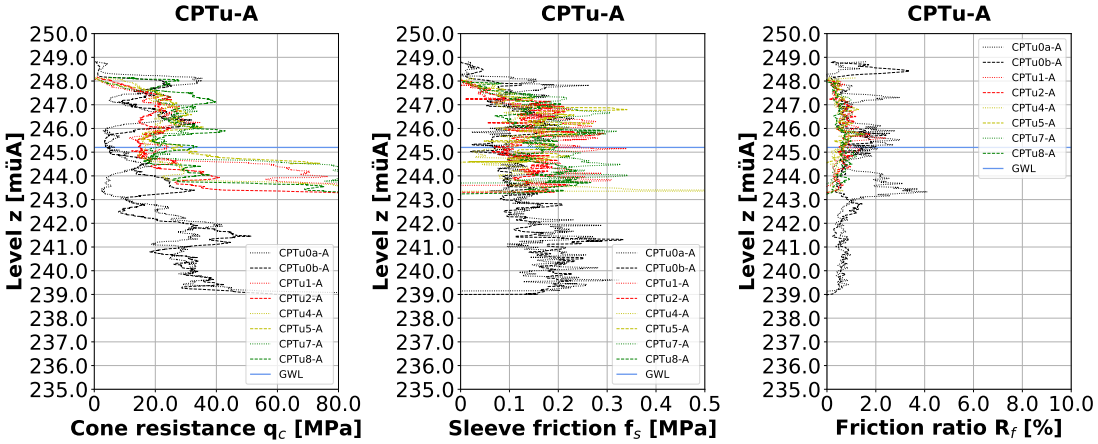

(a) original

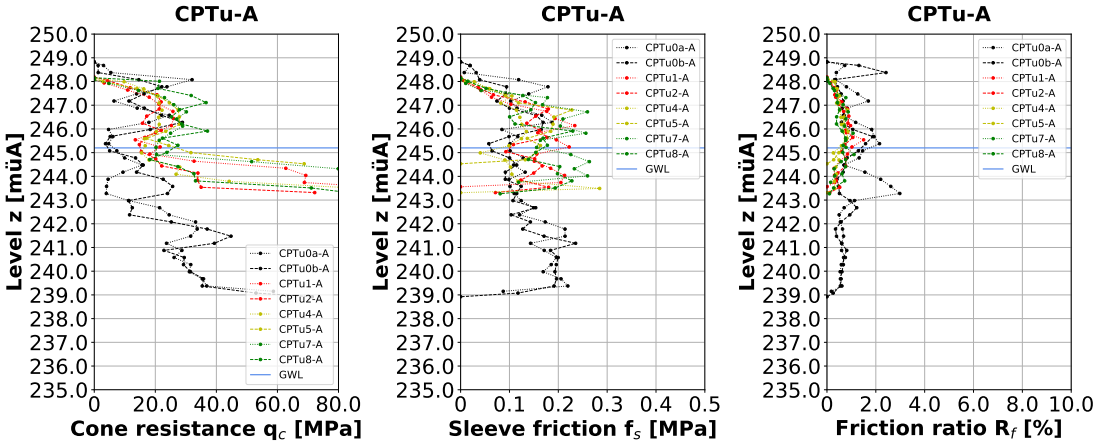

(b) averaged

Figure 15: Cone penetration tests with pore water pressure measurement - test area A, between four columns (1)

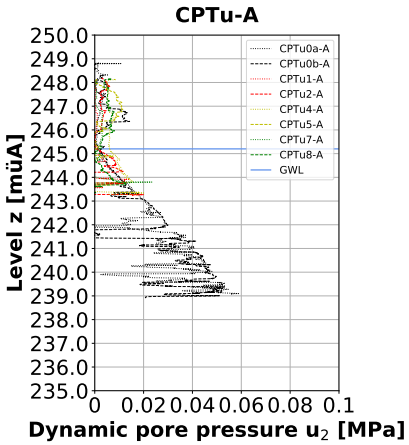

Figure 16: Cone penetration tests with pore water pressure measurement - test area A, between four columns (2)

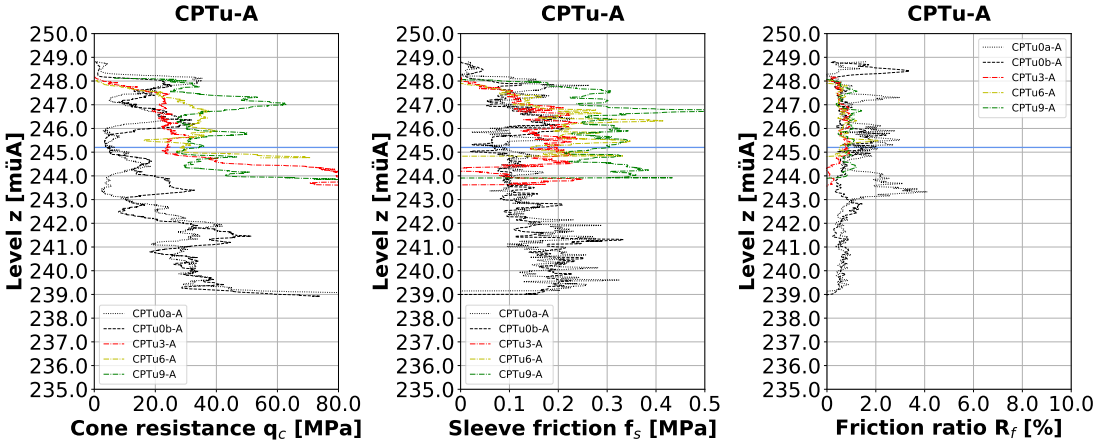

(a) original

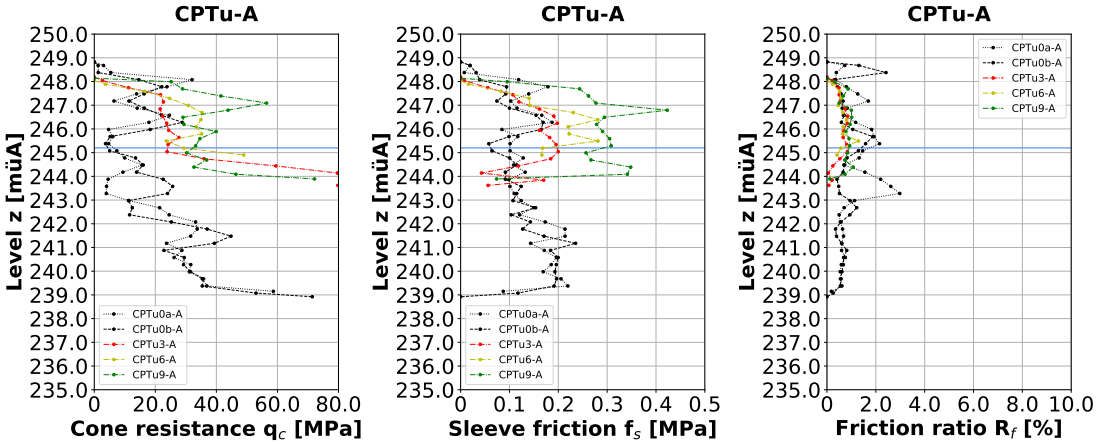

(b) averaged

Figure 17: Cone penetration tests with pore water pressure measurement - test area A, between two columns (1)

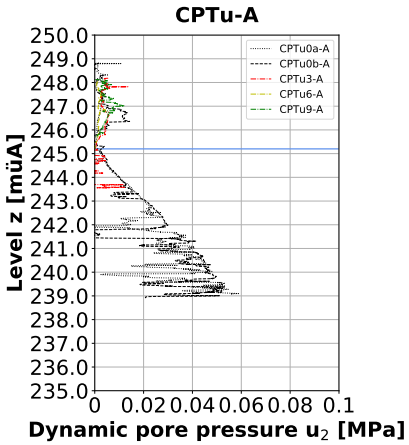

Figure 18: Cone penetration tests with pore water pressure measurement - test area A, between two columns (2)

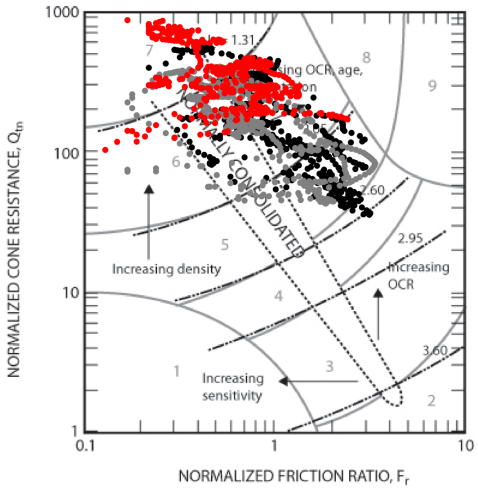

Figure 19: Normalized soil behaviour type chart (Robertson 2010) according to [18, p. 27] - CPTu0a-A (black), CPTu0b-A (grey) and CPTu1-A (red)

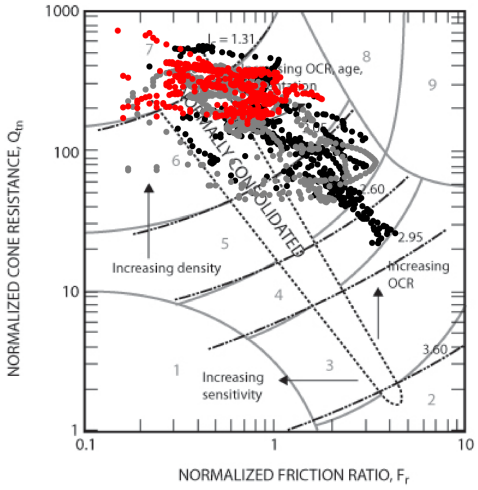

Figure 20: Normalized soil behaviour type chart (Robertson 2010) according to [18, p. 27] - CPTu0a-A (black), CPTu0b-A (grey) and CPTu2-A (red)

1 sensitive, fine grained
2 organic soils - clay
3 clays - silty clay to clay
4 silt mixtures - clayey silt to silty clay
5 sand mixtures - silty sand to sandy silt
6 sands - clean sand to silty sand
7 gravelly sand to dense sand
8 very stiff sand to clayey sand (heavily overconsolidated or cemented)
9 very stiff, fine grained (heavily overconsolidated or cemented)

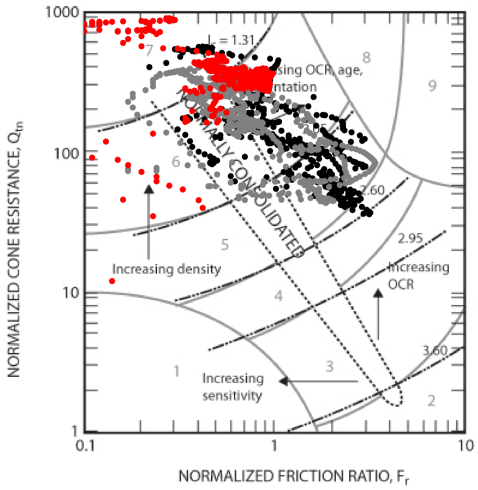

Figure 21: Normalized soil behaviour type chart (Robertson 2010) according to [18, p. 27] - CPTu0a-A (black), CPTu0b-A (grey) and CPTu3-A (red)

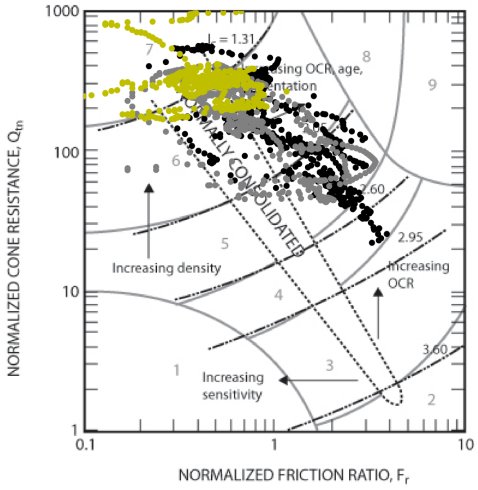

Figure 22: Normalized soil behaviour type chart (Robertson 2010) according to [18, p. 27] - CPTu0a-A (black), CPTu0b-A (grey) and CPTu4-A (yellow)

1 sensitive, fine grained
2 organic soils - clay
3 clays - silty clay to clay
4 silt mixtures - clayey silt to silty clay
5 sand mixtures - silty sand to sandy silt
6 sands - clean sand to silty sand
7 gravelly sand to dense sand
8 very stiff sand to clayey sand (heavily overconsolidated or cemented)
9 very stiff, fine grained (heavily overconsolidated or cemented)

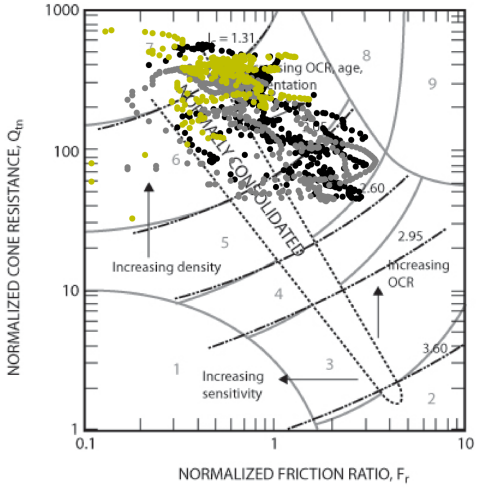

Figure 23: Normalized soil behaviour type chart (Robertson 2010) according to [18, p. 27] - CPTu0a-A (black), CPTu0b-A (grey) and CPTu5-A (yellow)

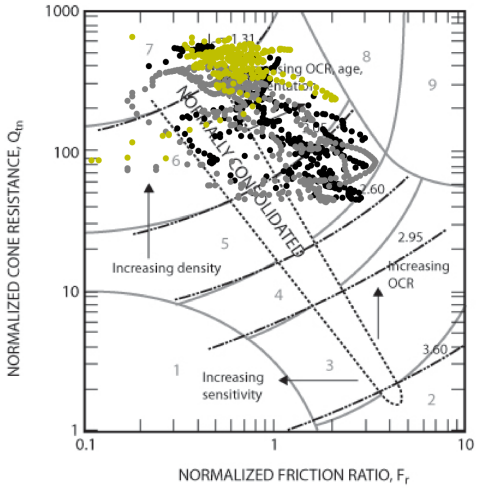

Figure 24: Normalized soil behaviour type chart (Robertson 2010) according to [18, p. 27] - CPTu0a-A (black), CPTu0b-A (grey) and CPTu6-A (yellow)

1 sensitive, fine grained
2 organic soils - clay
3 clays - silty clay to clay
4 silt mixtures - clayey silt to silty clay
5 sand mixtures - silty sand to sandy silt
6 sands - clean sand to silty sand
7 gravelly sand to dense sand
8 very stiff sand to clayey sand (heavily overconsolidated or cemented)
9 very stiff, fine grained (heavily overconsolidated or cemented)

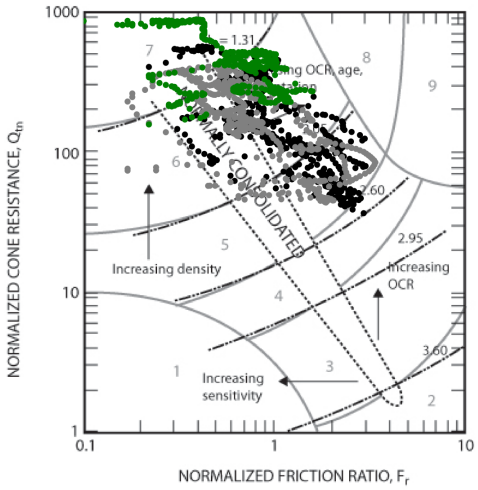

Figure 25: Normalized soil behaviour type chart (Robertson 2010) according to [18, p. 27] - CPTu0a-A (black), CPTu0b-A (grey) and CPTu7-A (green)

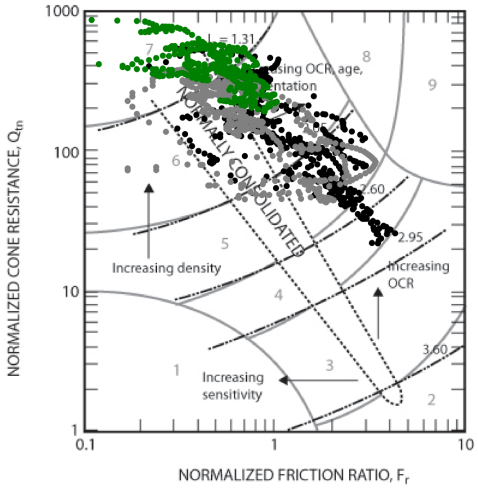

Figure 26: Normalized soil behaviour type chart (Robertson 2010) according to [18, p. 27] - CPTu0a-A (black), CPTu0b-A (grey) and CPTu8-A (green)

1 sensitive, fine grained
2 organic soils - clay
3 clays - silty clay to clay
4 silt mixtures - clayey silt to silty clay
5 sand mixtures - silty sand to sandy silt
6 sands - clean sand to silty sand
7 gravelly sand to dense sand
8 very stiff sand to clayey sand (heavily overconsolidated or cemented)
9 very stiff, fine grained (heavily overconsolidated or cemented)

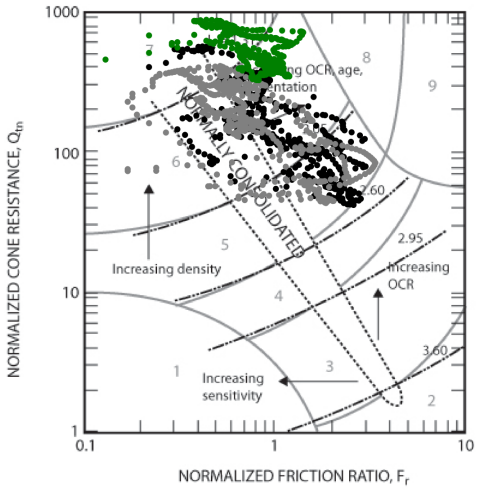

Figure 27: Normalized soil behaviour type chart (Robertson 2010) according to [18, p. 27] - CPTu0a-A (black), CPTu0b-A (grey) and CPTu9-A (green)

1 sensitive, fine grained
2 organic soils - clay
3 clays - silty clay to clay
4 silt mixtures - clayey silt to silty clay
5 sand mixtures - silty sand to sandy silt
6 sands - clean sand to silty sand
7 gravelly sand to dense sand
8 very stiff sand to clayey sand (heavily overconsolidated or cemented)
9 very stiff, fine grained (heavily overconsolidated or cemented)

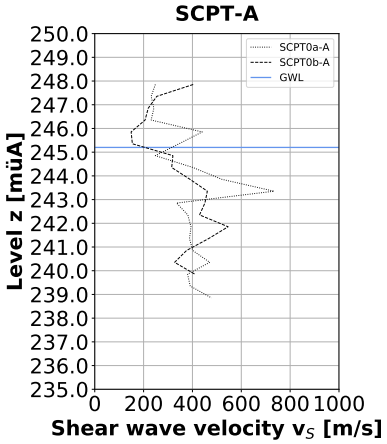

Figure 28: Seismic cone penetration tests - test area A, epoch 0

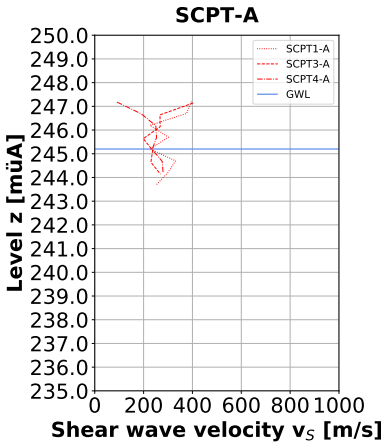

Figure 29: Seismic cone penetration tests - test area A, epoch 1

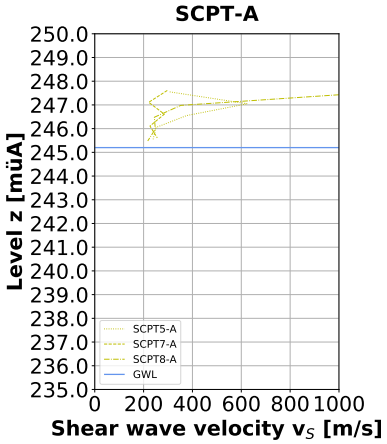

Figure 30: Seismic cone penetration tests - test area A, epoch 2

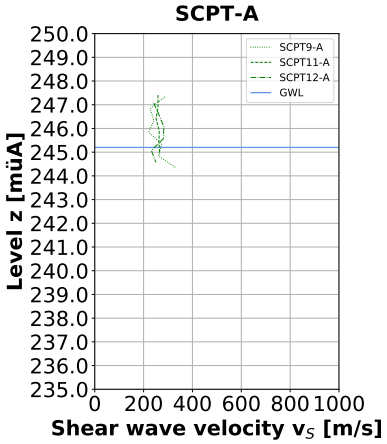

Figure 31: Seismic cone penetration tests - test area A, epoch 3

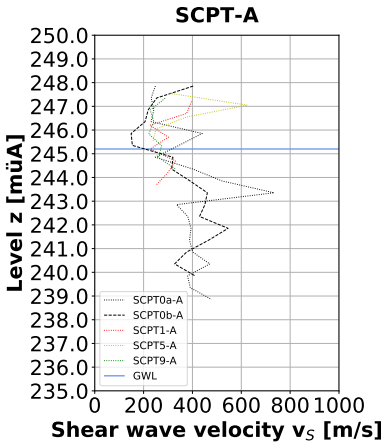

Figure 32: Seismic cone penetration tests - test area A, between four columns

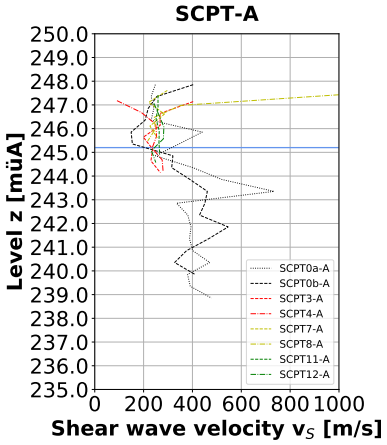

Figure 33: Seismic cone penetration tests - test area A, between two columns

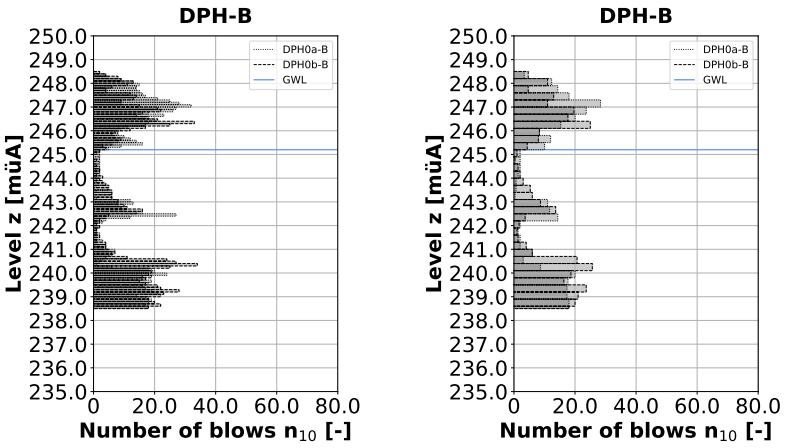

(a) original (b) averaged

Figure 34: Heavy dynamic probing tests - test area B, epoch 0

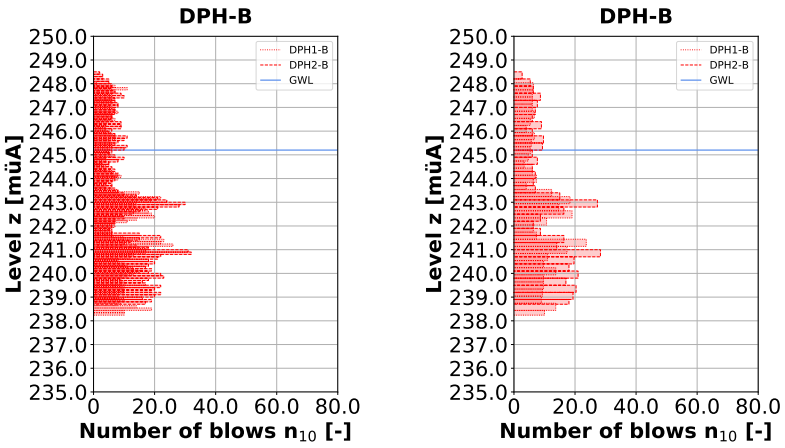

(a) original (b) averaged

Figure 35: Heavy dynamic probing tests - test area B, epoch 1

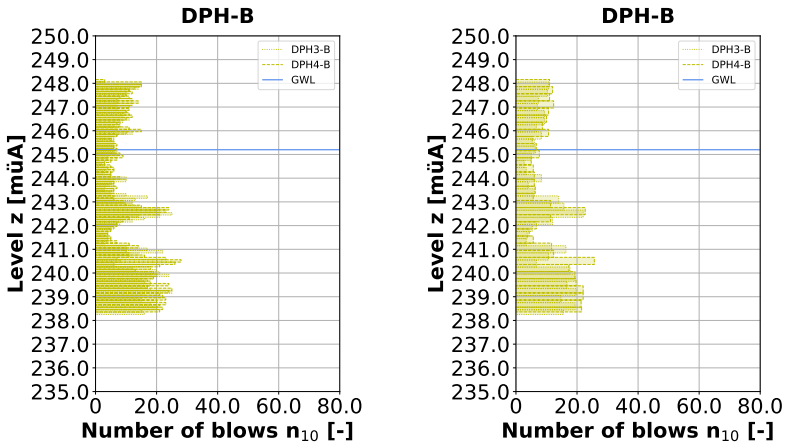

(a) original (b) averaged

Figure 36: Heavy dynamic probing tests - test area B, epoch 2

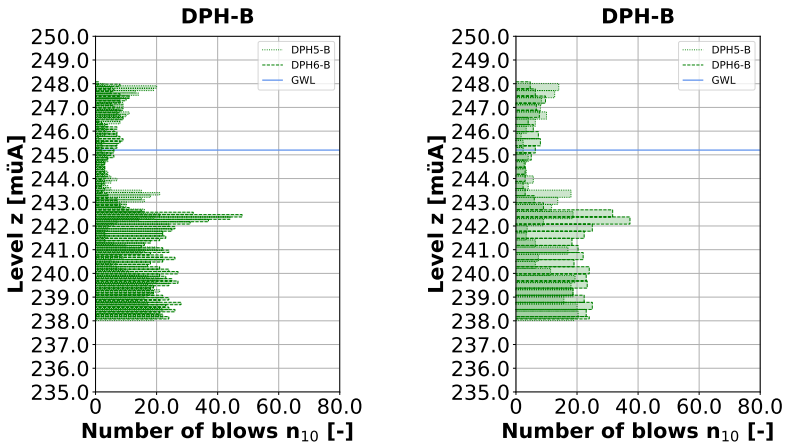

(a) original (b) averaged

Figure 37: Heavy dynamic probing tests - test area B, epoch 3

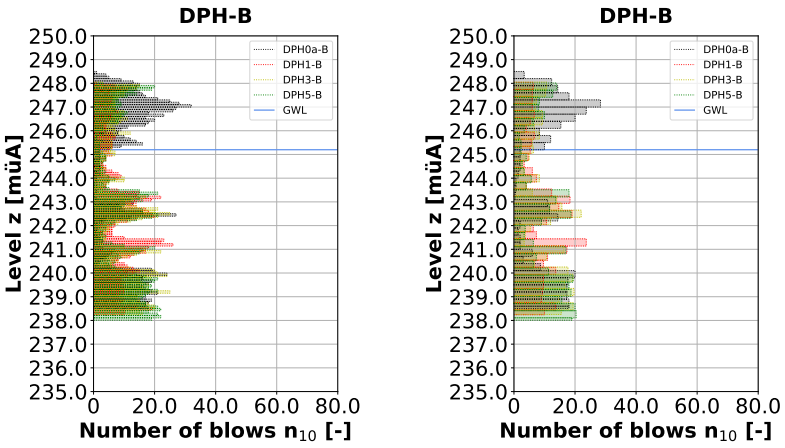

(a) original (b) averaged

Figure 38: Heavy dynamic probing tests - test area B, above left

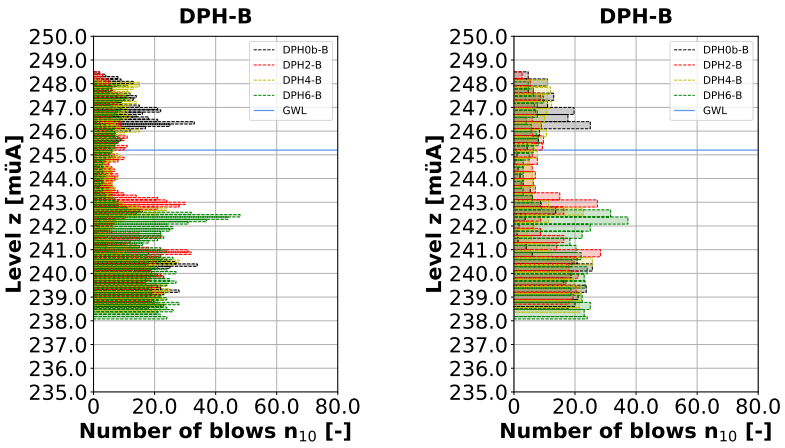

(a) original (b) averaged

Figure 39: Heavy dynamic probing tests - test area B, below right

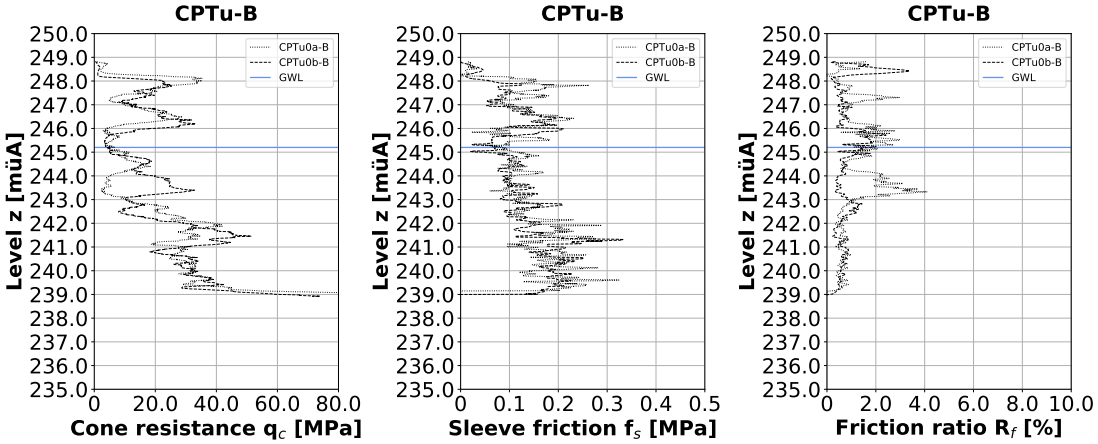

(a) original

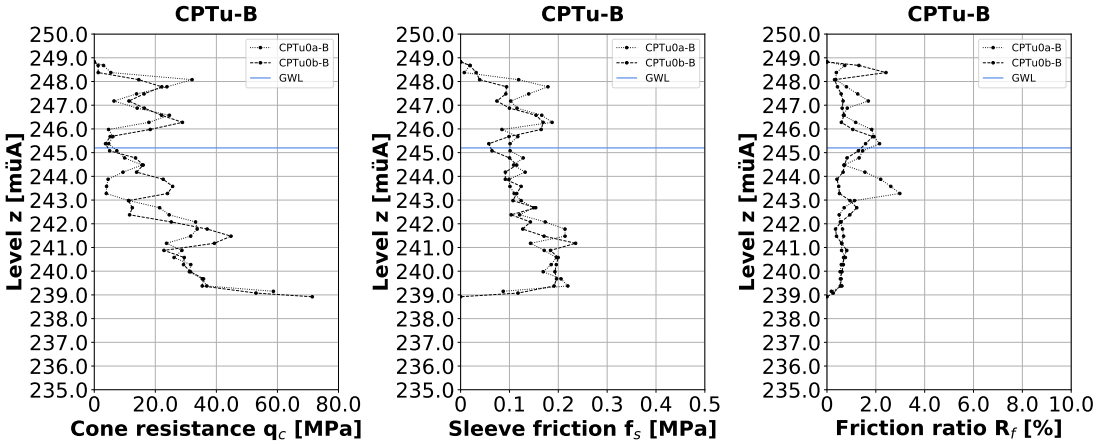

(b) averaged

Figure 40: Cone penetration tests with pore water pressure measurement - test area B, epoch 0 (1)

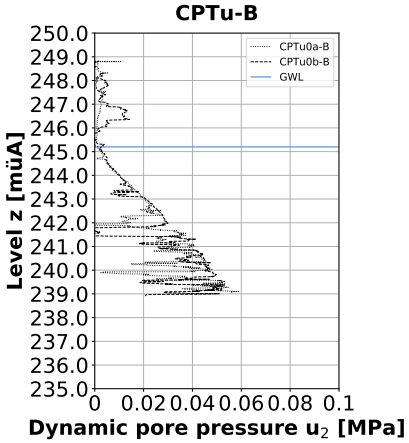

Figure 41: Cone penetration tests with pore water pressure measurement - test area B, epoch 0 (2)

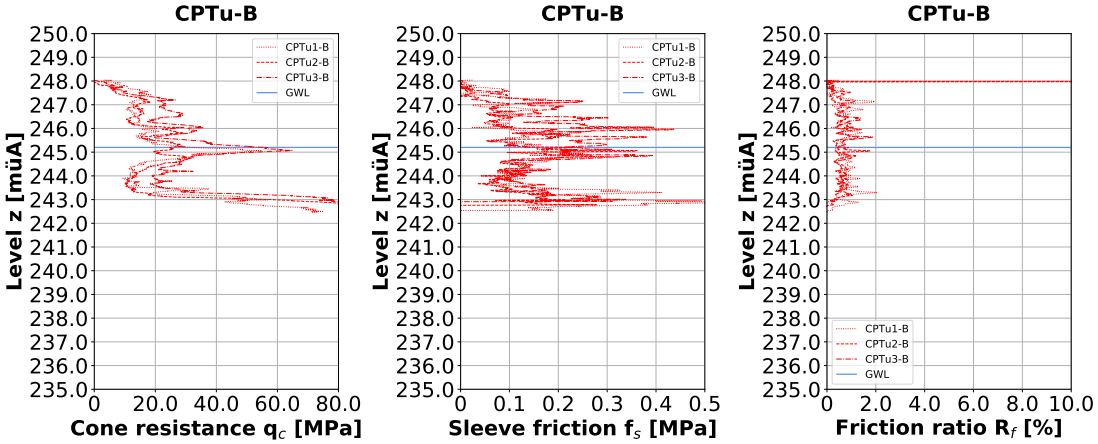

(a) original

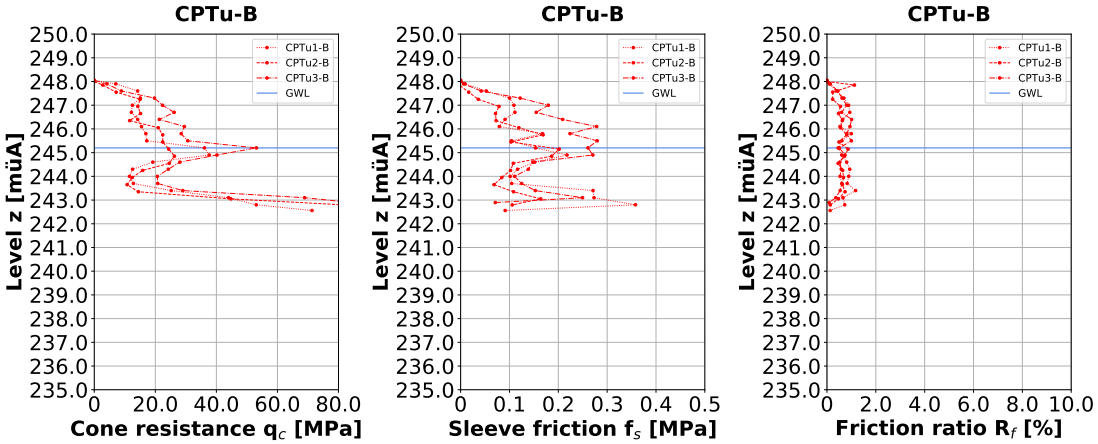

(b) averaged

Figure 42: Cone penetration tests with pore water pressure measurement - test area B, epoch 1 (1)

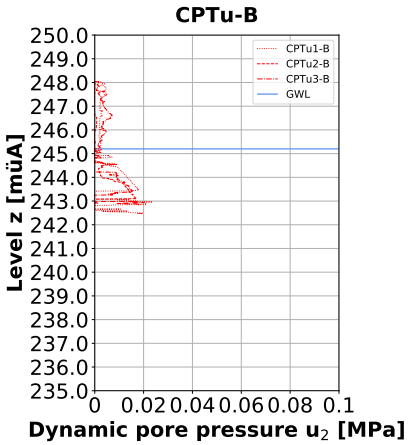

Figure 43: Cone penetration tests with pore water pressure measurement - test area B, epoch 1 (2)

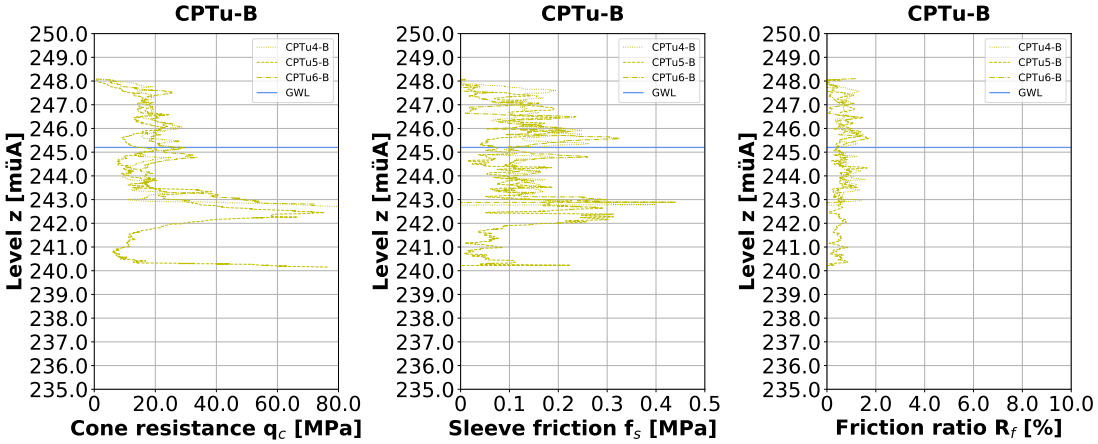

(a) original

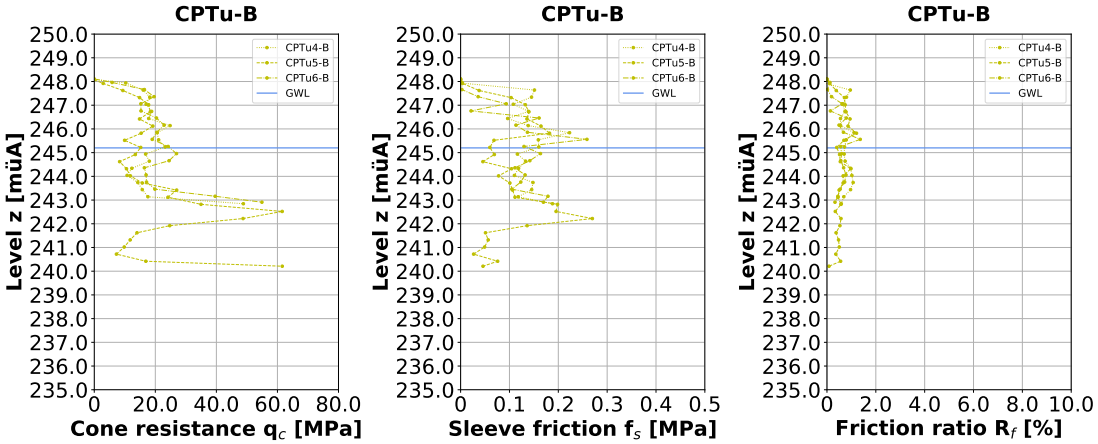

(b) averaged

Figure 44: Cone penetration tests with pore water pressure measurement - test area B, epoch 2 (1)

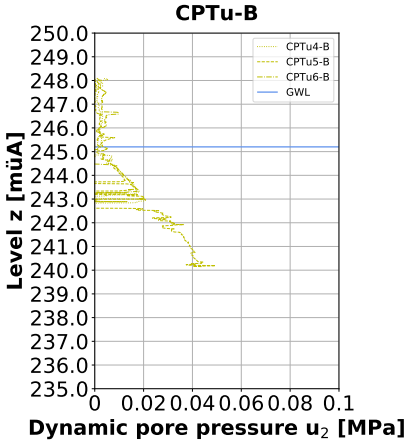

Figure 45: Cone penetration tests with pore water pressure measurement - test area B, epoch 2 (2)

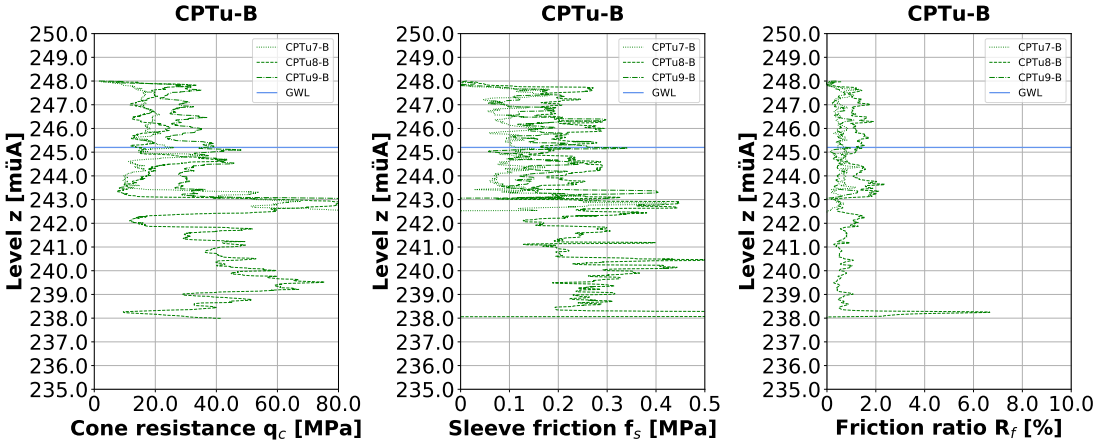

(a) original

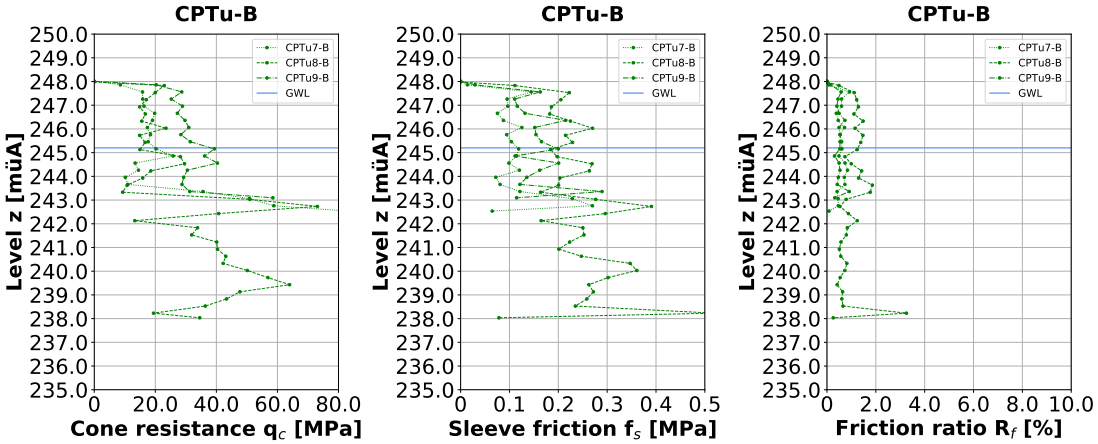

(b) averaged

Figure 46: Cone penetration tests with pore water pressure measurement - test area B, epoch 3 (1)

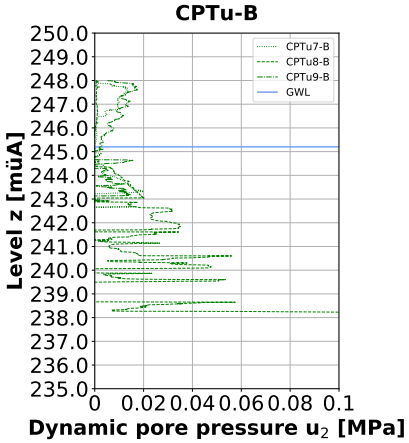

Figure 47: Cone penetration tests with pore water pressure measurement - test area B, epoch 3 (2)

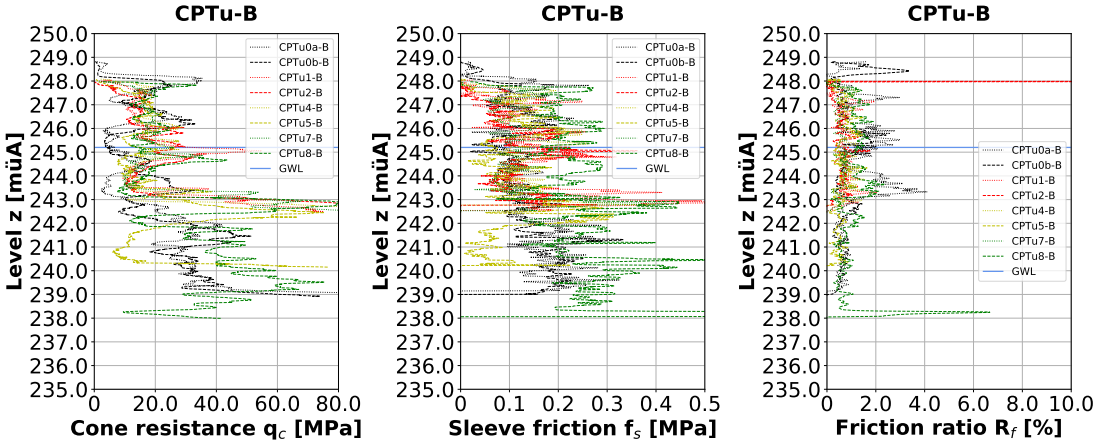

(a) original

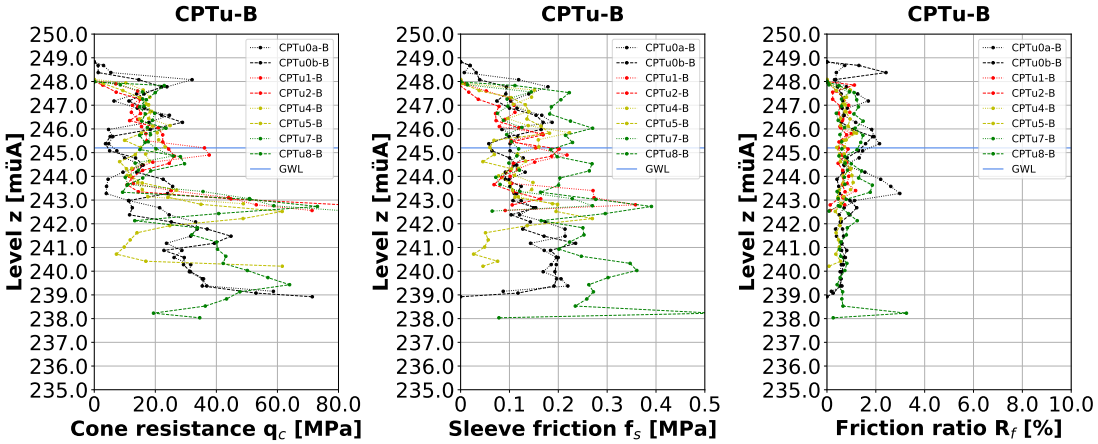

(b) averaged

Figure 48: Cone penetration tests with pore water pressure measurement - test area B, between four columns (1)

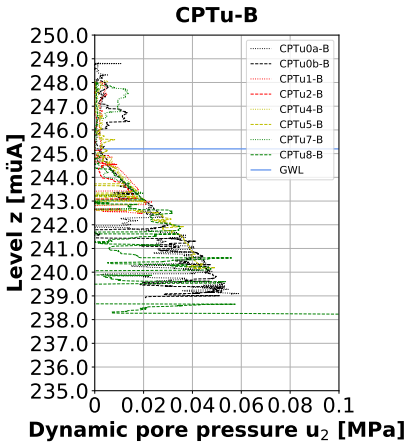

Figure 49: Cone penetration tests with pore water pressure measurement - test area B, between four columns (2)

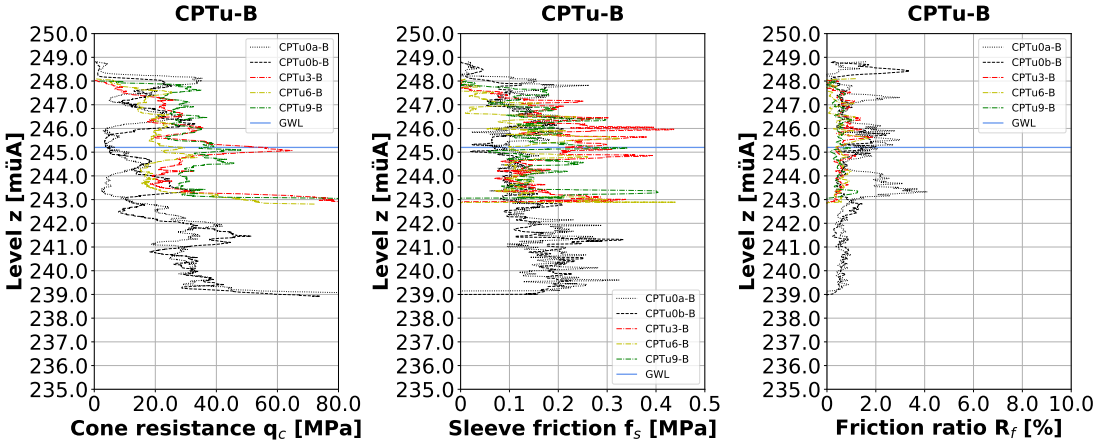

(a) original

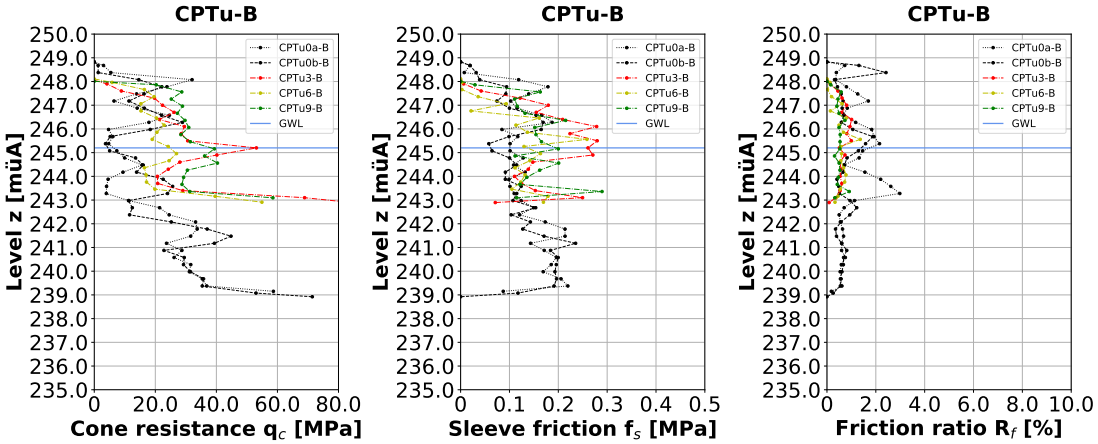

(b) averaged

Figure 50: Cone penetration tests with pore water pressure measurement - test area B, between two columns (1)

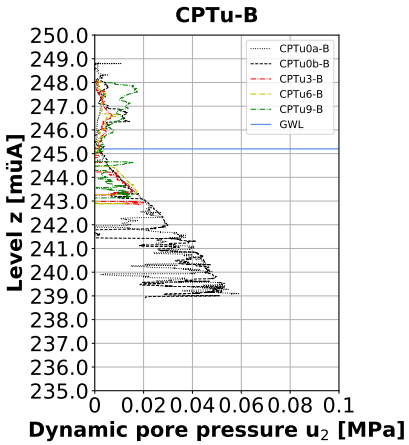

Figure 51: Cone penetration tests with pore water pressure measurement - test area B, between two columns (2)

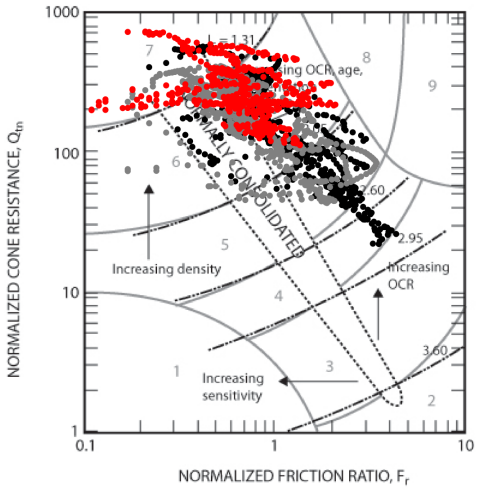

Figure 52: Normalized soil behaviour type chart (Robertson 2010) according to [18, p. 27] - CPTu0a-B (black), CPTu0b-B (grey) and CPTu1-B (red)

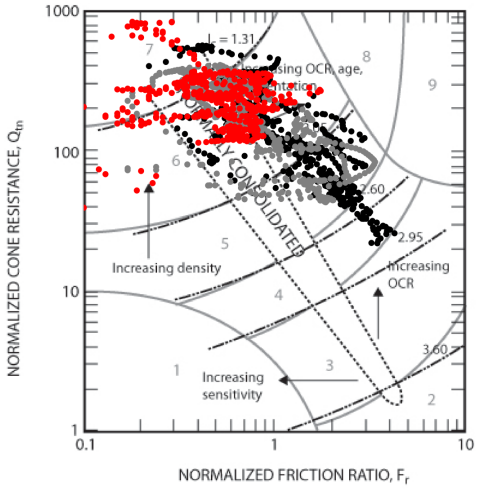

Figure 53: Normalized soil behaviour type chart (Robertson 2010) according to [18, p. 27] - CPTu0a-B (black), CPTu0b-B (grey) and CPTu2-B (red)

1 sensitive, fine grained
2 organic soils - clay
3 clays - silty clay to clay
4 silt mixtures - clayey silt to silty clay
5 sand mixtures - silty sand to sandy silt
6 sands - clean sand to silty sand
7 gravelly sand to dense sand
8 very stiff sand to clayey sand (heavily overconsolidated or cemented)
9 very stiff, fine grained (heavily overconsolidated or cemented)

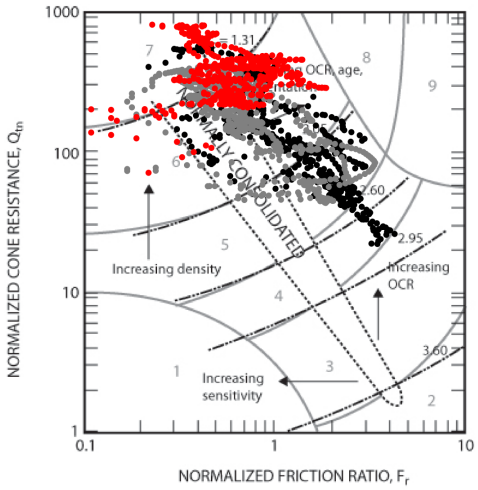

Figure 54: Normalized soil behaviour type chart (Robertson 2010) according to [18, p. 27] - CPTu0a-B (black), CPTu0b-B (grey) and CPTu3-B (red)

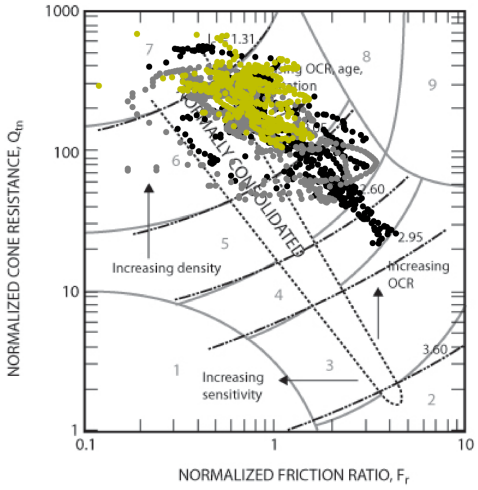

Figure 55: Normalized soil behaviour type chart (Robertson 2010) according to [18, p. 27] - CPTu0a-B (black), CPTu0b-B (grey) and CPTu4-B (yellow)

1 sensitive, fine grained
2 organic soils - clay
3 clays - silty clay to clay
4 silt mixtures - clayey silt to silty clay
5 sand mixtures - silty sand to sandy silt
6 sands - clean sand to silty sand
7 gravelly sand to dense sand
8 very stiff sand to clayey sand (heavily overconsolidated or cemented)
9 very stiff, fine grained (heavily overconsolidated or cemented)

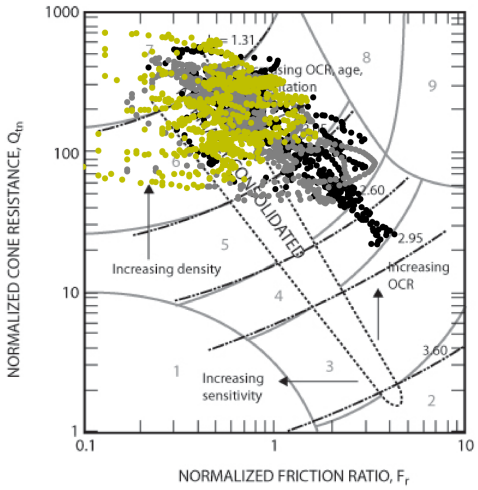

Figure 56: Normalized soil behaviour type chart (Robertson 2010) according to [18, p. 27] - CPTu0a-B (black), CPTu0b-B (grey) and CPTu5-B (yellow)

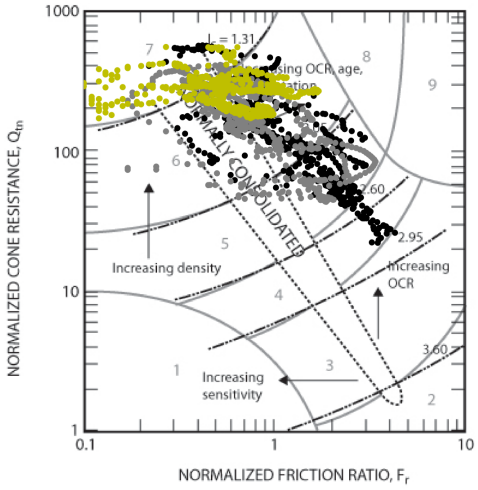

Figure 57: Normalized soil behaviour type chart (Robertson 2010) according to [18, p. 27] - CPTu0a-B (black), CPTu0b-B (grey) and CPTu6-B (yellow)

1 sensitive, fine grained
2 organic soils - clay
3 clays - silty clay to clay
4 silt mixtures - clayey silt to silty clay
5 sand mixtures - silty sand to sandy silt
6 sands - clean sand to silty sand
7 gravelly sand to dense sand
8 very stiff sand to clayey sand (heavily overconsolidated or cemented)
9 very stiff, fine grained (heavily overconsolidated or cemented)

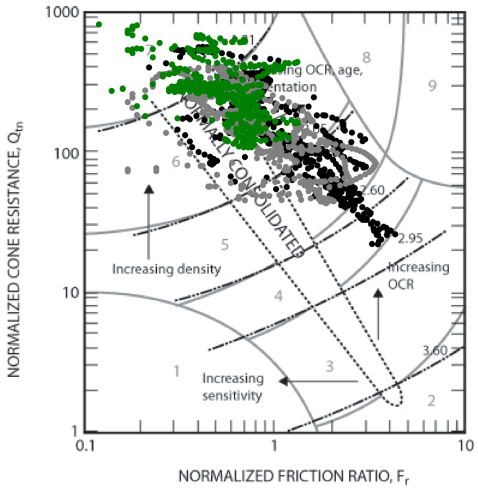

Figure 58: Normalized soil behaviour type chart (Robertson 2010) according to [18, p. 27] - CPTu0a-B (black), CPTu0b-B (grey) and CPTu7-B (green)

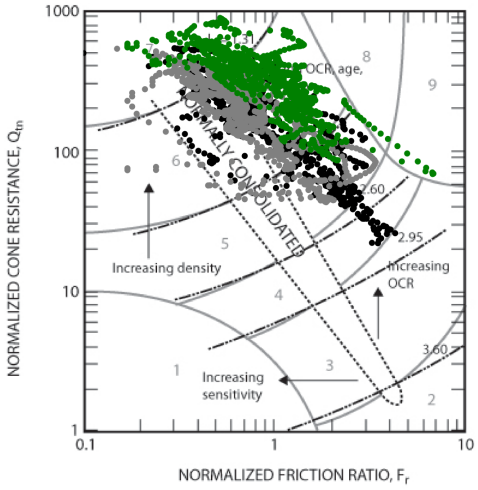

Figure 59: Normalized soil behaviour type chart (Robertson 2010) according to [18, p. 27] - CPTu0a-B (black), CPTu0b-B (grey) and CPTu8-B (green)

1 sensitive, fine grained
2 organic soils - clay
3 clays - silty clay to clay
4 silt mixtures - clayey silt to silty clay
5 sand mixtures - silty sand to sandy silt
6 sands - clean sand to silty sand
7 gravelly sand to dense sand
8 very stiff sand to clayey sand (heavily overconsolidated or cemented)
9 very stiff, fine grained (heavily overconsolidated or cemented)

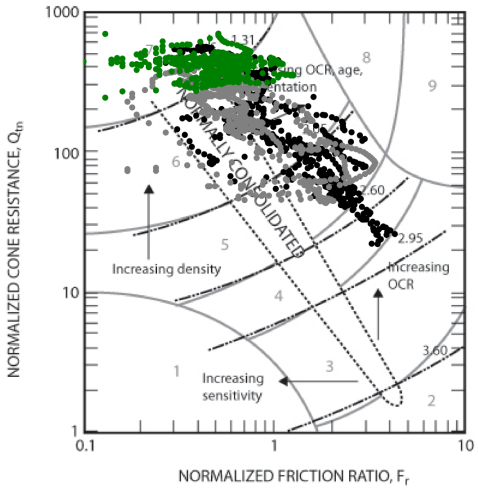

Figure 60: Normalized soil behaviour type chart (Robertson 2010) according to [18, p. 27] - CPTu0a-B (black), CPTu0b-B (grey) and CPTu9-B (green)

1 sensitive, fine grained
2 organic soils - clay
3 clays - silty clay to clay
4 silt mixtures - clayey silt to silty clay
5 sand mixtures - silty sand to sandy silt
6 sands - clean sand to silty sand
7 gravelly sand to dense sand
8 very stiff sand to clayey sand (heavily overconsolidated or cemented)
9 very stiff, fine grained (heavily overconsolidated or cemented)

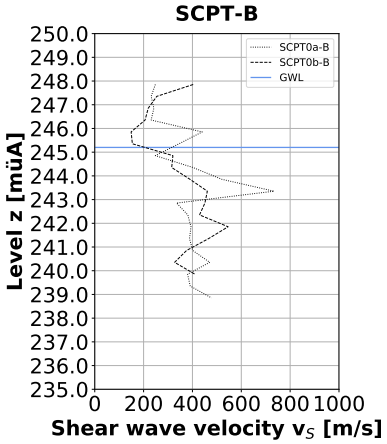

Figure 61: Seismic cone penetration tests - test area B, epoch 0

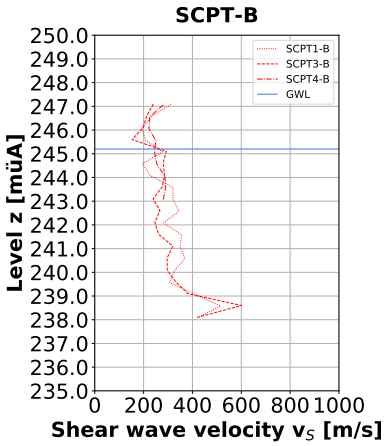

Figure 62: Seismic cone penetration tests - test area B, epoch 1

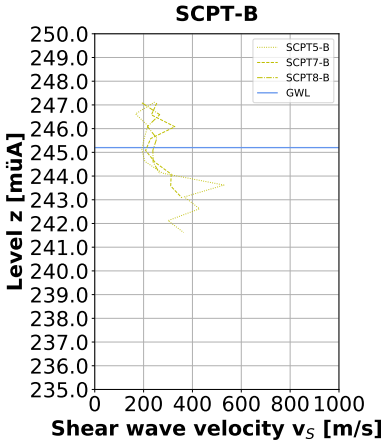

Figure 63: Seismic cone penetration tests - test area B, epoch 2

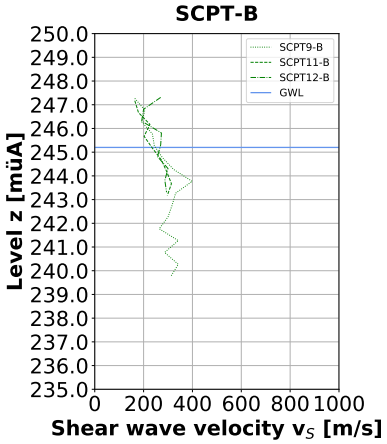

Figure 64: Seismic cone penetration tests - test area B, epoch 3

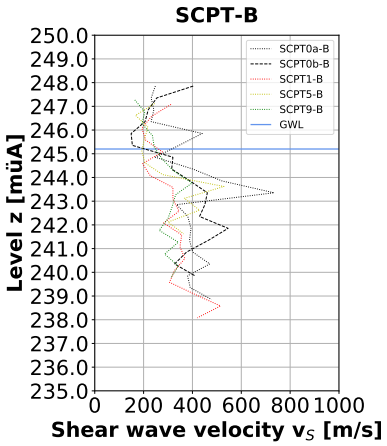

Figure 65: Seismic cone penetration tests - test area B, between four columns

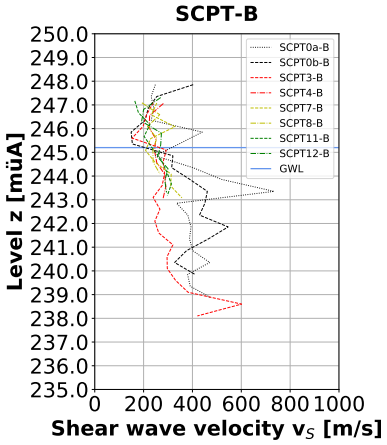

Figure 66: Seismic cone penetration tests - test area B, between two columns

6 Input data TEDDY inclinometer pipe

```
$------------------------------------------------------------------------------------------------------------
$ Graz University of Technology; Institute of Soil Mechanics, Foundation Engineering and Computational Ge
$ Master's thesis "Investigations on the horizontal stress state of non-cohesive soils due to deep vibro
$ LC1_SOFiSTiK_2D_without_4-elements
$ CADINP-based creation of the FE-calculation model with SOFiSTiK
$ Created by Daniel Gasser, Dipl.-Ing., BSc
$------------------------------------------------------------------------------------------------------------

+sys del $(projekt).cdb

!#!Kapitel Materials
+prog aqua
kopf Materials
echo voll

mate 1 e 2500 mue 0.34 gam 0 bez 'inclinometer pipe'
mate 2 e 1e-1 mue 0.00 gam 0 bez 'dummy layer'

ende

!#!Kapitel System
+prog sofimshc
kopf Cross section
echo voll voll

syst 2dsn gdir posy gdiv 100000
seit unie 7
steu tolg 0.0001
steu mesh 66 $ 34
steu hmin 1.25[mm]
steu deln 0

spt  1 x -55.0000 -55.0000 0.0000
spt  2 x -55.0000  55.0000 0.0000
spt  3 x  55.0000  55.0000 0.0000
spt  4 x  55.0000 -55.0000 0.0000
spt  5 x  42.0000   0.0000 0.0000
spt  6 x   0.0000  42.0000 0.0000
spt  7 x -42.0000   0.0000 0.0000
spt  8 x   0.0000 -42.0000 0.0000
spt  9 x  36.0000   0.0000 0.0000
spt 10 x   0.0000  36.0000 0.0000
spt 11 x -36.0000   0.0000 0.0000
spt 12 x   0.0000 -36.0000 0.0000

sln  1 npa  1  2 fix pp
sln  2 npa  2  3 fix pp
sln  3 npa  3  4 fix pp
sln  4 npa  4  1 fix pp
sln  5 npa  5  6 ; slnb xm 0 0 0
sln  6 npa  6  7 ; slnb xm 0 0 0
sln  7 npa  7  8 ; slnb xm 0 0 0
sln  8 npa  8  5 ; slnb xm 0 0 0
sln  9 npa  9 10 ; slnb xm 0 0 0
sln 10 npa 10 11 ; slnb xm 0 0 0
sln 11 npa 11 12 ; slnb xm 0 0 0
sln 12 npa 12  9 ; slnb xm 0 0 0

sar 1 grp 1 mnr 1 t 1000 mctl regm bez 'inclinometer pipe'
sarb out 5,6,7,8
sarb in 9,10,11,12
```



```
sar 2 grp 2 mnr 2 t 1000 mctl regm bez 'dummy layer'
sarb out 1,2,3,4
sarb in 5,6,7,8

ende

!#!Kapitel Load cases
+prog sofiload
kopf Load cases
echo voll

lf 1 bez 'load angle 360°'
line sln 5 typ pz p1 100
line sln 6 typ pz p1 100
line sln 7 typ pz p1 100
line sln 8 typ pz p1 100

ende

!#!Kapitel Calculation
+prog talpa
kopf Calculation
echo voll

steu solv 4

lf 1

ende
```

```
$------------------------------------------------------------------------------------------------------------
$ Graz University of Technology; Institute of Soil Mechanics, Foundation Engineering and Computational Ge
$ Master's thesis "Investigations on the horizontal stress state of non-cohesive soils due to deep vibro
$ LC1_SOFiSTiK_2D_with_4-elements
$ CADINP-based creation of the FE-calculation model with SOFiSTiK
$ Created by Daniel Gasser, Dipl.-Ing., BSc
$------------------------------------------------------------------------------------------------------------

+sys del $(projekt).cdb

!#!Kapitel Materials
+prog aqua
kopf Materials
echo voll

mate 1 e 2500 mue 0.34 gam 0 bez 'inclinometer pipe'
mate 2 e 1    mue 0.00 gam 0 bez 'dummy layer'

ende

!#!Kapitel System
+prog sofimshc
kopf Cross section
echo voll voll

syst 2dsn gdir posy gdiv 100000
seit unie 7
steu tolg 0.0001
steu mesh 66 $ 34
steu hmin 1.25[mm]
steu deln 0

spt  1 x -55.0000 -55.0000 0.0000
spt  2 x -55.0000  55.0000 0.0000
spt  3 x  55.0000  55.0000 0.0000
spt  4 x  55.0000 -55.0000 0.0000
spt  5 x  42.0000   0.0000 0.0000
spt  6 x   0.0000  42.0000 0.0000
spt  7 x -42.0000   0.0000 0.0000
spt  8 x   0.0000 -42.0000 0.0000
spt  9 x  35.8631  -3.1369 0.0000
spt 10 x  38.0000  -1.0000 0.0000
spt 11 x  38.0000   1.0000 0.0000
spt 12 x  35.8631   3.1369 0.0000
spt 13 x  27.5772  23.1409 0.0000
spt 14 x  27.5772  26.1630 0.0000
spt 15 x  26.1630  27.5772 0.0000
spt 16 x  23.1409  27.5772 0.0000
spt 17 x   3.1369  35.8631 0.0000
spt 18 x   1.0000  38.0000 0.0000
spt 19 x  -1.0000  38.0000 0.0000
spt 20 x  -3.1369  35.8631 0.0000
spt 21 x -23.1409  27.5772 0.0000
spt 22 x -26.1630  27.5772 0.0000
spt 23 x -27.5772  26.1630 0.0000
spt 24 x -27.5772  23.1409 0.0000
spt 25 x -35.8631   3.1369 0.0000
spt 26 x -38.0000   1.0000 0.0000
spt 27 x -38.0000  -1.0000 0.0000
spt 28 x -35.8631  -3.1369 0.0000
spt 29 x -27.5772 -23.1409 0.0000
spt 30 x -27.5772 -26.1630 0.0000
```



```
spt 31 x -26.1630 -27.5772 0.0000
spt 32 x -23.1409 -27.5772 0.0000
spt 33 x  -3.1369 -35.8631 0.0000
spt 34 x  -1.0000 -38.0000 0.0000
spt 35 x   1.0000 -38.0000 0.0000
spt 36 x   3.1369 -35.8631 0.0000
spt 37 x  23.1409 -27.5772 0.0000
spt 38 x  26.1630 -27.5772 0.0000
spt 39 x  27.5772 -26.1630 0.0000
spt 40 x  27.5772 -23.1409 0.0000

sln  1 npa  1  2 fix pp
sln  2 npa  2  3 fix pp
sln  3 npa  3  4 fix pp
sln  4 npa  4  1 fix pp
sln  5 npa  5  6 ; slnb xm 0 0 0
sln  6 npa  6  7 ; slnb xm 0 0 0
sln  7 npa  7  8 ; slnb xm 0 0 0
sln  8 npa  8  5 ; slnb xm 0 0 0
sln  9 npa  9 10
sln 10 npa 10 11
sln 11 npa 11 12
sln 12 npa 12 13 ; slnb xm 0 0 0
sln 13 npa 13 14
sln 14 npa 14 15
sln 15 npa 15 16
sln 16 npa 16 17 ; slnb xm 0 0 0
sln 17 npa 17 18
sln 18 npa 18 19
sln 19 npa 19 20
sln 20 npa 20 21 ; slnb xm 0 0 0
sln 21 npa 21 22
sln 22 npa 22 23
sln 23 npa 23 24
sln 24 npa 24 25 ; slnb xm 0 0 0
sln 25 npa 25 26
sln 26 npa 26 27
sln 27 npa 27 28
sln 28 npa 28 29 ; slnb xm 0 0 0
sln 29 npa 29 30
sln 30 npa 30 31
sln 31 npa 31 32
sln 32 npa 32 33 ; slnb xm 0 0 0
sln 33 npa 33 34
sln 34 npa 34 35
sln 35 npa 35 36
sln 36 npa 36 37 ; slnb xm 0 0 0
sln 37 npa 37 38
sln 38 npa 38 39
sln 39 npa 39 40
sln 40 npa 40  9 ; slnb xm 0 0 0

sar 1 grp 1 mnr 1 t 1000 mctl regm bez 'inclinometer pipe'
sarb out 5,6,7,8
sarb in 9,10,11,12,13,14,15,16,17,18,19,20,21,22,23,24,25,26,27,28,29,30,31,32,33,34,35,36,37,38,39,40

sar 2 grp 2 mnr 2 t 1000 mctl regm bez 'dummy layer'
sarb out 1,2,3,4
sarb in 5,6,7,8

ende
```

```
!#!Kapitel Load cases
+prog sofiload
kopf Load cases
echo voll

lf 1 bez 'load angle 360°'
line sln 5 typ pz p1 100
line sln 6 typ pz p1 100
line sln 7 typ pz p1 100
line sln 8 typ pz p1 100

ende

!#!Kapitel Calculation
+prog talpa
kopf Calculation
echo voll

steu solv 4

lf 1

ende
```

```
$------------------------------------------------------------------------------------------------------------
$ Graz University of Technology; Institute of Soil Mechanics, Foundation Engineering and Computational Ge
$ Master's thesis "Investigations on the horizontal stress state of non-cohesive soils due to deep vibro
$ LC1_SOFiSTiK_3D-unconstrained_without_4-elements
$ CADINP-based creation of the FE-calculation model with SOFiSTiK
$ Created by Daniel Gasser, Dipl.-Ing., BSc
$------------------------------------------------------------------------------------------------------------

+sys del $(projekt).cdb

!#!Kapitel Materials
+prog aqua
kopf Materials
echo voll

mate 1 e 2500 mue 0.34 gam 0 bez 'inclinometer pipe'

ende

!#!Kapitel System
+prog sofimshc
kopf Cross section
echo voll voll

syst 3D gdir negz gdiv 1000000
seit unie 7
steu tolg 0.0001
steu mesh 66 $ 34
steu hmin 10[mm]
steu deln 0

sto#H 3*10^3

spt  1 x  33.2597 -13.7766 0.0000
spt  2 x  38.8029 -16.0727 0.0000
spt  3 x  38.8029  16.0727 0.0000
spt  4 x  33.2597  13.7766 0.0000
spt  5 x  38.8029 -16.0727 #H

sln  1 npa  1  2
sln  2 npa  2  3 ; slnb xm 0 0 0
sln  3 npa  3  4
sln  4 npa  4  1 ; slnb xm 0 0 0
sln  5 npa  2  5

sar 1 grp 1 mnr 1 t 0 mctl regm h1 1.5[mm]
sarb out 1,2,3,4

ende

+prog sofimsha
kopf Extrusion & Rotation
echo voll voll

syst rest

bric prop mnr 1
grup 2
extr quad von sar 1 path sln 5
tran bric grp 2 phiz 45
tran bric grp 2 phiz 90
tran bric grp 2 phiz 180
```



```
quad prop mnr 1 t 0 kr negz
grup 3
extr sln von sln 2 path sln 5
tran quad grp 3 phiz 45
tran quad grp 3 phiz 90
tran quad grp 3 phiz 180

grup 1
tran quad grp 1 phiz 45
tran quad grp 1 phiz 90
tran quad grp 1 phiz 180
fede qgrp 1 dz -1 cp 1e10

let#xmin -50.0000[mm]
let#ymin -50.0000[mm]
let#zmin   0.0000[mm]
let#xmax  50.0000[mm]
let#ymax  50.0000[mm]
let#zmax   0.0000[mm]
mod knot xmin #xmin ymin #ymin zmin #zmin xmax #xmax ymax #ymax zmax #zmax fix zp
let#xmin -50.0000[mm]
let#ymin -50.0000[mm]
let#zmin       #H[mm]
let#xmax  50.0000[mm]
let#ymax  50.0000[mm]
let#zmax       #H[mm]
mod knot xmin #xmin ymin #ymin zmin #zmin xmax #xmax ymax #ymax zmax #zmax fix zp

ende

!#!Kapitel Load cases
+prog sofiload
kopf Load cases
echo voll

lf 1 bez 'load angle 360°'
quad grp 3 typ pz p 100

ende

!#!Kapitel Calculation
+prog ase
kopf Calculation
echo voll

steu solv 4

lf alle

ende
```

```
$------------------------------------------------------------------------------------------------------------
$ Graz University of Technology; Institute of Soil Mechanics, Foundation Engineering and Computational Ge
$ Master's thesis "Investigations on the horizontal stress state of non-cohesive soils due to deep vibro
$ LC1_SOFiSTiK_3D-unconstrained_with_4-elements
$ CADINP-based creation of the FE-calculation model with SOFiSTiK
$ Created by Daniel Gasser, Dipl.-Ing., BSc
$------------------------------------------------------------------------------------------------------------

+sys del $(projekt).cdb

!#!Kapitel Materials
+prog aqua
kopf Materials
echo voll

mate 1 e 2500 mue 0.34 gam 0 bez 'inclinometer pipe'

ende

!#!Kapitel System
+prog sofimshc
kopf Cross section
echo voll voll

syst 3D gdir negz gdiv 1000000
seit unie 7
steu tolg 0.0001
steu mesh 66 $ 34
steu hmin 10[mm]
steu deln 0

sto#H 3*10^3

spt  1 x  33.2597 -13.7766 0.0000
spt  2 x  38.8029 -16.0727 0.0000
spt  3 x  38.8029  16.0727 0.0000
spt  4 x  33.2597  13.7766 0.0000
spt  5 x  35.8631   3.1369 0.0000
spt  6 x  38.0000   1.0000 0.0000
spt  7 x  38.0000  -1.0000 0.0000
spt  8 x  35.8631  -3.1369 0.0000
spt  9 x  38.8029 -16.0727 #H

sln  1 npa  1  2
sln  2 npa  2  3 ; slnb xm 0 0 0
sln  3 npa  3  4
sln  4 npa  4  5 ; slnb xm 0 0 0
sln  5 npa  5  6
sln  6 npa  6  7
sln  7 npa  7  8
sln  8 npa  8  1 ; slnb xm 0 0 0
sln  9 npa  2  9

sar 1 grp 1 mnr 1 t 0 mctl regm h1 1.25[mm]
sarb out 1,2,3,4,5,6,7,8

ende

+prog sofimsha
kopf Extrusion & Rotation
echo voll voll
```



```
syst rest

bric prop mnr 1
grup 2
extr quad von sar 1 path sln 9
tran bric grp 2 phiz 45
tran bric grp 2 phiz 90
tran bric grp 2 phiz 180

quad prop mnr 1 t 0 kr negz
grup 3
extr sln von sln 2 path sln 9
tran quad grp 3 phiz 45
tran quad grp 3 phiz 90
tran quad grp 3 phiz 180

grup 1
tran quad grp 1 phiz 45
tran quad grp 1 phiz 90
tran quad grp 1 phiz 180
fede qgrp 1 dz -1 cp 1e10

let#xmin -50.0000[mm]
let#ymin -50.0000[mm]
let#zmin   0.0000[mm]
let#xmax  50.0000[mm]
let#ymax  50.0000[mm]
let#zmax   0.0000[mm]
mod knot xmin #xmin ymin #ymin zmin #zmin xmax #xmax ymax #ymax zmax #zmax fix zp
let#xmin -50.0000[mm]
let#ymin -50.0000[mm]
let#zmin       #H[mm]
let#xmax  50.0000[mm]
let#ymax  50.0000[mm]
let#zmax       #H[mm]
mod knot xmin #xmin ymin #ymin zmin #zmin xmax #xmax ymax #ymax zmax #zmax fix zp

ende

!#!Kapitel Load cases
+prog sofiload
kopf Load cases
echo voll

lf 1 bez 'load angle 360°'
quad grp 3 typ pz p 100

ende

!#!Kapitel Calculation
+prog ase
kopf Calculation
echo voll

steu solv 4

lf alle

ende
```

```
$------------------------------------------------------------------------------------------------------------
$ Graz University of Technology; Institute of Soil Mechanics, Foundation Engineering and Computational Ge
$ Master's thesis "Investigations on the horizontal stress state of non-cohesive soils due to deep vibro
$ LC2_SOFiSTiK_2D_without_4-elements
$ CADINP-based creation of the FE-calculation model with SOFiSTiK
$ Created by Daniel Gasser, Dipl.-Ing., BSc
$------------------------------------------------------------------------------------------------------------

+sys del $(projekt).cdb

!#!Kapitel Materials
+prog aqua
kopf Materials
echo voll

mate 1 e 2500 mue 0.34 gam 0 bez 'inclinometer pipe'
mate 2 e 1e-3 mue 0.00 gam 0 bez 'dummy layer'

ende

!#!Kapitel System
+prog sofimshc
kopf Cross section
echo voll voll

syst 2dsn gdir posy gdiv 100000
seit unie 7
steu tolg 0.0001
steu mesh 66 $ 34
steu hmin 1.25[mm]
steu deln 0

spt  1 x -55.0000 -55.0000 0.0000
spt  2 x -55.0000  55.0000 0.0000
spt  3 x  55.0000  55.0000 0.0000
spt  4 x  55.0000 -55.0000 0.0000
spt  5 x  38.8029 -16.0727 0.0000
spt  6 x  16.0727  38.8029 0.0000
spt  7 x -38.8029  16.0727 0.0000
spt  8 x -16.0727 -38.8029 0.0000
spt  9 x  36.0000   0.0000 0.0000
spt 10 x   0.0000  36.0000 0.0000
spt 11 x -36.0000   0.0000 0.0000
spt 12 x   0.0000 -36.0000 0.0000

sln  1 npa  1  2 fix pp
sln  2 npa  2  3 fix pp
sln  3 npa  3  4 fix pp
sln  4 npa  4  1 fix pp
sln  5 npa  5  6 ; slnb xm 0 0 0
sln  6 npa  6  7 ; slnb xm 0 0 0
sln  7 npa  7  8 ; slnb xm 0 0 0
sln  8 npa  8  5 ; slnb xm 0 0 0
sln  9 npa  9 10 ; slnb xm 0 0 0
sln 10 npa 10 11 ; slnb xm 0 0 0
sln 11 npa 11 12 ; slnb xm 0 0 0
sln 12 npa 12  9 ; slnb xm 0 0 0

sar 1 grp 1 mnr 1 t 1000 mctl regm bez 'inclinometer pipe'
sarb out 5,6,7,8
sarb in 9,10,11,12
```



```
sar 2 grp 2 mnr 2 t 1000 mctl regm bez 'dummy layer'
sarb out 1,2,3,4
sarb in 5,6,7,8

ende

!#!Kapitel Load cases
+prog sofiload
kopf Load cases
echo voll

lf 1 bez 'load angle 2 x 90°'
line sln 5 typ pz p1 100
line sln 7 typ pz p1 100

ende

!#!Kapitel Calculation
+prog talpa
kopf Calculation
echo voll

steu solv 4

lf 1

ende
```

```
$------------------------------------------------------------------------------------------------------------
$ Graz University of Technology; Institute of Soil Mechanics, Foundation Engineering and Computational Ge
$ Master's thesis "Investigations on the horizontal stress state of non-cohesive soils due to deep vibro
$ LC2_SOFiSTiK_2D_with_4-elements
$ CADINP-based creation of the FE-calculation model with SOFiSTiK
$ Created by Daniel Gasser, Dipl.-Ing., BSc
$------------------------------------------------------------------------------------------------------------

+sys del $(projekt).cdb

!#!Kapitel Materials
+prog aqua
kopf Materials
echo voll

mate 1 e 2500 mue 0.34 gam 0 bez 'inclinometer pipe'
mate 2 e 1e-3 mue 0.00 gam 0 bez 'dummy layer'

ende

!#!Kapitel System
+prog sofimshc
kopf Cross section
echo voll voll

syst 2dsn gdir posy gdiv 100000
seit unie 7
steu tolg 0.0001
steu mesh 66 $ 34
steu hmin 1.25[mm]
steu deln 0

spt  1 x -55.0000 -55.0000 0.0000
spt  2 x -55.0000  55.0000 0.0000
spt  3 x  55.0000  55.0000 0.0000
spt  4 x  55.0000 -55.0000 0.0000
spt  5 x  38.8029 -16.0727 0.0000
spt  6 x  16.0727  38.8029 0.0000
spt  7 x -38.8029  16.0727 0.0000
spt  8 x -16.0727 -38.8029 0.0000
spt  9 x  35.8631  -3.1369 0.0000
spt 10 x  38.0000  -1.0000 0.0000
spt 11 x  38.0000   1.0000 0.0000
spt 12 x  35.8631   3.1369 0.0000
spt 13 x  27.5772  23.1409 0.0000
spt 14 x  27.5772  26.1630 0.0000
spt 15 x  26.1630  27.5772 0.0000
spt 16 x  23.1409  27.5772 0.0000
spt 17 x   3.1369  35.8631 0.0000
spt 18 x   1.0000  38.0000 0.0000
spt 19 x  -1.0000  38.0000 0.0000
spt 20 x  -3.1369  35.8631 0.0000
spt 21 x -23.1409  27.5772 0.0000
spt 22 x -26.1630  27.5772 0.0000
spt 23 x -27.5772  26.1630 0.0000
spt 24 x -27.5772  23.1409 0.0000
spt 25 x -35.8631   3.1369 0.0000
spt 26 x -38.0000   1.0000 0.0000
spt 27 x -38.0000  -1.0000 0.0000
spt 28 x -35.8631  -3.1369 0.0000
spt 29 x -27.5772 -23.1409 0.0000
spt 30 x -27.5772 -26.1630 0.0000
```



```
spt 31 x -26.1630 -27.5772 0.0000
spt 32 x -23.1409 -27.5772 0.0000
spt 33 x  -3.1369 -35.8631 0.0000
spt 34 x  -1.0000 -38.0000 0.0000
spt 35 x   1.0000 -38.0000 0.0000
spt 36 x   3.1369 -35.8631 0.0000
spt 37 x  23.1409 -27.5772 0.0000
spt 38 x  26.1630 -27.5772 0.0000
spt 39 x  27.5772 -26.1630 0.0000
spt 40 x  27.5772 -23.1409 0.0000

sln  1 npa  1  2 fix pp
sln  2 npa  2  3 fix pp
sln  3 npa  3  4 fix pp
sln  4 npa  4  1 fix pp
sln  5 npa  5  6 ; slnb xm 0 0 0
sln  6 npa  6  7 ; slnb xm 0 0 0
sln  7 npa  7  8 ; slnb xm 0 0 0
sln  8 npa  8  5 ; slnb xm 0 0 0
sln  9 npa  9 10
sln 10 npa 10 11
sln 11 npa 11 12
sln 12 npa 12 13 ; slnb xm 0 0 0
sln 13 npa 13 14
sln 14 npa 14 15
sln 15 npa 15 16
sln 16 npa 16 17 ; slnb xm 0 0 0
sln 17 npa 17 18
sln 18 npa 18 19
sln 19 npa 19 20
sln 20 npa 20 21 ; slnb xm 0 0 0
sln 21 npa 21 22
sln 22 npa 22 23
sln 23 npa 23 24
sln 24 npa 24 25 ; slnb xm 0 0 0
sln 25 npa 25 26
sln 26 npa 26 27
sln 27 npa 27 28
sln 28 npa 28 29 ; slnb xm 0 0 0
sln 29 npa 29 30
sln 30 npa 30 31
sln 31 npa 31 32
sln 32 npa 32 33 ; slnb xm 0 0 0
sln 33 npa 33 34
sln 34 npa 34 35
sln 35 npa 35 36
sln 36 npa 36 37 ; slnb xm 0 0 0
sln 37 npa 37 38
sln 38 npa 38 39
sln 39 npa 39 40
sln 40 npa 40  9 ; slnb xm 0 0 0

sar 1 grp 1 mnr 1 t 1000 mctl regm bez 'inclinometer pipe'
sarb out 5,6,7,8
sarb in 9,10,11,12,13,14,15,16,17,18,19,20,21,22,23,24,25,26,27,28,29,30,31,32,33,34,35,36,37,38,39,40

sar 2 grp 2 mnr 2 t 1000 mctl regm bez 'dummy layer'
sarb out 1,2,3,4
sarb in 5,6,7,8

ende
```

```
!#!Kapitel Load cases
+prog sofiload
kopf Load cases
echo voll

lf 1 bez 'load angle 2 x 90°'
line sln 5 typ pz p1 100
line sln 7 typ pz p1 100

ende

!#!Kapitel Calculation
+prog talpa
kopf Calculation
echo voll

steu solv 4

lf 1

ende
```

```
$------------------------------------------------------------------------------------------------------------
$ Graz University of Technology; Institute of Soil Mechanics, Foundation Engineering and Computational Ge
$ Master's thesis "Investigations on the horizontal stress state of non-cohesive soils due to deep vibro
$ LC2_SOFiSTiK_3D-unconstrained_without_4-elements
$ CADINP-based creation of the FE-calculation model with SOFiSTiK
$ Created by Daniel Gasser, Dipl.-Ing., BSc
$------------------------------------------------------------------------------------------------------------

+sys del $(projekt).cdb

!#!Kapitel Materials
+prog aqua
kopf Materials
echo voll

mate 1 e 2500 mue 0.34 gam 0 bez 'inclinometer pipe'

ende

!#!Kapitel System
+prog sofimshc
kopf Cross section
echo voll voll

syst 3D gdir negz gdiv 1000000
seit unie 7
steu tolg 0.0001
steu mesh 66 $ 34
steu hmin 10[mm]
steu deln 0

sto#H 3*10^3

spt  1 x  33.2597 -13.7766 0.0000
spt  2 x  38.8029 -16.0727 0.0000
spt  3 x  38.8029  16.0727 0.0000
spt  4 x  33.2597  13.7766 0.0000
spt  5 x  38.8029 -16.0727 #H

sln  1 npa  1  2
sln  2 npa  2  3 ; slnb xm 0 0 0
sln  3 npa  3  4
sln  4 npa  4  1 ; slnb xm 0 0 0
sln  5 npa  2  5

sar 1 grp 1 mnr 1 t 0 mctl regm h1 1.5[mm]
sarb out 1,2,3,4

ende

+prog sofimsha
kopf Extrusion & Rotation
echo voll voll

syst rest

bric prop mnr 1
grup 2
extr quad von sar 1 path sln 5
tran bric grp 2 phiz 45
tran bric grp 2 phiz 90
tran bric grp 2 phiz 180
```



```
quad prop mnr 1 t 0 kr negz
grup 3
extr sln von sln 2 path sln 5
tran quad grp 3 phiz 45
tran quad grp 3 phiz 180

grup 1
tran quad grp 1 phiz 45
tran quad grp 1 phiz 90
tran quad grp 1 phiz 180
fede qgrp 1 dz -1 cp 1e10

let#xmin -50.0000[mm]
let#ymin -50.0000[mm]
let#zmin   0.0000[mm]
let#xmax  50.0000[mm]
let#ymax  50.0000[mm]
let#zmax   0.0000[mm]
mod knot xmin #xmin ymin #ymin zmin #zmin xmax #xmax ymax #ymax zmax #zmax fix zp
let#xmin -50.0000[mm]
let#ymin -50.0000[mm]
let#zmin       #H[mm]
let#xmax  50.0000[mm]
let#ymax  50.0000[mm]
let#zmax       #H[mm]
mod knot xmin #xmin ymin #ymin zmin #zmin xmax #xmax ymax #ymax zmax #zmax fix zp

ende

!#!Kapitel Load cases
+prog sofiload
kopf Load cases
echo voll

lf 1 bez 'load angle 2 x 90°'
quad grp 3 typ pz p 100

ende

!#!Kapitel Calculation
+prog ase
kopf Calculation
echo voll

steu solv 4

lf alle

ende
```

```
$------------------------------------------------------------------------------------------------------------
$ Graz University of Technology; Institute of Soil Mechanics, Foundation Engineering and Computational Ge
$ Master's thesis "Investigations on the horizontal stress state of non-cohesive soils due to deep vibro
$ LC2_SOFiSTiK_3D-unconstrained_with_4-elements
$ CADINP-based creation of the FE-calculation model with SOFiSTiK
$ Created by Daniel Gasser, Dipl.-Ing., BSc
$------------------------------------------------------------------------------------------------------------

+sys del $(projekt).cdb

!#!Kapitel Materials
+prog aqua
kopf Materials
echo voll

mate 1 e 2500 mue 0.34 gam 0 bez 'inclinometer pipe'

ende

!#!Kapitel System
+prog sofimshc
kopf Cross section
echo voll voll

syst 3D gdir negz gdiv 1000000
seit unie 7
steu tolg 0.0001
steu mesh 66 $ 34
steu hmin 10[mm]
steu deln 0

sto#H 3*10^3

spt  1 x  33.2597 -13.7766 0.0000
spt  2 x  38.8029 -16.0727 0.0000
spt  3 x  38.8029  16.0727 0.0000
spt  4 x  33.2597  13.7766 0.0000
spt  5 x  35.8631   3.1369 0.0000
spt  6 x  38.0000   1.0000 0.0000
spt  7 x  38.0000  -1.0000 0.0000
spt  8 x  35.8631  -3.1369 0.0000
spt  9 x  38.8029 -16.0727 #H

sln  1 npa  1  2
sln  2 npa  2  3 ; slnb xm 0 0 0
sln  3 npa  3  4
sln  4 npa  4  5 ; slnb xm 0 0 0
sln  5 npa  5  6
sln  6 npa  6  7
sln  7 npa  7  8
sln  8 npa  8  1 ; slnb xm 0 0 0
sln  9 npa  2  9

sar 1 grp 1 mnr 1 t 0 mctl regm h1 1.25[mm]
sarb out 1,2,3,4,5,6,7,8

ende

+prog sofimsha
kopf Extrusion & Rotation
echo voll voll
```



```
syst rest

bric prop mnr 1
grup 2
extr quad von sar 1 path sln 9
tran bric grp 2 phiz 45
tran bric grp 2 phiz 90
tran bric grp 2 phiz 180

quad prop mnr 1 t 0 kr negz
grup 3
extr sln von sln 2 path sln 9
tran quad grp 3 phiz 45
tran quad grp 3 phiz 180

grup 1
tran quad grp 1 phiz 45
tran quad grp 1 phiz 90
tran quad grp 1 phiz 180
fede qgrp 1 dz -1 cp 1e10

let#xmin -50.0000[mm]
let#ymin -50.0000[mm]
let#zmin   0.0000[mm]
let#xmax  50.0000[mm]
let#ymax  50.0000[mm]
let#zmax   0.0000[mm]
mod knot xmin #xmin ymin #ymin zmin #zmin xmax #xmax ymax #ymax zmax #zmax fix zp
let#xmin -50.0000[mm]
let#ymin -50.0000[mm]
let#zmin       #H[mm]
let#xmax  50.0000[mm]
let#ymax  50.0000[mm]
let#zmax       #H[mm]
mod knot xmin #xmin ymin #ymin zmin #zmin xmax #xmax ymax #ymax zmax #zmax fix zp

ende

!#!Kapitel Load cases
+prog sofiload
kopf Load cases
echo voll

lf 1 bez 'load angle 2 x 90°'
quad grp 3 typ pz p 100

ende

!#!Kapitel Calculation
+prog ase
kopf Calculation
echo voll

steu solv 4

lf alle

ende
```

7 External contributions

IDM-Erddruckmessungen zum Nachweis des Einflusses der Tiefenverdichtung

Markus Schwager, 5.12.2017

Aus theoretischer Sicht kann sowohl nummerisch wie auch analytisch beliebige horizontale Erddruckänderungen (d.h. jegliche Kombination von $\Delta\sigma_1$ und $\Delta\sigma_2$) mithilfe von IDM-Messungen bestimmt werden.

Aus praktischer Sicht sollte jedoch (a) der Sensitivität aufgrund des Randwertproblems und (b) der Verlässlichkeit der Verformungsmessung Beachtung geschenkt werden. Im Folgenden werden diese beiden Einflüsse diskutiert.

a) Sensitivität aufgrund des Randwertproblems

Unter der Voraussetzung einer beliebig genauen Messung könnte eine beliebige Kombination von $\Delta\sigma_1$ und $\Delta\sigma_2$ rückgerechnet werden. Hierzu ist mithilfe nummerischer Verfahren das Minimum der in Abbildung 1 beispielhaft gezeigten Zielfunktion F zu finden. Dieselbe Lösung kann auch analytisch gefunden werden.

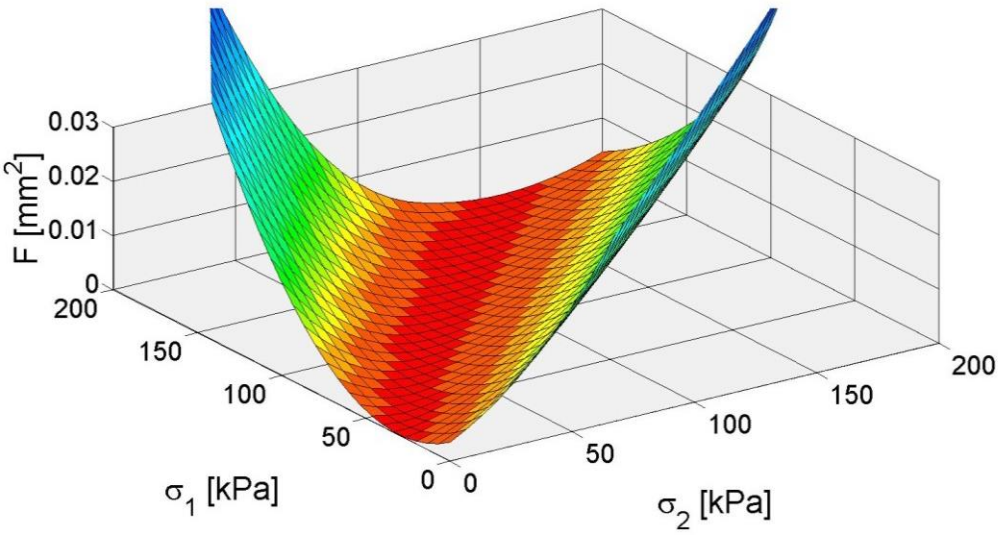

Abbildung 1

Die Zielfunktion F weist je nach Richtung eine stark unterschiedliche Krümmung auf. Somit ist die Sensitivität bei der Bestimmung der Erddrücke sehr unterschiedlich, je nachdem in welche Richtung man sich auf der Zielfunktion bewegt.

Um dennoch zu einer eindeutigen Lösung zu gelangen, können weitere Annahmen zu den Randbedingungen getroffen werden. Hierzu seien zwei Spezialfälle betrachtet (vgl. Abbildung 2):

Fall 1 : $\Delta\sigma_1 = \Delta\sigma_2$
Fall 2: $\Delta\sigma_1 = \nu_s \Delta\sigma_2$ (ebener Fall mit behinderten Verschiebungen zur Seite hin, $K_0 = \nu_s$)

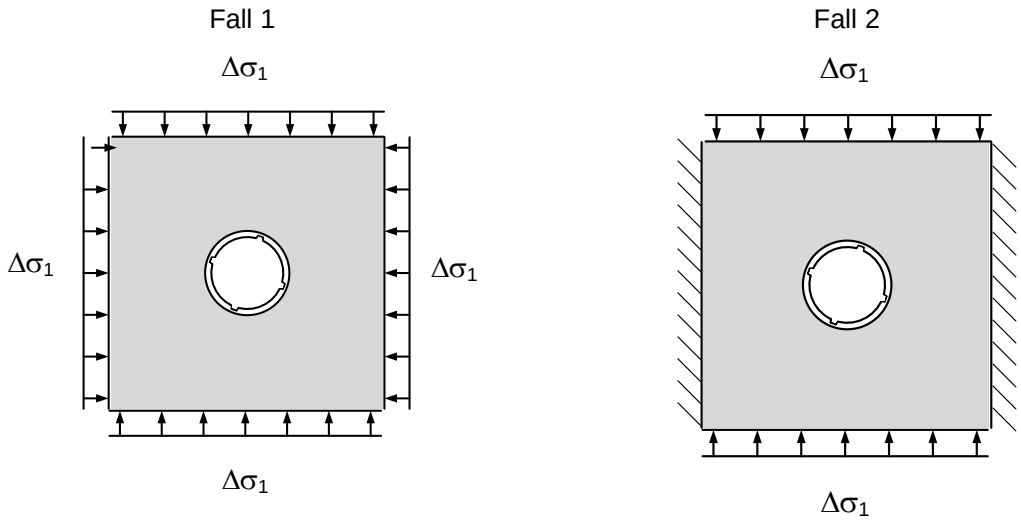

Abbildung 2

Beide Spezialfälle entsprechen einem ebenen Schnitt durch die Zielfunktion (vgl. Abbildung 1). Im Fall 1 ist die Krümmung der Zielfunktion und somit auch die Sensitivität deutlich geringer als im Fall 2:

Fall 1: $\Delta\sigma_1/\Delta D \approx 3.3\mathrm{kPa}/\mu\mathrm{m}$
Fall 2: $\Delta\sigma_1/\Delta D \approx 0.2\mathrm{kPa}/\mu\mathrm{m}$ (vgl. Abbildung 2-11 in der Dissertation)

Für den Feldversuch sind möglichst eindeutige Randbedingungen anzustreben. Nach Möglichkeit ist der ungünstige Fall 1 zu vermeiden. Der Fall 2 ist zu bevorzugen.
Sollen gleichmässige Druckänderungen aufgebracht werden, so sollen diese ausreichend gross sein, sodass diese trotz verringerter Sensitivität zuverlässig gemessen werden können.

b) Verlässlichkeit der Verformungsmessung

Gleichmässige und ungleichmässige Erddruckänderungen bedeuten auch unterschiedliche Anforderungen an die Messtechnik. Während gleichmässige Erddruckänderungen abhängig sind von der absoluten Durchmesseränderung, sind ungleichmässige Erddruckänderungen abhängig von der Ovalisierungsänderung:

Gleichmässige Erddruckänderungen, Fall1: $\Delta\sigma_1 = f(\Delta D)$
Ungleichmässige Erddruckänderungen, z.B. Fall 2: $\Delta\sigma_1 = f(\Delta\Omega) = f(A)$

Um die Ovalisierung festzustellen, ist es ausreichend die Differenz einzelner Durchmesser innerhalb einer Folgemessung zu detektieren; eine relative Messung der Durchmesser genügt. Systematische Unterschiede, welche zwischen den Folgemessungen auftreten, werden so eliminiert. Muss hingegen die absolute Durchmesseränderung gemessen werden, so werden diese systematischen Unterschiede nicht eliminiert. Die Messung der relevanten Rohrverformung ist somit bei ungleichmässigen Erddruckänderungen erheblich zuverlässiger als bei gleichmässigen Erddruckänderungen.

Sollen gleichmässige Erddruckänderungen festgestellt werden können, so ist vorzugsweise die Möglichkeit zu schaffen, systematische Unterschiede zwischen den Folgemessungen feststellen und berücksichtigen zu können.
Dies könnte geschehen, indem der Feldversuch so gestaltet würde, dass über einen bestimmten Rohrabschnitt hinweg keine Rohrverformungen zu erwarten wären.
So könnte beispielsweise das Inklinometerrohr deutlich tiefer vorgesehen werden, als die Tiefenwirkung der Verdichtung reicht. Alternativ könnte die Verrohrung über einen bestimmten Bereich im Bohrloch belassen werden, um das Inklinometerrohr von Erddruckänderungen abzuschirmen. Es wäre auch denkbar, das Bohrloch über einen bestimmten Bereich mit Beton zu verfüllen.

IDM-Erddruckmessungen zum Nachweis des Einflusses der Tiefenverdichtung (2)

Markus Schwager, 15.01.2018

Die Bestimmung der horizontalen Erddruckänderungen (d.h. einer Kombination von $\Delta\sigma_1$ und $\Delta\sigma_2$) ist deutlich verlässlicher, falls neben der Zielfunktion F (vgl. Abbildung 1 in Dokument 1) eine zweite Beziehung zwischen $\Delta\sigma_1$ und $\Delta\sigma_2$ vorliegt, welche sich üblicherweise aus den Randbedingungen ergibt (vgl. Abbildung 2 in Dokument 1).
Kann solch eine Beziehung gefunden werden, so kann die Berechnung der Erddruckänderungen mithilfe analytischer Lösungen erfolgen. Liegt keine solche Beziehung vor, so können die Erddruckänderungen bestimmt werden, indem mithilfe einer FE-Modellierung der ganzen Geometrie (d.h. der Stopfsäulen und der Inklinometerrohre) diejenige Spannungsänderung in der Stopfsäule gesucht wird, welche den Verformungen des Inklinometerrohres entspricht.

Im Folgenden sei eine solche Beziehung für die gegebene radialsymmetrische Geometrie einer einzelnen Stopfsäule vorgeschlagen.

a) Beziehung zwischen $\Delta\sigma_1$ und $\Delta\sigma_2$ unter Annahme elastischen Bodenverhaltens

Betrachtet wird eine horizontale elastische Scheibe im ebenen Spannungszustand ($\Delta\sigma_z = 0$). Die Scheibe sei radialsymmetrisch; der initiale Spannungszustand sei $\sigma_r = \sigma_t = \sigma_0$ (vgl. Abbildung 1). Am Rand der Stopfsäule wird die Spannung $\sigma_r(r = r_{StS}) = \sigma_{StS}$ aufgebracht.

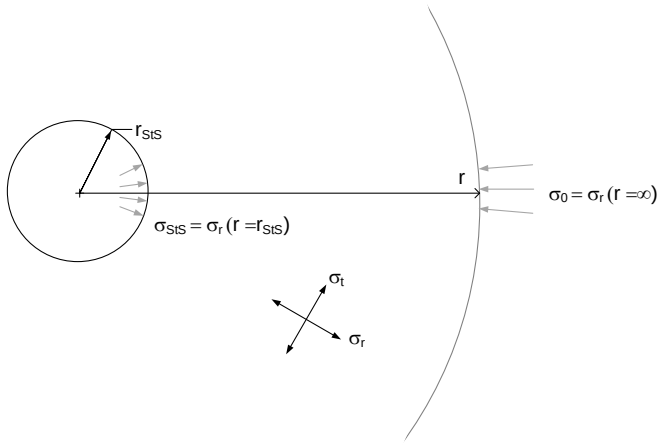

Abbildung 2: Randwertproblem gegeben durch eine radialsymmetrische Scheibe.

Aus dem Hookschen Gesetz folgt

$$\varepsilon_r = \frac{1}{E}\left((\sigma_r - \sigma_0) - \nu(\sigma_t - \sigma_0)\right) \quad (1)$$

$$\varepsilon_t = \frac{1}{E}\left((\sigma_t - \sigma_0) - \nu(\sigma_r - \sigma_0)\right) \quad (2)$$

$$\varepsilon_z = -\frac{\nu}{E}\left((\sigma_r - \sigma_0) + (\sigma_t - \sigma_0)\right) \quad (3)$$

Die kinematischen Relationen sind

$$\varepsilon_{\mathrm{r}} = \frac{\mathrm{d}u}{\mathrm{d}r} \tag{4}$$

$$\varepsilon_{\mathrm{t}} = \frac{u}{r} \tag{5}$$

Aus Gleichgewicht folgt

$$\frac{\mathrm{d}\sigma_{\mathrm{r}}}{\mathrm{d}r} = \frac{\sigma_{\mathrm{t}} - \sigma_{\mathrm{r}}}{r} \tag{6}$$

Aus (4) und (5) folgt

$$\varepsilon_{\mathrm{r}} = \varepsilon_{\mathrm{t}} + r\frac{\mathrm{d}\varepsilon_{\mathrm{t}}}{\mathrm{d}r} \tag{7}$$

Setzt man (1) und (2) in (7) ein, so ergibt sich

$$(1+\nu)\frac{\sigma_{\mathrm{r}} - \sigma_{\mathrm{t}}}{r} = \frac{\mathrm{d}\sigma_{\mathrm{t}}}{\mathrm{d}r} - \nu\frac{\mathrm{d}\sigma_{\mathrm{r}}}{\mathrm{d}r} \tag{8}$$

Setzt man anschliessend (6) in (8) ein, so findet man

$$\frac{\mathrm{d}\sigma_{\mathrm{r}}}{\mathrm{d}r} = -\frac{\mathrm{d}\sigma_{\mathrm{t}}}{\mathrm{d}r} \tag{9}$$

Eine Zunahme von σ_{r} bewirkt also eine betragsmässig gleiche Abnahme von σ_{t}. Deshalb muss die Summe von σ_{r} und σ_{t} konstant sein. Es gilt somit

$$\sigma_{\mathrm{r}} + \sigma_{\mathrm{t}} = 2\sigma_0 \tag{10}$$

Ersetzt man in (8) σ_{t} mithilfe von (9) und (10), so folgt

$$2\sigma_{\mathrm{r}} + r\frac{\mathrm{d}\sigma_{\mathrm{r}}}{\mathrm{d}r} = 2\sigma_0 \tag{11}$$

Unter Berücksichtigung der Randbedingung $\sigma_{\mathrm{r}}(r = r_{\mathrm{StS}}) = \sigma_{\mathrm{StS}}$ ergeben sich die Lösungen

$$\sigma_{\mathrm{r}}(r) = \sigma_0 - (\sigma_0 - \sigma_{\mathrm{StS}})\left(\frac{r_{\mathrm{StS}}}{r}\right)^2 \tag{12}$$

$$\sigma_{\mathrm{t}}(r) = \sigma_0 + (\sigma_0 - \sigma_{\mathrm{StS}})\left(\frac{r_{\mathrm{StS}}}{r}\right)^2 \tag{13}$$

Die Erddruckänderungen ($\Delta\sigma_{\mathrm{r}} = \sigma_{\mathrm{r}} - \sigma_0; \Delta\sigma_{\mathrm{t}} = \sigma_{\mathrm{t}} - \sigma_0$) ergeben sich somit zu

$$\Delta\sigma_{\mathrm{r}}(r) = \Delta\sigma_{\mathrm{StS}}\left(\frac{r_{\mathrm{StS}}}{r}\right)^2 \tag{14}$$

$$\Delta\sigma_{\mathrm{t}}(r) = -\Delta\sigma_{\mathrm{StS}}\left(\frac{r_{\mathrm{StS}}}{r}\right)^2 \tag{15}$$

Daraus folgt die Beziehung zwischen $\Delta\sigma_1$ und $\Delta\sigma_2$

$$\frac{\Delta\sigma_{\mathrm{t}}}{\Delta\sigma_{\mathrm{r}}} = \frac{\Delta\sigma_2}{\Delta\sigma_1} = -1 \tag{16}$$

b) Beziehung zwischen $\Delta\sigma_1$ und $\Delta\sigma_2$ unter Annahme elasto-plastischen Bodenverhaltens

Gehen von der Randbedingung $\sigma_r(r = r_{StS}) = \sigma_{StS}$ grosse Drücke aus, so bildet sich eine plastische Zone um die Stopfsäule. Unter Annahme undrainierter Verhältnisse ergibt sich das Kriterium für ein Versagen in der Ebene nach Tresca zu

$$\sigma_r - \sigma_t = 2s_u \tag{17}$$

Es bleibt zu prüfen, ob es allenfalls auch zu einem Versagen aus der Ebene d.h. zu einem passiven Bruch zur Geländeoberfläche hin kommen kann.

Innerhalb der plastischen Zone gilt (17) und (6). Es folgt daraus

$$\frac{d\sigma_r}{dr} = -\frac{2s_u}{r} \tag{18}$$

Unter Berücksichtigung der Randbedingung $\sigma_r(r = r_{StS}) = \sigma_{StS}$ ergeben sich die Lösungen

$$\sigma_r(r) = \sigma_{StS} + 2s_u \ln\left(\frac{r_{StS}}{r}\right) \tag{19}$$

$$\sigma_t(r) = \sigma_{StS} + 2s_u \left(\ln\left(\frac{r_{StS}}{r}\right) - 1\right) \tag{20}$$

Die Erddruckänderungen ($\Delta\sigma_r = \sigma_r - \sigma_0; \Delta\sigma_t = \sigma_t - \sigma_0$) ergeben sich somit zu

$$\Delta\sigma_r(r) = \Delta\sigma_{StS} + 2s_u \ln\left(\frac{r_{StS}}{r}\right) \tag{21}$$

$$\Delta\sigma_t(r) = -\Delta\sigma_{StS} + 2s_u \left(\ln\left(\frac{r_{StS}}{r}\right) - 1\right) \tag{22}$$

An der äusseren Begrenzung der plastischen Zone (d.h. bei Radius r_{pl}) gilt sowohl (10), (17) wie auch (19). Es folgt

$$r_{pl} = r_{StS} e^{\frac{\sigma_{StS} - \sigma_0}{2s_u} - \frac{1}{2}} \tag{23}$$

Ausserhalb der plastischen Zone ($r \geq r_{pl}$) gelten die elastischen Beziehungen (12) und (13). Die Randbedingung ist jedoch anzupassen: $r_{StS} = r_{pl}$; $\sigma_{StS} = \sigma_r(r_{pl})$.

Der Verlauf von σ_r und σ_t ist in Abbildung 2 dargestellt.

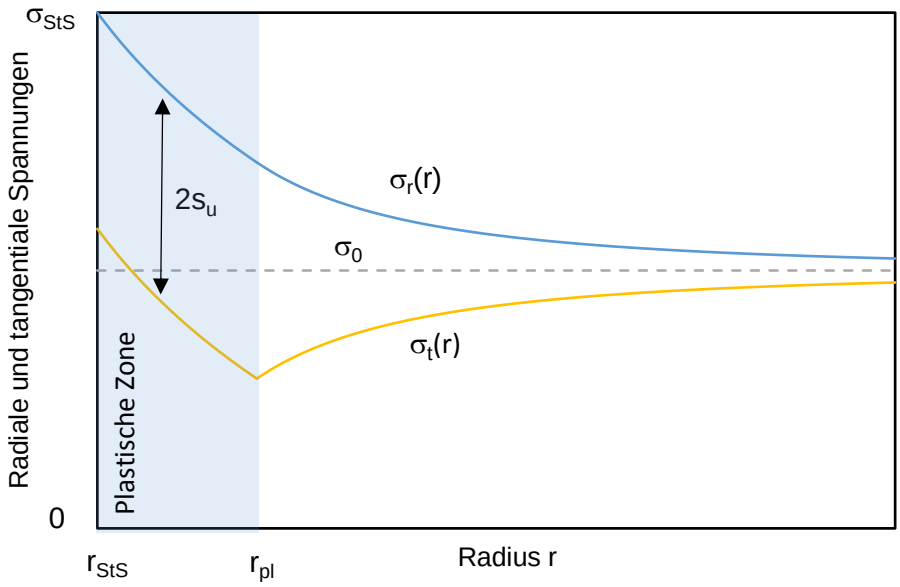

Abbildung 2: Verlauf von σ_r und σ_t mit zunehmendem Abstand von der Stopfsäule.

c) Schlussfolgerungen

Sowohl innerhalb wie ausserhalb der plastischen Zone konnte eine Beziehung zwischen $\Delta\sigma_1$ und $\Delta\sigma_2$ gefunden werden.

Für $r \leq r_{pl}$: $\Delta\sigma_1 - \Delta\sigma_2 = 2s_u$

Für $r \geq r_{pl}$: $\frac{\Delta\sigma_2}{\Delta\sigma_1} = -1$

Diese beiden Beziehungen ermöglichen allenfalls eine verlässlichere Bestimmung der Erddruckänderungen.

d) Anmerkungen zum Setup des Grossversuchs

Aus obigen Überlegungen ergeben sich drei Folgerungen für das Setup des Grossversuchs:

1) Die Spannungszustände ausserhalb der plastischen Zonen (d.h. in den elastisch bleibenden Bereichen) können superponiert werden. Liegen die Inklinometerrohre in diesen elastisch bleibenden Bereichen, so können die durch die Stopfsäulen (1, 2 und 3) verursachten Spannungsänderungen in einer ersten Näherung unabhängig von der Spannungsgeschichte bestimmt werden. Liegen die Inklinometerrohre jedoch innerhalb der plastischen Zonen einzelner Stopfsäulen, so gestaltet sich die Interpretation der gemessenen Rohrverformungen deutlich schwieriger.

   Zudem führt die Beziehung zwischen $\Delta\sigma_1$ und $\Delta\sigma_2$ in den elastisch bleibenden Bereichen zu grösseren Rohrverformungen, da die beiden Hauptspannungsinkremente ein unterschiedliches Vorzeichen aufweisen. Die Sensitivität der IDM-Erddruckmessungen ist somit in den elastisch bleibenden Bereich vermutlich grösser als in den plastischen Zonen.

   Nach Möglichkeit sind deshalb die Abstände von den Inklinometerrohren zu den Stopfsäulen so vorzusehen, dass die Inklinometerrohre ausserhalb möglicher plastischer Zonen liegen. Dies vereinfacht die Interpretation der gemessenen Rohrverformungen und erhöht vermutlich die Genauigkeit der Erddruckbestimmung.

2) Zudem sollen in den Inklinometerrohren nach Möglichkeit auch die Horizontalverschiebungen gemessen werden (herkömmliche Inklinometermessung). Anhand der mittleren Dehnung zwischen den Inklinometerrohren und den Stopfsäulen kann allenfalls beurteilt werden, ob plastische Verformungen aufgetreten sind.

3) Je homogener der initiale Spannungszustand ist, desto einfacher ist die Interpretation der gemessen Rohrverformungen. Nach Möglichkeit soll deshalb die Stopfsäule 1 als allererste Stopfsäule erstellt werden.